Nanodosimetric Properties of Very High Energy Electrons through pBR322 Plasmid DNA Studies

A thesis submitted to the University of Manchester for
the degree of Doctor of Philosophy
in the Faculty of Science and Engineering

2020

Kristina L. Small

Contents

Word Count: 50044

Abstract

1 in 2 people will suffer from cancer during their lifetime and, in the UK, around a third of patients will be treated with radiotherapy, primarily with X-rays. Three decades of research and development into high-gradient linear accelerator technology has resulted in Very High Energy Electrons (VHEE) in the range 100-250 MeV being a potentially viable radiotherapy modality. Advantageous characteristics of VHEE include sufficient penetrative range to treat deep-seated tumours, measured relative insensitivity to inhomogeneities, reduced lateral penumbra and improved dose distribution. VHEE beams can be delivered and controlled rapidly using scanning magnets, making it a candidate for FLASH radiotherapy, a technique involving treatment at ultra-high dose rates – *in vitro* and *in vivo* studies present strong evidence of a normal tissue sparing effect.

For successful translation of VHEE theory to the clinic, we must understand the effects of VHEE on fundamental biological structures and how these effects compare with well-established modalities. To achieve this, a dose conversion known as Relative Biological Effectiveness (RBE) is required.

The primary aim of this project was to quantify the characteristics of VHEE RBE and to compare with other radiotherapy modalities. Traditionally, cell survival is used to measure RBE *in vitro,* however survival is the end-point of a damage and repair process. To gain fundamental understanding of the biological difference between VHEE and other modalities, it is necessary to separate the nanodosimetric physics qualities of VHEE by looking directly at how damage is induced. DSB yield was therefore selected as the endpoint for RBE calculation, determined following a series of pBR322 plasmid irradiation experiments, the first of their kind for VHEE, at the CLEAR user facility (CERN, 100-200 MeV) and the Christie NHS Foundation Trust (6-15 MeV). ^{60}Co X-ray irradiation provided a reference point for RBE calculations. VHEE RBE varied from 1.1-1.2 over 100-200 MeV, indicating that physical effects of VHEE are similar to that of established modalities. This provides confidence that biological effects including cell death will also be similar – a key step on the road to clinical implementation.

Experimental DSB yields were compared with GEANT4-DNA plasmid irradiation simulations of electron track structure, with the aim of producing an accurate Monte Carlo model of VHEE-induced DNA damage. This involved the adaptation of GEANT4-DNA physics constructors to allow modelling of electron track structure above 1 MeV. Parameter optimisation resulted in good agreement between GEANT4-DNA and experimental DSB yields. These damage mechanisms could then be applied to the modelling of biological effects such as DNA damage repair and cell death, with predictions informing treatment planning for clinical cases.

As VHEE has been highlighted as a compatible modality for FLASH, a dose-rate variation study was carried out at the CLEAR facility to determine whether a FLASH effect could be observed when irradiating pBR322 DNA at ultra-high dose rates, presenting as a significant decrease in DSB yield. As plasmid

irradiation experiments lack many key features causing a FLASH effect (primarily well-oxygenated water), variation between Conventional and FLASH-irradiated samples was not expected. No statistically significant difference between DNA damage yields was observed, it can be suggested that a FLASH effect is not present at the nanoscale under these conditions.

A secondary aim of the research was to investigate the range of VHEE beams in various tissues. As part of the steps towards clinical implementation of VHEE, an understanding of the behaviour of treatment beams inside the patient is vital from a treatment planning point of view. As part of this research, a semi-empirical expression for VHEE beam range was produced, dependent on beam energy and the composition of the material through which it travels, using data from simulations of VHEE beams travelling through different media using TOPAS.

Declaration

No portion of the work referred to in the thesis has been submitted in support of an application for another degree or qualification of this or any other university or other institute of learning.

Copyright

1. The author of this thesis (including any appendices and/or schedules to this thesis) owns certain copyright or related rights in it (the "Copyright") and s/he has given The University of Manchester certain rights to use such Copyright, including for administrative purposes.

2. Copies of this thesis, either in full or in extracts and whether in hard or electronic copy, may be made only in accordance with the Copyright, Designs and Patents Act 1988 (as amended) and regulations issued under it or, where appropriate, in accordance with licensing agreements which the University has from time to time. This page must form part of any such copies made.

3. The ownership of certain Copyright, patents, designs, trademarks and other intellectual property (the "Intellectual Property") and any reproductions of copyright works in the thesis, for example graphs and tables ("Reproductions"), which may be described in this thesis, may not be owned by the author and may be owned by third parties. Such Intellectual Property and Reproductions cannot and must not be made available for use without the prior written permission of the owner(s) of the relevant Intellectual Property and/or Reproductions.

4. Further information on the conditions under which disclosure, publication and commercialisation of this thesis, the Copyright and any Intellectual Property and/or Reproductions described in it may take place is available in the University IP Policy (see http://documents.manchester.ac.uk/DocuInfo.aspx?DocID=2442 0), in any relevant Thesis restriction declarations deposited in the University Library, The University Library's regulations (see http://www.library.manchester.ac.uk/about/regulations/) and in The University's policy on Presentation of Theses

Acknowledgements

I would firstly like to thank my supervisors, Roger Jones and Michael Merchant for their guidance, encouragement and above all support over the past four years. Throughout my PhD, I have been able to rely on their knowledge and expertise to help me solve the various problems I have had in my studies.

Secondly, thank you to my friends and colleagues in the MEW group, Louie Hancock, Lucy Whitmore, Pip van den Elzen and Nathan Roche. Aside from providing valuable feedback as I wrote my thesis, you have made journeys to and from the Cockcroft a little bit easier.

I would also like to thank various members of the PRECISE group at the Christie, including Karen Kirkby for supporting my experiments, Adam Aitkenhead for his scanning expertise and Amy Chadwick, Elham Santina and Rebecca Morris for their unending patience in teaching a physicist how to be a biologist (sort of). Special thanks to my lab partner Nicholas Henthorn, for helping to plan and run the plasmid experiments, providing a lot of coding support and cutting the time spent running gels in half.

Regarding experiments, I must of course thank the groups at the various facilities I have worked at during the course of my PhD. Thanks to Wilfrid Farabolini, Roberto Corsini, Davide Gamba and Antonio Gilardi at CLEAR, to Deepa Angal-Kalinin, James Jones, Mark Surman and Rob Smith at Daresbury Laboratories and Ruth Edge and Andy Smith at the Dalton Cumbrian Facility.

I also have to thank my family, particularly Mum and Dad, who have been a constant source of love and support during these past four years – particularly when the going got tough. They have always encouraged and inspired me to become a scientist and have provided plenty of laughs and pictures of Lottie the dog along the way.

Finally, thank you to Ben. Along with listening to every complaint over four years and living with my forgetfulness, he has also spent seven months in lockdown while I wrote this and still wants to marry me. He's awesome.

Chapter 1 – Introduction

1.1. Motivation and Aims

Radiotherapy, the use of ionising radiation to kill cancer cells, is used in the treatment of 40% of successfully treated cancer patients. Various modalities are used, including photons, low-energy electrons and, as of 2018 in the UK, high-energy protons.

This project investigates the use of Very High Energy Electrons (VHEE) in the energy range 100-250 MeV as a potential modality for radiotherapy treatment. Initially proposed as a potential radiotherapy modality in 2000[1], VHEE beams have demonstrated, through computational and experimental studies, several beneficial characteristics for clinical treatment. These include increased penetrative range for treatment of deep-seated tumours[2], insensitivity to inhomogeneities[3,4] and improved dose conformality[5,6], reducing the radiation dose delivered to healthy tissues compared to conventional X-ray plans. Methods of VHEE dosimetry have also been investigated[7], allowing the dose delivered by a VHEE beam to be accurately measured – a key requirement for clinical use.

While there have been several investigations into the physical behaviour of VHEE beams there have been, at time of writing, no investigations into VHEE radiobiology to indicate if VHEE therapy could be an effective treatment. Radiobiology, the study of ionising radiation on living structures, is vital to understand the effects which VHEE irradiation can have on the body and how these effects compare with those caused by irradiation with clinically established radiotherapy modalities. This is a key step on the path to clinical implementation of VHEE therapy – *in vitro* and *in vivo* experiments can be used to prove the efficacy of VHEE therapy compared with other modalities, providing a strong argument for their clinical use.

The aim of this project was therefore to study the fundamental biological effects of VHEE radiotherapy. It is widely accepted that DNA damage is the primary mechanism resulting in cell death following exposure to ionising radiation, in particular single- and double-strand breaks (SSBs and DSBs respectively). The measurement of single- and double-strand breaks following irradiation by

VHEE radiation was therefore focused on. The double-strand break yield was then used to calculate the Relative Biological Effectiveness (RBE) of VHEE – defined as the ratio of biological effectiveness of one type of radiation relative to a reference radiation type, typically ^{60}Co X-rays, given the same dose.

RBE gives a direct clinical comparison between the effectiveness of different radiotherapy modalities – protons, for example, have a generalised RBE value of 1.1. RBE can be measured based on a variety of biological endpoints, including DSB yield and, most commonly, cell survival fraction. While there is, at time of writing, no experimental data available on RBE of electrons above 50 MeV, studies at current clinical energies support the clinical assumption that 6-15 MeV electrons have an RBE of 1. As electrons at the clinical VHEE range (100-250 MeV), like photons, have a low Linear Energy Transfer (LET), it is hypothesised that VHEE will have a similar effect on DNA as photons and hence an RBE close to 1.

Determining DNA damage yields and so calculating VHEE RBE_{DSB} was achieved through a series of plasmid experiments at various facilities both in the UK and abroad, outlined in Table 1 below. Plasmids are an excellent biological tool to measure DNA damage with caused by different radiation modalities - they have no repair mechanisms, allowing pure damage to be measured and can be irradiated in wet and dry environments, allowing contributions of direct and indirect radiation effects to be compared (explained in more detail in section 1.4.)

Facility	Radiotherapy Modality	Date
CLARA, Daresbury Laboratory	20-40 MeV electrons	Dec 2018, Jan 2019
Dalton Nuclear Facility	Co-60 X-rays	Feb 2019
Christie NHS Foundation Trust	6-15 MeV electrons	Apr 2019
CLEAR, CERN	100-200 MeV electrons	Jul 2019

Table 1 – Details of experiments carried out during the PhD, including facility, radiotherapy modality and date

The plasmid experiment at CERN was the world's first study on DNA irradiation with VHEE beams. Resulting experimental DNA damage yields could then be compared with those from detailed plasmid irradiation simulations carried out using the Monte Carlo track structure code GEANT4 (version 4.10.2)[8] – a well-established code widely used for radiotherapy modelling. The GEANT4-DNA module will be used to model the plasmid DNA irradiation.

Interest in FLASH therapy, the delivery of ultra-high dose rate (>40 Gy/s) radiotherapy, has been rapidly growing due to observations of significant sparing of healthy tissue and reduced radiation-induced side effects. As part of this project, the first studies on the biological effects of VHEE FLASH radiotherapy on DNA were carried out at CERN to establish if a FLASH effect could be determined at the molecular scale.

A secondary aim of this project was to investigate the properties of VHEE beams as they travel through various media. To this end, the first comprehensive study of VHEE beam range in different materials was carried out, resulting in the development of a semi-empirical expression for VHEE beam range based on TOPAS Monte-Carlo simulations. TOPAS is a layered software for GEANT4[8], designed to provide a simpler user interface for improved flexibility, reliability and repeatability in Monte Carlo simulations[9]. While initially designed for proton therapy applications, the software has been extended to include multiple radiotherapy modalities, including electrons.

As an introduction, this chapter will consist of a broad overview of cancer biology and treatment, with a focus on radiotherapy. The mechanisms behind radiotherapy and the principles of treatment, including cell survival, the Linear Quadratic (LQ) model, a commonly used mathematical model to describe cell killing, for both developed by Chadwick and Leenhouts[10], and treatment planning will be covered. The different modalities in radiotherapy treatment will also be discussed, and finally an overview of the thesis structure will be given.

1.2. Cancer

Cancer is a group of diseases caused by an accumulation of genetic damage – which may be inherited (genetic mutations passed on from parent to offspring) or may be the result of environmental factors – causing uncontrollable cell division due to changes in normal cell behaviour[11].

There are over a hundred types of human cancers[12], making a fundamental understanding of the disease extremely difficult. A seminal review paper by Hanahan and Weinberg[13] suggested that each cancer cell genotype is a manifestation of six alterations to the cell's physiology, allowing the cancer to develop. These six changes are shared by most, if not all, human cancers:

1. **Self-sufficiency in growth signalling pathways:** Normal cells require growth signals from the surrounding environment before they can start to proliferate. Tumour cells have a greatly reduced dependence on these signals – they can generate their own and so proliferate more frequently.
2. **Insensitivity to anti-growth signals:** Healthy cells respond to anti-growth signals to prevent uncontrolled growth. These signal pathways in tumour cells are often damaged, allowing the cell to ignore the signals and proliferate unregulated.
3. **Evading apoptosis:** Apoptosis (programmed cell death) is a major source of cell attrition (reduction in cell number). Sensors in the cell monitor the environment and, if necessary, send signals to effectors which will trigger apoptosis. In cancer cells, the genes which trigger this process have been damaged, so apoptosis will not occur. Radiotherapy plays a key role in mitigating this – ionising radiation such as VHEE, results in DNA damage which, if it cannot be repaired by the cell, will result in the cell triggering apoptosis.
4. **Limitless replicative potential:** Normal cells have an intrinsic limit on the number of times they can divide – a limit which the cancer cells must overcome to produce a macroscopic tumour. The key for this unlimited replication lies in telomeres – repetitions of nucleotides, the building block molecules of DNA, at the ends of chromosomes to protect against deterioration. As a cell divides, these telomeres gradually shorten – the length limits the number of cell divisions to around 50-70 times. Cancer cells can extend these telomeres indefinitely, so extending their

replication potential[14]. Again, ionising radiotherapy such as VHEE can mitigate this by damaging the DNA, which can lead to the cell losing the ability to replicate.

5. **Sustained angiogenesis:** Cells in a tissue must be within 100 μm of a capillary to ensure the supply of oxygen and nutrients for survival. Angiogenesis (the formation of new blood vessels) can be 'switched on' by the rebalancing of genetic inductors and inhibitors. With a steady supply of oxygen and nutrients, the tumour can continue to grow.
6. **Tissue invasion and metastasis:** Eventually, a primary tumour will produce cells capable of invading nearby tissues or travelling to distant sites to establish secondary tumours, or metastases – the cause of 90% of cancer deaths.

1.3. Cancer Incidence and Mortality in the UK

363,000 new cancer cases are diagnosed each year in the UK with 166,000 deaths each year[15], making cancer the leading cause of death in the UK – 27.4% of all deaths in 2017[16]. The four most prevalent cancers in the UK, breast, prostate, lung and bowel, account for 53% of all new cancer cases (Fig. 1.1)[17] and 45% of cancer deaths, with a fifth of all cancer deaths being caused by lung cancer[18].

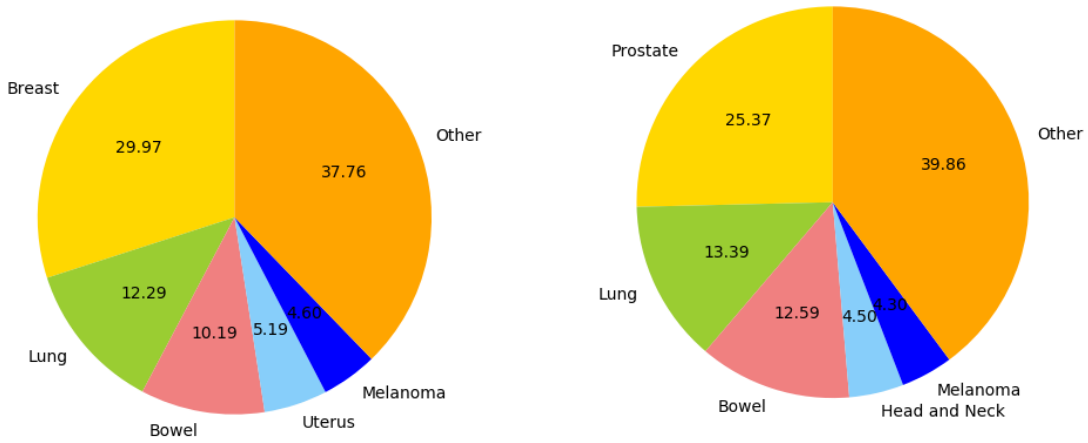

Figure 1.1 - Most common cancers in (left) females and (right) males according to CRUK in 2016. Graph made using data taken from [13]

Incidences of cancer have been steadily increasing over recent decades, with Cancer Research UK (CRUK) predicting a further 2% increase from 2014 and 2035 due to the general population aging[19]. Cancer is overwhelmingly a disease of the elderly, as indicated in Fig. 1.2, with 95% of deaths occurring in patients over 50. This is due to genetic damage accumulating with age, making the likelihood of cancer increasingly likely. Survival rates have increased from 24 – 50% between 1971 and 2011[20] though with variation between cancers - those for traditionally late-diagnosed cancers (e.g. lung, pancreatic) have remained low.

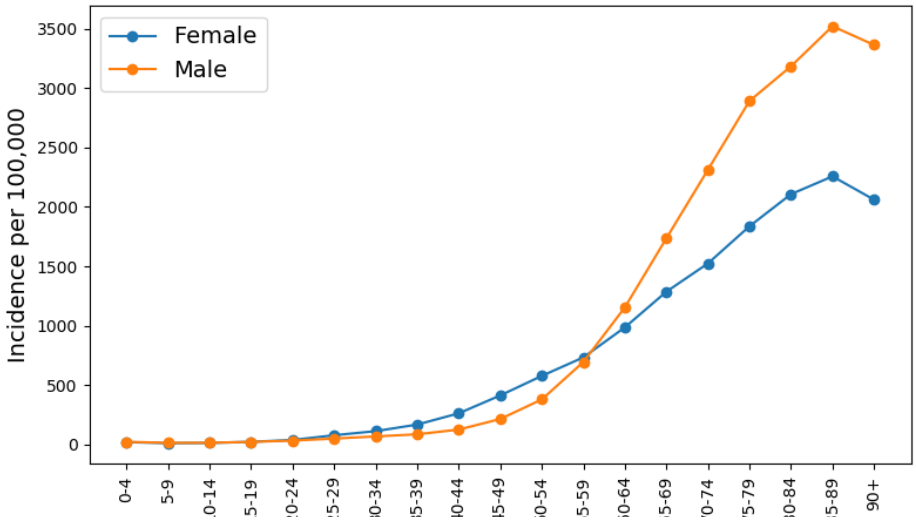

Figure 1.2 - Cancer incidence per 100,000 people in the UK according to CRUK in 2016. It is clear that cancer is overwhelmingly a disease of the elderly. Graph produced in Python using data taken from [13]

1.4. Cancer Treatment in the UK

Following cancer diagnosis, a patient will undergo curative (with the aim of getting rid of the disease) or palliative (to relieve symptoms and improve the patient's quality of life) treatment involving surgery, chemotherapy, radiotherapy or, most commonly, a combination of treatments. In a review of primary treatment in 2017, 45% of patients had surgery, 28% underwent chemotherapy treatment and 27% underwent radiotherapy[21]. The choice of treatments depended on the staging of the primary cancer, the current health of the patient including their ability to cope with the treatment and the patient's own preference. The following section looks at the three treatment options in more detail.

1.4.1. Surgery

Before the 20th century, surgery was the only option available to patients to effectively treat their cancer. Historically used as a last resort due to the huge risk to the patient, the introduction of general anaesthesia, improved hygiene practices and the introduction of antibiotics in the 19th and 20th centuries dramatically improved the effectiveness of surgery[22].

Surgery is now used to establish a diagnosis through biopsies and investigative surgery, to cure the cancer or used palliatively to relieve symptoms in some advanced or incurable cancer cases.

The surgeon's aim is to excise the cancer in its entirety along with any adjacent tissue to which the cancer may have spread. Plastic or reconstructive surgery may be required following major surgery to reduce any defect or deformity for the patient. Surgical tumour removal will also aid in the cure of cancer-related weight loss (cachexia). In more advanced cancer cases, surgery will usually be used in combination with other treatments to increase the likelihood of a cure[23].

1.4.2. Chemotherapy

In 1945, it was observed that a gas used in the First World War destroyed dividing cells. On further study, nitrogen mustard was found to be clinically effective against cancer cells, resulting in the birth of modern chemotherapy[22].

Chemotherapy, or cytotoxic, drugs are highly effective on dividing cells. As cancer cells divide much more frequently, they are more likely to be affected by cytotoxic drugs than normal cells[24]. Chemotherapy is typically delivered with a palliative goal, to reduce the cancer to relieve symptoms or to increase the patient's remaining lifespan, or a curative goal, to eradicate the disease. Curative chemotherapy is often delivered following surgery or radiotherapy to treat cancers in which there is a known risk that residual cancer cells may be present in the body, even if they are undetectable.

1.4.3. Radiotherapy

Radiotherapy is the delivery of ionising radiation to a well-defined region of the body to treat a malignant tumour. Both superficial and deep-seated tumours can be treated with radiotherapy, reducing the need for invasive surgery and allowing difficult-to-reach areas to be treated effectively. Radiotherapy is

commonly used in combination with surgery and chemotherapy to increase the likelihood of cure. It is also employed as a palliative treatment to shrink a tumour, control its growth or to manage painful symptoms – particularly for lung or brain tumours – and to make the remainder of a patient's life as comfortable as possible[22].

X-rays were discovered in 1895 by Rontgen[25] and, within a year, were being used X-rays to treat cancer patients[26]. As linear accelerator technology improved throughout the 20th century, the energy of X-rays increased, allowing the treatment of tumours much deeper into the body. Improvements in imaging, methods of beam delivery and beam control/steering have resulted in radiotherapy being a much more precise and accurate treatment, reducing normal tissue toxicity and improving curative rate[27].

The aim of any radiotherapy treatment is to deliver the maximum possible dose to the tumour while minimising the dose delivered to surrounding healthy tissue. The primary mechanism behind radiotherapy in the damage of cellular DNA. Ionising radiation causes damage to nucleic DNA through two mechanisms[28], with a schematic shown in Fig. 1.3:

1. **Direct damage** – caused by the interaction of the primary particle with the nucleic acid structure
2. **Indirect damage** – caused by interaction with the nucleic acid structure of secondary particles (including toxic hydroxyl radicals) produced due to the interactions between primary particles and water molecules within the cell.

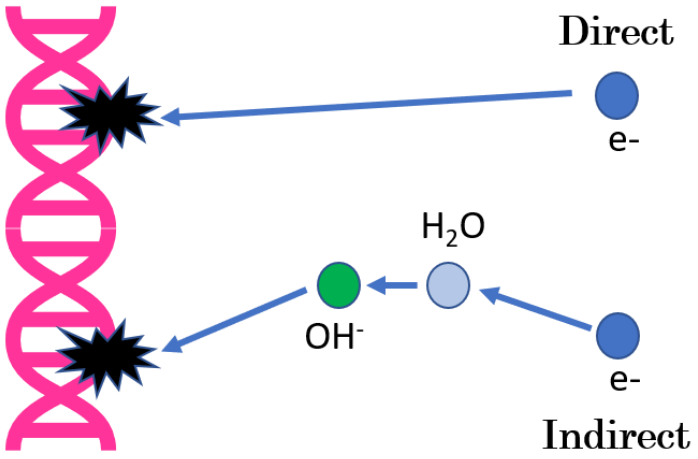

Figure 1.3 - Schematic of direct and indirect DNA damage caused by exposure to ionising radiation

While DNA can be damaged in a number of different ways, the two most lethal types of damage are SSBs and DSBs (see Fig. 1.4), in which one or both strands of the DNA are broken. A DSB can form if two SSBs occur on opposite strands within a certain distance – usually 10 base pairs (a sub-unit of DNA). If these breaks are left unrepaired, or are repaired incorrectly, the cell will lose its ability to reproduce effectively which may, in turn, result in the activation of one of three processes[29]:

1. Apoptosis – a method of programmed cell death that is highly regulated, caused by the cell sensing stress or by receiving signals from nearby stressed cells
2. Mitotic catastrophe – a method of cell death which occurs due to the cell entering the mitotic (division) phase early as a result of radiation-induced DNA damage
3. Senescence – a state of permanent cell-cycle arrest, induced following DNA damage that is particularly hard to repair. Rather than a method of cell death, this is considered a growth-retardation mechanism

Apoptosis and mitotic catastrophe are the most likely outcomes following radiation-induced DNA damage, with the likelihood of each highly dependent on the tissue being irradiated. It would be expected that similar results would be observed following VHEE irradiation.

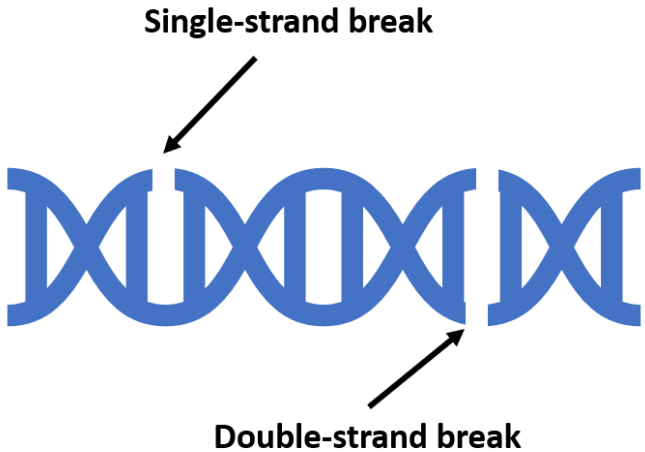

Figure 1.4 - Schematic of a single-strand break (SSB) and a double-strand break (DSB) in DNA. Figure produced by the author

There are two main methods of radiotherapy, differing in their delivery:

1. **External Beam Radiotherapy (EBRT)**: the most common form of radiotherapy treatment, in which a beam of radiation is directed very precisely at a particular region within a patient to irradiate the tumour (Fig. 1.5). In the UK, typical radiotherapy beams are bremsstrahlung spectra of 6 MV, though 10 and 15 MV are also used. Low-energy electrons employed for the treatment of surface cancers (such as skin). 70 MeV protons have been used to treat some eye cancers at the Clatterbridge Cancer Centre since 1989, while the first high-energy proton therapy centre was opened in 2018 at the Christie NHS Foundation Trust. The first clinical trial using carbon ions was carried out in 1994[30], with centres currently operational in Japan (5), Germany (2) and Italy (1). Each radiotherapy modality will be discussed in greater detail in Section 1.5.
2. **Brachytherapy:** the use of radioactive sources placed within or on a site involved with a tumour (Fig. 1.6). The primary advantage of brachytherapy is that, due to the inverse square law, there is a rapid dose fall-off within a short distance, so minimising the dose delivered to healthy tissue in the region. Brachytherapy is commonly used in the treatment of prostate, cervical and breast cancers[31].

Figure 1.5 - A typical external beam radiotherapy treatment suite

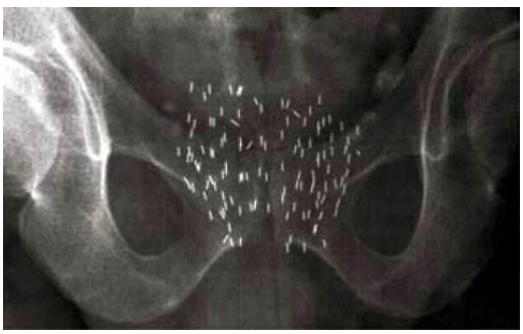

Figure 1.6 - X-ray of radioactive seeds implanted for treatment of prostate cancer

1.5. Principles of External Beam Radiotherapy

1.5.1. Cell Survival and the LQ Model

The efficacy of a radiotherapy treatment can be quantified by cell survival, in which the percentage of cells that are still alive after receiving a specified radiation dose is measured. By plotting cell survival against received dose, a cell survival curve can be built up for a particular cell type – a useful tool for determining the treatment dose[32].

Several cell survival models were formulated following the early development of radiotherapy to understand the effect of radiation on cells. Following irradiation of bacteria, exponential response curves were observed leading to the single-target, single-hit hypothesis[33] – if ionising radiation caused a damaging event (a hit), in a sensitive cellular region (a target), cell death will occur. Assuming that these hits are Poisson distributed, survival is modelled as:

$$S = e^{-xD} \tag{1.1}$$

where x is the probability per unit dose of a lethal hit and D is the delivered dose.

On irradiation of more complex mammalian cells, this hypothesis did not explain the shouldered curves observed. Instead, the single-hit, multi-target model was developed, assuming that cells contain multiple targets[34]. If a cell contains m targets, the likelihood of < m targets being hit, or the survival probability, is:

$$S = 1 - (1 - e^{-xD})^m \tag{1.2}$$

This model reproduces a shouldered curve with an initial gradient of zero. Further radiobiological studies found disagreements at very high and very low doses, as well as the observation of survival curves with non-zero initial gradients.

To try and solve these discrepancies, Kellerer and Rossi[35] and Chadwick and Leenhouts[10] separately developed models based on a mult-target, multi-hit model. Here, we focus on Chadwick and Leenhouts' model, based on fitting survival to a linear-quadratic (LQ) equation. Their model was based on the following theory, outlined by Brenner[36]:

1. Ionising radiation produces double-strand breaks on cellular DNA, with the yield being proportional to the dose delivered
2. DSBs can be repaired by the cell with first-order repair rate constant λ:

$$\lambda = \ln\left(\frac{2}{T_{1/2}}\right) \tag{1.3}$$

   where $T_{1/2}$ is the half-life of sublethal damage (not individually lethal, but which could accumulate to cause lethal damage) repair
3. If the DSBs are repaired incorrectly, this can cause lethal chromosomal aberrations
4. Single radiation tracks are capable of causing lethal damage, again with the yield being proportional to the radiation dose delivered

DSBs occur in one of two ways – either through a single particle breaking both strands, or through two separate particles causing SSBs on opposite strands within a certain distance. The number of DSBs caused by the first method (single-track) can be given by the following:

$$N_1 = n_0\{1 - e^{-k_0 D\Delta}\} \tag{1.4}$$

where n_0 is the number of sites where a DSB can occur through this method, k_0 is probability that a DSB will occur and Δ is the proportion of dose D which causes a DSB through this method.

The number of DSBs caused by the second method (two-track) is given by the following:

$$N_2 = \varepsilon n_1 n_2 f_1 f_2\{1 - e^{-kD(1-\Delta)}\}^2 \tag{1.5}$$

where ε is the proportion of SSBs which combine to form a DSB, n_1 and n_2 are the number of critical bonds on DNA strands 1 and 2 respectively ($n_1 = n_2$), f_1 and f_2 are the proportions of unrepaired broken bonds on each DNA strand, k is the probability per bond per unit dose that a break occurs and $(1 - \Delta)$ is the proportion of dose which causes a DSB through the two-track method.

The total DSB yield can therefore be calculated as a sum of the DSBs induced by each method:

$$Y = N_1 + N_2 = n_0\{1 - e^{-k_0 D\Delta}\} + \varepsilon n_1 n_2 f_1 f_2\{1 - e^{-kD(1-\Delta)}\} \tag{1.6}$$

By assuming that f_0 is the proportion of unrepaired DSBs and that p is a proportionality factor linking DSB production with cell death (as detailed in the assumptions), Poisson statistics can be used to derive an expression for cell survival for small k and k_0:

$$S = e^{-Y} = e^{-pf_0n_0k_0\Delta D} \cdot e^{-pf_0n_1n_2f_1f_2k^2(1-\Delta)^2D^2} \tag{1.7}$$

This therefore allows cell survival to be written in the form:

$$S = e^{-\alpha D-\beta D^2} \tag{1.8}$$

$$\alpha = -pf_0n_0k_0\Delta \qquad \beta = -pf_0n_1n_2f_1f_2k^2(1-\Delta)^2$$

This is the LQ model for a treatment consisting of a single dose. As treatment is usually fractionated (split into smaller fractions, delivered over several days or weeks, a dose protraction factor[37] is included:

$$S = e^{-\alpha D-\beta GD^2} \tag{1.9}$$

$$G = \frac{2}{D^2}\int_0^\infty \dot{D}(t)dt \int_0^t e^{-\lambda(t-t')}\dot{D}(t')dt' \tag{1.10}$$

where D(t) is the dose rate variation during treatment. The second integral refers to the first DSB, which was caused at time t' and may undergo repair based on the repair rate λ. The first integral refers to a second DSB, caused at a later time t, which may interact with DSBs produced earlier in order to produce further lethal damage. For a single treatment, G = 1.

The shape of the curve depends on the ratio of the parameters α and ß, as demonstrated for prostate adenocarcinoma and head and neck small cell carcinoma in Fig. 1.7 – the α/ß ratio is used more frequently clinically than the individual parameters:

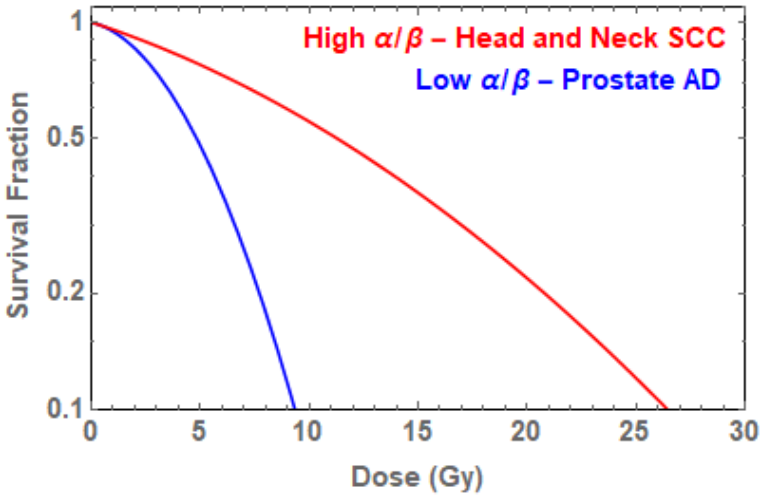

Figure 1.7 - Cell survival curves for tissues with low and high α/ß ratios. The low α/ß ratio curveis more quadratic due to the ß term dominating while the high α/ß ratio curve is more linear due to the α term dominating.

- A low α/ß ratio, e.g. for prostate adenocarcinoma, results in a more curved cell survival curve and indicates a greater dependency on the quadratic (ß) component. A low ratio typically represents late-responding tissues, which express their damage months or years after irradiation. Normal tissues are often late-responding, with a high sensitivity to fraction size and dose rate and a large repair capacity[38].

A high α/ß ratio, e.g. for head and neck small cell carcinoma, results in a more linear cell survival curve, indicating a greater dependency on the linear (α) component. Tissues with a high ratio are typically early-responding, expressing damage within days or weeks following irradiation,and include cancerous tissue or fast-growing normal tissues[39].While the LQ model has been used clinically for nearly 50 years, research into radiobiology and cell survival has resulted in the LQ model being viewed as phenomenological rather than purely mechanistic, useful for fitting survival curves rather than predicting them. It breaks down at high doses, and is not suitable for modelling cell survival in hypofractionated treatments, involving fewer fractions of larger doses[40,41].

A great deal of research is being carried out into this field, with aims to develop cell survival models which describe the response to radiation in a more mechanistic way – in terms of initial damage or repair rates for example. As the mechanisms governing cell death occur over a wide range of physical and time scales, these models are becoming increasingly specialised. An area particularly relevant to this project is the research carried out on the nanodosimetric scale, in which Monte Carlo codes, e.g. GEANT4-DNA[42] or TOPAS-nBio[43], are used to

determine the energy deposited to DNA during interaction with radiation and the resulting damage this causes. This damage can then be used to determine biological effects, such as DNA repair and misrepair[44–46]. Nanodosimetry is discussed further in the next section.

Despite its limitations, the LQ model is still the primary radiobiological tool used by clinicians. Its lasting success is primarily due to its simplicity and ease of use, particularly when comparing treatment plans[40]. Producing cell survival curves which can be fitted to the LQ model following cell irradiation with VHEE beams would provide a strong argument for clinical implementation of VHEE therapy as comparison of treatment schedules using different modalities would be simple to compare.

1.5.2. DNA Damage and Nanodosimetry

It is clear that the effectiveness of radiotherapy can be measured through cell killing. When just one radiotherapy modality is considered, the rate of cell killing can be correlated to the dose delivered. Being able to measure cell survival in terms of dose is very useful, as dose is a quantity which (for conventional treatments) can be measured relatively easily. This is crucially important for quality assurance (QA) in treatment design to ensure that patients consistently receive the correct treatment.

However, dose is not a perfect predictor of biological effect. Biological effect varies with the radiotherapy modality being used – the dose required to cause a particular biological effect using X-rays is not necessarily the same as the dose required for the same effect using a different modality.

It is therefore desirable to plan radiotherapy treatment using a metric based directly on a biological endpoint such as cell kill, rather than on dose. This metric must be relatively straight-forward to measure as quality assurance must be carried out regularly to ensure consistently accurate treatment delivery. Alternative metrics for treatment planning could include tumour shrinkage or Normal Tissue Complication Probability, however these are considerably more complicated to model, involving cell-to -cell signalling and the tumour microenvironment.

As has been established, cell kill is a function of DNA damage, caused by ionisations resulting from inelastic interactions between ionising radiation and

cellular structures. Initially, track structure (the pattern of energy deposition of ionising radiation interactions with matter) was determined over volumes corresponding to cellular structures believed to be the necessary target to induce cell death, such as the nucleus. As these volumes are typically micrometres in diameter, the study of these interactions became known as microdosimetry[47].

However, a study by Brenner and Ward[48] indicated that the number of ionisation clusters resulting from irradiation with different types of particles correlated to the yield of DSBs – the primary damage most likely to result in cell death. The conclusion was that radiation damage to cells is related to the size of ionisation clusters induced by ionising particles on or close to the DNA – within a few nanometres, rather than micrometres.

Therefore, the concept of nanodosimetry may be more suitable than microdosimetry for determining the biological effect of a radiotherapy modality. As ionisation cluster size correlates to the number of DSBs and so the likelihood of cell death, a suitable metric is the nanoscale energy deposition to DNA[49].

The aim of nanodosimetry is to determine these energy depositions and the size of the resulting ionisation clusters. These can then be linked to biologically relevant quantities, namely single- and double-strand DNA breaks. Two processes linking these have been proposed:

1. **Grosswendt** – this simple process makes the assumption that an ionisation cluster size of 1 corresponds to an SSB, while a cluster size of two or more corresponds to a DSB[50]. This assumption fits with the results observed by Brenner and Ward[48].
2. **Garty** – this is a combinatorial approach, assuming firstly (like Grosswendt) that ionisation cluster size is linked to DNA damage and also that any ionisation in the target volume is equally likely to cause a strand break and that ionisations are evenly distributed along the DNA strands. If two ionisations on opposite strands occur within a specified distance, a DSB is induced[51].

The measurement of ionisation cluster sizes can be carried out both experimentally and computationally. In the last two decades, several nanodosimeters have been developed including the jet counter[52], the track nanodosimetric counter[53] and the ion-counting dosimeter[54]. The concept behind

each involves measuring the ionisation cluster size following irradiation of a macroscopic volume of low-pressure gas. The result is rescaled to a nanodosimetric volume of water.

These cluster sizes have been used as a benchmark for the results obtained from Monte Carlo simulation of particle track structure in nanodosimetric water volumes. These Monte Carlo codes can be used to model track structure, determine the sizes of the resulting ionisation clusters and convert the cluster pattern to DNA SSBs and DSBs. While several codes are available, including Monte Carlo N-Particle (MCNP)[55] and PARTRAC[56], we will focus on GEANT4-DNA[42]. A detailed description of GEANT4-DNA will be given in Chapter 4.

The track structure through a volume depends on the radiation quality (the particle type and energy) and specifically the Linear Energy Transfer (LET) of the radiation. Higher LET radiation particles such as alpha particles have dense track structures relative to low LET particles such as photons or electrons[57]. As a low LET particle type, it can be hypothesised that VHEE will cause similar numbers of DNA lesions as photons (see Table 1.2).

DNA Lesion	Number per cell per Gy
DSB	40
SSB	1000
Base damage	>2000
DNA-DNA crosslinks	30

Table 1.2. An approximate number of DNA lesions per cell per 1 Gy of dose delivered for photons[57]

Currently, there is no data available on the nanodosimetry of VHEE. Nanodosimetry is a rapidly developing field for more established radiotherapy modalities such as X-rays and protons. Therefore, understanding the dependency of DNA damage on nanoscale energy depositions from VHEE will contribute to a mechanistic model of cell damage and survival for VHEE – one which can be compared with other radiotherapy modalities to obtain a value for the relative biological effectiveness of RBE based on DNA damage.

Chapters 4 and 5 aim to achieve this by initially investigating the SSB and DSB yields resulting from irradiation of plasmid DNA with VHEE and comparing the yields to those from other radiotherapy modalities. The results will also provide

a benchmark for Monte Carlo track structure simulations of VHEE interactions with plasmid DNA using GEANT4-DNA. Energy depositions will be scored on a DNA model and converted to DNA damages, which will be compared to experimental damage observations.

1.5.3. Tumour Control Probability and Normal Tissue Control Probability

Cell survival models can be used to produce expressions for Tumour Control Probability (TCP) and Normal Tissue Complication Probability (NTCP)[58]. TCP is the probability of zero clonogens (cells that have the ability to reproduce) surviving inside a tumour. A TCP curve can be produced by modelling the probability of damage using Poisson statistics[59]. A Poisson distribution is given by the following:

$$P(k) = e^{-\lambda}\frac{\lambda^k}{k!} \tag{1.11}$$

where k is the number of surviving clonogens and λ is the number of events. From the LQ model, λ can be written as:

$$\lambda = n\,S(D) \tag{1.12}$$

where n is the number of clonogens before irradiation and S(D) is the survival fraction given in equation 1.9. As tumour control is achieved when all clonogenic cells are dead (k=0), the probability for tumour control is:

$$P(0) = e^{-nS(D)} \tag{1.13}$$

NTCP is the probability of complications occurring in an organ or tissue on delivery of a particular radiation dose. Unlike TCP, there is no simple mathematical model available due to NTCP being dependent on several cell mechanisms and there being different types of dose-induced complications to consider.

Typically, TCP is greater than NTCP for an identical dose as malignant cells tend to have an increased number of faulty DNA repair mechanisms compared with normal cells. This means that the malignant cells have a higher likelihood of damage mis-repair and a lower rate of successful repair in general compared with healthy cells. At time of writing, there is no TCP/NTCP data available for VHEE due to the lack of biological studies. TCP and NTCP allow clinicians to weigh up the risks and benefits when planning radiotherapy treatments. A

balance must be found between the probability of tumour control and an acceptable probability of radiation-induced complications in normal tissues. This links to the original aim of radiotherapy – to deliver as high a dose as possible to cancerous tissue while minimising that delivered to healthy tissue. The therapeutic window is a conceptual quantity describing the space between TCP and NTCP curves and is shown in Fig. 1.8. The larger the window, the more likely that the radiotherapy treatment is to be both safe for normal tissue and effective at controlling the tumour[60].

The therapeutic ratio is defined as the relationship between the probabilities of tumour control and normal tissue damage:

$$TR = TCP(1 - NTCP) \tag{1.14}$$

A higher therapeutic ratio indicates that a higher dose can be delivered to the tumour before normal tissue becomes significantly damaged, increasing the likelihood of curing the patient. By establishing the distribution of VHEE DNA damage and subsequently RBE_{DSB}, this will help to determine if conventional NTCP models can be applied. This will, in turn, aid clinicians in determining which modality would be most appropriate for a patient's treatment.

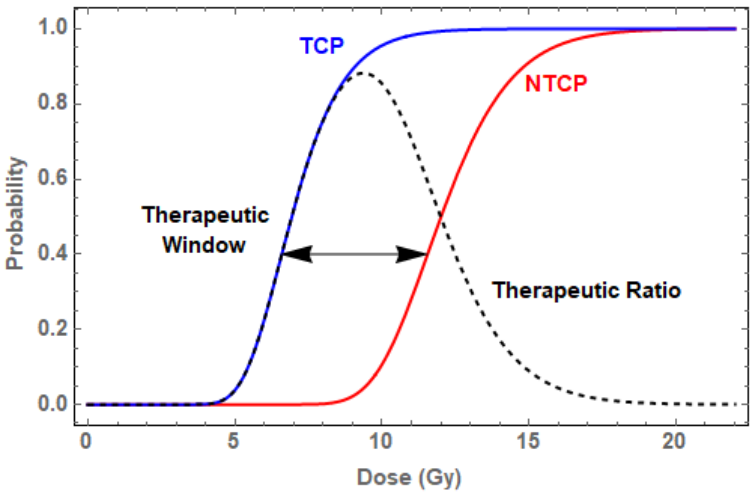

Figure 1.8 - Tumour control probability and normal tissue complication probability plotted against radiation dose. Image adapted from [58]

1.5.4. Treatment Planning

Before delivering the dose, treatment planning is required to identify where to deliver the radiation, and how much dose is required[61,62]. The region of interest will be imaged and the Gross Tumour Volume (GTV) outlined by the clinical oncologist – this volume is likely to change from clinician to clinician due to slight differences in reading the scans.

A margin is then drawn around the GTV to form the Clinical Target Volume (CTV). This contains the GTV and a surrounding area which may contain microscopic disease that has spread from the primary cancer. It may also contain at-risk regions, including lymph nodes.

A second margin is added to the CTV – the Planning Target Volume (PTV). This is included to account for setup uncertainties, machine tolerance and intra-treatment variations (including weight loss) and ensures that the prescribed dose is delivered to the CTV.

Finally, clinicians must clearly delineate any organs at risk (OAR) in the treatment plan. These are organs whose radiosensitivity is such that the dose received during treatment may be significant compared with its tolerance (based on the TCP curve). This may require a change in the beam arrangement or planned dose. An example of these margins and outlining of an OAR is shown in Fig. 1.9 in the treatment of a brain tumour using 3D Slicer v4.10[63,64].

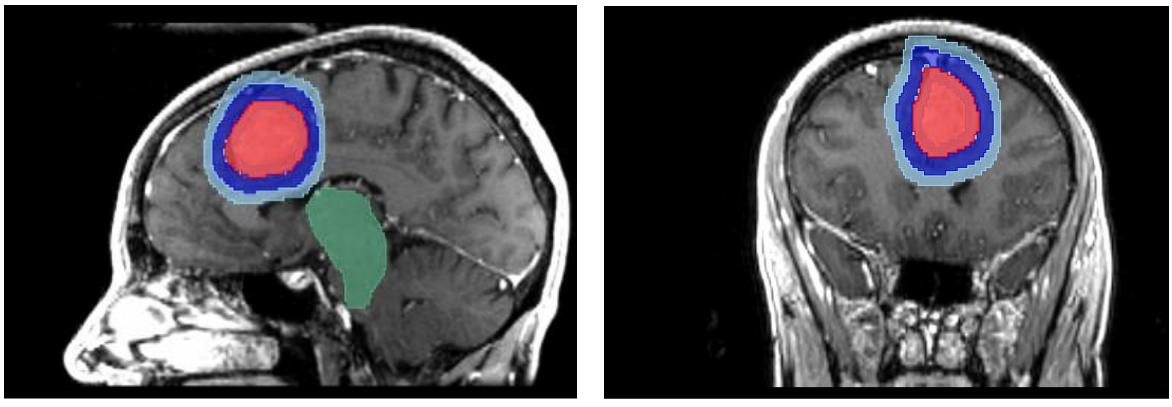

Figure 1.9 – Sagittal (left) and coronal (right) views of treatment plan for a brain tumour. GTV (red), CTV (dark blue) and PTV (light blue) highlighted along with an organ-at-risk (green). Image produced by Louie Hancock (colleague) using 3D Slicer v4.10 [63,64].

Treatment planning is an area of significant interest in VHEE therapy, as superior treatment plans compared with current modalities provide a strong argument for clinical implementation of VHEE therapy. Publications by

Bazalova-Carter[5] and Schuler[6] have produced treatment plans using VHEE for a number of clinical cases which have been repeatedly shown to be superior to VMAT plans in terms of dose conformality and organ-at-risk sparing. While these plans were produced using software typically used for photon treatment planning, work is currently underway to produce a treatment planning software designed specifically for VHEE therapy at the University of Manchester.

1.5.5. Fractionation

The majority of treatment plans recommend a total dose to be delivered to a patient which will be split into a number of smaller sub-doses, typically 1 – 2 Gy, to be delivered over a period of a few weeks. This splitting is known as fractionation and is based on a number of factors related to tumour biology – the 5 Rs of radiotherapy[65,66].

- **Repair** – DNA can be damaged both lethally and sub-lethally. The cell will try to repair this sub-lethal damage, although a characteristic of malignant cells is a loss of certain functions – including DNA repair mechanisms. Therefore, fractionation will benefit those healthy cells with functioning repair mechanisms, allowing damaged healthy cells to repair sub-lethal damage between fractions.
- **Redistribution** – Different cells in a tumour will be at different stages in the cell cycle. Certain stages of this cycle are more radiosensitive than others – G_2 and M phases, during which the cell prepares for and undergoes mitosis[67], are more radiosensitive, for example, than the S phase, during which DNA is synthesised. Delivering a short, smaller radiation dose will damage many more cells in radiosensitive phases than in radioresistant phases. Cells will continue through the cycle during the time between treatments, with some moving into the radiosensitive phases when the next dose is delivered.
- **Reoxygenation** – Oxygen levels are closely linked to the efficacy of radiotherapy. Tumours have poor vasculature compared to normal tissue, leading to them becoming hypoxic. Hypoxic conditions result in a reduction of a tumour's radiosensitivity. By fractionating treatment, the outer, more radiosensitive regions of the tumour, with superior blood supply, will be treated first. As the tumour shrinks, the hypoxic regions

will gain improved blood supply – they will no longer be hypoxic and so become more radiosensitive.

- **Repopulation** – On receiving a dose of radiation, cell death will occur in both healthy and cancerous tissue. Leaving time between doses will allow normal tissues to replace these dead cells, reducing side effects to the patient. However, accelerated tumour growth may occur if the cancerous cells are replaced faster than the healthy cells.
- Radiosensitivity – Radiosensitivity is not a constant quantity. It can vary between different tissues, and even varies within an individual cell depending on its cell cycle phase. The advantages of the above 4 Rs with regard to fractionation benefits depend heavily on radiosensitivity, which may in turn depend on radiotherapy modality. At present, there is no radiosensitivity data available for VHEE – investigations are required to determine if VHEE radiosensitivity is similar to photons or charged particles.

1.6. Radiotherapy Modalities

1.6.1. X-Rays

X-rays were the earliest used modality for radiotherapy. Early treatments were crude, with little to no understanding of the biological effects of X-rays, unreliable equipment and an inability to accurately calculate the dose being delivered to the patient. Due to the low energy of the X-rays that could be produced, only surface tumours or malignancies could be effectively treated with radiotherapy[68].

X-rays interact with matter through three mechanisms, with the probability of each mechanism depending on the energy of the primary photon[69] (Fig. 1.10):

1. Photoelectric Effect – this occurs between an incident photon and an atomic electron (typically inner-shell). If the photon has sufficient energy to overcome the shell binding energy, it will transfer its energy to the electron, which will escape the atom with kinetic energy

$$K.E. = E_\gamma - binding\ energy \qquad 1.15$$

where E_γ is the energy of the photon. The atom will then be ionised. The probability of the photelectric effect depends not only on the photon's energy, but also on the atomic number of the material through which the photon is traversing. In water, the photoelectric effect is the dominant photon interaction up to ~30 kV.

2. Compton Scattering – This interaction involves an incident photon interacting with an atomic electron (typically outer shell), overcoming the binding energy and transferring some energy to the electron in the form of kinetic energy. The remaining energy is emitted as a photon with lower energy than the incident photon.

   In water, the Compton effect dominates for energies from 100 kV to 20 MV. This is the dominant interaction in tissue at the clinical energies used in radiotherapy treatment.

   The probability depends on the electron density of the material through which the photon is traversing and varies with the atomic number and mass. As this value is essentially constant for elements heavier than hydrogen, the Compton effect only depends on the physical density of the material.

3. Pair Production – At energies above a few MV, a photon may interact with the nuclear Coulomb field to produce and electron-positron pair. All the photon's energy is transferred to the rest mass and kinetic energy of
   the two particles. For pair production to occur, the photon must have a minimum energy of 1.022 MV (2 M_e), with the probability of this occurring increasing with photon energy.
   In water, pair production only becomes significant >10 MV, so accounts for little absorbed dose to a patient undergoing standard radiotherapy treatment.

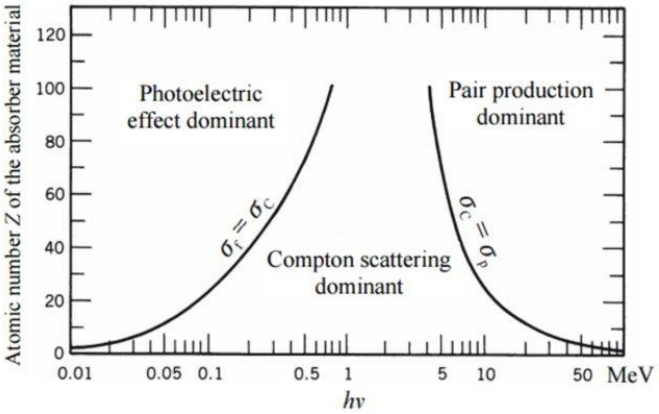

Figure 1.10 - Relative contribution of photon-matter interaction with energy. Taken from [69]

Clinical X-ray beams are produced following the collision of electron beams with a high Z material, usually tungsten, via Bremstrahlung radiation. The electrons in the beam are produced at a cathode. This cathode is heated and electrons are released through a process known as thermionic emission. These electrons are then accelerated to the required energy in a radio-frequency (RF) linear accelerator.

Following acceleration to the desired energy, the electron beam is directed to the X-ray target using a series of steering and focusing magnets. On impact with the high Z the electrons will decelerate, resulting in the production of X-rays via Bremstrahlung with a spectrum of energies. The mean energy of the photons produced is approximately a third of that of the maximum. The target is angled such that most of the resulting X-rays are emitted in a specific direction. The X-rays can then be shaped using flattening filters and multi-leaf collimators to achieve the correct shape for a patient's treatment. Percentage depth-dose curves for 6 and 10 MV Bremstrahlung spectra with a flat field of 10x10 cm^2 are shown in Fig. 1.11, with phase space data for an Elekta Precise linac provided by the International Atomic Energy Agency's Nuclear Data Service, generated by Tonkopi *et al.*[70]

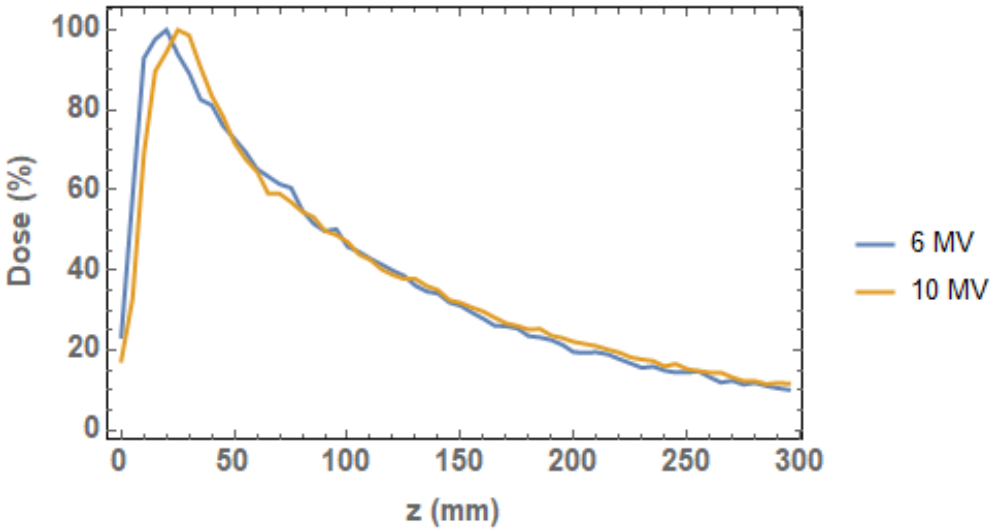

Figure 1.11 – On-axis PDD curves for 6 and 10 MV Bremstrahlung spectra of 10x10 cm² flat field. Phase space data taken from 70

1.6.2. Proton and Heavy Ion Therapy

In recent years, ion therapy, particularly proton therapy, has been gaining prevalence around the world. Proton therapy was proposed by Robert Wilson in 1946[71]. The first patient was treated in 1954 at the Lawrence Berkeley National Laboratory[72]. Due to technological limitations, particularly in designing proton cyclotrons that could readily fit inside clinical facilities, it was not until 1989 that the first hospital-based proton therapy centre was built. This was the Clatterbridge Centre for Oncology[73], capable of delivering proton beams up to 70 MeV. As 70 MeV proton beams have a range of approximately 4cm, they are not used in the treatment of deep-seated tumours but are instead used to treat rare eye cancers.

The first hospital-based proton therapy centre was opened at the Loma Linda Medical Centre in California in 1990 with the aim of treating deep-seated tumours. Since then, the number of proton therapy centres has increased rapidly – as of Sep 2020 there are 110 centres in operation and 64 centres either under construction or in the planning stages[74]. In the UK, the NHS has invested £250 million in building two proton therapy centres at the Christie NHS Foundation Trust (first patients treated in Dec 2018) and at University College London Hospital (first treatments planned in 2020)[75]. The number of carbon ion therapy centres has also increased over recent years, with 13 in operation and 7 either under construction or in planning stages.

The primary advantage to proton and heavy ion therapy is its characteristic depth dose profile – specifically the 'Bragg peak,' discovered by W. H. Bragg[76]. Protons and heavy ions typically deposit dose in the form of ionisation events, with the probability of ionisation increasing with decreasing energy. The rate of energy loss can be described by the Bethe-Bloch expression[77]:

$$\frac{S}{\rho} = -\frac{1}{\rho}\frac{dE}{dx} = 4\pi N_A r_e^2 m_e c^2 \frac{Z}{A}\frac{z^2}{\beta^2}\left[\ln\frac{2m_e c^2\gamma\beta^2}{I} - \beta^2\right] \qquad 1.16$$

where N_A is Avogadro's number, r_e and m_e are the classical radius and mass of an electron respectively, Z and A are the atomic number and atomic weight of the absorbing material, ß = v/c where v is the velocity of the particle and c is the speed of light and I is the mean excitation energy of the absorbing material. It is the proportionality of the stopping power to the inverse square of the velocity which gives rise to the characteristic dose distribution curve and Bragg peak, as is clear in Fig. 1.12.

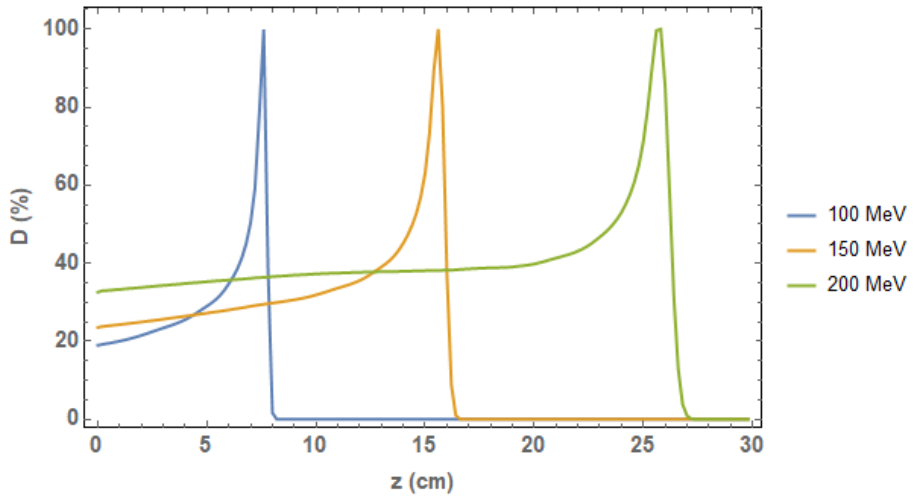

Figure 1.12 – On-axis PDD curves for 100, 150 and 200 MeV proton beams through a 30x30x30 cm³ water phantom. Data obtained through TOPAS simulation of proton beams through water. As beam energy increases, depth of Bragg peak increases

Clinically, a single monoenergetic beam is not suitable for treatment as the narrow Bragg peak will not cover the whole tumour. A uniform dose can be delivered to the whole tumour by using a spread-out Bragg peak (SOBP) – an array of monoenergetic beams of graded energies arranged such that a treatment dose is achieved over the desired tumour volume[78], as shown in Fig. 1.13.

The main clinical advantage of proton and heavy ion therapy is the finite range of the Bragg peak, or SOBP, determined by the rapid dose fall-off, resulting in

negligible dose beyond the tumour – particularly important for paediatric patients who have a significant risk of developing secondary cancers decades after radiotherapy treatment[72].

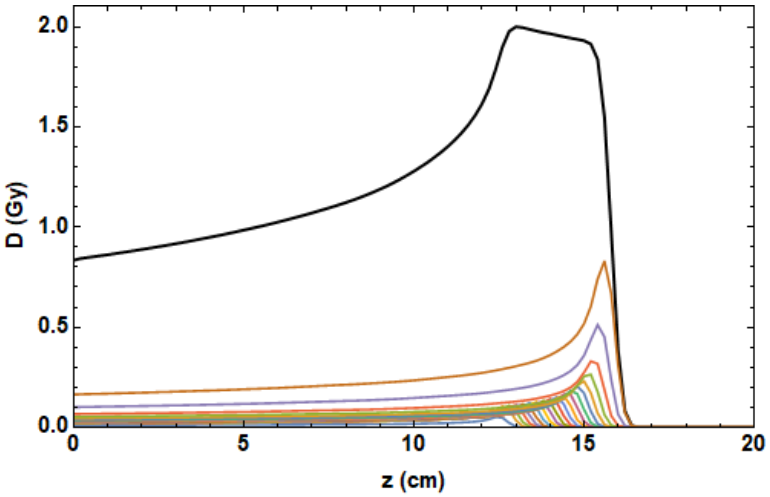

Figure 1.13 - Spread-out Bragg peak (SOBP) for 150 MeV protons. Produced through weighting 20 individual mono-energetic Bragg peaks – dose distribution data obtained through TOPAS simulations of proton beams through water delivering 5.8 nC, corresponding to a typical treatment fraction of 2 Gy

1.6.3. Low Energy Electrons

While X-rays have proven effective at treating deep-seated tumours and, to a lesser extent, superficial tumours, the nature of their dose deposition is not advantageous for certain tumour cases. Due to their slow dose fall-off, X-rays are not ideal for cases in which the tumour volume is very close to OARs, cases where dose to normal tissue behind the tumour must be carefully controlled, or in treatment of superficial tumours.

Superficial malignancies, such as skin cancers, can be treated using low-energy electrons, typically in the energy range 6-15 MeV, though X-rays are still the dominant modality. A stable electron beam is produced as discussed in the previous section, with the tungsten target removed to prevent X-ray beam production.

As electrons travel through a medium, they interact with atomic orbital electrons and atomic nuclei through Coulombic interactions[69]. During interactions, the electrons lose kinetic energy through collisional losses (due to interactions with orbital electrons causing excitation or ionisation) and radiative losses (due to interactions with atomic nuclei).

The rate of energy loss is known as the total mass-energy stopping power, and consists of the collisional and radiative mass stopping powers[69]:

$$\frac{S}{\rho} = \left(\frac{S}{\rho}\right)_{col} + \left(\frac{S}{\rho}\right)_{rad} = -\frac{1}{\rho}\frac{dE_K}{dx} \qquad 1.17$$

where S is the stopping power, ρ is the material density and dE_K/dx is the loss of energy E per unit path length x.

Total and collisional stopping power are important clinical quantities as they are used in the calculation of electron beam range and dose respectively.

As observed in the PDD curve in Fig. 1.14, electrons exhibit a high surface dose and a rapid dose fall-off on delivery of their maximum dose. This makes low-energy electron beams suitable for surface treatments as normal tissue beyond the treatment region will not receive high doses – reducing the risk of secondary, radiation-induced cancers developing at a later stage. The PDD curves shown in Fig 1.14 were produced using phase-space data on electrons from a Varian Clinac 2100CD, using electrons of energies 6 and 9 MeV in a 10x10 cm^2 flat-field beam. This data was taken from the International Atomic Energy Agency Nuclear Data Services, published by Brualla *et al.*[79]

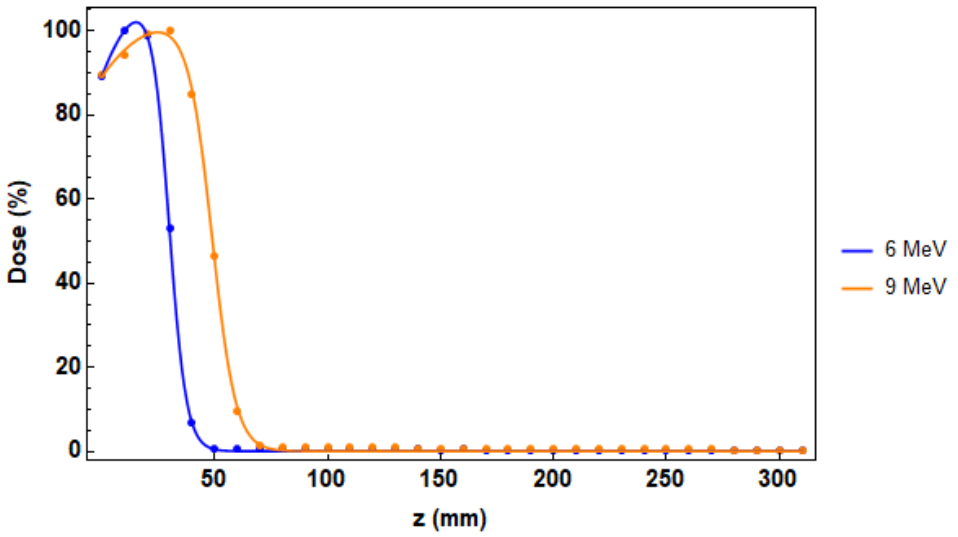

Figure 1.14 - On-Axis percentage depth-dose curve for 6 and 9 MeV electrons. 10x10 cm^2 flat fields produced using phase-space data produced by 79

However, the characteristics of low-energy electron beams make them highly unsuitable for treatment of tumours more than a few centimetres into the body. Aside from the obvious issue of not being able to reach the tumour with sufficient energy to deliver a treatment dose, low energy electron beams scatter

when travelling through a medium. For a patient, this would result in high radiation doses being delivered to healthy tissue in front of and around the target region.

To successfully treat deep-seated tumours, it was suggested by DesRosiers[1,2] that the energy of the electron beam must be increased to 150-250 MeV – Very High Energy Electron (VHEE) beams. As mentioned briefly in section 1.1, electron beams at this energy not only have the ability to reach deep-seated tumours but have also been found to be insensitive to inhomogeneities and, thanks to their charge and mass-to-charge ratio, can be rapidly scanned, reducing delivery time and providing a potential modality for FLASH radiotherapy, the delivery of high dose-rate radiotherapy (> 40 Gy/s)[80,81]. The advantageous characteristics of VHEE beams and their suitability for FLASH radiotherapy are covered in much greater detail in Chapter 2.

1.7. Contents and Overview

The thesis will be formed of five further chapters, structured as follows:

- Chapter 2 – This will take the form of a literature review for VHEE and FLASH radiotherapy. The history of both will be covered, along with studies on the characteristics and advantages of VHEE and FLASH therapies. The technological requirements for each will also be reviewed, including accelerator technology and dosimetry.
- Chapter 3 – The development of a semi-empirical range expression for VHEE beams in tissue will be covered in this chapter. A review of the Monte Carlo particle tracking code TOPAS will be made, and the code will be validated by reproducing an established proton range expression. Electron range will be defined, and a semi-empirical electron range expression will be produced and analysed.
- Chapter 4 –Plasmid irradiation experiments carried out during the PhD will be covered, starting by introducing plasmids, why they are used in radiobiological experiments and briefly reviewing previous plasmid irradiation studies with other modalities. The full experimental method will be described, along with sample processing and analysis to obtain the damage yields. Results from each study at various experimental

facilities will be analysed, with break yields compared between the different modalities and energies, and experimental results compared with simulation results from the previous chapter

- Chapter 5 – Plasmid irradiation simulations with different radiotherapy modalities will be described, along with an overview of the GEANT4-DNA module. Single- and double-strand break yields caused by different modalities will be compared.
- Chapter 6 – The thesis will end with a discussion of the project, with results from both computational and experimental studies analysed. Finally, potential future work will be explored to see how VHEE radiobiology can be extended, and what further research is required for VHEE to be used in a clinical setting.

Chapter 2 – VHEE and FLASH Radiotherapy

2.1. Introduction

The use of Very High Energy Electrons (VHEE) in the energy range 100-250 MeV was suggested as a solution to the issues associated with low energy electrons highlighted in the previous chapter. This chapter aims to demonstrate why VHEE may be a suitable modality for radiotherapy treatment by reviewing the available literature on different aspects of VHEE research, outlining the technological advances which have made VHEE therapy viable for use in clinical settings and studying the characteristics of VHEE beams.

Section 2.2. will review published studies on VHEE radiotherapy from its initial investigation by DesRosiers *et al.*[1,2]. Key clinical aspects will be covered, including VHEE treatment planning and comparison with established radiotherapy modalities and methods of dosimetry, with results highlighting the potential and suitability of VHEEs for radiotherapy.

Technology requirements will be covered in section 2.3, beginning with an overview of the requirements for a VHEE treatment machine. A review of possible acceleration methods for VHEE will follow and the section will conclude with a review of current literature available on VHEE treatment design.

Section 2.4 will describe the physical characteristics of VHEE beams and their associated advantages in radiotherapy treatment, including dose distribution, lateral spread and relative insensitivity to inhomogeneities. Comparisons of these characteristics will be made to other radiotherapy modalities, in particular low energy electrons. These characteristics will be shown through simulations using TOPAS, a user-friendly wrapper for the Monte Carlo particle tracking code GEANT4. These results will indicate the advantages to patient treatment of VHEE therapy.

One particular advantage of VHEE is the ability to deliver dose rapidly. This links VHEEs to FLASH radiotherapy – a rapidly developing field involving the delivery of radiation at ultra-high dose rates (> 40 Gy/s), with observations of significantly reduced radiation-induced side effects. Section 2.5 will give a

review of published FLASH studies along with current research on incorporating VHEEs in FLASH.

The chapter will conclude with a summary of the areas in VHEE radiotherapy which require further research, including an understanding of VHEE beam behaviour and the radiobiological effects of VHEE, and how this thesis aims to fill in some of these knowledge gaps.

2.2. Why VHEE?

Clinical electrons (6-15 MeV) may be suitable for treatment of superficial cancers but are unsuited to treatment of deep-seated cancers. Their poor penetrability, typically two or three centimetres into the body as demonstrated in Fig. 1.14, prevents a particle beam from reaching tumours deep inside the body. Low-energy electron beams also deliver a high surface dose, increasing the risk of acute and long-term radiation effects such as radiation burns and development of secondary skin cancers respectively. Finally, low-energy electron beams exhibit significant lateral beam spread as they travel through a material. This can result in dose delivery to healthy tissue surrounding the region of interest and may again result in increased side effects during treatment and the possibility of secondary cancers developing in the years after treatment.

The concept of radiotherapy with Very High Energy Electrons (50-250 MeV) was introduced by C. DesRosiers in her doctoral thesis and accompanying papers[1]. The premise was to see if increasing the energy of electrons used in cancer treatment could resolve the issues associated with low energy electrons and provide a preferential treatment to photons.

These early studies by DesRosiers employed Monte Carlo simulations to investigate VHEE beam characteristics and dose distribution and make comparisons with similar photon beams. 200 MeV electron beams were found to be capable of penetrating over 30 cm in a water phantom. Phantoms are typically used as a model to measure dose delivered by a radiotherapy beam, and water is often used as it has a similar density to the human body.

Interest in VHEE radiotherapy research has grown over the past two decades, including studies on treatment planning, dose delivery and dosimetry. In 2002, the first optimised treatment plan for VHEE was developed by C. Yeboah et.

al.[82]. The same year, a comparison was made between optimised treatment plans for VHEE therapy and intensity-modulated X-ray therapy (IMXT), in which the radiation dose is shaped to the tumour by modulating the intensity of the X-ray beam during treatment. VHEE therapy proved superior at sparing Organs At Risk (OARs) in the prostate cancer treatment plan compared with IMXT[83].

Further treatment plan comparisons were carried out in 2014 by Bazalova-Carter et. al.[5] between 100 MeV VHEE therapy and Volumetric Modulated Arc Therapy (VMAT), a type of IMRT in which the linac rotates around the patient during treatment, modulating the intensity and changing the beam shape as it rotates. A number of clinical cases were tested, including paediatric brain, lung and prostate. The dosimetric advantage of VHEE over VMAT was demonstrated, with superior treatment plans (improved tumour coverage and reduced OAR doses) for the three cases. Fig 2.1a shows axial (L) and coronal (R) dose maps of the VHEE and VMAT paediatric brain treatment plans, with OAR and tumour outlined. OAR sparing of 30% to temporal lobes and 70% to cochlea was observed in the VHEE plan compared with the VMAT plan.

Similar results were found in a 2016 study by the same group[6] when comparing 100 MeV and 200 MeV VHEE to VMAT and Proton Pencil Beam Scanning (PPBS). Four clinical cases – paediatric brain, head and neck, lung and prostate – were compared. Again, the VHEE cases were found to be superior or similar to the VMAT cases, with improved dose conformity and OAR dose reduction at 200 MeV compared to 100 MeV. While PPBS was found to be the better method overall, 100 and 200 MeV VHEE plans did show reduced doses to some OAR – Fig 2.1b for example shows the OAR doses for the paediatric brain case, with VHEE plans delivering lower doses to the brainstem, chiasm and spinal cord compared with VMAT and PPBS plans.

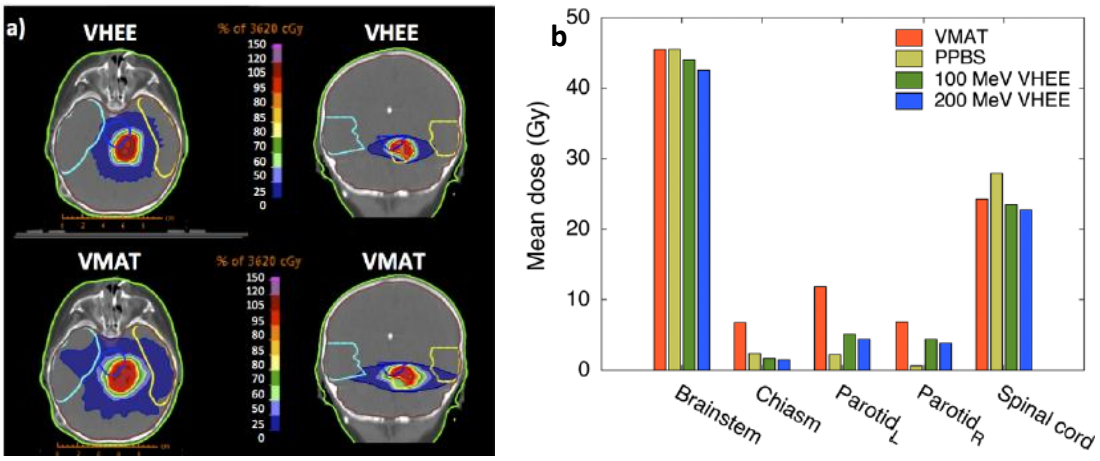

Figure 2.1 – a) Dose maps for treatment of paediatric brain tumour with 100 MeV VHEE and conventional VMAT. VHEE plan delivered lower or comparable doses to all OARs compared with VMAT. Image taken from [5]. b) Figure 1 - Mean dose delivered to OARs during treatment of paediatric brain tumour. VHEE delivered lower doses to all OARs than VMAT and, for some OARs, than PPBS. Image taken from [6]

As it is vital to accurately know the dose being delivered to a patient during treatment, research into VHEE dosimetry has been carried out in the last decade – specifically to determine if current dosimetry methods can be used with VHEE beams. The earliest study by Lundh et al.[84] conducted an experimental study using a 120 MeV electron beam. Doses recorded by phosphorescent screens on a polystyrene phantom agreed with Monte Carlo simulations to within 5%.

Further experiments involving irradiation of EBT2 Gafchromic film using 135 MeV electrons at the ALPHA-X facility[85] and 165 MeV electrons at the SPARC linac facility[86] were carried out in 2014 by A. Subiel *et al.*[7]. Depth dose curve comparison with Monte Carlo simulations in FLUKA[87,88] indicated the

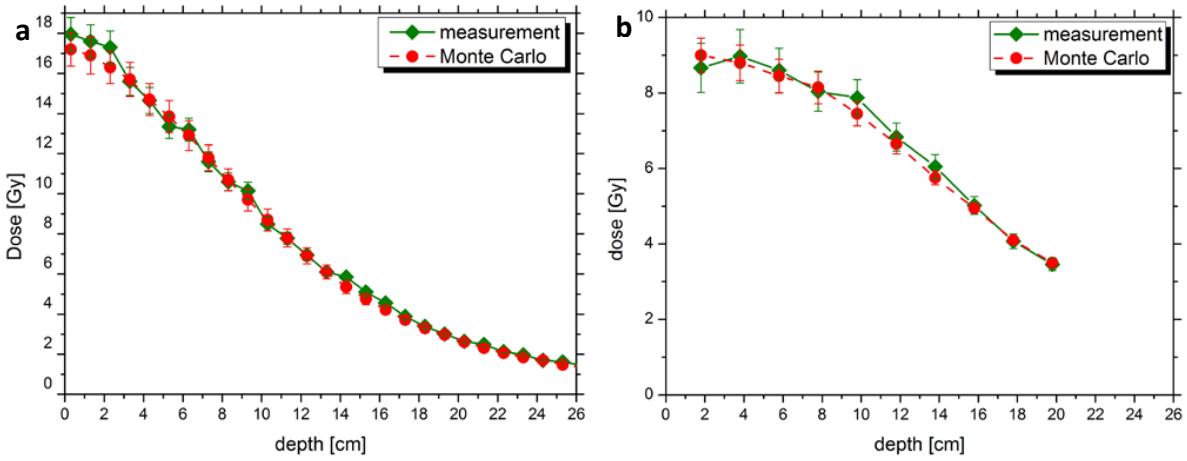

Figure 2.2 – Comparison between measurement and MC simulations for depth-dose profile of a) 165 MeV electron beam (SPARC) and b) 135 MeV electron beam (ALPHA-X). Images taken from [7]

suitability of EBT2 film as a dosimeter for VHEE, as indicated by Fig. 2.2. Standard errors of 1-2.5% and 1-2% were measured for the 135 MeV and 165 MeV electron beams respectively compared to Monte Carlo data, suggesting that EBT2 film is indeed a suitable dosimeter for VHEE.

2.3. Accelerator Technology for VHEE

The level of interest in VHEE as a potential radiotherapy treatment has been motivated by the development of robust methods for high-gradient acceleration. Currently, low energy electron beams for radiotherapy are produced using treatment machines built around linear accelerators, involving a series of accelerating fields used to accelerate the electrons. These typically have an accelerating gradient of 4-8 MeV/m.

The production of VHEE beams in a clinical facility therefore poses a problem. The beams must be produced over a distance of 3-4 m to prevent the need to build new, expensive facilities to house the accelerator, requiring accelerating gradients in the region of 100 MeV/m. The following high-gradient accelerating methods could provide a solution to this issue:

1. **X-band RF Linear Accelerators** – The aim of any particle accelerator is to deliver energy to a charged particle beam by the application of an electric field. Photon and low-energy electron beams are currently produced by RF linacs. In an RF linac, in which power is delivered by a radio frequency source (a magnetron or klystron), a harmonic, time-varying electric field is applied[89]. The beam is split into bunches, which arrive in accelerating cavities when the electric field is the correct polarity for acceleration.

   Linear accelerators have the ability to produce high-energy and high-intensity beams with small diameter and energy spread. Due to the particles travelling in a straight line, no power is lost due to synchrotron radiation (the radiation emitted by charged particles subject to radial acceleration). As RF linac technology improved, accelerators with increasing frequencies were developed[90]. A VHEE treatment machine would require an accelerating gradient of the order of 100 MeV/m, which has been achieved in recent years using accelerators operating at X-band

frequency (~12 GHz). X-band linacs can use a shorter length for a given power to reach a particular beam energy due to their higher shunt impedance per unit length (a measure of the effectiveness of a cavity at producing an axial voltage for a given dissipated power over a specified length[91]) and higher maximum permissible electric field strength.
Over the last two decades, progress has been made in the production of high-gradient X-band linacs, with the International Linear Collider (ILC)[92] and subsequently the Compact LInear Collider (CLIC) programs[93]. Development of X-band accelerating structures for CLIC at the University of Manchester (in collaboration with CERN and Morikawa Ltd.) has resulted in the repeated production of accelerating gradients of ~100 MeV/m[94]. Over 74,000 of these structures will be required for electrons and positrons to reach the planned 3 TeV in CLIC.
Adapting CLIC technology, based on the CERN Linear Electron Accelerator for Research (CLEAR) prototype[95], an S-band linac, could result in the production of compact, high-gradient medical linacs with accelerating gradients of 80-100 MeV/m. These would be capable of producing 250 MeV electron beams over 3-4 m – suitable for installation in current clinical radiotherapy facilities.

Figure 2.3 - CLEAR accelerator at CERN [151], with energy range 60-200 MeV.

2. **Laser-plasma wakefield accelerators (LPWA)** – The accelerating gradient of conventional RF linacs are limited to approximately 100 MeV/m due to electromagnetic breakdown[96]. This makes the building of GeV or TeV accelerators extremely expensive as the accelerator must be very long. A potential solution is to use a plasma – a fluid of ions and free electrons.

Laser-plasma wakefield acceleration has been studied as a novel acceleration method since the late 1970s. When an intense laser is fired through a plasma, the free electrons in the plasma are pushed away from the laser pulse by the ponderomotive force – the force experienced by charged particles travelling through the electric field produced by the laser pulse. Electrons are then pulled back by the positive ions in the plasma. As their momentum has increased, the electrons overshoot and oscillate about their original position, forming a plasma wave. This forced ion and electron separation excites a wakefield – defined as a longitudinal electron density wave – which travels behind the laser pulse.

The separation also results in the generation of a very high electric field which can be used to accelerate charged particles that are either injected into the plasma wave or pulled directly from the target plasma. As the wakefield travels at the same velocity as the laser pulse, the charged particles can be accelerated to relativistic energies[97].

The strong electric fields produced on firing the laser through the plasma result in extremely high accelerating gradients – electrons have been accelerated to 1 GeV over just 3.3 cm at the Lawrence Berkeley National Laboratory. Using conventional accelerating methods requires an accelerating distance of 64 m to reach the same energy[98]. LPWA therefore has the potential to develop ultra-compact linear accelerators, capable of accelerating electrons to 250 MeV in less than a centimetre.

LPWA does come with disadvantages, however. Plasma acceleration is currently around 100 times less efficient than conventional accelerator methods. The power requirement and associated cost to run such an accelerator would be too high for most hospitals. In addition, the stability of the beams is currently unsuitable for clinical use. Beams produced so far exhibit large jitter in energy, charge and position[97]. If used in radiotherapy treatment, this would result in variations in dose delivered and the position of delivery – dangerous for the patient, who may receive too high or too low a dose or may receive a high dose to surrounding OARs.

Designs for a VHEE treatment machine have been developed in recent years. In 2013, a patent was submitted for a machine called PHASER – Pluri-directional

High-energy Agile Scanning Electronic Radiotherapy[99]. This machine is designed to deliver VHEE radiotherapy treatments using a high-gradient linear accelerator to produce the VHEE beams and is shown in Fig. 2.4. The beam delivery system aimed to eliminate the need for moving parts (particularly a slow-moving, heavy gantry) either by using multiple accelerating structures with beam windows arranged radially around the patient or by electromagnetically steering the beam to the target from any direction. Both would provide 360º target coverage.

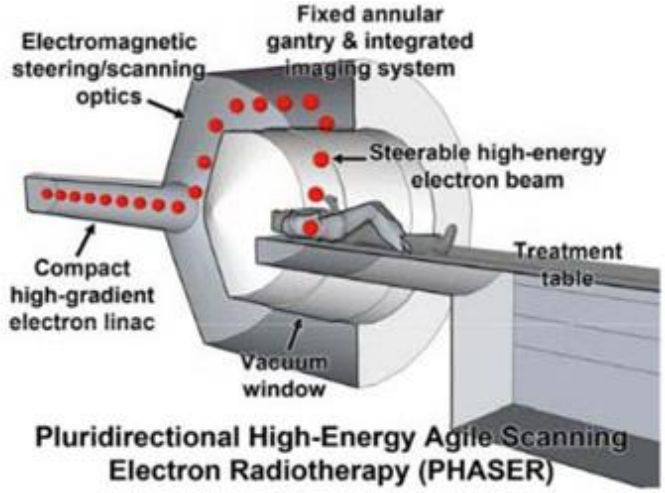

Figure 2.4 - Schematic of the patented PHASER treatment delivery system. The patient is moved into a circular, non-moving gantry, with beams capable of being steered to the target over 360º. Image taken from [121]

2.4. Characteristics and Advantages of VHEE Beams

2.4.1. Increased Range

By increasing the energy of the electron beams, the beam can travel much further into body and can deliver sufficient dose for effective treatment. This can be demonstrated by looking at the on-axis percentage depth dose (PDD) curves for electron beams over the energy range 15 – 250 MeV as they travel through a 30 x 30 x 30 cm^3 water phantom – see Fig. 2.5.

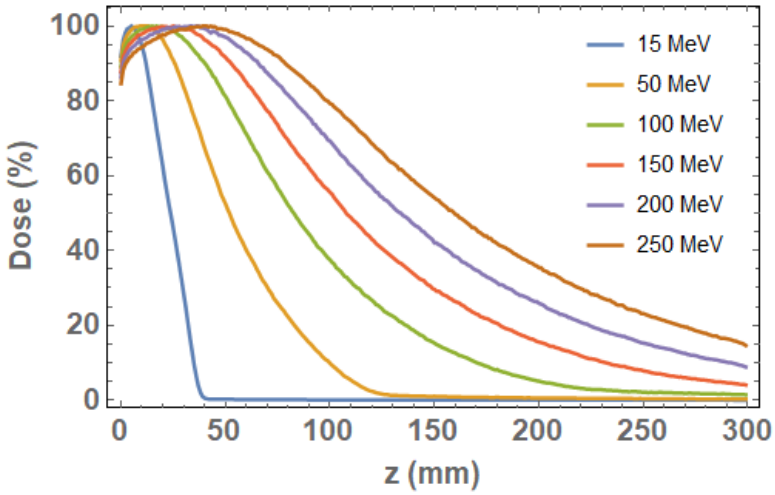

Figure 2.5 – On-axis percentage depth-dose curve for Gaussian electron beams at energy 15-250 MeV with beam sigma of 5mm consisting of 10^6 electrons travelling through a 30x30x30 cm^3 water phantom. Simulated using TOPAS

Crucially, VHEE beam range is also comparable to that of modalities currently used to treat deep-seated tumours – 15 MV photons and high-energy protons (see Fig. 2.6).

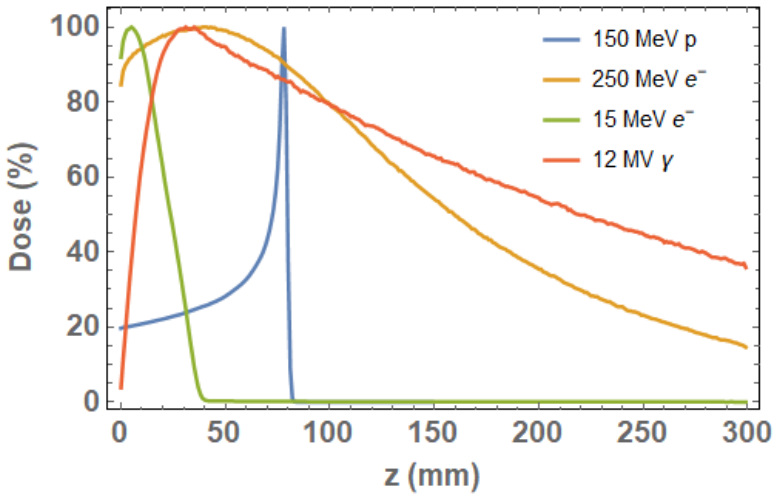

Figure 2.6 – On-axis percentage depth-dose curves for Gaussian beams of 15 MeV and 250 MeV electrons, 150 MeV protons and 12 MV photons with beam sigma of 5mm consisting of 10^6 particles travelling through a 30x30x30 cm^3 water phantom. Simulated using TOPAS

2.4.2. Insensitivity to Inhomogeneities

Unfortunately, patients are rather more complicated than simple water phantoms, being made up of tissues of varying density and composition. To produce an accurate, effective treatment plan, the effect of these inhomogeneous regions on a particle beam's behaviour must be understood.

This effect has been studied extensively in proton therapy, in particular the effect of unplanned inhomogeneities on the Bragg peak position[100]. Monte Carlo simulation studies[101,102] have consistently indicated that the presence of inhomogeneous regions in the beam path result in significant shifts in the Bragg peak, and therefore significant range uncertainty. Clinically, this can result in high radiation doses being delivered to healthy tissues (increasing acute side effects and the probability of a secondary cancer developing several years after treatment) and the tumour not receiving the prescribed radiation dose.

The effect of inhomogeneities of VHEE beams was initially studied by DesRosiers[2] through Monte Carlo simulations with PENELOPE (Penetration and ENErgy Loss of Positrons and Electrons)[103]. Simulations were carried out by firing a beam through a water phantom containing air bubbles or bone inserts. Similar simulations were carried out as part of this project using TOPAS (a wrapper for the Monte Carlo particle tracking code GEANT4[8,9,104], which will be described in detail in Chapter 3) to demonstrate the effects of these inhomogeneities and how the effect differs between protons and electrons. The simulations consist of a beam with σ = 5mm, delivering a charge of 1.6 pC to a 30 x 30 x 30 cm^3 water phantom – a schematic of the phantoms with and without inserts are shown in Fig. 2.7.

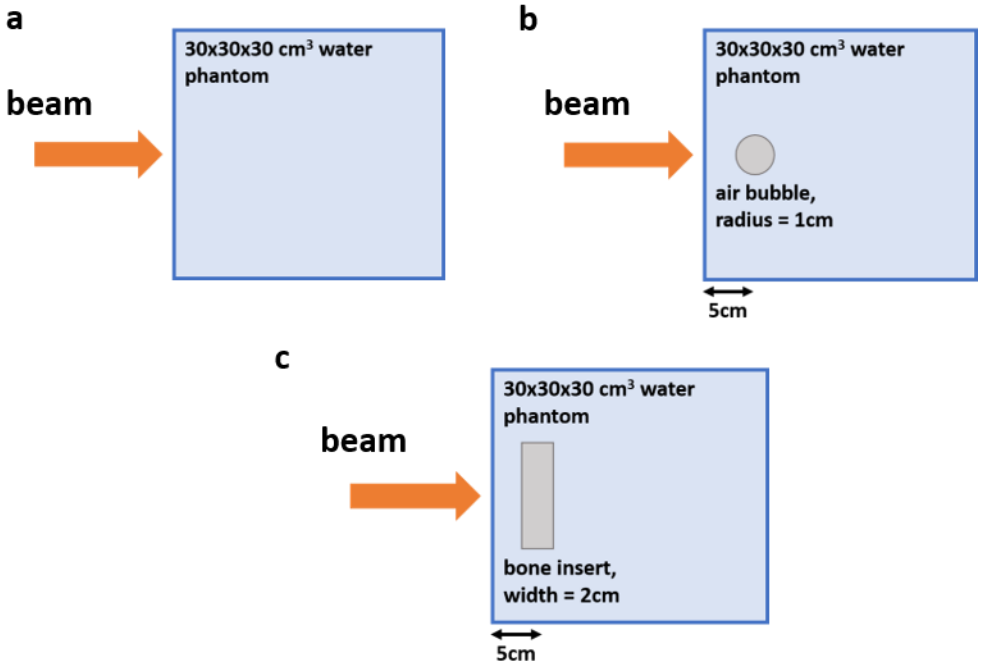

Figure 2.7 - TOPAS simulation setup for a) homogeneous water phantom and water phantoms containing b) an air bubble of radius 1 cm and c) a bone insert of width 2 cm. The centre of each insert is positioned at a depth of 5 cm in the phantom

The results of these simulations are presented in Fig. 2.8, with a-c showing dose maps for 150 MeV proton beam simulations and d-f showing dose maps for 150 MeV electron beam simulations. It can be surmised from the Monte Carlo simulations that the dose distribution of VHEE beams is not significantly affected by the presence of inhomogeneities.

The phenomenon was demonstrated experimentally by Lagzda *et al.*[3,4,105] following an experimental study using 205 MeV electrons at the CLEAR facility. A polypropylene water phantom was constructed in which air and bone-equivalent inserts could be positioned. The dose delivered along the phantom was measured with EBT3 Gafchromic film inserted at several positions along the phantom to produce PDD curves.

Experimental PDD curves for different inhomogeneities were compared to study the effect of inhomogeneities and compared to Monte Carlo TOPAS simulations to validate the use of TOPAS for VHEE dosimetry to within 5%. Simulated and experimental dose profiles were found to be consistent with each other, and the lack of significant deviation between dose profiles of different media suggest that the dose distribution of VHEE beams is relatively unaffected by the presence of inhomogeneities.

This characteristic suggests that VHEE beams could be well-suited to treatment of inhomogeneous regions in the body. This could include the bowel due to the presence of air cavities and in particular the lungs, due to the highly heterogeneous nature of chest cavity consisting of muscle, bone, lung tissue and air pockets.

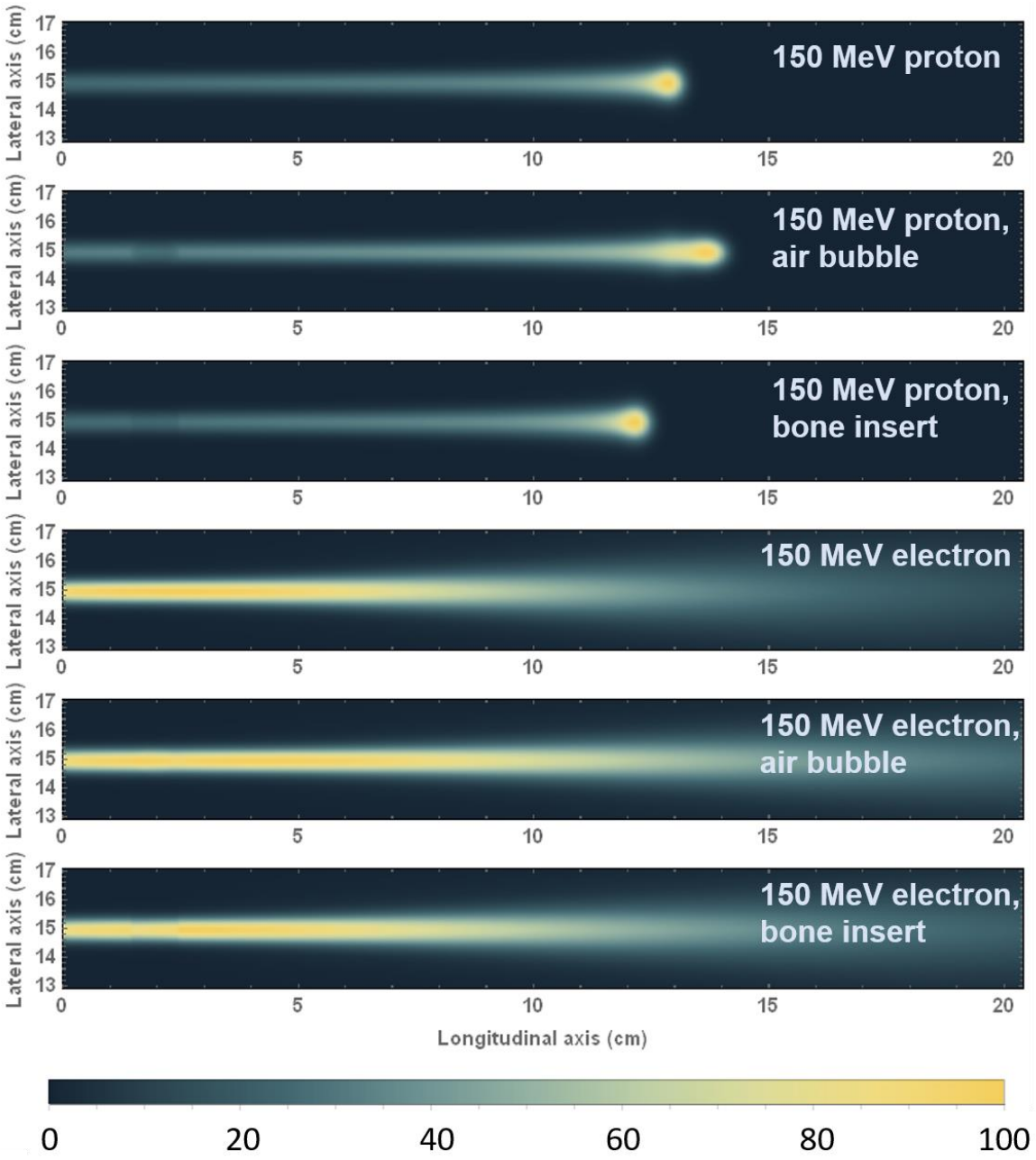

Figure 2.8 - Beam profiles for 150 MeV proton and electron beams (Gaussian, σ = 5mm, 10^6 electrons) travelling through water phantoms with no inhomogeneity, an air bubble of radius 0.5 cm or a bone insert with width 1 cm placed at a depth of 2 cm in the phantom. Proton dose maps indicate significant sensitivity to inhomogeneities (Bragg peak shift) while electron dose maps do not.

2.4.3 Dose Distribution

A further disadvantage of low energy electron beams is their large lateral scatter compared to proton or photon beams. This means that as a beam travels through a material, it will laterally spread. This could result in dose being delivered to surrounding healthy tissue. To successfully treat a tumour while avoiding irradiation of healthy tissue, this beam spread must be reduced.

DesRosier[2] suggested that increasing the beam energy of the electron beam could reduce the lateral beam scattering. This was tested by simulating Gaussian electron beams of varying energy (50-250 MeV) using TOPAS and measuring the beam sigma as it travels through a 30x30x30 cm^3 water phantom. Fig. 2.9 and Table 2.1 below indicate that this hypothesis was true – as the energy is increased from 50 to 250 MeV, the relative change in beam width is reduced.

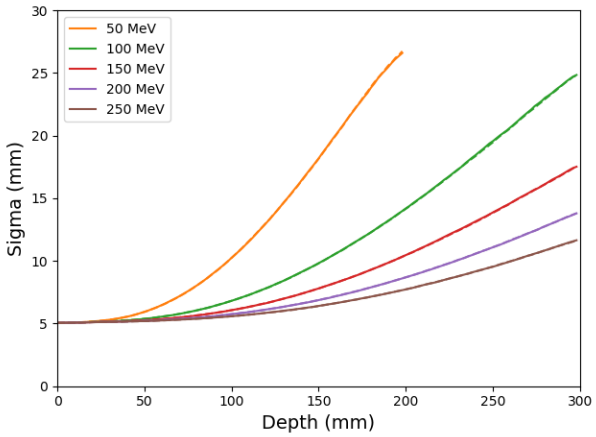

Figure 2.9 - Lateral beam sigma in the x-plane vs. phantom depth for 15-250 MeV electron beams. Data acquired following simulation of Gaussian electron beams (σ = 5mm) travelling through a 30x30x30 cm^3 water phantom using TOPAS

Beam Energy (MeV)	Initial σ (mm)	Final σ (mm)	% Increase
50	5.037	26.72	430.5
100	5.035	24.464	385.9
150	5.031	17.518	248.2
200	5.031	13.793	174.2
250	5.032	11.642	131.4

Table 2.1. Comparison of initial (5mm) and final Gaussian beam σ consisting of 10^6 electrons after travelling through a 30cm cubic water phantom.

While VHEE beams could be effective at treating deep-seated tumours with relatively reduced lateral scattering compared to low energy beams, they do exhibit a high exit and entrance dose. As is clear from the PDD curve in Fig. 12, proximal and distal tissue also receives a high dose.

This issue is not experienced in proton therapy treatments. The primary advantage of the Bragg peak is the very small volume over which the dose is delivered, after which the rapid dose fall-off means that the distal tissue receives a negligible dose. In order to fully cover the tumour volume, a Spread-Out Bragg Peak (SOBP) can be produced using a weighted combination of monoenergetic Bragg peaks[78]. The prescribed volume is treated, while maintaining the advantageous dose fall-off beyond the tumour (Fig. 2.10).

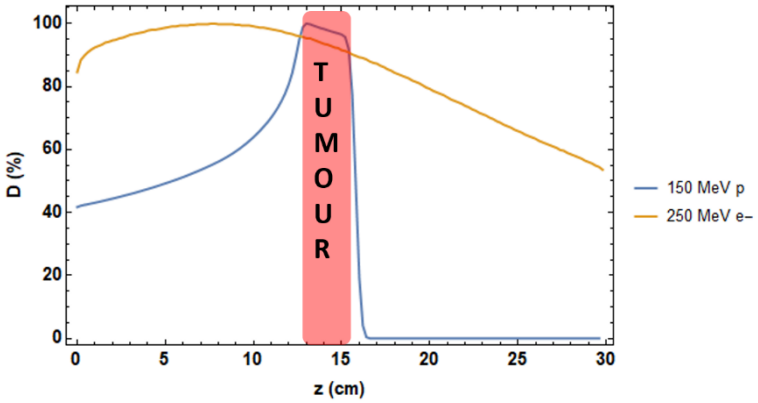

Figure 2.10 - Comparison of tumour coverage by 150 MeV proton SOBP and 250 MeV electron beam

While electron beams do not exhibit this Bragg peak, it was suggested by Glinec *et al.*[106] that the entrance and exit doses could be reduced by focusing the electron beam using quadrupole magnets, an example of which is shown in Fig. 2.11. Charged particles travelling in an accelerator experience a Lorentz force[107]:

$$\vec{F} = q\left(\vec{E} + \vec{v} \times \vec{B}\right) \qquad (2.1)$$

where q is the particle's charge, $\vec{v}$ is the particle's velocity and $\vec{E}$ and $\vec{B}$ are the strengths of the electric and magnetic fields acting on the particle respectively. As the magnetic force term is greater than the electric term, magnetic deflection of the particle beam is more effective than electrostatic.

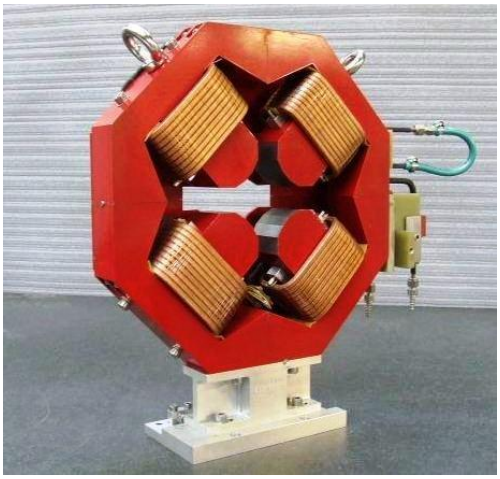

Figure 2.11 - Example of a quadrupole magnet used in the TRIUMF accelerator (www.triumf.ca)

A study was carried out by Glinec *et al.*[106] using the Monte Carlo particle tracking code GEANT4 to investigate focusing effects of quadrupoles on a 170 MeV electron beam produced by a laser-plasma accelerator. Analysis found a 15% decrease in lateral penumbra when focusing the beam compared to not focusing the beam at 10 cm within a target water phantom.

Further simulation, carried out using FLUKA by the Strathclyde group[108], indicated that 200 MeV VHEE beams could be used to irradiate small (1 cm^3) volumetric elements by focusing the beams using quadrupoles organised in a FODO lattice. This lattice contains two types of quadrupole – an F quadrupole (horizontally focusing but vertically defocusing), and a D quadrupole (vertically focusing but horizontally defocusing). By separating these magnets, the overall effect is to focus the beam in both horizontal and vertical planes, reducing beam spread (Fig. 2.12). Simulations in this study involved varying the focus geometry, quantified by the f-number – defined as the ratio between the focal length of the magnetic lens and the diameter of the beam travelling through the lens.

The success of quadrupole focusing and the ability to scan a VHEE beam indicates that large or irregularly-shaped tumours could be treated by scanning a VHEE beam over the required volume.

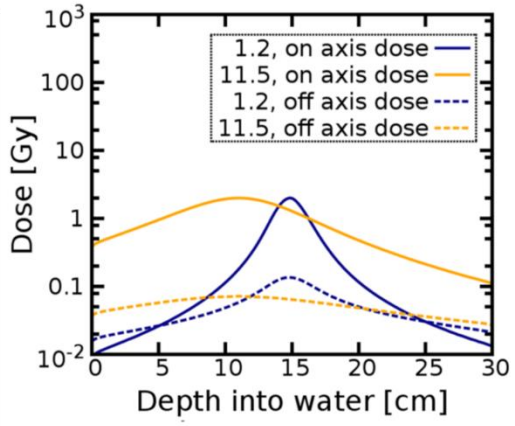

Figure 2.12 – On-axis dose-depth curve for 200 MeV electron beam focused at 15 cm into a water phantom with varying f-numbers, taken from [34]

2.4.4. Rapid Delivery of VHEE Beams

A limiting factor to the efficacy and efficiency of radiotherapy is time. A typical X-ray radiotherapy session lasts around 15 minutes, with the following factors contributing to this treatment time:

1. X-ray production – the production of X-rays via Bremsstrahlung is an inefficient process, with clinical beams having a Bremstrahlung efficiency of ~3% in terms of the X-ray power output from the electrical input.
2. Gantry rotation – treatment plans are optimised through the delivery of radiation beams at multiple angles. This requires the use of a gantry to move the beam source around the patient. Due to the weight of the gantry (typically several tons), this mechanical motion is very slow.

The production of VHEE beams, unlike X-ray beams, does not involve this Bremsstrahlung process. Production is more efficient and requires fewer particles to deliver the equivalent dose with X-rays, reducing production time[5]. As part of this project, the number of particles required to deliver a maximum dose of 1 Gy to a water phantom was calculated based on TOPAS simulations of 15 MV photon and 250 MeV electron beams travelling through a water phantom. The results are shown in Table 2.2.

Modality	No. Particles required for 1 Gy
15 MV photons	**3.37×10^{12}**
200 MeV electrons	**2.28×10^{11}**

Table 2.2. Number of particles required to deliver a maximum dose of 1 Gy into a water phantom. Maximum dose obtained from TOPAS simulations of on-axis PDD curves for 15 MV photon and 200 MeV electron beams (Gaussian with σ = 5mm)

It is also possible to exploit the fact that electrons are charged particles to reduce delivery time. A charged particle beam, unlike an X-ray beam, can be steered using an electromagnetic field. Through accurate control of the beam, a beam can be scanned over a treatment volume very quickly compared to the mechanical motion of a gantry.

Electrons also have a much lower rest mass compared to heavy ions – 0.511 MeV/c^2 compared to 938 MeV/c^2 for a proton. Dipole magnets are used to steer particle beams, with the strength of a magnetic field required to bend a beam given by the beam rigidity equation[109]:

$$B\rho = \frac{p}{q} \tag{2.2}$$

where B is the magnetic field strength, ρ is the bending radius and p and q are the particle's momentum and charge respectively. Electron beams require a magnetic field of around 1/5 to 1/3 the strength of that required by the proton beam within the energy range associated with VHEE (50-250 MeV), as indicated in Fig. 2.13. The reduced magnetic field strength required allows electron beams to be scanned more rapidly than the equivalent proton beam.

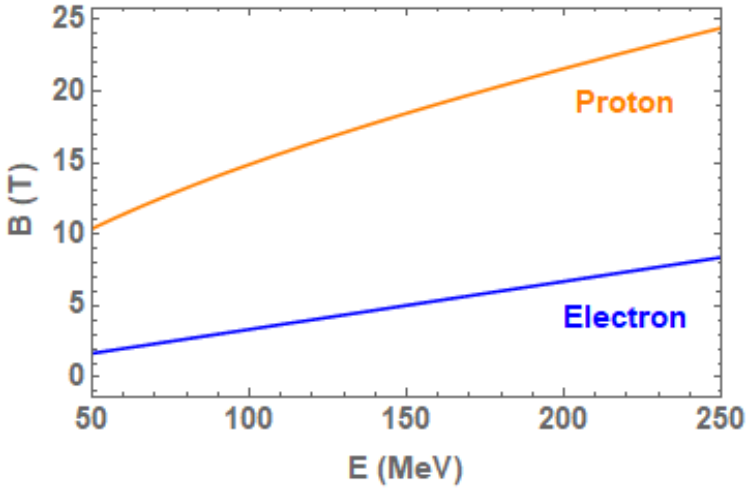

Figure 2.13 - Dipole magnetic strength required to provide a bending radius of 10 cm to VHEE and proton beams over energy range 50-250 MeV. Graph produced in Mathematica

Both improved beam production efficiency and electromagnetic scanning could potentially allow a treatment fraction to be delivered over a sub-second timescale. This rapid delivery may aid in resolving a further treatment issue – that of patient, tumour or organ motion during treatment.

Intra-treatment motion comes from many sources, including breathing, cardiac motion, organ filling (such as the bladder or sinuses) and musculoskeletal motion. Preventative measures can be taken to minimise this motion, with these including the use of masks or frames to fix the target region in position and, for thoracic irradiation, breath-holding or respiratory gating[110]. These methods still have associated uncertainty, potentially resulting in slight tumour misalignment and delivery of dose to healthy tissue.

Rapid delivery may improve the efficiency of such techniques, or even make them unnecessary. By delivering the prescribed fraction in under a second, physiological motion can essentially be frozen, allowing improved accuracy, improvements in paediatric treatments (patients are typically anaesthetised, which may be traumatic for both patient and parent) and increased patient throughput.

2.5. FLASH Radiotherapy

2.5.1. What is FLASH Radiotherapy?

The ability to deliver treatment over sub-second timescales makes VHEE a potentially suitable modality for FLASH radiotherapy. FLASH is a technique in which a radiation dose is delivered rapidly to the patient – typically with a dose rate in excess of 40 Gy/s compared to conventional dose rates of ~0.03 Gy/s[81].

Use of ultra-high dose rates in radiotherapy has been studied as far back as the 1970s and 80s[111–113], typically in vitro due to technical limitations in delivering these ultra-high dose rates over sufficiently large field sizes. These initial studies did not indicate significant improvements in high dose rate irradiation over treatment with conventional dose rates. As a result, interest in high dose rate radiotherapy waned. Since 2014, however, there has been a rapid resurgence in interest in high dose rate radiotherapy due to observations of drastically reduced radiation-induced side effects.

The following sections form a review of recent work in the field of FLASH radiotherapy, including the characteristics and advantages associated with the technique, the technological requirements to deliver it and the potential for VHEE FLASH radiotherapy.

2.5.2. Characteristics and Advantages of FLASH Radiotherapy

The primary advantage of FLASH radiotherapy is the increased differential response[80] between normal and tumour tissue. This can give two results. Firstly, if the treatment dose is kept the same, the likelihood of normal tissue complication is lower – reducing the severity of side effects suffered by the patient. Alternatively, the increased differential response can mean that the treatment dose can be increased. This will increase the likelihood of tumour control while maintaining normal tissue complication probability. This is made clear in the TCP/NTCP curves in Fig. 2.14.

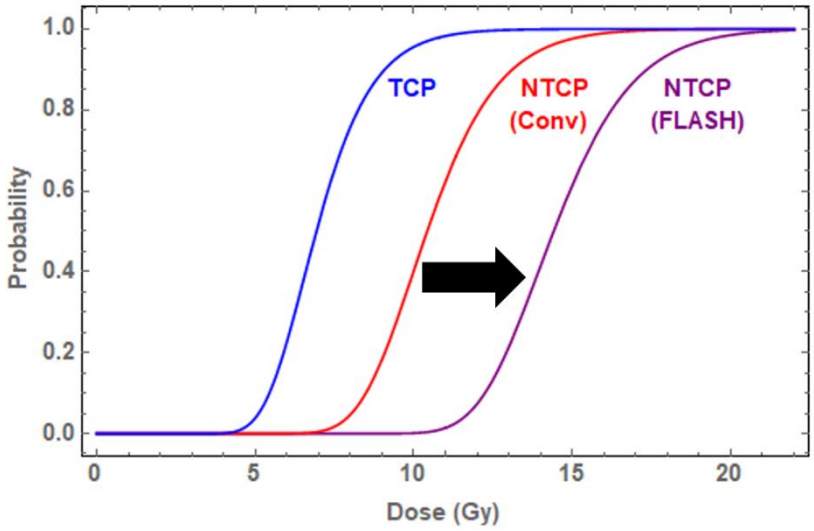

Figure 2.14 – TCP/NTCP curve indicating differential response of FLASH therapy. Normal tissue can receive a higher dose before complications occur following FLASH radiotherapy. Graph produced in Mathamtica

A series of studies have been carried out to investigate how FLASH therapy can reduce radiation-induced side effects in comparison to conventional radiotherapy. The first FLASH experiments were carried out at the Lausanne University Hospital (CHUV) using 4.5 MeV electrons produced by an experimental linac capable of generating both conventional (often referred to as 'Conv' in the literature) and FLASH dose rates.

Initial thoracic irradiation of mice indicated that, unlike the equivalent Conv-RT dose, FLASH-RT did not induce formation of excess fibrous tissue (fibrogenesis) in the lung. Radiation-induced side effects were observed during a

FLASH dose-escalation study, though at higher doses than those at which the same effects were observed after Conv-irradiation – indicating an increased tolerance of normal tissue to FLASH irradiation.

A similar study[114] involving whole-brain irradiation (WBI) of mice found that cognitive function including memory formation and learning was increasingly preserved on escalating the radiation dose rate to FLASH levels (>40 Gy/s). This indicated the potential for a promising method for brain treatment (see Fig. 2.15a).

The promising results from the early studies led to further investigation into the FLASH effect on higher mammals[115]. Pig skin (a good approximation for human skin) was irradiated with identical doses at Conv and FLASH dose rates. No toxicity or long-term hair loss was observed following FLASH-RT, while following Conv-RT, the skin showed ulceration, necrosis and permanent hair loss as observed in Fig. 2.15b.

Investigations into tumour control by FLASH-RT were also carried out. Initial mouse studies involved human breast cancer, head and neck carcinoma and lung tumours and compared both tumour control and side effects following FLASH-RT and Conv-RT[80]. In all cases, FLASH-RT was as efficient at repressing tumour growth as Conv-RT at equivalent doses while not inducing side effects. Dose escalation studies for the HNC and lung cases indicated that tumour control improved with increased dose (as expected), but increasing the dose did not cause the side effects observed at lower dose Conv-RT.

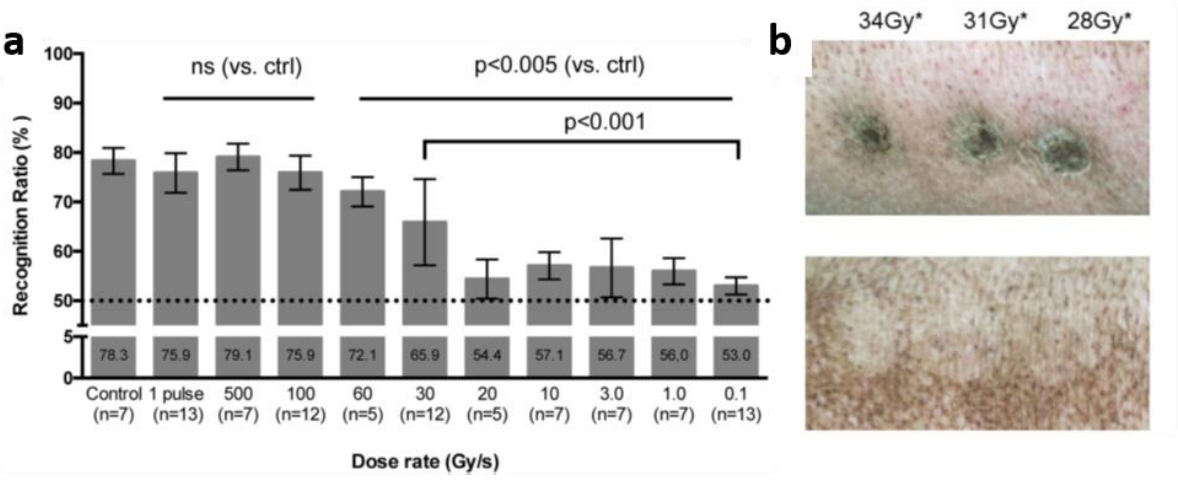

Figure 2.15 - a) Result of mouse memory study following irradiation with electrons at various dose rates. Improved memory sparing observed for FLASH dose rates compared with conventional dose rates. Image taken from [115] b) Pig skin following electron irradiation at (top) conventional dose rate and (bottom) FLASH dose rate - note lack of skin lesions and hair regrowth on FLASH-irradiated skin. Image taken from [116]

A phase I clinical trial was then carried out[115], involving a dose escalation study on cats to determine the maximum tolerated dose, with secondary endpoints being observation of normal tissue tolerance in the irradiated field and disease survival. Complete tumour responses (no tumour evidence) were observed in all cats and only one cat out of the group of six experienced any limiting side effects. The maximum tolerated dose was not reached during the dose escalation study, indicating that higher doses could be tolerated.

Following the success of FLASH in treatment of mice and cats, the first human patient was treated in 2019[116]. A 3.5 cm cutaneous lymphoma was irradiated with a single fraction of 15 Gy and followed up for six months. Complete tumour response was observed after 5 weeks, with no recurrence and only mild side effects (redness and swelling) experienced in the first few weeks following irradiation.

In conclusion, FLASH radiotherapy has displayed in a limited number of experiments increased differential response between healthy and tumour tissue, being as efficient (if not superior) as conventional radiotherapy at controlling tumours while significantly and dramatically reducing the side effects experienced. Positive results over different tumour types, organs and species indicate that this could be a very effective cancer treatment, making FLASH a very exciting field of research[117,118].

2.5.3. Technological Requirements of FLASH Radiotherapy

Any FLASH radiotherapy machine must, by definition, be capable of delivering very high dose rates. Initial FLASH studies reached these dose rates by modifying existing medical linacs. These modifications are outlined in Lempart et al.'s 2018 paper[119], which aimed to produce FLASH dose rates using a medical linac such that any modifications made were quick to implement, reversible and would not interfere with normal clinical treatment.

Various parameters were altered to achieve FLASH dose rates: the electron gun current was adjusted for maximum output; the pulse charge rate and repetition frequency were increased; scattering foils were removed from the beam path. Such modifications resulted in successful production of high dose-rate beams (up to 1000 Gy/s depending on the position at which dose rate was measured).

Accurate dosimetry is a key requirement for FLASH radiotherapy but is difficult at high dose rates. Current radiotherapy dosimetry protocols are not designed for such extreme conditions, so new methods are required. In the mouse memory study[114], the dose at the surface of a water phantom was measured using an ionisation chamber, EBT-3 Gafchromic film and alanine pellets, with all methods indicating that the prescribed 10 Gy was accurately delivered.

In Jorge *et al.*'s study[120], Thermo-Luminescent Dosimeter (TLD) chips were placed in recently-euthanised mouse skulls during irradiation, also validating that the prescribed 10 Gy was delivered to the mouse brains. Such results indicate that these methods are suitable for FLASH dosimetry – this was verified following similar dose measurements in the mini-pig and cat studies.

2.5.4. VHEE and FLASH Radiotherapy

The FLASH effect has been observed with radiotherapy modalities other than low energy electrons. In 2018, for example, a further mouse WBI study was carrying out using high dose rate X-ray beams produced at the European Synchroton Radiation Facility (ESRF) in France[121], with a similar FLASH effect (cognitive function preservation) observed for X-rays as for electrons.

A FLASH proton device has also been developed for small animal irradiation with Buonanno et al.'s 2019 paper[122] on the biological effects of FLASH on normal cells indicating that FLASH-irradiated cells, unlike conventionally-irradiated cells, did not suffer from long-term detrimental effects, including inflammatory responses.

While both modalities exhibit the desired FLASH effect, clinical translation is likely to be difficult. For X-ray FLASH, the power of the accelerator must be at least 100 times greater than that for low energy electron FLASH due to lower production efficiency (Bremsstrahlung conversion). For proton FLASH, current dose rates are around 200 Gy/s for fast-scanning pencil beams. While this would cause a FLASH effect, the beam must be scanned over the whole tumour volume. This takes several seconds at best, meaning that a mean FLASH dose rate will not have been achieved over the tumour – required for the beneficial clinical effects.

This leaves VHEE as the likely option for FLASH treatment of deep-seated tumours. Recent developments in the PHASER machine discussed in section 2.2

have investigated using the machine to deliver FLASH radiotherapy[123]. The current machine concept employs the use of an electron accelerator, with compact, lightweight klystrons known as klystrinos providing the power. These can be combined, with 16 klystrinos powering 16 individual linacs, arranged radially around the patient. This negates the requirement for a mechanically rotating gantry. A concept design is shown in Fig. 2.16.

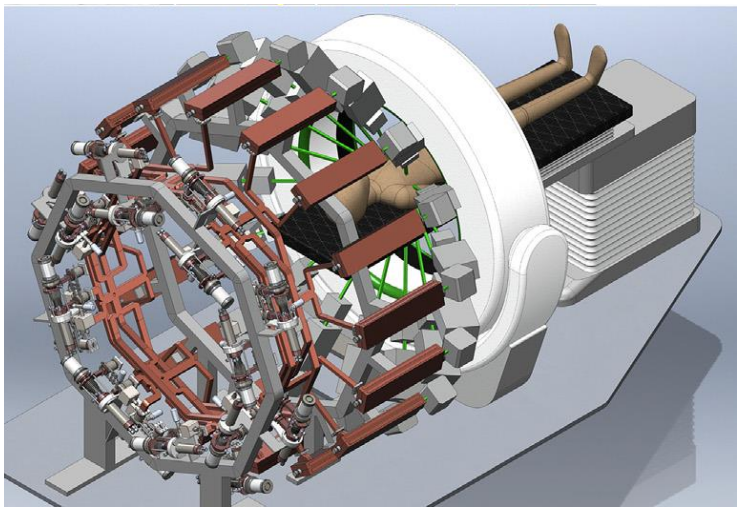

Figure 2.16 - Conceptual design for 16-linac PHASER treatment machine for FLASH radiotherapy with VHEE. Each linac contains a scanning system to give 360° coverage of the target. Image taken from [53]

While the PHASER FLASH machine is designed for 10 MV X-ray irradiation, the technology can be adapted for use with VHEE beams – by applying a higher peak power by using more klystrinos, a higher accelerating gradient can be achieved, and therefore a higher beam energy over the same distance.

2.6. Conclusion

The overviews in this chapter indicate the potential for VHEE radiotherapy as a treatment modality and its compatibility with FLASH radiotherapy, with particular suitability for curative treatment of highly heterogeneous regions such as the lung or bowel. Cancers in such regions are typically treated with radiotherapy in order to relieve symptoms as part of palliative, rather than curative, care.

Physical characteristics (such as dose distribution and range) of VHEE beams have shown to be advantageous for radiotherapy. Treatment planning was

discussed in section 2.3, with studies by Bazalova-Carter[5] and Schuler[124] showing the superiority of VHEE treatment plans compared to VMAT treatment plans with improved dose conformity and OAR sparing. Currently, there is no analytical understanding of the VHEE beam as it travels through material, including the range of the beam, which can lead to uncertainties in treatment planning. Such a topic has been researched extensively in proton therapy[125,126], in order to produce more accurate treatment plans.

Producing an analytical expression for VHEE beam range could improve treatment planning by reducing the complexity of calculations – currently Monte Carlo simulations are used in treatment planning calculations, requiring a great deal of computational power and time. Chapter 3 therefore covers the development of a semi-empirical expression for the range of VHEE beams in various media, based on simulations of the beam travelling through phantoms of different materials using TOPAS. By producing an analytical expression for VHEE beam range, range calculations can be made rapidly, which may also allow for quick modification of a patient's plan as they progress through their treatment.

There are several areas of research which have so far not been explored – areas which are key in terms of the clinical implementation of VHEE radiotherapy, in particular radiobiology. Radiobiology is a field of medical science involving the study of the effects of ionising radiation on biological structures and is crucial in the comparison of different radiotherapy modalities, with a key quantity of a modality being its RBE. At present, there is no published data available on VHEE RBE. By determining this quantity, clinical comparisons between VHEE and other established radiotherapy modalities can be made.

Chapter 4 will look at the damage VHEEs cause at the nanodosimetric level – the physical and chemical damage that is sustained by the DNA following VHEE irradiation – and how that compares with the damage caused by other, clinically established modalities, including photons, by calculating RBE with DSBs as the biological endpoint. If the physical and chemical effects of VHEE are similar to those caused by photons, this gives confidence that the biological effects, such as DNA damage repair and cell death, should also be similar – a step towards clinical implementation.

Radiobiological modelling is also an area of VHEE research in which there is little available data. Computational modelling is a widely used tool for clinically established modalities, allowing predictions of the effects of ionising radiation on biological structures to be made without performing experiments – radiobiological experiments in particular can exhibit wide variation across datasets. Such models can be used to determine RBE of a particular modality. Chapter 5 investigates the development of a DNA damage model for VHEE based on earlier models for proton-induced DNA damage and using the data obtained in Chapter 4 as a comparison.

Chapter 3 – Development of a Semi-Empirical Range Expression for Electron Beams in Various Media

3.1. Introduction

Analysis of percentage depth-dose (PDD) curves show that VHEE beams are capable of penetrating sufficiently far into the body to treat deep-seated tumours[2]. In order to optimise such treatment plans, it is vital to understand how a radiation modality distributes dose as it travels through the patient, as well as to know precisely how far into the body the VHEE beams are travelling. The ability to accurately determine the dose distribution and range results in reduced uncertainties associated with imaging, patient setup and beam delivery. Reducing uncertainties could permit reduction in treatment volume – beneficial for the patient as less healthy tissue surrounding the region of interest is irradiated[127].

Monte Carlo algorithms are commonly utilised tools in radiotherapy, with applications from calculation of dosimetric quantities to treatment planning[128,129]. The increase in available computing power has resulted in a number of Monte Carlo treatment planning studies, including Accuray, Ray Station, Monaco and Eclipse, with the latter two produced by Elekta and Varian respectively, two of the leading radiotherapy treatment machine manufacturers. Further research is being carried out into the incorporation of geometry packages into commercially available Monte Carlo software such as GEANT4[8] and PENELOPE[103] to allow treatment planning. However, such algorithms require a great deal of computational power and can be very time-consuming. For day-to-day clinical dose calculation, it is beneficial to use an analytical expression to accurately describe the central on-axis dose distribution of a particle beam and reduce the need for Monte Carlo simulations, as is the case for protons[125]. Using such a description for the dose distribution, an analytical expression for the range of an electron beam through a medium could also be determined, providinga tool for clinicians to perform rapid calculations.

The aims of this chapter are therefore to investigate how the dose distribution of electron beams can be described analytically, how the range of electron beams through a material can be defined, and how the range changes with beam energy and target material. The overall focus of the chapter is to determine an expression for the expression for the range of electron beams with energy up 250 MeV based on an analytic understanding of the dose distribution of electron beams.

While the general definition of particle range is the distance through which it travels in a medium before particle energy becomes negligible[130], several clinical definitions are used for different radiotherapy modalities.

The main complication is that patients are not simple, homogeneous blocks of water, instead being made up of tissues of varying densities and elemental composition. As discussed in Chapter 2, these inhomogeneities can have an effect on the dose distribution of a beam travelling through them[3,4]. Therefore, the description of range will be determined by taking into account a range of tissues and materials found in the human body as well as non-organic materials, such as the treatment couch or treatment masks.

In section 3.2, definitions of range for various radiotherapy modalities will be given, with emphasis placed on the proton range and a review of the range expression in Bortfeld's papers[125,126]:

$$R = \alpha E^{p} \tag{3.1}$$

where R is the beam range, E is the energy of the proton beam (assumed to be monoenergetic), α is approximately proportional to the ratio of the square root of the effective atomic mass and the density of the medium through which the beam is traversing and p is a constant.

Electron beam range data was then fitted to this expression to determine if the Bortfeld model could also be used to describe electron beam range as well as proton beam range following a computational study of electron beams travelling through different media using the Monte Carlo particle tracking code TOPAS (TOol for PArticle Simulations). An overview of this code, specifically designed for radiotherapy use, will be detailed along with the simulation setup in section 3.3.

In section 3.4, the methodology of calculating the energy range will be described based on an analytical understanding of dose distribution, along with determining the dependency of electron beam range to the various parameters in Eq. 3.1 and fitting the range data to Eq. 3.1. It is noted that, due to the differences in the behaviour of protons and electrons, there is no analytical justification for the use of Eq. 3.1 to describe electron beam range. This equation is being applied purely from a fitting perspective, with range dependencies on parameters including energy, density and effective atomic mass determined through fitting to simulation data. The chapter will conclude with a discussion of the model and its comparison to computational results, along with how the model can be validated experimentally.

3.2. Beam Range in Radiotherapy

3.2.1. Photons

As shown in on-axis PDD curve in Fig. 3.1, photons are still delivering significant dose as the beam leaves the patient. Rather than using range, particular depth characteristics are instead used to describe a photon beam[131]. On leaving the treatment head, a photon beam will travel a distance through air, known as the source-to-surface distance (SSD)[131]. The beam will then deliver a surface dose D_s to the patient. The dose delivered will increase rapidly as it travels through the patient, reaching a maximum D_{max} at depth z_{max}. The dose delivered then gradually decreases exponentially until the beam exits the patient at z_{exit} (Fig. 3.1).

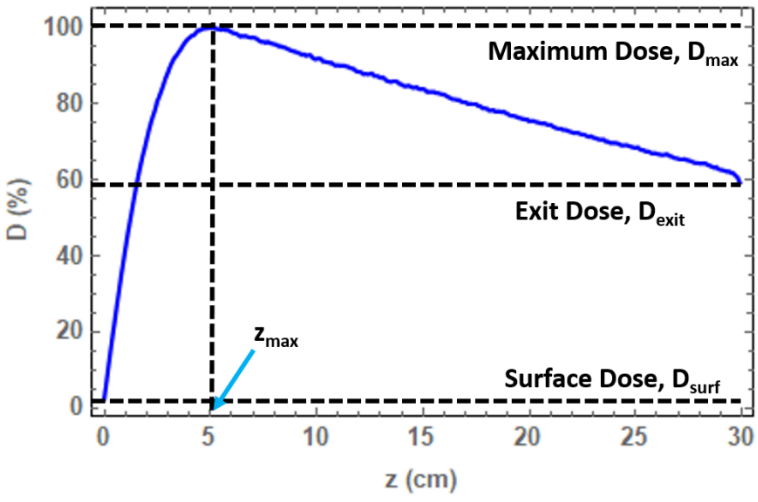

Figure 3.1 - PDD curve of 12 MV photon beam through a water phantom, indicating surface dose, exit dose and maximum dose with corresponding depth. PDD curve plotted using data from TOPAS simulation

3.2.2. Protons

Due to continuous energy loss during travel through a medium, protons have a defined range as the dose rapidly falls to a negligible level after delivering the maximum dose. The range is defined as the distance at which half of the protons travelling through a medium have come to rest[132].

It is important to note that small variations are observed in proton energy due to the energy loss of individual protons. This effect, known as range straggling, arises due to the stochastic nature of absorption and deflection of protons. There is energy variation from proton to proton and, as proton beam range is dependent on energy, range variation will also be observed. This contributes to range uncertainty[127], as does the variation in angular deflection of protons due to scattering as protons traverse a medium. This is a major issue in clinical proton therapy and an intensely researched topic. As a result, proton range is an average quantity – defined for the beam, rather than for individual particles.

Proton range can be defined in terms of dose, as the position at which the dose falls to 80% of its maximum value – this corresponds to the range at which 50% of the protons have come to rest[100]. This means that the 80% fall-off position is independent of energy spread. Proton range is shown in Fig. 3.2.

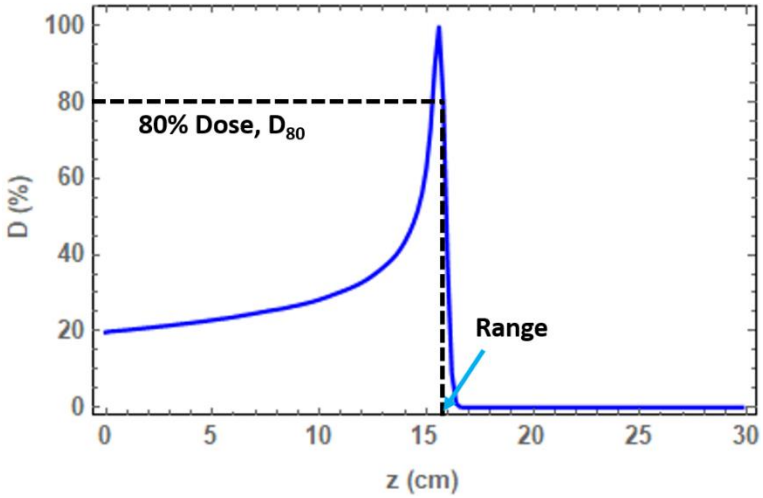

Figure 3.2 - PDD curve of a 150 MeV proton beam through a water phantom, indicating 80% dose and corresponding depth – the definition of proton range according to Paganetti [101]. PDD curve plotted using data from TOPAS simulation

Proton range can be calculated analytically, the benefits of which include speed and practicality in the clinic and a reduction in computational power which would be required if using Monte-Carlo calculation methods[127].

Bragg and Kleeman[76] were able to show, by plotting the logarithms of energy and range, that the relationship between range R and energy E of a proton beam can be described as a power law. Through further experimentation involving sending protons through gases of varying density and molecular composition, proton beam range was also found to be linearly dependent on the square root of the effective atomic mass A_{eff} and the inverse of the density ρ of the medium through which it is travelling:

$$R = \frac{c\sqrt{A_{eff}}}{\rho} E^p = \alpha\, E^p \tag{3.2}$$

where the effective atomic mass A_{eff} is calculated using (3.3):

$$\sqrt{A_{eff}} = \sqrt{f_1 A_1 + f_2 A_2 + \cdots + f_n A_n} \tag{3.3}$$

where f_1, …, f_n are the fractions of constituent elements in the material, with each element having atomic mass A_1, …, A_n.

Bortfeld[126] fitted this expression to data from the ICRU 49 report on proton and alpha stopping power and range, obtaining values for the constant p = 1.77 and α = 0.0022 for 10-200 MeV proton beams travelling through water. This study will be used as a base line for verification of TOPAS in section 3.4.

3.2.3. Electrons

Electrons, while also charged particles, have a very different PDD curve shape to protons, with the main difference being the absence of a Bragg peak. As there is no defined point at which the dose rapidly drops to a negligible level, different definitions are used for electron beam range in the clinic.

It is important to note that, by range, it is the depth of penetration of the beam that is being measured. A quantity known as the Continuous Slowing Down Approximation (CSDA) range is often used in physics to describe electron range – this is the sum of individual electron path lengths, or the distance travelled by an electron until it comes to rest[133]:

$$R_{CSDA} = \int_0^{E_0} \left[\frac{S(E)}{\rho}\right]^{-1} dE \tag{3.4}$$

where $[S(E) / \rho]^{-1}$ is the reciprocal of the electron's stopping power and E_0 is the electron's initial kinetic energy. It tends not to be used clinically as it represents the mean path length of the electron, rather than its depth of penetration in a particular direction. Clinically, the following definitions may be used for the range, based on low energy electron PDD curves[134]:

1. Maximum Dose Range, R_{max} – the depth at which the maximum dose is delivered
2. Practical Range, R_p – the depth at which the tangent plotted at the inflection point of the PDD curve intersects with the extrapolation line of background due to Bremsstrahlung.
3. Therapeutic Range, R_T – the clinically relevant section of the electron dose profile. This is recommended to be the depth at which the PDD curve has fallen to 90% of its maximum value.
4. 50% Range, R_{50} – the depth at which the PDD curve has fallen to 50% of its maximum value.

These ranges are shown with a PDD curve for 50 MeV electrons in Fig. 3.3. For the purpose of this investigation and based on its clinical relevance, an expression for the practical and therapeutic ranges of electron beams was developed.

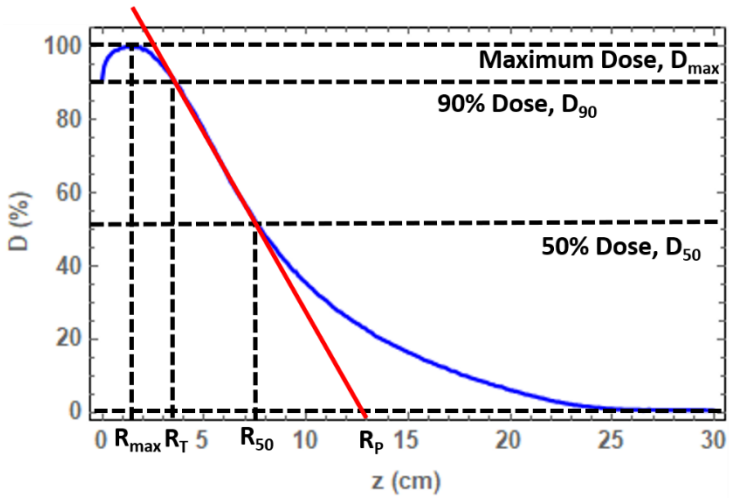

Figure 3.3 – PDD curve of 50 MeV electrons through a water phantom, indicating the many definitions of electron range. PDD curve plotted using data from TOPAS simulation

3.3. VHEE Beam Simulations using TOPAS

3.3.1. Monte Carlo Simulations in Radiotherapy

Monte Carlo methods are a class of computational algorithms that use repeated random sampling (in which a subset of individuals is chosen randomly from a larger set) to solve problems that are probabilistic or deterministic in nature[135].

Monte Carlo simulations are used to model phenomena over a broad range of applications, including high-energy particle physics, cosmology and computational biology. They are used to solve problems which do not have analytical solutions and to provide an alternative to potentially difficult, time-consuming or costly experiments.

An application that is of particular interest in this project is the use of Monte Carlo techniques in radiotherapy treatment planning. Monte Carlo simulations have been used since the early days of their development to solve particle beam transport and dosimetry[136]. Use has increased rapidly since the 1970s thanks to the increased availability of computing power.

Increasingly complex simulations are now possible, including the modelling of 3D geometries of treatment heads or particle detectors and the ability to produce high-quality treatment plans based on patient CT data. Monte Carlo particle tracking codes allow a range of particles to be modelled and a range of dosimetry-related quantities to be measured, including fluence and kerma[128].

While several Monte Carlo particle tracking codes are available to users, including MCNP (Monte-Carlo N-particle)[55], PENELOPE (Penetration and ENErgy LOss of Positrons and Electrons)[103] and FLUKA (FLUktuierende KAskade)[87,88], this study will involve the use of just one – GEANT4 (GEometry ANd Tracking)[8] and its user-friendly platform, TOPAS (TOol for PArticle Simulation)[9,137]. The following section will provide a brief overview of both GEANT4 and TOPAS.

3.3.2. GEANT4

GEANT4 is a freely available object-oriented software toolkit, written in C++, which is designed to model particles travelling through and interacting with matter[8,138]. GEANT4 was designed and developed as a collaboration at CERN to produce a high-functioning and flexible detector simulation for future high-

energy particle physics experiments, but is now used in a wide range of applications outside of high-energy particle physics, including astro-, nuclear and accelerator physics as well as radiobiology[42,139]. This is due to the set of physics models designed to handle interactions of many types of particles with matter over a very wide energy range.

The code itself is also highly customisable, with users able to design simulations to their specific requirements, thanks to a highly modular design. Each module covers a specific domain, including:

- geometry and materials of the system
- fundamental particles involved
- generation of primary particle events
- particle tracking through matter and electromagnetic fields
- physical processes determining a particle's interaction
- generation and storage of event and tracking data
- visualisation of system and particle tracks
- user interface.

A further advantage is the ability for users to develop their own applications. In particular, object-oriented methods allow users to modify or create their own physics lists by reducing their complexity – little modification to the main code is required. Various studies have identified the physics lists that are most suitable for radiotherapy physics, with those used in the study listed below[140]:

- G4EmStandardPhysics_option4 – used for standard electromagnetic interactions. Option 4 contains the widest range of models, allowing modelling at electron energies from 0 – 100 TeV
- G4HadronElasticPhysics – governs elastic processes (scattering etc.) for hadrons
- G4HadronPhysicsQGSP_BIC_HP – a highly precise list, governs elastic and inelastic processes for hadrons
- G4IonBinaryCascadePhysics – used for inelastic ion interactions
- G4EmExtraPhysics – used to model photonuclear processes
- G4StoppingPhysics – used to model stopping power physics

3.3.3. TOPAS

Monte Carlo codes are currently under-utilised in radiotherapy treatment planning, particularly proton therapy[9]. VMCpro[141] is currently used in dose calculation, but limitations in geometry and secondary particle modelling limits its application to treatment planning. GEANT4 does not have these limitations – being capable of supporting complex geometries and accurately tracking secondary particles, it is an ideal candidate for particle therapy modelling and treatment planning.

However, GEANT4 is currently not widely used in the clinic, in part due to differences in requirements between clinical medical physicists and high energy particle physicists (the original user base) such as speed, geometric complexity and repeatability as well as the relative complexity of GEANT4 due to its flexible, modular nature. This means that the advantages of Monte Carlo algorithms for treatment planning are not being exploited in the clinic. Use in this area could result in reduced treatment uncertainty margins and therefore a reduction in the volume of healthy tissue irradiated during treatment.

TOPAS was developed through a collaboration between the SLAC National Accelerator Laboratory, the University of California San Francisco Cancer Centre and Harvard Medical Centre to resolve these issues[9]. TOPAS was designed as a user code layered over GEANT4 and is made up of the standard GEANT4 software with additional code to make GEANT4 easier to control and so more accessible for users without advanced C++ knowledge.

The aim of TOPAS was to run simulations that are both reliable and repeatable – being able to produce precisely what the user intends using accurate physics and to reproduce these results from simulation to simulation, so reducing sources of error in a setup between users[137].

This reliability and repeatability comes from the use of a parameter file. All simulations are built with the same compiled code, built by TOPAS – the only difference between models being the input parameter file(s). These files specify every input, with parameter names defining each major part of the setup[142]:

- Ge – geometry components
- So – particle sources
- Ph – physics

- Sc – scoring, or the creation of voxelised geometries in which a quantity, such as dose, can be measured
- Gr – graphics, for visualisation of the setup
- Tf – time-dependent behaviours
- Ts – TOPAS, i.e. for overall control of the simulation.

The parameter names are also assigned settings depending on their value:

- s – string, e.g. to define a phantom material
- b – Boolean, e.g. to initiate or prevent an action
- i – integer
- d – double.

TOPAS version 3.1 was used in this project, with GEANT4.10.03.p01 built in. The following section will detail the validation of TOPAS for calculating the range of charged particles in matter.

3.4. Validation of TOPAS for Calculating Proton Beam Range in Matter

In order to validate TOPAS for the use of charged particles in matter, a simple comparative study was carried out. As detailed in Section 3.2, Bortfeld[126] obtained the following expression for the range of monoenergetic proton beams travelling through water:

$$R = 0.0022\, E^{1.77} \tag{3.5}$$

by fitting NIST PSTAR proton range data[143,144] for a beam travelling through water over the energy range 10-200 MeV. It was therefore proposed to simulate similar beams travelling through a 40x40x40 cm^3 water phantom in TOPAS – the simulation setup is shown in Figure 3.4.

The water phantom was split into voxelised geometries known as bins, with 400 in the x, y and z planes, to measure the dose deposited at different regions along the phantom.

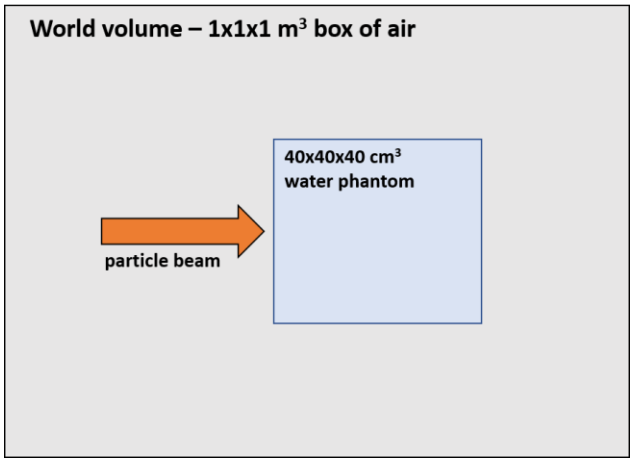

Figure 3.4 - Simulation setup for proton beam travelling through a water phantom

Dose is defined as the amount of energy deposited in a medium per unit mass and is measured in units of Gray[28], where 1 Gy = 1 J kg^{-1}. By measuring the on-axis dose (the dose delivered in the central x voxel) along the z-plane of the phantom, a percentage depth-dose curve, in which the dose is normalised, can be plotted.

From the on-axis PDD curve, and using the definition provided by Paganetti[100], the range of the proton beam can be obtained. This was repeated for 10-200 MeV beams, as specified by Bortfeld[126]. Figure 3.5 shows the proton beam range plotted against energy.

The range-energy data was then fitted to the power law expression (3.1) for range using the NonLinearModelFit function in Mathematica, resulting in the following expression:

$$R = 0.00226\, E^{1.765} \tag{3.6}$$

As is clear from both Fig. 3.5 and the information in Tables 3.1 and 3.2, the fit obtained by Bortfeld based on experimental data and the fit obtained using TOPAS simulations of proton beams in a water phantom compare very favourably, both in terms of the values obtained for the constants and R^2 and χ^2 goodness-of-fit values. It can be concluded that TOPAS is a suitable model to measure the range of charged particle beams through matter.

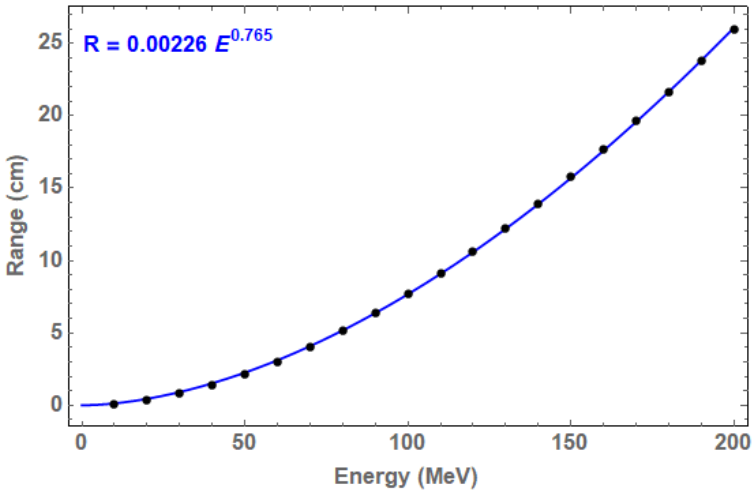

Figure 3.5 - Proton range in water with increasing energy. Range data is fitted to the Bortfeld expression to determine the constants α and p, with these then compared to constants determined by Bortfeld[12]

Constant	Bortfeld	TOPAS
α	0.0022	0.0023
p	1.77	1.77

Table 3.1. Comparison of equation constants based on Bortfeld[126] and TOPAS data for proton range in water

Data	R^2 Value	χ^2 Value
Bortfeld	0.999987	0.0524128
TOPAS	0.999967	0.035641

Table 3.2. Comparison of goodness-of-fit for Bortfeld[126] and TOPAS expressions for proton range in water

3.5. Calculating Electron Beam Range in Different Media

3.5.1. Simulation Setup

On validating the use of TOPAS to determine proton range, the next stage of investigation was to carry out similar simulations using electron beams. As in the previous section, the simulation setup consisted of a Gaussian electron beam with beam sigma (σ) of 5mm containing 10^6 particles, corresponding to a charge of 0.16 pC, travelling through a 30 x 30 x 30 cm^3 phantom (Fig. 3.4). The phantom was voxelised into 150 x 150 x 150 bins to allow on-axis dose to be scored.

The materials used in this study are detailed in Table 3.3 below and were chosen for their relevance in patient treatment. Densities and elemental compositions for each material are taken from the GEANT4 Materials database, accessible through user interface commands[140]. The majority of materials are tissues found in the human body, although a bone insert has also been included as, in any experimental studies, this would be used instead of human bone.

Material	Density ρ (g cm^{-3})	$\sqrt{A_{eff}}$
Adipose	0.95	3.455
Blood	1.06	3.754
Brain	1.04	3.743
Bone Insert	1.45	4.194
Compact Bone	1.85	4.303
Cortical Bone	1.92	4.671
Lung Tissue	1.04	3.770
Skeletal Muscle	1.05	3.746
Skin	1.09	3.708
Soft Tissue	1.03	3.677
Water	1.00	3.784

Table 3.3. Properties of materials used in TOPAS simulations. Density taken from GEANT4 materials database and $\sqrt{A_{eff}}$ calculated using Eq. 3.3

3.5.2. Data Fitting

On completion of beam simulation through different materials, the dose distribution data must be fitted to allow calculation of the various range parameters detailed in section 3.2. The on-axis dose data was fitted using an equation developed by Meigooni and Das[145].

This fit is taken from a study on the development of an analytical expression for monoenergetic, central on-axis PDD curves for low-energy electrons. They proposed the use of an expression combining a second-order polynomial with an exponential function:

$$D(z) = \frac{a_1 z^2 + a_2 z + a_3}{1 + \exp[a_4(z - a_5)]} \tag{3.7}$$

where D is the dose being delivered by the beam at depth z (measured in cm) and a_n are free parameters obtained using a non-linear regressive function. On comparison with Monte Carlo simulation data for 1–60 MeV electron beams in water, aluminium and copper phantoms and for 6-22 MeV electron beams produced by a medical linac, the expression was found to agree with computational and experimental data to within 1.5%.

While the Meigooni-Das equation has proven to be a good fit for electrons up to 60 MeV[145], there is no data available for higher energy electrons. As the planned energy range for VHEE is 250 MeV, it must be determined whether this is also a suitable equation for dose distribution curves of higher energy electrons. Preliminary TOPAS simulations were therefore carried out, with electron beams of energies 10-250 MeV consisting of 10^6 particles with $\sigma = 5$ mm travelling through a 30 x 30 x 30 cm^3 water phantom – see Fig. 3.4 for a similar schematic of this setup. The on-axis PDD curve was plotted for each energy, the Meigooni-Das equation fitted to the data and goodness of fit determined by calculating R^2. The results are detailed in Fig. 3.6 and Table 2.4 below. Relative error was calculated for the fits and the fit was found to agree with the dose data to within 2%.

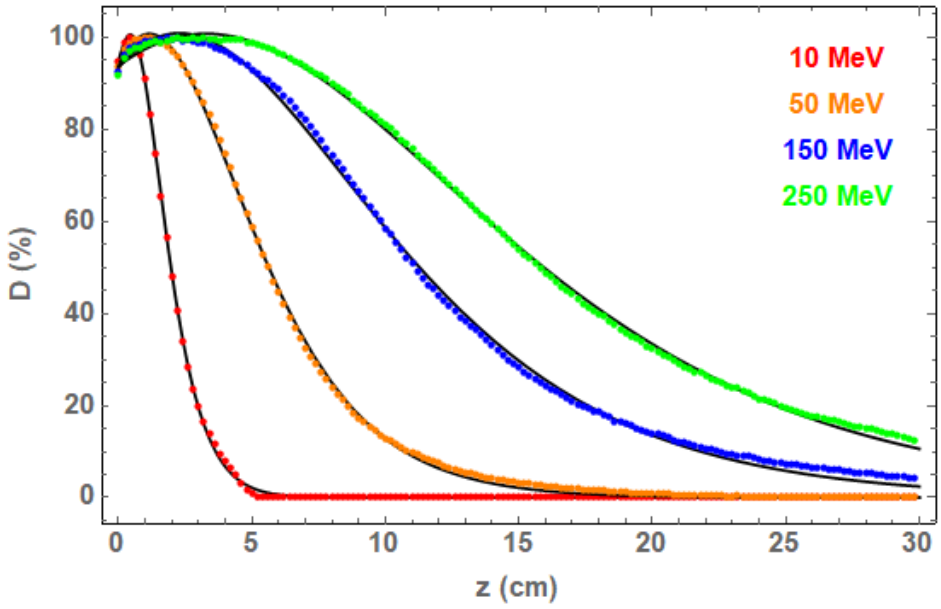

Figure 3.6 - PDD data fitted to Meigooni-Das equation for electron beams with energy in range 10-250 MeV

Energy (MeV)	R^2
10	0.999773
50	0.999633
150	0.999484
250	0.999818

Table 3.4. R^2 values for Meigooni-Das equation fit to electron PDD data for 10-250 MeV

Based on the goodness-of-fit for high energy electron dose profiles, it was concluded that the Meigooni-Das is a suitable fitting method for VHEE beams as well as low energy beams.

3.5.3. Determining Therapeutic Range

On fitting the depth-dose profile to the Meigooni-Das equation, the therapeutic range was determined for an electron beam of a particular energy by setting Eq. 3.7 to 90% of the maximum dose. This is then solved to determine the depth z at which the dose is 90% of the maximum. This depth must be beyond that of the maximum dose.

The practical range is calculated by plotting the tangent at the steepest part of the PDD curve beyond the maximum dose and determining the depth at which the tangent intersects with the extrapolation line of the Bremsstrahlung tail – shown in Fig. 3 in section 3.2. Practical and therapeutic range for electron beams of energy 10-250 MeV are shown in Fig. 3.7.

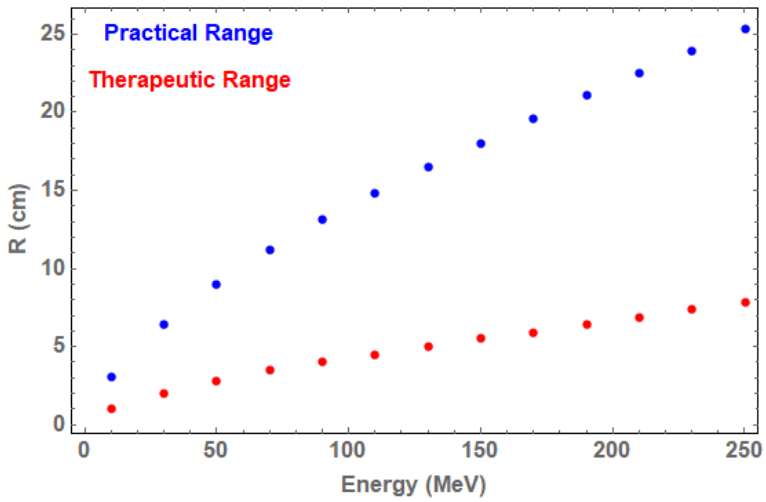

Figure 3.7 - Practical and therapeutic range data for 10-250 MeV electron beams through a water phantom

3.6. Determining an Expression for Electron Beam Range

3.61. Energy Dependence

To determine if electron beam range could be fitted using the proton expression detailed by Bortfeld[125,126], the dependency of electron range on the relevant parameters must be established. To do this, electron beams of energy 10-250 MeV containing 10^6 particles with σ = 3 mm were simulated in TOPAS travelling through 30 x 30 x 30 cm^3 phantoms made of the materials listed in Table 3.3, voxelised into 150 x 150 x 150 bins – see Fig. 3.8 for a TOPAS visualisation of the setup.

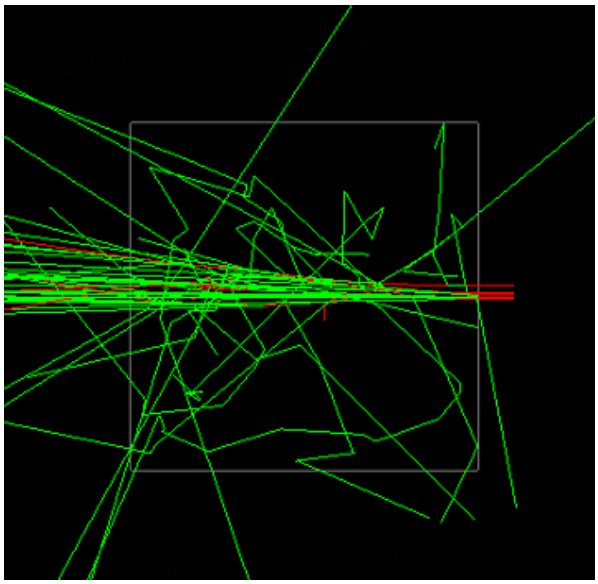

Figure 3.8 - TOPAS visualisation of electron beam and phantom setup. Red tracks represent movement of electrons through the phantom while green tracks represent secondary photons

10^6 electrons were found to be suitable for these simulations on comparison between 10 statistically independent samples. 10^6 electrons with energy 150 MeV were simulated travelling through a water phantom and the on-axis dose scored. The standard error of the mean of these runs was calculated and found to be within 0.3%, indicating that 10^6 particles provides an acceptable level of accuracy for these simulations.

In the Bortfeld expression, range and energy are related through a power law. To determine if this is also the case for electrons, a log-log plot must be plotted. If the data can be fitted to a straight line, this indicates a power-law

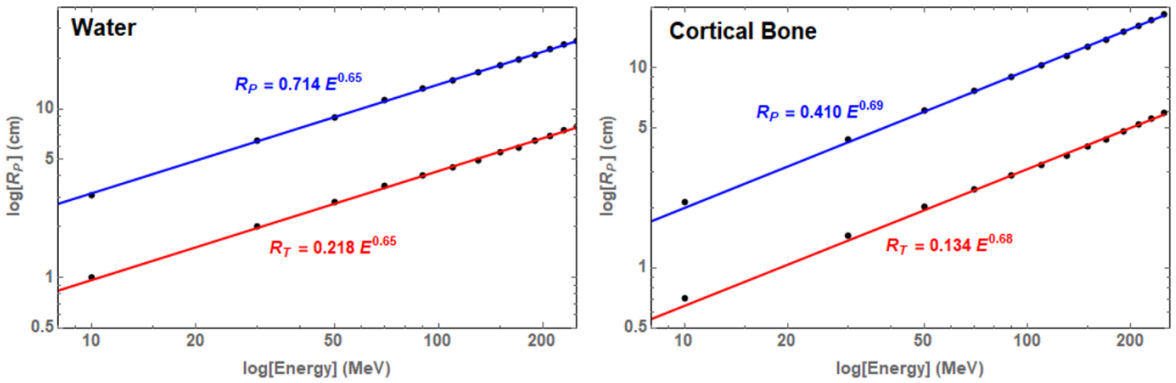

Figure 3.9 - Log-log plots for practical range and therapeutic range of electron beams in water (left) and cortical bone (right). Straight line indicates a power-law relationship. Log of energy and range taken and fitted to a straight-line equation – c) shows this for practical range and d) for therapeutic range. The gradient of the line is equivalent to the constant p

relationship. This plot is shown for both R_P and R_T in water and cortical bone in Fig. 3.9.

The log of energy and range data was taken and fitted to a straight-line equation, with the gradient being equivalent to the constant p in the Bortfeld expression. The goodness of fit was determined for both practical and therapeutic ranges, and the fit plotted together with the data, with R^2 values given in Table 3.5. Both the figures and the R^2 values indicate that the relationship between energy and practical and therapeutic range can be approximated using a power law.

Material	Range	p	R^2
Water	Practical	0.646	0.999976
	Therapeutic	0.647	0.999748
Cortical Bone	Practical	0.677	0.999919
	Therapeutic	0.683	0.999712

Table 3.5 – Determining power-law constant p for range data of 10-250 MeV electron beams travelling through water and cortical bone

3.6.2. Density and A_{eff} Dependence

Similar processes were carried out to determine the dependence of electron beam range on the density and effective atomic mass of the material through which the beam traverses. According to the Bortfeld expression, proton range is approximately proportional to the square root of the effective atomic mass and approximately inversely proportional to the density.

For 50, 150 and 250 MeV electron beams, the practical and therapeutic ranges were plotted against the inverse of the density for each tissue. Straight-line equations were then fitted to both sets of data and R^2 value calculated to determine the goodness-of-fit. The results are shown in Fig. 3.10 and associated percentage error in Fig. 3.12 and indicate that both practical and therapeutic electron beam ranges are approximately inversely proportional to the density of the material through which the beam travels.

Practical and therapeutic ranges were also plotted against the ratio of the square root of the effective atomic mass and the inverse of the density for each tissue. As with the density dependency, straight-line equations were fitted to data and R^2 values calculated. The results are shown in Fig. 3.11 and associated percentage error in Fig. 3.13, indicating that practical and therapeutic range are approximately proportional

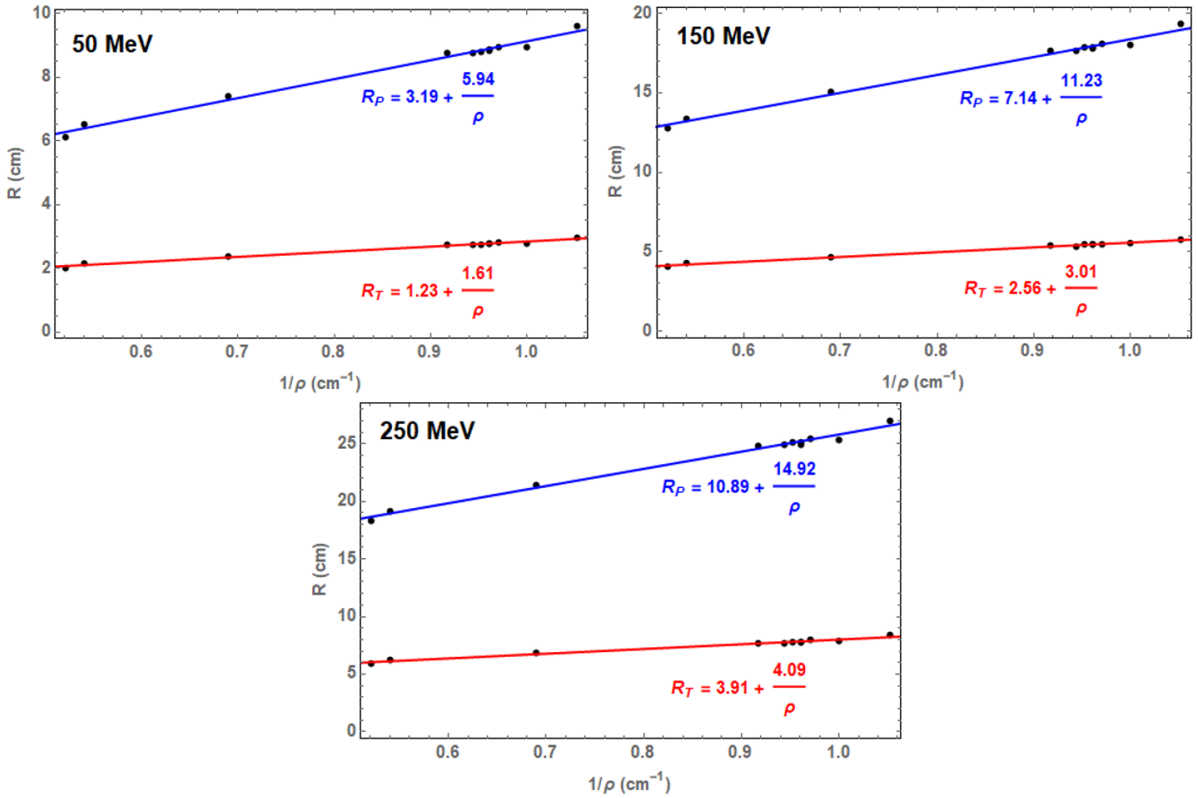

Figure 3.10 – Practical and therapeutic range plotted against 1/ρ for 50, 150 and 250 MeV electron beams through various media Data fitted to a straight-line equation to determine linear relationship between range and density

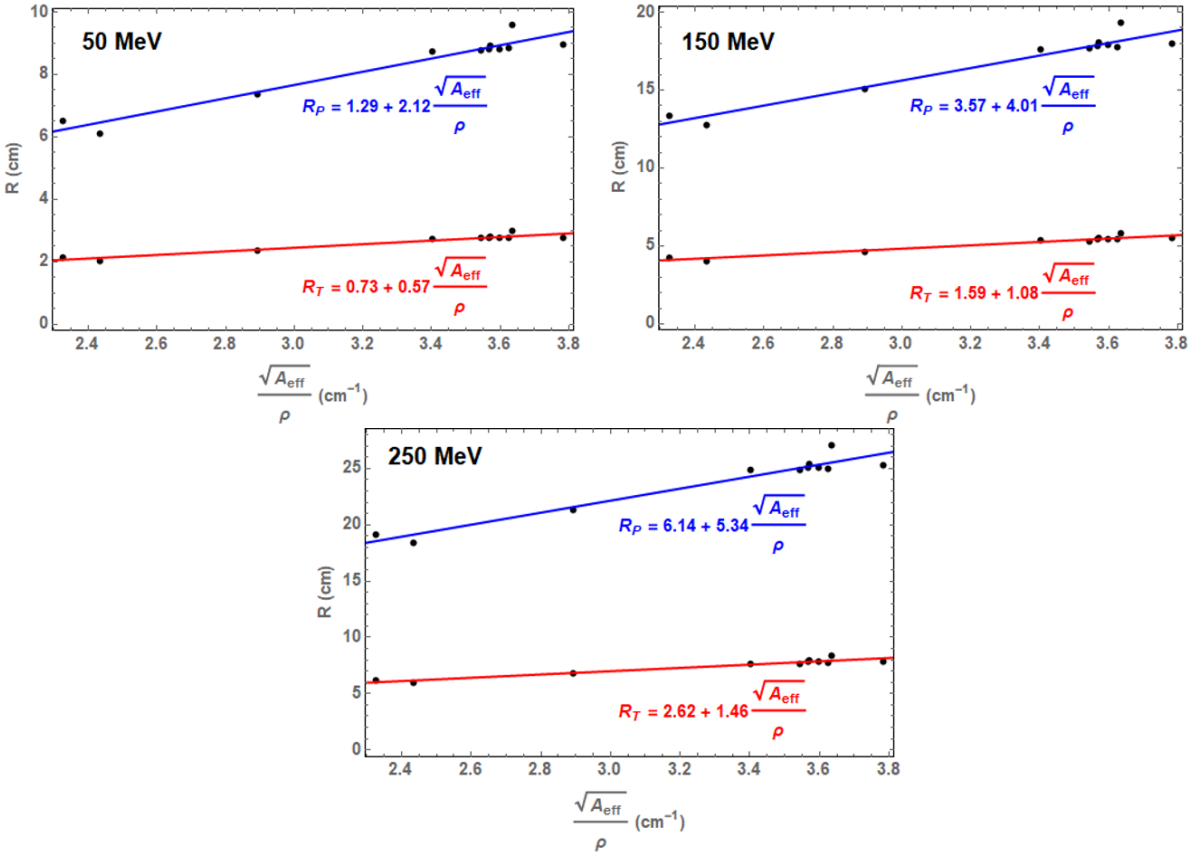

Figure 3.11 - Practical and therapeutic range plotted against $\sqrt{A_{eff}/\rho}$ for 50, 150 and 250 MeV electron beams through various media. Data fitted to a straight-line equation to determine linear relationship between range and ratio of the square root of the effective atomic mass and density

to the square root of the effective atomic mass and the inverse of the density of the material.

In conclusion, analysis of the dependencies of the practical and therapeutic ranges of electron beams has indicated that an equation based on the Bortfeld equation for proton beam range is a suitable model for electron beams.

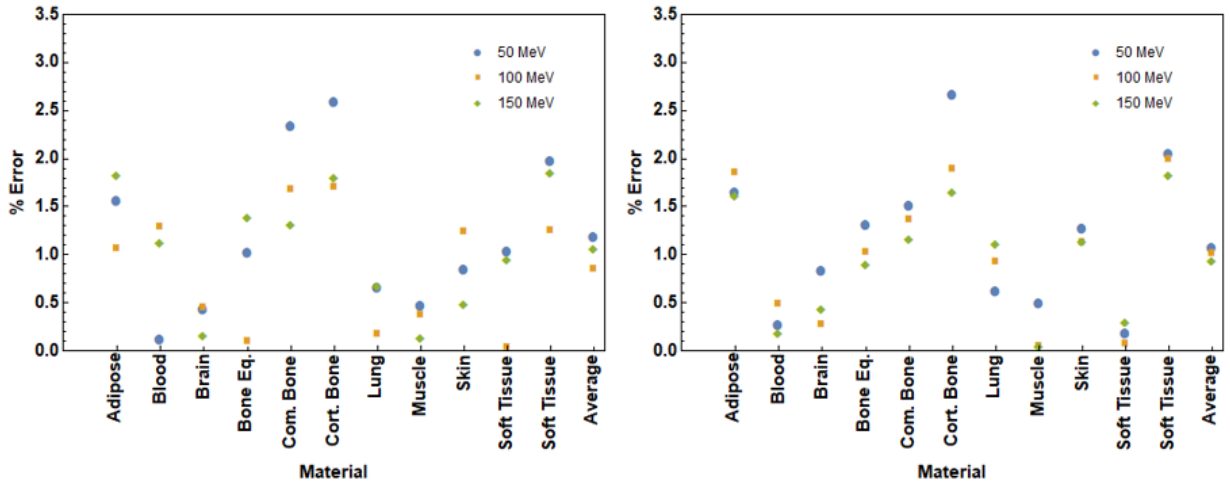

Figure 3.12 – Percentage errors calculated for material density dependency fits for all materials at 50, 150 and 250 MeV. Average percentage error across all materials also included

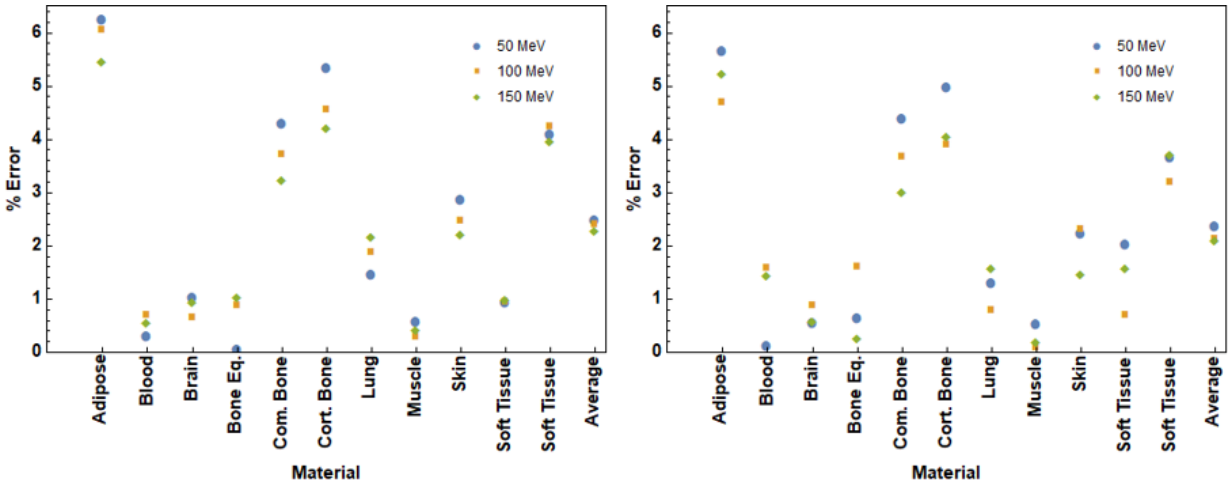

Figure 3.13 – Percentage errors calculated for ratio of the square root of the effective atomic mass to material density dependency fits for all materials at 50, 150 and 250 MeV. Average percentage error across all materials also included

3.6.3. Fitting Range Data to Bortfeld Range Equation

On establishing that the Bortfeld equation for proton beam range was suitable for use with electron beams, the range data for different tissues was fitted to the equation to determine the values for constants α and p for each tissue, with R^2 and χ^2 values calculated to determine the goodness-of-fit of the equation. The constants and goodness-of-fit values are given in Table 3.8 for practical range and Table 3.9 for therapeutic range, with the data and corresponding fits for each tissue shown in Fig. 3.14.

Tissue	α	p	% Error at 250 MeV	R^2 Value
Adipose	0.735 ± 0.020	0.653 ± 0.005	0.06	0.999931
Blood	0.692 ± 0.012	0.641 ± 0.011	4.38	0.999697
Brain	0.669 ± 0.012	0.648 ± 0.003	4.70	0.999991
Bone Eq.Insert	0.546 ± 0.011	0.663 ± 0.004	0.64	0.999963
Compact Bone	0.455 ± 0.011	0.677 ± 0.009	0.31	0.999946
Cortical Bone	0.410 ± 0.012	0.687 ± 0.006	0.85	0.99919
Lung	0.701 ± 0.012	0.646 ± 0.003	0.56	0.999972
Muscle	0.687 ± 0.012	0.651 ± 0.004	0.34	0.999964
Skin	0.680 ± 0.012	0.651 ± 0.003	0.44	0.999973
Soft Tissue	0.695 ± 0.012	0.651 ± 0.003	0.60	0.999971
Water	0.714 ± 0.011	0.646 ± 0.003	0.27	0.999976

Table 3.8 – Constants determined for practical range data fitting for all materials. Percentage error calculated between fitted range and range determined from TOPAS simulations at 250 MeV, with an average percentage error of 1.20% across all materials

Tissue	α	p	% Error at 250 MeV	R^2 Value
Adipose	0.227 ± 0.012	0.650 ± 0.010	1.76	0.999746
Blood	0.214 ± 0.011	0.647 ± 0.010	0.82	0.999740
Brain	0.210 ± 0.011	0.653 ± 0.011	1.32	0.999721
Bone Equivalent Insert	0.165 ± 0.012	0.671 ± 0.015	1.73	0.999841
Compact Bone	0.151 ± 0.009	0.671 ± 0.011	1.03	0.999696
Cortical Bone	0.134 ± 0.008	0.683 ± 0.011	1.90	0.999712
Lung	0.216 ± 0.010	0.646 ± 0.09	1.84	0.999791
Muscle	0.207 ± 0.011	0.656 ± 0.010	0.90	0.999744
Skin	0.209 ± 0.009	0.651 ± 0.008	1.19	0.999835
Soft Tissue	0.209 ± 0.013	0.656 ± 0.012	1.71	0.999651
Water	0.218 ± 0.011	0.647 ± 0.010	1.20	0.999748

Table 3.9 – Constants determined for therapeutic range data fitting for all materials. Percentage error calculated between fitted range and range determined from TOPAS simulations at 250 MeV, with an average percentage error of 1.40% across all materials

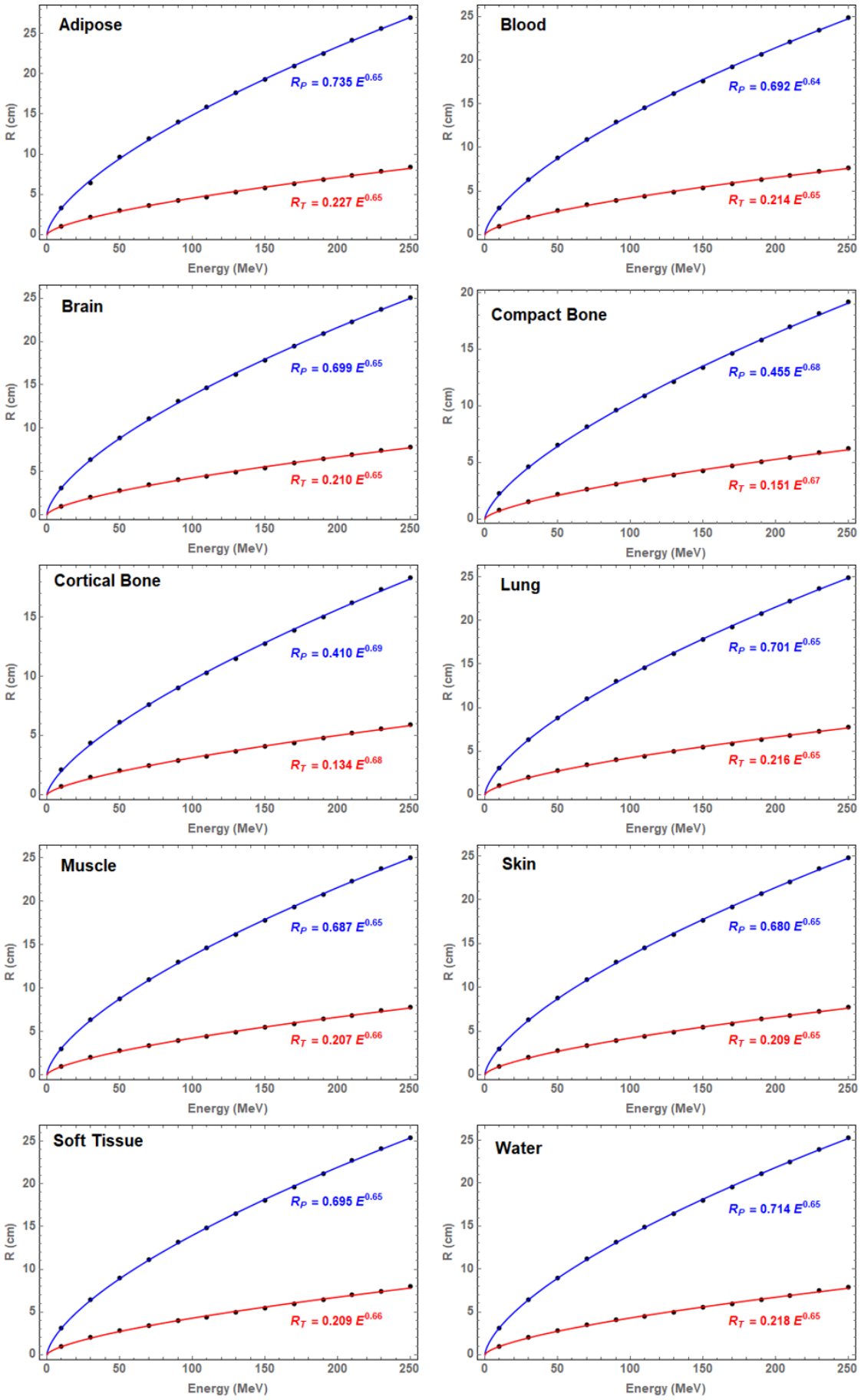

Figure 3.14 - Practical and therapeutic range data fitted to Bortfeld equation for various tissues

3.7. Discussion and Conclusion

The primary aim of this chapter was to investigate the application of a semi-empirical equation for the practical and therapeutic ranges of proton beams in various media to electrons, reducing the need for time-consuming Monte Carlo range calculations in treatment planning and allowing rapid adaptations in treatment plans when necessary.

Range data was produced using TOPAS, validated through a comparative study with proton beams. A simplified expression for proton data was presented by Bortfeld[125,126], indicating that the range of a monoenergetic proton beam is dependent on the beam energy and the effective atomic mass and density of the material through which the beam travels (see Eq. 3.1.).

The Bortfeld equation was fitted to the range data in water over 10-200 MeV and constants α and p determined. TOPAS and published values for α and p agree to within 2.73% and 0.28% respectively, giving confidence that TOPAS was determined to be suitable for determining the range of charged particle beams – in agreement with several TOPAS validation studies already published[146,147].

Electron beams over the energy range 10-250 MeV were then simulated travelling through phantoms of patient-relevant materials. It was established that the high energy electron PDD curve data could be fitted successfully using the Meigooni-Das equation, allowing practical and therapeutic ranges to be calculated.

The Bortfeld proton beam range equation was used as a model for electron beam range, validated by determining that electron beam range had the same parameter dependencies as proton beam range. Electron beam range is related to energy through a power law and is approximately proportional to the ratio of the square root of the effective atomic mass and the density through which the beam is travelling.

Practical and therapeutic ranges were fitted to this equation and the constants α and p determined for each tissue. R^2 and χ^2 values for each tissue indicated that the equations for each tissue fit extremely well to the TOPAS range data. For improved accuracy, it would be recommended that there is a unique α and p

value for each tissue or material, though these values were found to be very similar for tissues or materials with a similar density to water – this is the case for many human tissues, with bone a notable exception.

A key extension of this work would be to validate the range expressions experimentally. This would involve film irradiation experiments similar in design to those carried out by Lagzda *et al.*[3,4,105] on film dosimetry and insensitivity to inhomogeneities.

A phantom would be designed, allowing EBT-XD Gafchromic film to be inserted at several positions along the z-axis. The material of the phantom would depend on the tissue in question, with tissue- and bone-equivalent materials used in place of the real thing. The phantom would be placed in front of an electron beam and irradiated at several energies. By determining the dose delivered to the Gafchromic films along the phantom, a PDD curve could be built up for each energy and the dose distribution data fitted to the Meigooni-Das equation to allow the calculation of practical and therapeutic ranges.

The experimental R_P and R_T values could then be compared directly to the predicted model values. Good agreement will not only increase confidence in the accuracy of the electron beam range equation but will also further validate the use of TOPAS as a method of simulating the behaviour of very high energy electron beams in matter.

To conclude, it has been established that it is possible to fit the Meigooni-Das dose distribution equation to VHEE beams, providing an analytical description of VHEE dose distribution. From this, accurate expressions for the practical and therapeutic ranges have been produced for electron beams up to 250 MeV, based on earlier work on proton beam range and using dose distribution data produced using the TOPAS. This equation has the potential to allow clinicians to make rapid amendments to a patient's treatment based on observations and imaging during treatment. Experimental validation would be desirable and can be achieved by adapting experimental setups that have already proven successful in the past.

Chapter 4 – Experimental Comparison of Plasmid DNA Damage Yields between VHEE and other Radiotherapy Modalities

4.1. Introduction

As outlined in Chapter 1, the primary mechanism causing cell death or senescence (the stopping of cellular division) following exposure to ionising radiation is DNA damage, with the most lethal damages being single- and double-strand breaks (SSBs and DSBs respectively)[28].

Knowledge of DNA damage yields is a useful comparative tool for the various radiotherapy modalities, both established and novel. The primary clinical tool for such comparison is the Relative Biological Effectiveness, defined as the ratio of biological effectiveness of a type of ionising radiation compared with a reference radiation – typically ^{60}Co photons[32]. While the most common biological endpoint for RBE calculation is cell survival, determined through a clonogenic assay following cell irradiation, DSB yield can also be used as an endpoint, calculated using equation 4.1:

$$RBE_{DSB} = \frac{DSB_X}{DSB_R} \tag{4.1}$$

where DSB_X is the DSB yield for a specified radiation type and DSB_R is the yield for a reference radiation – ^{60}Co photons in this case. Proton RBE has a general value of 1.1, meaning that protons are 10% more effective at cell killing than ^{60}Co photons[148].

At the time of writing, there is very limited experimental data available on either the radiobiological effects or the RBE of VHEE. This chapter presents the results of a series of plasmid DNA irradiation experiments carried out to determine the yields of SSBs and DSBs in plasmid DNA resulting from exposure to VHEEs and compares this yield to those resulting from other radiotherapy modalities. From this, a first calculation of VHEE RBE_{DSB} was made.

These experiments took place at a number of accelerator and clinical facilities, with low energy electron irradiations (6-15 MeV) carried out at the Christie NHS Foundation Trust[149] (Manchester, UK) using a clinical treatment machine and ^{60}Co X-ray carried out at the Dalton Cumbrian Facility[150] (Whitehaven, UK) using an FTS Model 812 gamma irradiator (1.17 and 1.33 MeV). VHEE experiments were performed at the CERN Linear Electron Accelerator for Research (CLEAR) user facility at CERN[151] (Geneva, Switzerland) over an energy range of 100-200 MeV. Wet plasmid irradiations were performed at all three facilities, while dry irradiations were performed at CLEAR and DCF. Comparison of dry and wet plasmid DSB yields allowed the contribution of direct and indirect radiation effects to DNA damage to be measured. RBE_{DSB} was determined for 6-15 MeV and 100-200 MeV electrons using ^{60}Co DSB yields as the reference point.

Due to wide dose rate range available at CLEAR, an extension of the VHEE DNA irradiation study was carried out, investigating the effect of varying dose rate on DSB yield. As covered in more detail in Chapter 2, ultra-high dose rate (FLASH) radiotherapy has been seen to show comparable tumour control but with an increased normal tissue sparing and is an exciting prospect for radiotherapy[80,81]. We investigated the effects on plasmid DNA damage to determine if a FLASH effect (in this case, a change in DSB yield) could be observed at a nanoscopic level following VHEE irradiation. This study was motivated by a lack of experimental data at the nanoscopic level for FLASH irradiation. Understanding the behaviour of DNA when exposed to variable dose rates can indicate whether a FLASH effect is indeed observed at the nanoscale and can offer an improved understanding of the primary mechanisms of the FLASH effect.

This chapter is structured as follows. An overview of plasmid DNA and its use in radiobiological experiments will be covered in section 4.2. Section 4.3 details the experimental preparation, including sample preparation, irradiation setup and dosimetry using radiochromic film. An overview of the experimental facilities at which the DNA irradiations were carried out and the experimental setup at each facility is given in section 4.4. Analytical techniques, including plasmid separation, image analysis and fitting methods used to determine SSB and DSB yield are outlined in section 4.5. The results from the set of

experiments are presented in section 4.6, covering the measurement of SSB and DSB yields following irradiation with the three modalities mentioned above, the associated RBE_{DSB} calculation (including the first VHEE RBE calculation) and comparison with published RBE data. The results of the dose rate variation study at CLEAR will also be presented. The chapter will conclude with a summary of key results, limitations within the experiments and an outline of future plans, including cell survival studies.

4.2. Plasmids

4.2.1. What is a Plasmid?

The term plasmid usually refers to extrachromosomal (outside the nucleus) genetic elements which are capable of replicating independently within cells[152]. They are found in most species of bacteria and can also be found in some archea (single-celled organisms with no nucleus) and some simple eukaryotic cells (which do contain a nucleus)[153] – see Fig. 4.1. Plasmids play a key role in the genetic diversity of bacteria and can have a variety of different roles – including antibiotic resistance[154].

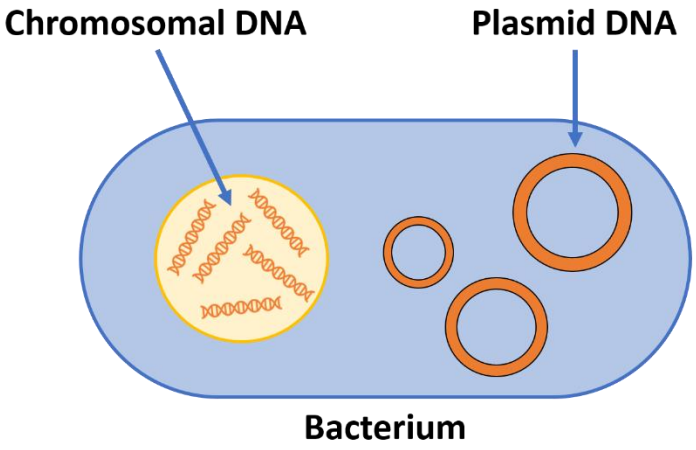

Figure 4.2 - Schematic of chromosomal DNA and plasmid DNA in a bacterium. Note that the plasmid DNA is not to scale

The geometry of a plasmid typically exists in a closed loop form, though linear plasmids have been observed in some species of bacteria. Circular plasmids can have different topologies, as shown in Fig. 4.2, resulting from the presence (or not) of nicks or breaks in the DNA strand[155]. Plasmids usually exist in a supercoiled form – a closed circular structure which is coiled or looped around itself. If one of the plasmid DNA strands is broken (a single-strand break), the

supercoiled structure will relax, resulting in an open-circular form. If both strands are broken (a double-strand break), the structure will open up, resulting in a linear form[156]. Supercoiled, open-circular and linear will be abbreviated to SC, OC and L from this point onwards. This variation in topology makes plasmids an excellent tool for radiobiological studies – covered further in the next section.

Plasmid length is typically measured in units of kilo-base pairs (kbp), with a base pair defined as a unit of DNA consisting of two nucelobases bound by hydrogen bonds. Plasmids can vary in size from one or two to many hundreds of kbp – such large plasmids can contribute a significant proportion of a bacterium's overall genome.

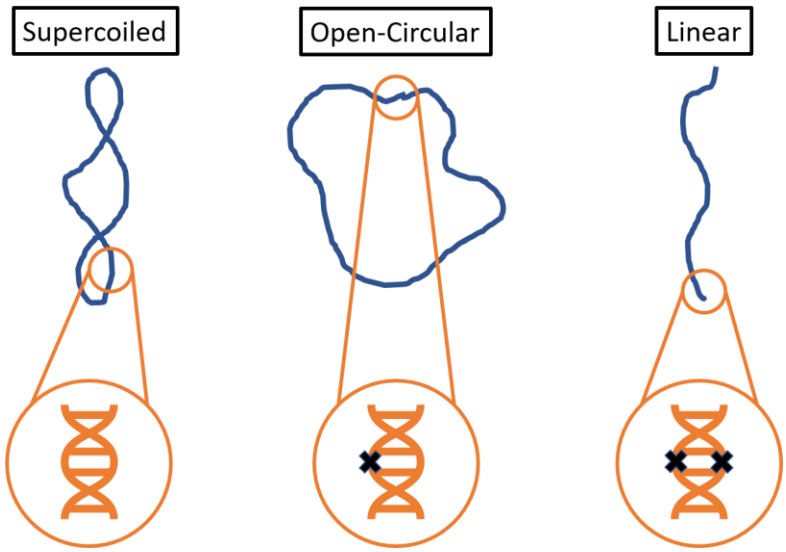

Figure 4.3 - Schematic of supercoiled (SC), open-circular (OC) and linear (L) plasmid forms and corresponding DNA damage. 'X' marks DNA backbone damage

4.2.2. Plasmids in Radiobiological Studies

Extracted plasmid DNA is a commonly used *in vitro* model for radiobiological experiments due to its lack of repair capability[157]. Following exposure to ionising radiation, a eukaryotic cell will attempt to repair any resulting DNA damage[65]. Whilst useful to determine the rate of DNA repair and cell death, these mechanisms can hinder the measurement of DNA damage. By using plasmid DNA extracted from bacterial cells as a simplified model, these repair mechanisms present within the cell are not possible, allowing DNA damage resulting from radiation exposure only to be determined.

Plasmids can be exposed to radiation in a 'dry' or 'wet' (aqueous) environment. In a dry environment, any DNA damage is the result of direct radiation effects only[28]. In a wet environment, in which the plasmid DNA is suspended in liquid water, DNA damage results from both direct (from the primary particle) and indirect radiation effects, due to the production of free radicals following interactions between ionising radiation and water molecules. By irradiating plasmids in both environments, the contribution of direct and indirect radiation effects to total DNA damage can be determined for a particular type of radiation.

Finally, the changes in topology following DNA damage allows damaged plasmids to be identified relatively easily. The different plasmid forms, SC, OC and L, can be separated through agarose gel electrophoresis (AGE). This technique is commonly used in biochemistry to separate mixtures of macromolecules such as DNA and RNA[158] and is described in greater detail in the Analysis section of this chapter. The different forms of plasmid can be detected through AGE up to a length of tens of kbp.

Thanks to the relatively simple analysis methods involved, plasmid irradiation studies have been employed to investigate a diverse range of radiobiological properties following DNA exposure to radiation. Fundamental properties such as the lower energy deposition limit for causing DNA damage have been measured[159–161], along with determining break yield dependence on radiation energy and LET[162,163]. This is particularly relevant for proton and heavy ion therapy due to the variation of LET and subsequently RBE with position on the Bragg curve[100]. Investigations into damage clustering (several damages occurring within a small section of DNA) have also been carried out using plasmids, with the damage cluster size corresponding to the likelihood of cell death and being a key quantity in the field of nanodosimetry[164,165].

DSB yield following plasmid irradiation was selected for RBE calculation in this set of experiments, having been an established biological endpoint for determining RBE in several studies involving different radiotherapy modalities. Nikjoo and Lindberg's review[166] summarises the experimental and computational studies into RBE calculation using DSB induction following irradiation with photons and extremely low energy (up to 100 keV) electrons. As expected, DSB yield was found to vary significantly with energy and,

correspondingly, LET. As electron energy increased from 0.1 to 100 keV, DSB yield and RBE decreased as LET decreased, with RBE values measured close to 1 above 10 keV.

Established experimental methods therefore provide confidence in an RBE study on plasmid irradiation using VHEE rather than traditional radiotherapy modalities. While electron RBE calculations based on DSB yield have been performed in the past, they have been at a much lower energy scale than would be clinically relevant (up to 100 keV). The experiments detailed in this chapter provide RBE calculations for current clinical electron energies (6-15 MeV) and VHEE energies (100-200 MeV).

4.3. Experiment Preparation

4.3.1. Plasmid Sample Preparation

pBR322 plasmid DNA, a cloning vector isolated from E. coli. bacteria with a length of 4.361 kbp[167] was selected for these experiments. It is a well-established model for DNA damage studies[157,168,169] with its length being particularly suitable for analysis with AGE. pBR322 plasmid was purchased from New England BioLabs[170] and was delivered in 10mM Tris-HCL and 1mM EDTA to prevent relaxation of the supercoiled plasmid structure at a concentration of 1000 ng/µl. New England BioLabs indicate that most plasmid samples on arrival consists of approximately 90% supercoiled plasmid – see Section 4.5 for validation of this.

Wet and dry samples were irradiated in this series of experiments to determine the contribution of direct and indirect effects to total DNA damage. The dry and wet plasmid samples were prepared at the Oglesby Cancer Research Centre[171] (OCRC) biology laboratory according to the following protocol and are shown in Fig. 4.3:

1. **Dry samples:** 1000 ng/µl plasmid solution was diluted to an assumed concentration of 100 ng/µl with distilled, deionised water. A 5 µl droplet of the solution was pipetted on to the marked centre of a Permafrost glass microscope slide with length 75mm, width 25mm and thickness 1mm. The slide was then left at room temperature to allow the water to

evaporate, leaving a thin layer of pBR322 plasmid DNA in the slide. Evaporation typically took 30-45 minutes.

2. **Wet samples:** 1000 ng/µl plasmid solution was diluted as for the dry samples to an assumed concentration of 100 ng/µl. Specified volumes, either 15 or 30 µl were then pipetted into sealable 1.5 ml Eppendorf tubes. Larger volumes of solution were used compared to dry samples to allow for larger quantities of DNA to be irradiated at once, rather than carrying out multiple irradiations of smaller quantities.

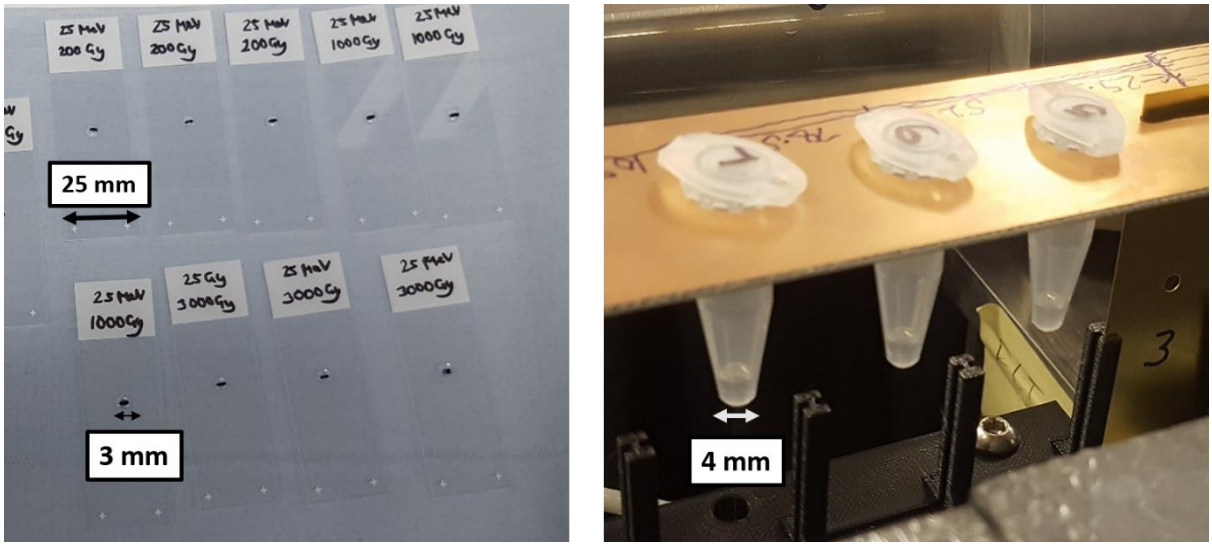

Figure 4.4 – (Left) Dry plasmid samples, dried on marked glass microscope slides. (Right) Wet plasmid samples held in 1.5 ml Eppendorf tubes

The plasmid solution was diluted from the stock concentration of 1000 ng/µl because the concentration of DNA required for a successful AGE measurement is much lower than the original concentration (typically 50-60 ng/µl). A concentration of 100 ng/µl was chosen to ensure a successful measurement while using the plasmid DNA as efficiently as possible. Following preparation, all samples, including controls, were stored at -20ºC until required.

4.3.2. Dose Delivery

Based on established plasmid irradiation studies, dry plasmid samples received dose in the range 0-6000 Gy, while wet samples received 0-60 Gy. These dose ranges were chosen based on a review of earlier plasmid irradiation studies[157,168,169] using different modalities, with the range extended to ensure that some DNA damage would be observed. The large difference in dose between the two plasmid environments arises because of the contribution of direct and

indirect radiation effects. Plasmid irradiation studies with protons, for example, have shown that in excess of 99% of total DNA damage is due to indirect effects – observed in wet plasmid samples[157]. Therefore, in order to generate observable damage yields, dry samples must receive proportionally higher radiation doses.

Sham irradiation were included in the experiments, in which a sample would be present in the irradiation area but would not be directly exposed to the radiation source. These were compared with control samples (samples which had been stored at the location of preparation) to indicate if samples have been affected by the production of any secondary particles or affected by the transportation between the irradiation facility and the OCRC biological laboratory.

4.3.3. Dosimetry with EBT-XD Gafchromic Film

Dosimetry is vital in radiotherapy to determine the quantity of ionising radiation received by a patient during a radiotherapy treatment. A key dosimetry method in this project was the analysis of irradiated EBT-XT Gafchromic film[172], particularly for experiments in which real-time dosimetry was not possible

Gafchromic film is a brand of radiochromic film commonly used in quality assurance (QA) testing for radiographic equipment. The film consists of an active layer (approximately 25 µm thick) which contains a dye. Exposure to ionising radiation triggers a solid-state polymerisation reaction in the dye, resulting in the active layer darkening. The higher the dose received, the darker the film becomes. This layer is sandwiched between two matte-polyester substrate layers, each of thickness 125 µm (see Fig 4.4)[173].

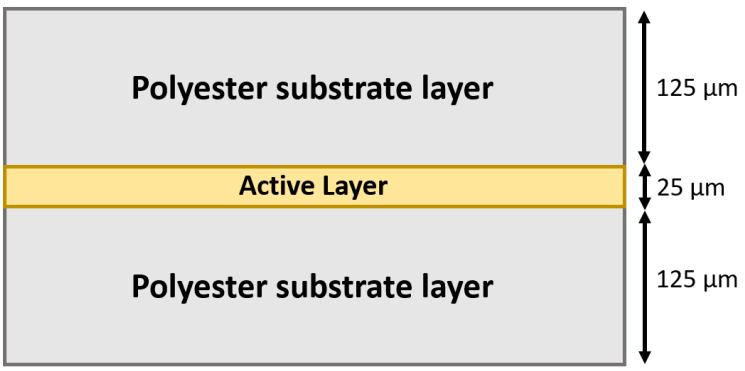

Figure 5.4 - Schematic of EBT-XD Gafchromic film, showing the active layer sandwiched between two polyester substrate layers

Colour change in the active film layer is instantaneous, though the colour change process can continue for several hours following exposure. It is therefore recommended that films are scanned at least 24 hours after irradiation. All films used in these experiments were labelled to ensure the same orientation throughout. While not in use, the film was stored in a box to avoid extreme temperature changes or exposure to sunlight, which causes film darkening over time.

As radiation delivery at CLEAR is measured in terms of charge rather than dose due to the detectors available (an Integrated Current Transformer in this case), EBT-XD film was used to verify the conversion between beam charge and dose. EBT-XD film was chosen over EBT3 film (another commonly-used film) because of the higher dose range – up to 60 Gy for EBT-XD[173] film compared with up to 20 Gy for EBT3 film[174].

Film calibration was carried out at the NHS Christie Foundation Trust using an Elekta Synergy treatment unit with 15 MeV electrons. Since film is a secondary dose standard, calibration of the film with irradiation of known doses is required to accurately determine the response of films receiving an unknown dose – as is the case in the CLEAR plasmid irradiation experiments. While similar calibrations have been carried out by Lagzda *et al.*[4,105], a separate calibration was performed for this project due to slight manufacturing variations between batches of EBT-XD film. Films were irradiated over a dose range of 0-50 Gy, with dose delivery uncertainty measured to be less than 2% for the treatment unit.

The films were irradiated sandwiched between water equivalent solid phantoms with a square field of 20 cm x 20 cm with the scanned films shown in Fig. 4.5.

The irradiated films were then scanned at the Christie using an Epson Expression 10000 XL Pro flatbed scanner[175]. This scanner included a transparency unit to allow the scanning of Gafchromic film. Films were scanned according to the Physics Dosimetry Quality Manual protocol[176] at resolutions of 150 dpi to produce 48 bit images, i.e. 16 bits per colour channel for the EBT-XD film.

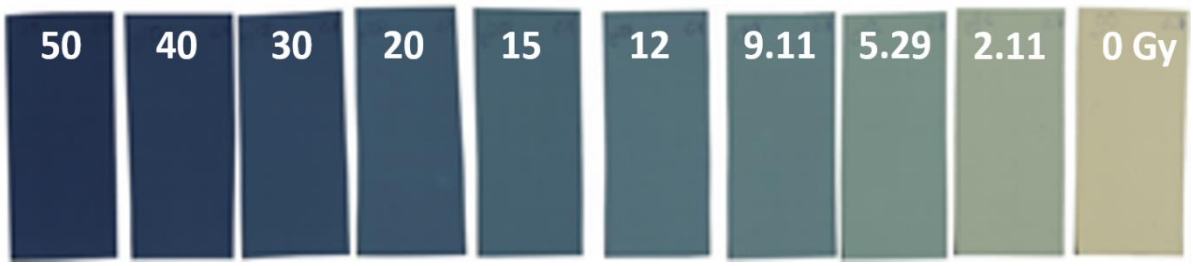

Figure 4.5 - EBT-XD Gafchromic films irradiated with 15 MeV electron beams at the Christie NHS Foundation Trust using an Elekta Synergy treatment unit over a dose range of 0-50 Gy

For radiochromic film, the darker the film means the higher the dose deposition within the film. This dosimetry is measured in terms of the optical density (OD)[176]:

$$OD = -\log_{10}\left(\frac{PV}{2^{16}-1}\right) \tag{4.2}$$

where PV is the mean pixel value of the scanned 16-bit image for each colour channel (red, green, blue), measured over a defined region of interest. OD values for the various doses are then fitted to the following equation to determine dose as recommended by the Physics Dosimetry Quality Manual:

$$Dose = (a \times b^{OD}) + c \tag{4.3}$$

where a, b and c are fit parameters and OD is the optical density, This fit was performed for each of the three colour channels using a bespoke Python code, as shown in Fig. 4.6, with R^2 and relative errors measured for each channel as shown in Fig 4.7.

Relative dose error was found to be <5% for the red and green channels for the majority of dose points, in agreement with the errors stated by the manufacturer. The relative error for the blue channel was higher on average, making the red and green channels more suitable for experimental film analysis.

Colour Channel	a	b	c	R^2
Red	0.00201	27280	-5.52	0.9994
Green	0.0304	3180	-11.64	0.9993
Blue	0.00102	222351	-22.36	0.9985

Table 4.1. Fit parameters a, b and c for red, green and blue colour channels based on Eq. 4.2 for received dose and goodness of fit measurement R^2

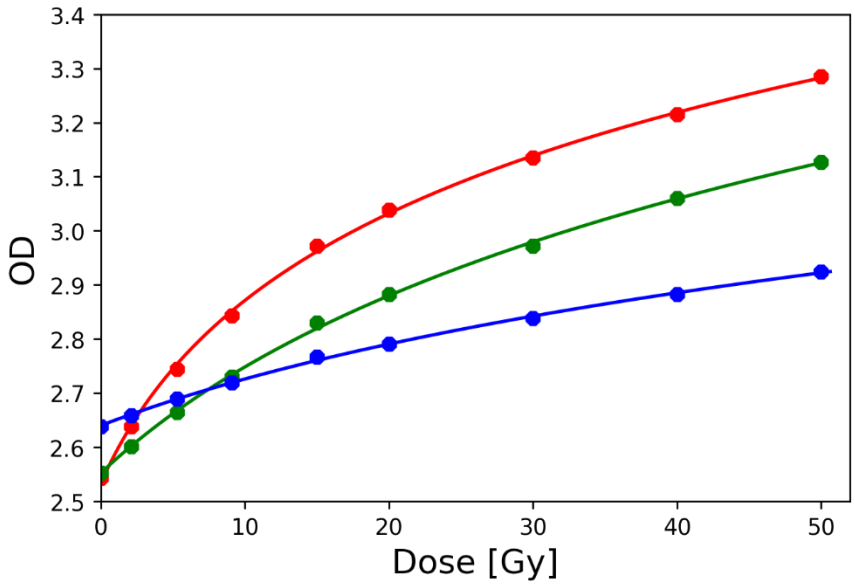

Figure 4.6 - Optical density data following EBT-XD film irradiation with 15 MeV electrons, fitted to dose using Eq. 4.2.

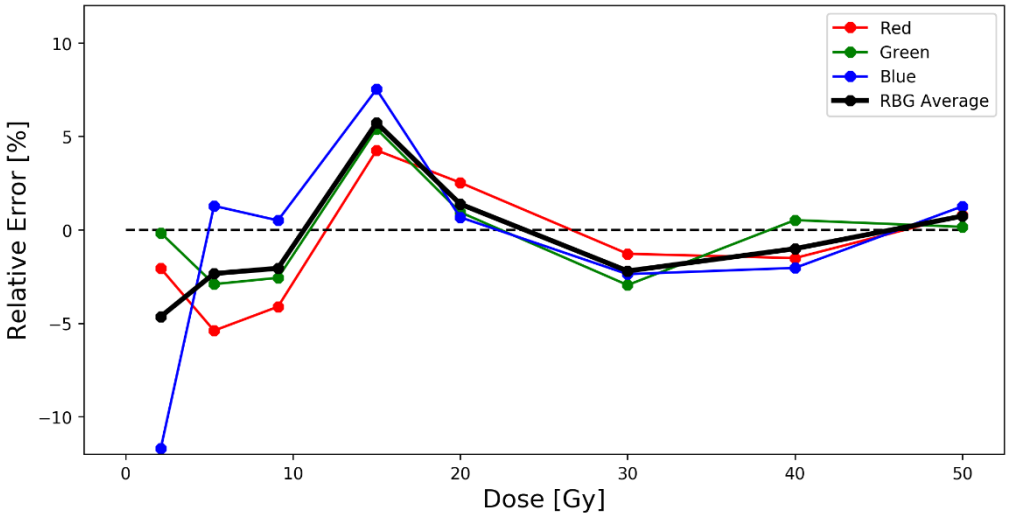

Figure 4.7 - Relative error between film data and data fit using Eq. 4.2 for each colour channel and averaging over all three colour channels (black). Red and green channels are most suitable for dosimetry

4.4. Experiment Setup

4.4.1. VHEE Plasmid Irradiation at CLEAR

CLEAR is an S-band linear accelerator designed primarily for research and development applications and component studies for planned and proposed machines at CERN[151]. Such applications include component testing for LHC upgrading, high-gradient acceleration methods as well as novel concepts including plasma and terahertz acceleration[95,177–179].

The CLEAR user facility was selected for plasmid irradiation experiments as it is capable of producing stable electron beams with energy in the region of 50-220 MeV – covering a large proportion of the proposed clinical range for VHEE. The facility also has a strong history of VHEE experiments in recent years, including insensitivity to inhomogeneities and dosimetry studies carried out by researchers at the University of Manchester[4,105] and the University of Strathclyde[180]. The aim of this study was to irradiate dry and wet plasmids with electron beams of 100-200 MeV to measure the contribution of direct and indirect radiation effects to total DNA damage and to determine a damage dependence on VHEE energy and LET. A further aim was to investigate the effect of dose rate variation on DNA damage to determine if a FLASH effect was observable at the nanoscale.

CLEAR is housed in the previous CLEX experimental area in Building 2010 on the CERN Meyrin site (Switzerland). The beamline is housed in an accelerator hall with an approximate length of 42 m and width of 7.8 m, consisting of the 25 m CALIFES injector and the 16 m user beam line, shown in Fig. 4.8.

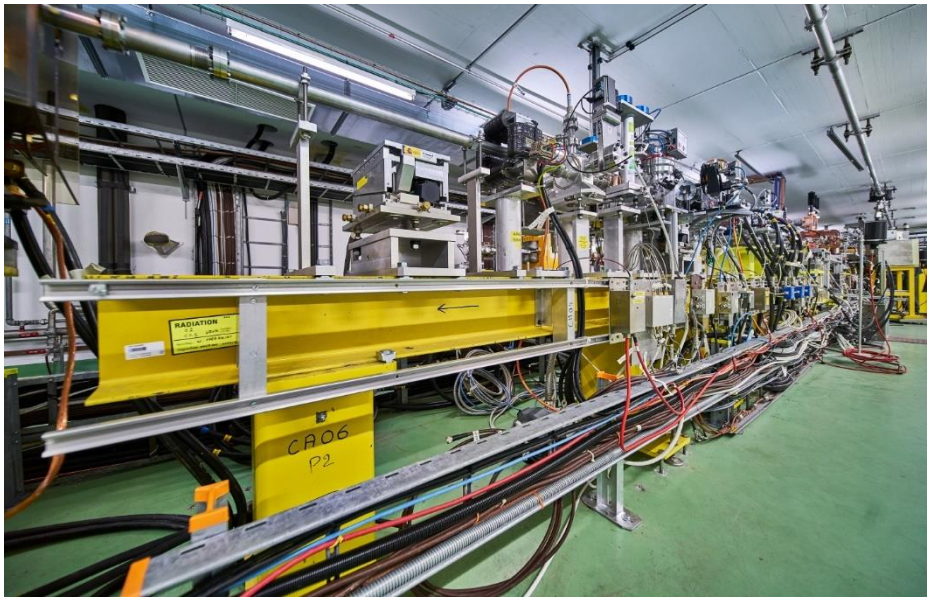

Figure 4.8 - CLEAR user facility at CERN, Geneva. Accelerator is housed in the former CLEX experiment hall

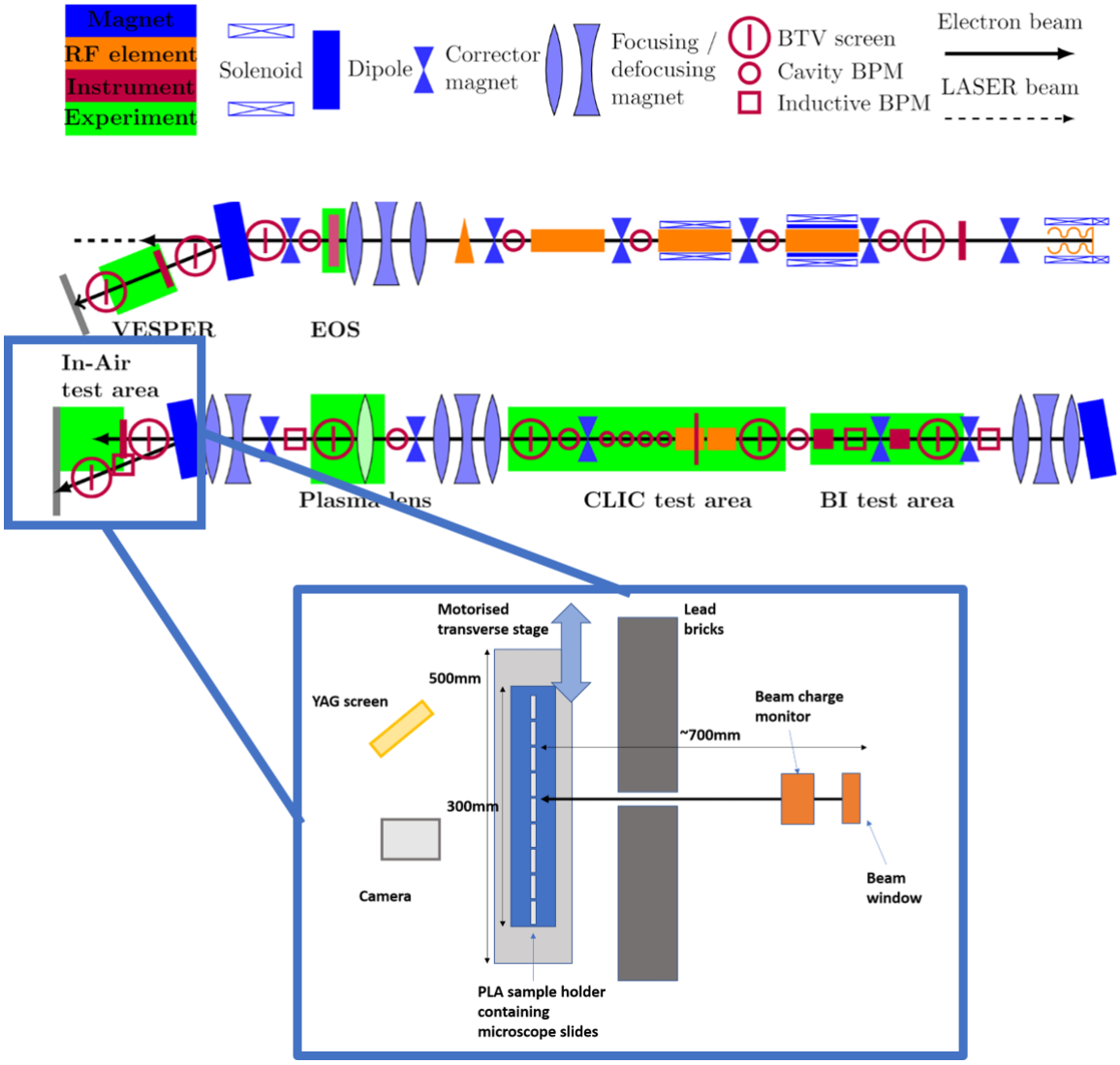

Figure 4.9 - Schematic of the CLEAR beamline showing the two experimental set-up areas - the VESPER area and the in-air test area. Positions of beam diagnostic equipment also shown. Schematic taken from [51]

The CALIFES (*Concept d'Accélérateur Linéare pour Faisceau d'Electron Sonde)* injector was designed to test and prove the feasibility of novel two-beam accelerator technology for the proposed Compact LInear Collider (CLIC). This injector was then adapted as the injector for the CLEAR beamline.

The beamline has two experimental areas. The first, VESPER[181] (the Very energetic Electron facility for Space Planetary Exploration missions in harsh Radiative environments) has been used for dosimetry and inhomogeneity studies. Plasmid irradiation experiments, however, were performed on the in-air testing stand at the end of the beamline. The beam reaches this area after exiting the accelerator 20cm after the final dipole through a 100 µm thick

aluminium window. The beam then follows a 1 m long path through air before reaching a concrete beam dump.

The plasmid irradiation experiment was installed in this 1 m space on an optical table. The beam charge, rather than the dose, is measured using a Bergoz Integrated Current Transformer (ICT). CLEAR is capable of delivering electron bunches of charge 0.01-10 nC. The dose delivered to a sample depends on the bunch charge, but also the size of the beam – radiochromic film is therefore used to determine the dose delivered to a sample. A dipole spectrometer (with absolute accuracy of 1%) is used to measure the beam energy as it leaves the CALIFES injector and a YAG (Yttrium Aluminium Garnet) screen, placed approximately 2 cm behind the plasmid sample setup, determines the beam position, shape and width. The beam parameters for CLEAR are given in Table 4.2.

Parameter	**Value**
Beam energy	60-220 MeV
Bunch Charge	0.01-10 nC
Bunch Length	1-4 ps
Bunch Frequency	1.5 GHz
RF Frequency	3.0 GHz
Bunches per Train	1-200
Beam Repetition Rate	0.83-10 Hz
RMS Energy Spread	< 0.2%

Table 4.2. Beam parameters for the CLEAR user facility at CERN. Taken from [51], with bunch charge updated according to values available during the plasmid irradiation experiment. σ based on assumption of a Gaussian beam

For the dry plasmid experimental setup, with schematics and a photograph shown in Fig. 4.10, a 3D printed polylactic acid (PLA) slide holder was designed and printed at the Cockcroft Institute. The prepared microscope slides were slotted into the holder, which was mounted on to a transverse motorised stage approximately 70 cm from the aluminium beam exit window. To ensure that X-rays produced by the beam did not interact with the plasmid samples, lead bricks were placed in front of the sample holder, leaving a small gap for the

beam to travel through. This ensured that any damage observed on the plasmid samples was caused by VHEEs only.

For the wet sample setup, of which schematics and a photograph are shown in Fig. 4.11, an aluminium rack was built which could be affixed to the PLA sample holder on the transverse stage. The Eppendorf tubes were slotted into the rack, with the plasmid solution at the base of the tube held at the same position as the dry samples to avoid the need for height adjustments.

Plasmid samples were irradiated with Gaussian electron beams of energies 100, 150 and 200 MeV, with dry samples receiving 0-6000 Gy and wet samples receiving 0-50 Gy. The positions of the plasmid samples on the stage were recorded and, from the control room, samples were moved in front of the beam and irradiated. On receiving the prescribed dose, the stage was shifted to expose the next sample to the beam, with the beam shut off between irradiations. Once all irradiations were complete, access to the beam hall was granted and samples replaced.

Wet samples were irradiated at varying dose rates – conventional (Conv) samples were irradiated with a dose rate of ~0.5 Gy/s by decreasing beam frequency (0.83 Hz) and increasing the number of bunches per train. The FLASH dose rates were reached by increasing the train charge and delivering the radiation in ultra-short (~ps) single-bunch pulses at an increased frequency of 10 Hz, resulting in dose rates in excess of 10^8 Gy/s.

As no real-time dosimetry was available at the CLEAR facility, Monte Carlo simulations were performed using TOPAS to determine the charge needed for a required dose. The experimental setup was simulated, for both dry and wet plasmid samples, and beam energy, charge and size measurements from diagnostics, taken just before irradiation were included. Simulations were run with a beam containing 10^6 electrons, corresponding to a charge of approximately 0.16 pC and the dose delivered to the sample scored. This was then scaled up to the required dose to determine the charge to be delivered to a sample. This is shown in Table 4.3.

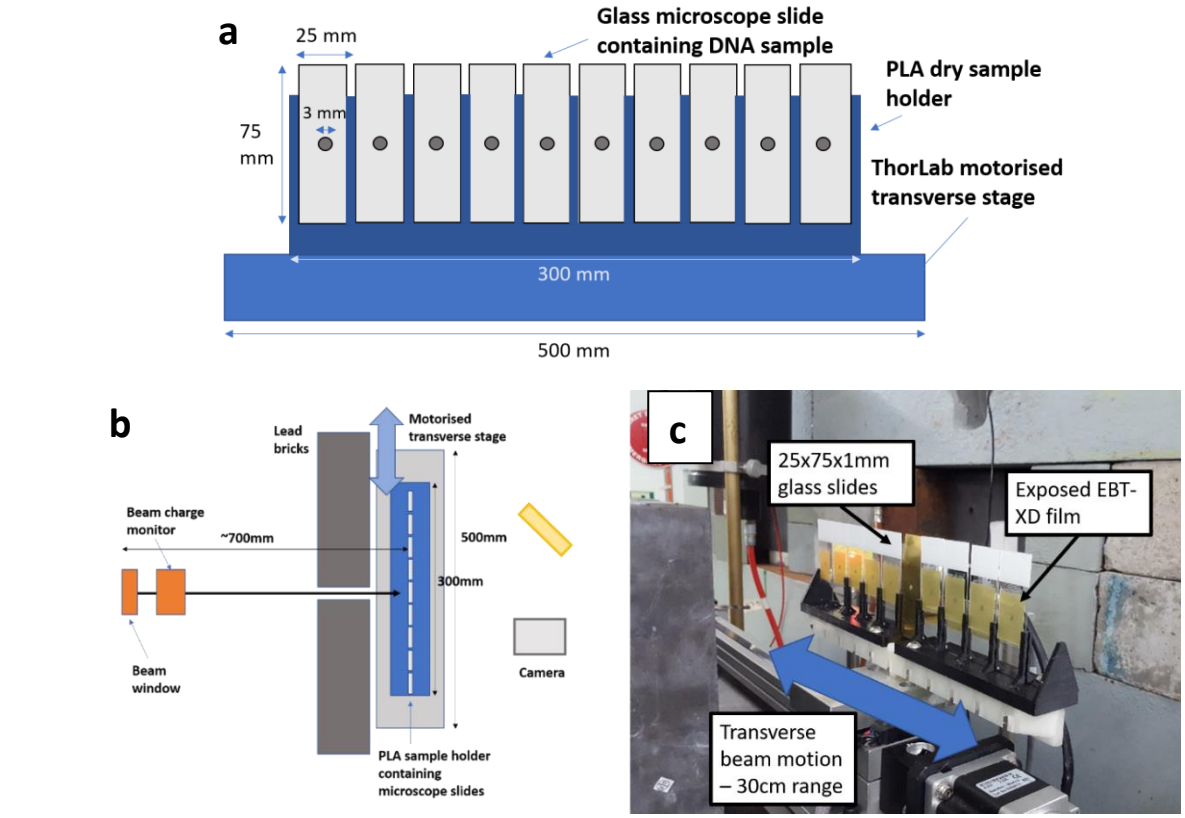

Figure 4.10 – a) Face-on and b) birds-eye view schematics and c) photograph of experimental setup for dry plasmid irradiation.

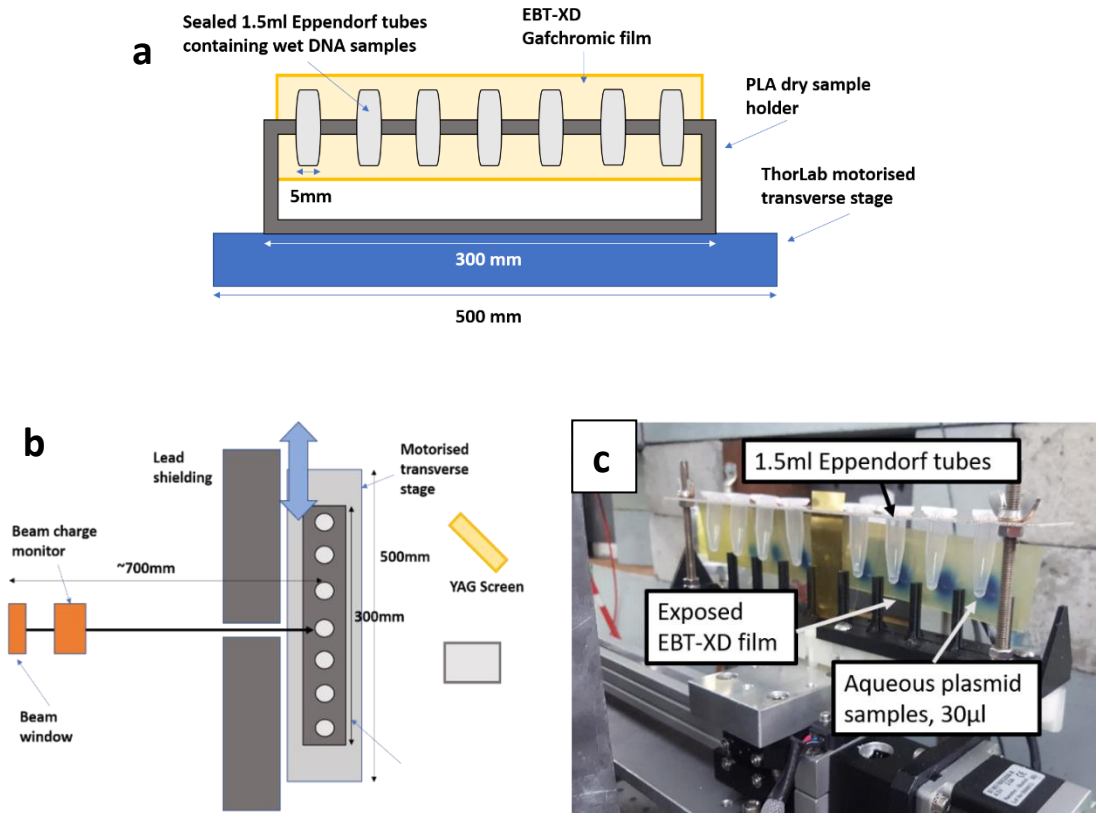

Figure 4.11 – a) Face-on and b) birds-eye view schematics and c) photograph of experimental setup for wet plasmid irradiation.

Energy (MeV)	Dose Rate (Gy/s)	Gaussian profile after target σ_x (mm)	Gaussian profile after target σ_y (mm)	Dose from 0.16pC (Gy)	Charge for 10 Gy (pC)
200	Conv	4.0	4.0	3.39×10^{-4}	4470
	FLASH	5.0	5.0	2.65×10^{-4}	6030
150	Conv	3.8	3.1	3.21×10^{-4}	4990
	FLASH	3.8	3.1	3.21×10^{-4}	4990
100	Conv	5.0	5.0	1.65×10^{-4}	9720
	FLASH	5.0	5.0	1.65×10^{-4}	9720

Table 4.3. Determining charge required by the CLEAR beam to deliver a dose of 10 Gy to a plasmid sample. TOPAS simulations used beam energy and sigma to measure dose following irradiation with 0.16 pC. Charge scaled up to determine requirement for 10 Gy

It is important to note, however that, as the glass slide is very thin, there is no build-up region. This could result in the dose delivered not matching the dose requested, i.e. energy is transferred from the beam to the target (in this case the plasmid on the glass slide) but is not delivered in the target – no charged particle equilibrium. It may be that 1 Gy of absorbed dose is in fact 1 Gy of kerma (kinetic energy released in matter), corresponding to a slightly lower value of absorbed dose. The dose across the glass slide was therefore measured following TOPAS simulations of a 100, 150 or 200 MeV electron beam consisting of 10^7 electrons and with σ = 3mm incident on a 1mm thick glass slide with the results shown in Fig. 4.12 below. A discrepancy of +13-14% was measured between the surface dose and the maximum dose across the slide – see Table 4.4. This was accounted for in calculations of SSB and DSB yield (covered in section 4.5.4) by reducing the requested dry dose by 13-14%, depending on the beam energy.

Energy (MeV)	Surface Dose (Gy)	Maximum Dose (Gy)	ΔDose
100	0.00230781	0.00200575	13.1
150	0.00250927	0.0021693	13.5
200	0.0025154	0.00216574	13.9

Table 4.4. Discrepancy between surface dose and maximum dose across glass microscope slide following 100, 150 or 200 MeV electron irradiation

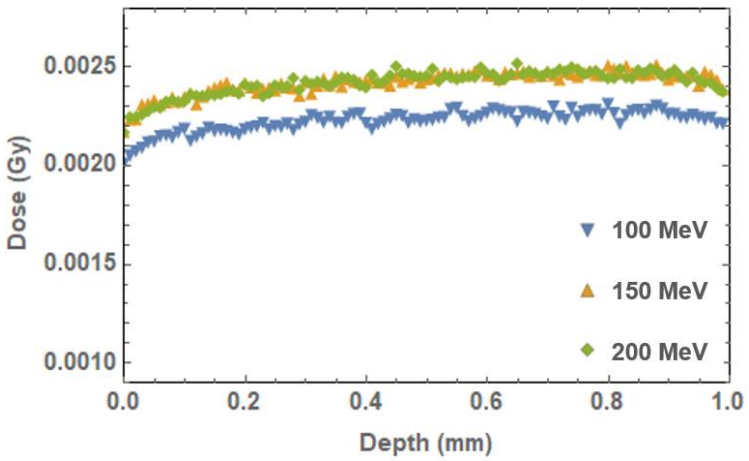

Figure 4.12 – Results of a set of TOPAS simulations to measure variation in dose across a 1mm thick glass microscope slide. Simulation performed with 10^7 electrons at 100, 150 and 200 MeV. Maximum discrepancy between dose across the slide was determined to be 13.1, 13.5 and 13.9% for 100, 150 and 200 MeV electrons respectively

EBT-XD Gafchromic film was placed behind the dry samples to check that the samples were fully covered by the beam. Due to the high doses delivered, the film was not used to determine the dose as it is only usable for doses up to ~60 Gy – it was therefore saturated on receiving the doses delivered to the samples. Dry plasmid samples were measured to be ~3 mm in diameter. The Gaussian beam spread was set to $\sigma_{x,y}$ ~ 3-4 mm in the x and y planes to ensure full coverage of the sample whilst leaving adjacent samples un-irradiated.

EBT-XD film was also placed behind the wet samples in order to determine that the sample was fully covered by the beam during irradiation and to measure the dose that was received by the plasmid. As the sample size for the wet plasmids was ~4 mm, the beam spread was similarly increased to $\sigma_{x,y}$ ~ 5mm in the x and y planes to ensure full sample coverage. This film is visible behind the samples

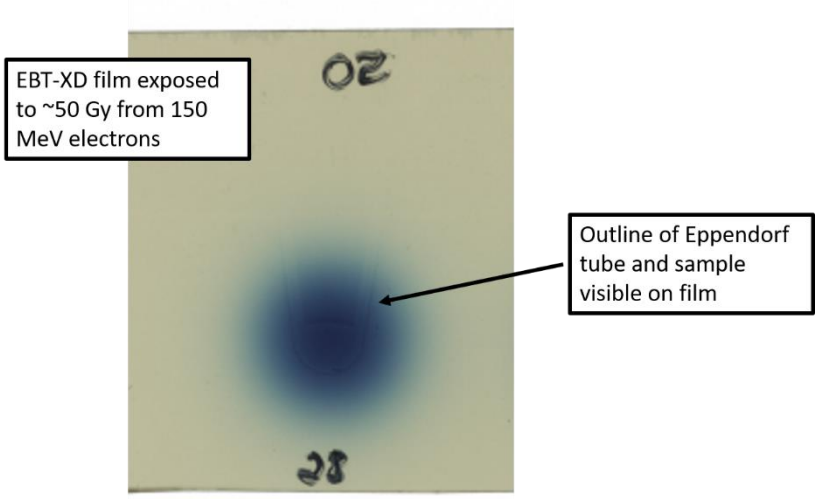

Figure 4.13 - EBT-XD Gafchromic film following exposure to 150 MeV electrons, receiving 50 Gy. The outline of the Eppendorf tube and aqueous sample are visible

in Fig. 4.11c and is shown in greater detail, with the outline of the Eppendorf and aqueous plasmid sample visible in Fig. 4.13.

4.4.2. ^{60}Co γ Plasmid Irradiation at DCF

The Dalton Cumbrian Facility (DCF) is a radiation science and nuclear engineering research base that forms part of the University of Manchester's Dalton Nuclear Institute[150]. Based in Whitehaven, Cumbria, DCF provides a range of radiation sources for commercial and academic research. The aim of this experiment was to irradiate dry and wet plasmid samples to measure DNA damage. This would form the reference for RBE calculations with low energy electrons and VHEE.

^{60}Co photon plasmid irradiations were carried out using an FTS Model 812 gamma irradiator[182] (see Fig 4.13). Photons with energies of 1.17 and 1.33 MeV are produced by three ^{60}Co sources located at the back of the irradiation chamber, in which samples were placed. Due to the nature of varying dose rate with distance from the ^{60}Co sources, plasmid samples were affixed to a turntable placed inside the irradiation chamber and rotated at a rate of 12 rpm to ensure that samples received the same average dose rate.

Dosimetry was performed using two methods. The first involved the use of a RadCal 10X6-0.18 ionisation chamber (Fig. 4.14) which was placed inside the irradiation chamber. The dosimeter was then attached to the turntable and irradiated for two minutes, with the final dose recorded. A dose rate in terms of

Gy/min was obtained and used to determine irradiation time for samples requiring a particular dose.

Figure 4.14 - FTS Model 812 gamma irradiator at DCF

EBT-XD Gafchromic film was also irradiated to provide a comparison with the irradiation chamber. 5 squares of film were affixed to the turntable and irradiated with 5 Gy. A square was removed and a further 5 Gy delivered to the remaining samples. This was repeated until the final sample, receiving 25 Gy, was removed from the chamber.

To improve the efficiency of the experiment and as dose rate was not relevant, dose was delivered cumulatively to the plasmid samples. Dry samples were irradiated over a dose range of 1000-6000 Gy (see Table 4.4), repeated three times Wet samples of volume 15 µl were irradiated over a dose range of 5-50 Gy, repeated four times.

Dry irradiations were performed using all three ^{60}Co sources, with ionisation chamber measurements giving an average dose rate of 102.15 Gy/min. All dry samples were affixed to the turntable as shown in Fig 4.15(a), placed in the irradiation chamber and received an initial dose of 1000 Gy. Three samples were then removed and labelled as 1000 Gy samples. This process of irradiation and removal of samples was repeated.

Dry Sample Doses (Gy)	Aqueous Sample Doses (Gy)
0	0
1000	5
2000	10
3000	20
4500	30
6000	40
-	50

Table 4.5. Doses delivered to dry and aqueous plasmid samples with ^{60}Co photons

Wet samples were irradiated in a similar manner. The Eppendorf tubes were affixed to the turntable as shown in Fig. 4.15(b) and irradiated cumulatively with samples removed at regular intervals. Samples received. Both dry and wet samples were removed from the freezer one hour before irradiation to ensure they were fully defrosted before irradiation.

Due to the lower dose requirement of the wet samples, the dose rate was reduced in order to increase the accuracy of the low dose delivery and to improve dose uniformity with the turntable. Dose rate was reduced firstly by using just one of the three available ^{60}Co sources. Secondly, three lead blocks, each of thickness 12 mm, were placed in front of the source to attenuate the emitted photons. The ionisation chamber was irradiated for two minutes and an average dose rate of 2.5 Gy/min was measured.

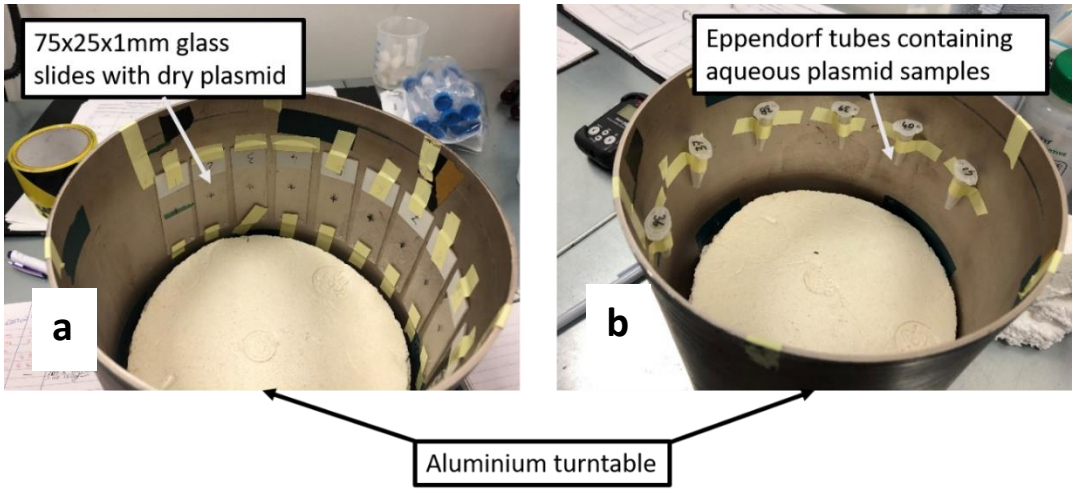

Figure 4.15 - a) Dry plasmid samples on glass microscope slides and b) wet plasmid samples in 1.5 ml Eppendorf tubes, both affixed to the inside of an aluminium turntable to ensure uniform dose rate

4.4.3. Low Energy Electron Plasmid Irradiation at the Christie NHS Foundation Trust

The Christie NHS Foundation Trust manages the Christie Hospital, a cancer treatment centre in Manchester, UK. The Christie is home to one of the world's largest radiotherapy sites, providing IMRT and VMAT treatment, stereotatic radiotherapy, brachytherapy, image-guide radiotherapy and, as of 2018, high-energy proton therapy[149].

Plasmid irradiation experiments were carried out at the Christie to measure the DNA damage yields resulting from exposure to clinical electron beams with energy 6-15 MeV. This allows for comparison of DNA damage yield and RBE to VHEE, with further investigation into a relationship between DNA damage and electron energy or LET.

An Elekta Synergy treatment unit[183], shown in Fig. 4.16 was used for plasmid irradiation experiments and is capable of producing both electron and photon beams depending on clinical requirement. Electrons are produced by an electron gun and accelerated in the accelerating waveguide through energy transfer from a high-power radio frequency (RF) field set up by an RF power generating system. The beam then travels through the gantry to the treatment head, controlled using dipole and quadrupole magnets, where it is scattered with a scattering foil to cover the field size required for a particular treatment[184].

Figure 4.16 - Elekta Synergy treatment unit used for low energy electron irradiation of wet plasmid samples

Only wet plasmid samples were irradiated at the Christie as the treatment machine is not designed for delivery of the very large doses required for dry plasmid irradiation. We therefore did not want to risk causing any damage to a machine whose primary function was to treat patients. Plasmid samples were prepared in the MCRC biology laboratory and transported in a cool box to the Christie radiotherapy department. Samples were removed from the freezer one hour before irradiation to ensure that they were fully defrosted at room temperature just before irradiation.

The treatment head of the Elekta Synergy unit was rotated 90° clockwise to provide horizontal irradiation of the samples. The samples were placed in the aluminium Eppendorf tube holder described in section 4.4.1. To ensure uniform coverage of the samples, a 20 x 20 cm^2 applicator was attached to the treatment head. EBT-XD film was attached to the sample holder and irradiated with the plasmid samples to confirm the dose received by the plasmid samples. The holder containing the samples and EBT-XD film was mounted on to water-equivalent solid phantom blocks to ensure that the samples and film were within the irradiation field. The samples and film were positioned 2 cm beyond the applicator. The experimental setup is shown in Fig. 4.17.

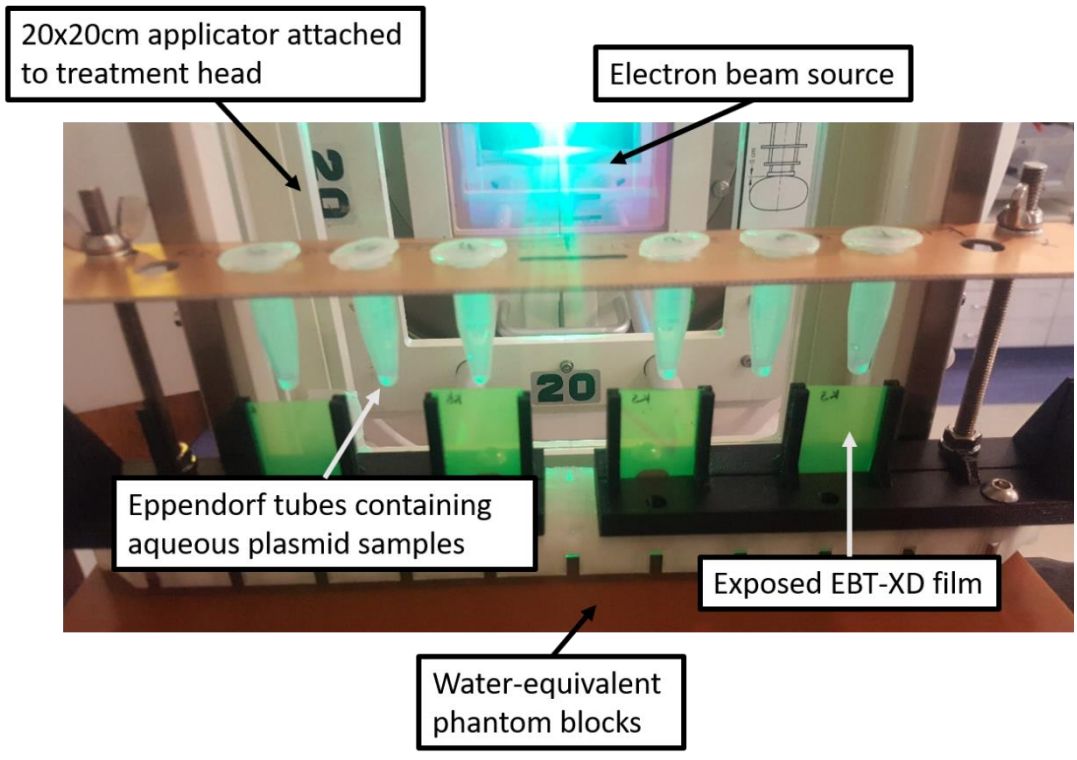

Figure 4.17 - Experimental setup for wet plasmid irradiation with low energy electrons at the Christie. Applicator, samples, electron beam source, EBT-XD film and water equivalent solid phantoms labelled

Note that the Eppendorf tubes were held in air rather than in a water phantom, as would be the case for X-ray irradiation. When irradiating with photons, there exists a higher uncertainty at doses delivered at a shallow depth in a material. This is caused by forward- and back-scattered secondary electrons not reaching equilibrium at these shallow depths. This effect in turn results in a steep gradient in the corresponding PDD curve. As this issue is not faced using electrons, samples can be irradiated in air as the dose uncertainty is reduced.

Dose corrections were required because of the experiment setup. Typically, treatment machines deliver dose in monitor units (MU), with a common definition taken from the 'Handbook of Radiotherapy Physics: Theory and Practice'[185] being:

> 'the monitor chamber reads 100 MU when an absorbed dose of 1 Gy is delivered at a point at the depth of maximum dose in a water-equivalent phantom whose surface is at the isocentre of the machine with a field size at the surface of 10 cm x 10 cm.'

A correction factor based on the sample position being 2 cm from the applicator and using a field size of 20 x 20 cm^2 was determined using reference tables to be 1.11. These reference tables describe the dose correction factor as a function of applicator size and distance from applicator. As they are used in patient treatment, they have been carefully commissioned.

30 µl plasmid samples were irradiated with electron beams at 6, 10 and 15 MeV and received doses of 5, 10, 20, 30, 40 and 50 Gy (see Table 4.6). Samples were then returned to the OCRC biology laboratory and stored at -20°C.

Dose (Gy)	6 MeV Dose (MU)	10 MeV Dose (MU)	15 MeV Dose (MU)
0	0	0	0
5	556	537	509
10	1112	1074	1018
20	2224	2148	2036
30	3336	3222	3084
40	4448	4296	4072
50	5560	5370	5090

Table 4.6. Conversion of dose in Gray (Gy) to monitor units (MU) for each energy value according to Christie reference tables

4.5. Analysis

4.5.1. Determining Dose with EBT-XD Film

For experiments in which real-time dosimetry cannot be performed, EBT-XD film provided information on the dose delivered by a radiation source. To determine the dose received by the film, the optical density for each colour channel is calculated over a defined region of interest. The dose received by the film can then be determined by substituting the optical density into Eq. 4.3 with the relevant fit parameters based on the 15 MeV Christie calibration curve.

While film calibration was carried out using a flat field at the Christie NHS Foundation Trust, film irradiation at the CLEAR user facility was performed using pencil beams. These were confirmed to be Gaussian beams using the YAG screen situated 2-3 cm behind the plasmid samples. The EBT-XD film placed directly behind the samples can, in addition to measuring the dose received, also be used to determine the Gaussian nature of the beam and to measure the beam sigma.

To do this, the two-dimensional optical density for a particular colour channel was fitted to a two-dimensional elliptical Gaussian function, shown in Fig. 4.18:

$$D(x,y) = A\exp\left[-\frac{(\cos\theta\,(x-\mu_x)+\sin^2\theta(y-\mu_y))^2}{2\sigma_x^2} - \frac{(\cos\theta\,(y-\mu_y)+\sin^2\theta(x-\mu_x))^2}{2\sigma_y^2}\right] \quad (4.4)$$

where A is the amplitude of the Gaussian, θ is the angle of the 2D Gaussian from the prime axis, μ_x and μ_y are the x and y positions of the maximum optical density value and σ_x and σ_y are the beam standard deviations in the x and y axes (horizontal and vertical planes respectively). The goodness of fit was measured for the Gaussian fits of each CLEAR irradiation, with $R^2 > 0.998$.

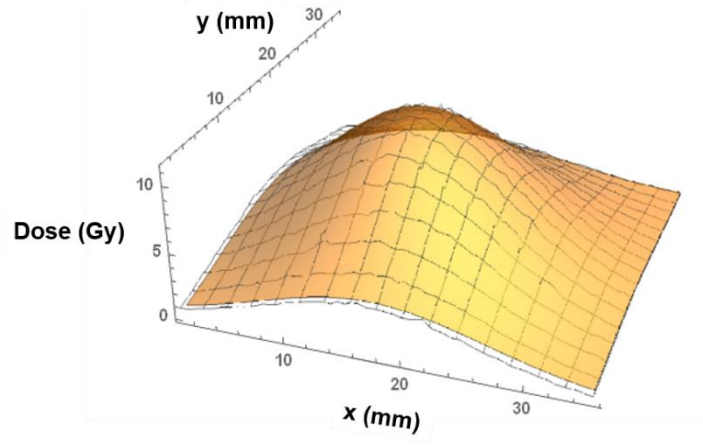

Figure 4.18 - 2D Gaussian fit to optical density data measured from EBT-XD film following irradiation by 100 MeV electrons

4.5.2. Agarose Gel Electrophoresis

Electrophoresis is a method of separating molecules in a mixture through the application of an electric field across a medium. Charged molecules are attracted towards the oppositely charged electrode and migrate through the medium towards it. The speed of migration depends on the size and shape of the molecule, as well as the magnitude of charge[158].

A small, highly charged molecule, for example, will travel more rapidly along the medium than a large molecule with a low charge. Tightly coiled molecules, such as supercoiled plasmids, will also travel more rapidly compared to those with relaxed, open structures as the medium will provide less resistance. Separated groups of molecules form distinct bands along the medium, visible following UV imaging.

In the plasmid irradiation experiments described in this chapter, the plasmid forms following irradiation were separated using agarose gel electrophoresis. Agarose gel, a refined and purified version of agar gel (extracted from seaweed), is a common medium because, unlike agar, it contains fewer charged sulphate and carboxylic groups[186]. These groups generate significant electroosmotic flow (EOF), which can result in broadening and distortion of the bands[187].

The method for agarose gel electrophoresis of irradiated plasmid samples is detailed below and the setup shown in Fig. 4.19.

1. **Preparing the gel**
    - Add 2 g agarose to a conical flask with 200 ml 1x TAE buffer and 20 µl SYBR safe DNA stain (used to visualise the DNA). This stain is used as a safer option than the commonly used, but carcinogenic, ethidium bromide[188].
    - Heat mixture in 30 s intervals in a microwave until the agarose has completely dissolved.
    - Leave to cool until the flask is cool enough to handle.
    - Pour the gel into a water-tight tray in electrophoresis tank slowly to prevent formation of bubbles. Pop any which form with a pipette tip.
    - Insert comb to create wells for loading the plasmid samples.
    - Leave to set for ~45 mins. Remove comb and fill electrophoresis tank with 0.5x TAE buffer until gel is fully submerged

2. **Preparing the plasmid samples**
    - Take up dry samples from the microscope slides with 5 µl distilled deionised water and place in an Eppendorf tube
    - Add 1 µl Gel Loading Dye, Purple (6x) to each sample. The loading dye increases the sample density so the sample will sink to the bottom of the gel well. The vivid colour allows the progress of samples along the gel to be monitored.
    - Divide large wet samples into 5 µl samples, pipetting each into an Eppendorf tube. Add 1 µl Gel Loading Dye, Purple (6x) to each sample.
    - Prepare the Supercoiled DNA ladder[189] and the 1 kbp+ DNA ladder[190] (formerly the 2-Log DNA ladder) for reference markers:
        - Dilute 1 µl of the Supercoiled DNA ladder in 4 µl distilled deionised water.
        - Add 1 µl Gel Loading Dye, Purple (6x) to the sample
        - Repeat the process for 1 kbp+ DNA ladder

- Prepare the EcoRI sample – a restriction enzyme that specifically cuts DNA at ~4000 bp[191], used in this analysis to indicate the position of the linear plasmid band
    - Mix 10 µl of unirradiated DNA solution at 100 ng/µl with 1 µl EcoRI solution and 5 µl 10x NEB Buffer EcoRI. Make up to 50 µl with distilled deionised water.
    - Incubate the sample in a water bath at 37°C for 60 minutes
    - Take 5 µl of the solution and mix with 1 µl Gel Loading Dye, Purple (10x)
- Following preparation of all samples, pipette each sample into an individual well in the gel. Record the contents of each well.

3. **Running the gel**
    - Place the lid on the electrophoresis tank, ensuring the electrodes are connected correctly
    - Connect to a DC power pack and set the power supply to a constant voltage of 100 V.
    - Samples will migrate across the gel for ~120 minutes, or until they have migrated 70-80% along the gel.
    - On completion of the run, leave the gel in the buffer until ready for analysis to prevent drying or cracking.

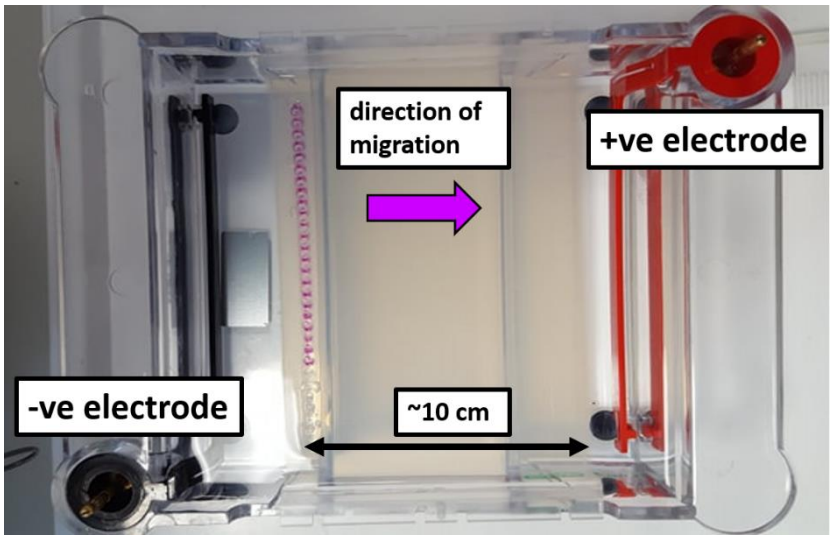

Figure 4.19 - Agarose electrophoresis tank containing agarose gel with dyed plasmid samples in wells. Direction of DNA migration shown

Following electrophoresis, the gels were imaged using a BioRad ChemiDoc MP UV imager. The tray on which the gel was placed was cleaned and moistened with distilled deionised water before each use to remove any contaminants from previous usage and to prevent drying or cracking of the gel.

Images were taken over a range of exposure times (0.1-5 seconds) to determine optimal exposure, i.e. plasmid bands were sufficiently bright for analysis but not over-exposed. Typically, the optimal exposure was 0.3-0.4 seconds, though this did vary between gels.

The gel images (see Fig. 4.20) show three distinct bands, corresponding to SC, OC and L plasmid forms, with the relative proportion of each varying with the dose received. The following section details how the intensity of the bands are used to determine the relative proportion of each plasmid form in a sample.

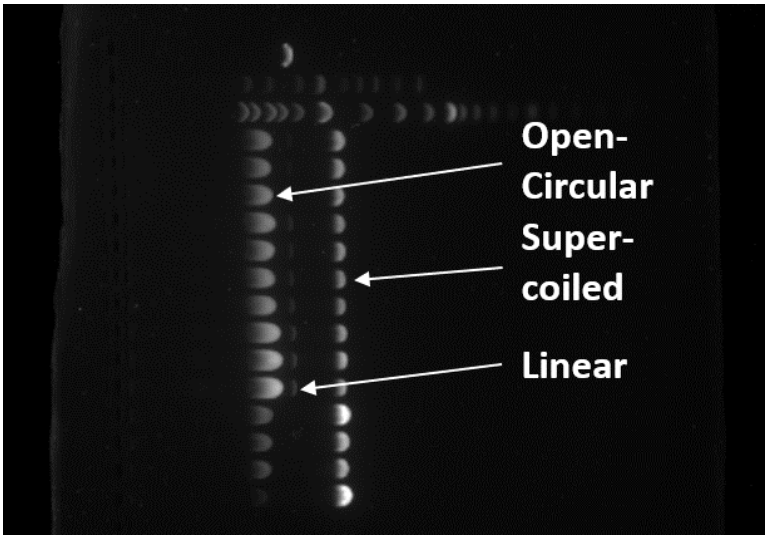

Figure 4.20 - UV image of agarose gel showing distinct supercoiled, open-circular and linear plasmid bands

Images of the gel were modified by subtracting the background image from the gel image to subtract the background signal from the gel and to remove any smudges or contaminants which may have been present on the tray. The background of the subtracted image was determined by mapping the small regions of the gel, omitting locations where the plasmid bands were present, and measuring the mean intensity over that area. This background was then subtracted from the band intensity to determine the plasmid band intensity only.

4.5.3. Calculating Plasmid Form Proportions

The intensities of the plasmid sample bands were determined using Fiji[192], an open-source image processing package based on the Java application ImageJ[193,194], used in biological image analysis.

The sample band was determined by mapping a line across the centre of the sample bands and measuring the intensity. The gel background was subtracted from the sample intensity to give the background-corrected intensity for each pixel. This was then normalised by dividing each pixel intensity by the maximum pixel intensity in that region.

To determine the SC, OC and L plasmid proportions, intensity was plotted with pixel value. The SC, OC and L plasmid bands appear as distinct peaks on this plot, as shown in Fig. 4.21. The proportion of a particular plasmid form is determined by integrating the signal over the peak. Each proportion can then be normalised with respect to the sum of the three plasmid proportions:

$$SC_{norm} = \frac{SC}{SC + OC + L} \tag{4.5}$$

For a set of irradiations, plasmid proportion is plotted against the dose (see Fig. 4.22). This data is used to calculate the yield of SSBs and DSBs in units of breaks per Mbp per Gy by fitting to a set of equations describing each plasmid form. This fitting process is detailed in the following section.

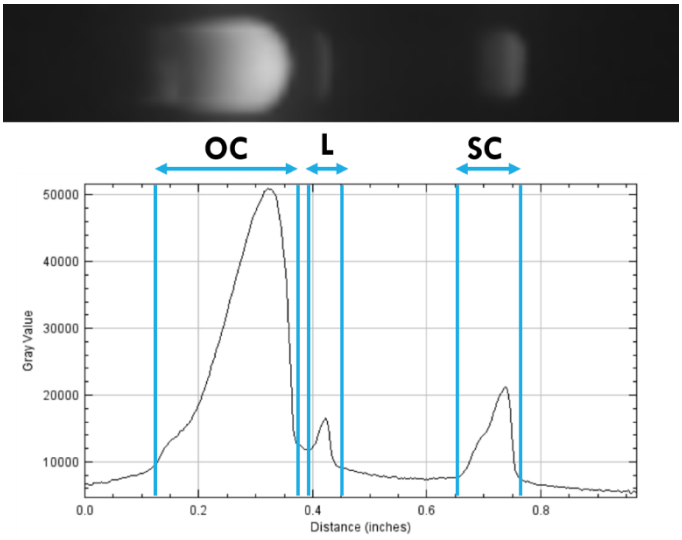

Figure 4.21 - Plot of intensity along the agarose gel following electrophoresis. Peaks corresponding to supercoiled, open-circular and linear plasmid forms are highlighted

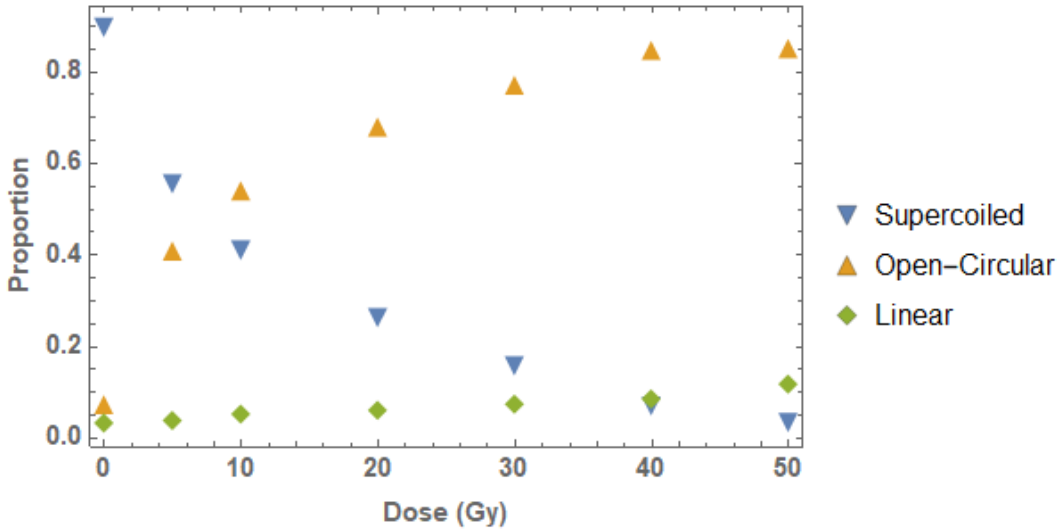

Figure 4.22 - Proportions of supercoiled, open-circular and linear plasmid forms following photon irradiation of wet plasmids

4.5.4. Calculating SSB and DSB Yields

Following calculation of the plasmid form proportions, the data was fitted to obtain values for the SSB and DSB yields. Two mathematical fits were used to calculate the yields due to their established use in similar plasmid irradiation studies.

The first fit was developed by Cowan *et al.*[195], who developed a set of equations to determine DNA damage caused by enzymes such as DNase I, which can 'nick' a DNA strand, resulting in an SSB. The model makes the critical assumption that, if two SSBs occur on opposite strands sufficiently close to one another, a DSB is induced. A simplified version of this model, which does not account for this method of DSB induction due to the high levels of complexity and difficulty in implementation, has been used in plasmid studies in which the plasmid damage is caused by irradiation, rather than enzyme interaction. This model consists of three equations to which the SC, OC and L proportions:

$$SC(D) = \frac{e^{-(\mu_0+\mu D)}}{1+\phi_0+\phi D} \tag{4.6}$$

$$OC(D) = \frac{1-e^{-(\mu_0+\mu D)}}{1+\phi_0+\phi D} \tag{4.7}$$

$$L(D) = \frac{\phi_0+\phi D}{1+\phi_0+\phi D} \tag{4.8}$$

where D is the dose delivered to the plasmid in Gy, μ and φ are the average SSB and DSB yields respectively in units of Mbp^{-1} Gy^{-1} and μ_0 and φ_0 are the yields at zero dose.

The second fit was developed by McMahon and Currell[156], with the specific aim of fitting the results of agarose gel electrophoresis following plasmid DNA irradiation using non-linear regression models to improve the accuracy of the resulting fit. As in the Cowan fit, the McMahon fit consists of three equations to link the dose dependent proportions of SC, OC and L to SSB and DSB induction:

$$SC(D) = S_0 e^{-(\mu D + \phi D)} \tag{4.9}$$

$$OC(D) = e^{-\phi D}\left[e^{-\frac{1}{2}\mu^2 \rho D^2}(S_0 + C_0) - S_0 e^{-\mu D}\right] \tag{4.10}$$

$$L(D) = 1 - (S_0 + C_0)e^{-\left(\phi D + \frac{1}{2}\mu^2 \rho D^2\right)} \tag{4.11}$$

While both fits are used to produce values for the SSB and DSB yields (μ and φ respectively), a key difference is the inclusion of the parameter ρ, the distance within which two SSBs on opposite backbones must occur to induce a DSB, in the McMahon model - not explicitly accounted for in the Cowan fit.

The SC and OC plasmid data from the experiments outlined in this chapter were fitted to the corresponding equations for both the Cowan and McMahon fits to determine the values of μ and φ with a least-square error non-linear fit using a code written in Mathematica (version 11.2)[196]. The efficacy of this fitting method is indicated by the agreement between the L equations for both models and the linear plasmid data – see Fig. 4.23.

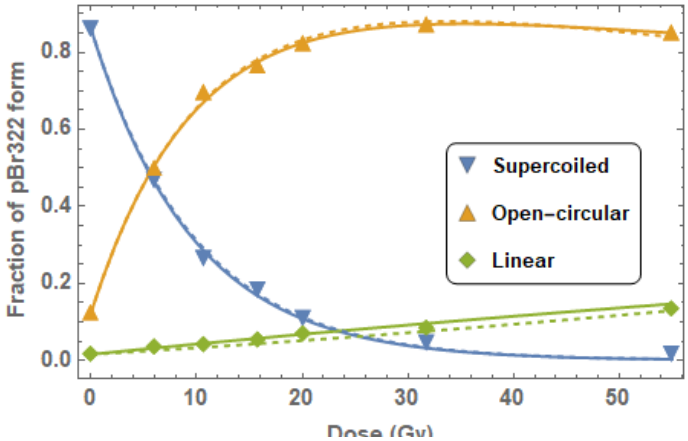

Figure 4.23 – Proportions of supercoiled, open-circular and linear plasmid forms following 200 MeV electron irradiation fitted to the Cowan (solid line) and McMahon (dashed line) equations

While both the McMahon and Cowan fits are good, for the purposes of this project only the McMahon fit will be used. This is because the McMahon fit was developed specifically for the purpose of fitting data resulting from agarose gel electrophoresis analysis of irradiated plasmid DNA. Vysin *et al.*[157] found the McMahon fit to be more robust than the Cowan fit for determining DSB yield, providing more confidence in the use of the McMahon model in this project.

4.6. Plasmid Irradiation Experiment Results

4.6.1. Plasmid Preparation

Preliminary tests were performed on the pBR322 plasmid DNA to determine that the experimental design was robust and to investigate any possible sources of error. One potential issue was the sinking of plasmid DNA in the wet samples. As the samples would be held vertically for significant periods of time at room temperature, there was a concern that gravity would cause the DNA in the solution to sink to the bottom of the Eppendorf tube, resulting in non-uniform plasmid irradiation.

To address this, a simple test was devised, in which nine samples of 30 µl plasmid solution at concentration 100 ng/µl were prepared and held in Eppendorf tubes. At 15 minute intervals, 1 µl of solution was taken from the centre of the sample and the concentration measured using a Nanodrop™ OneOne^{C} Microvolume UV-Vis Spectrophotometer. This was repeated and averaged over three measurements. This process was repeated until two hours had elapsed, as this was a typical length of time over which samples would be kept at room temperature during the experiment before being returned to the freezer. The average concentration at each interval is shown in Table 4.7 and Fig. 4.24 below. The statistically insignificant variation in concentration at the centre of the sample indicates that the plasmid DNA does not sink to the bottom of the Eppendorf tube over time, instead remaining suspended uniformly through the sample solution.

Time (min)	Concentration (ng/µl)
0	98.57 ± 2.02
15	100.93 ± 0.50
30	101.07 ± 0.57
45	100.6 ± 0.53
60	100.43 ± 0.21
75	101.93 ± 0.57
90	100.47 ± 0.14
105	101.07 ± 0.95
120	99.7 ± 0.24

Table 4.7. Variation of plasmid solution concentration with time. Standard error calculated based on three concentration measurement repeats

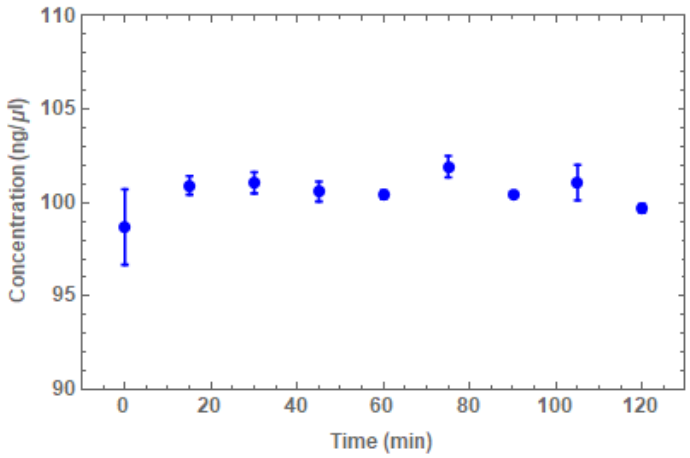

Figure 4.24 - Variation of plasmid solution concentration with time to determine if plasmid DNA sinks over time. Standard error based on three concentration measurement repeats

The second test was to determine the effect that the drying process had on the plasmid structure. There was a concern that the drying process may cause small nicks, or single-strand breaks, in the plasmid DNA. This would need to be taken into account when measuring damage yields following the experiment to determine the damage arising from exposure to ionising radiation and the damage arising from the experimental setup.

To determine this, the average plasmid proportions were measured from dry and wet control samples used in the CLEAR experiments and compared. These samples remained unirradiated in cold storage (-20°C) in the biology laboratory at the Manchester Cancer Research Centre throughout the experiment and

measured along with the irradiated samples following irradiation at CERN. These measurements are given in Table 4.8.

Control Sample	Supercoiled	Open-Circular	Linear
Dry	0.867 ± 0.004	0.100 ± 0.003	0.033 ± 0.001
Wet	0.877 ± 0.008	0.096 ± 0.006	0.027 ± 0.002

Table 4.8. Plasmid proportion data for dry and wet control samples from the CLEAR experiment, compared to determine if the drying process has an effect on plasmid proportions

As is clear from the measurements in Table 4.6, the drying process does not appear to have an effect on the plasmid proportions, as the supercoiled and open-circular proportions are very similar between the wet and dry samples. No drying effect will be included in the calculation of SSB and DSB yield for dry plasmid samples.

4.6.2. VHEE Plasmid Irradiation at CLEAR

This section details the results from the experiments carried out at the CLEAR user facility, in which plasmid samples were irradiated with electron beams at 100-200 MeV. The results are split into four sections: a review of the effects of transportation on the plasmid samples; damage yields following dry plasmid irradiation and investigating DNA damage dependency on electron energy and LET; damage yields following wet plasmid irradiation and investigating damage dependency on electron energy, LET and dose rate; a comparison between damage yields of dry and wet irradiated plasmid samples to determine the contribution of direct and indirect radiation effects to total DNA damage following VHEE irradiation.

4.6.2.1. Plasmid Stability during Transportation

For dry plasmid samples, the diluted plasmid solution was transported to CERN via courier service and samples dried on the glass microscope slides onsite. A further shipment of pBR322 plasmid, held in a solution of 10 mM Tris-HCl and 1mM EDTA[30,31], was sent from New England BioLabs to CERN in order to prepare the aqueous plasmid samples. Samples were subject to temperature fluctuation throughout the journey and were scanned with X-rays on arriving at customs, receiving a dose of approximately 0.3 mGy. The plasmid in buffer

solution was then diluted with purified water and samples placed in Eppendorf tubes. For both wet and dry samples, control samples were prepared and stored at -20°C at the Oglesby Cancer Research Centre, Manchester.

Sham dry and aqueous samples were prepared at CERN and mounted on to the sample holder but not directly exposed to the beam. Following the return of the samples to Manchester the three plasmid proportions (supercoiled (SC), open-circular (OC) and linear (L)) for control and sham samples were compared to determine the effect of transportation on the plasmid DNA. The results are presented in Table 4.9.

Sample Type	SC	OC	L
Control (Dry)	0.867 ± 0.004	0.100 ± 0.003	0.033 ± 0.001
Sham (Dry)	0.270 ± 0.013	0.690 ± 0.011	0.038 ± 0.002
Control (Wet)	0.877 ± 0.008	0.096 ± 0.006	0.027 ± 0.002
Sham (Wet)	0.882 ± 0.008	0.091 ± 0.007	0.027 ± 0.001

Table 4.9. – Comparison of the plasmid proportions in control and sham (unirradiated samples transported to and from CLEAR) plasmid samples. Standard error based on three gel electrophoresis repeats and four control samples for each gel

The data in Table 4.9 indicates that transportation in dilute solution did have affect the proportion of plasmid forms before irradiation with high proportions of open-circular plasmid observed compared to the control samples. This indicates a relaxing of the plasmid structure, resulting in SSBs that are not caused by irradiation. Transportation did not have a significant effect on the linear plasmid proportion, as the temperature increases experienced are not sufficiently energetic to cause DSBs. It was therefore likely that only the DSB yield data following dry plasmid irradiation will be reliable and usable – SSB yield data is unlikely to be reliable due to the contribution of SSBs arising from temperature fluctuations.

The effects of transportation were not significant on the aqueous samples because the samples were transported in a more concentrated buffer solution, which prevented the relaxation of the plasmid structure.

4.6.2.2. VHEE Irradiation of Dry Plasmid DNA

Dry plasmid samples were irradiated with electron beams of energies 100, 150 and 200 MeV over a dose range of 0-6000 Gy.

The results of these irradiations are given in Table 4.10 and in Fig. 4.25, with standard errors calculated based on three AGE repeats. Charge jitter (shot-to-shot variation in the bunch charge) was calculated to be 0.86%, 0.47% and 0.33% for 200, 150 and 100 MeV electron beams respectively.

Energy (MeV)	LET (keV/µm)	µ (Mbp^{-1} kGy^{-1})	φ (Mbp^{-1} kGy^{-1})
100	0.2202	69.81 ± 8.4	3.66 ± 0.4
150	0.2238	80.30 ± 3.1	3.71 ± 0.1
200	0.2263	50.27 ± 4.2	3.83 ± 0.5

Table 4.10. SSB (µ) and DSB (φ) yields calculated using the McMahon fit for dry plasmid irradiation with 100, 150 and 200 MeV electron beams. Standard errors calculated based on three sample repeats

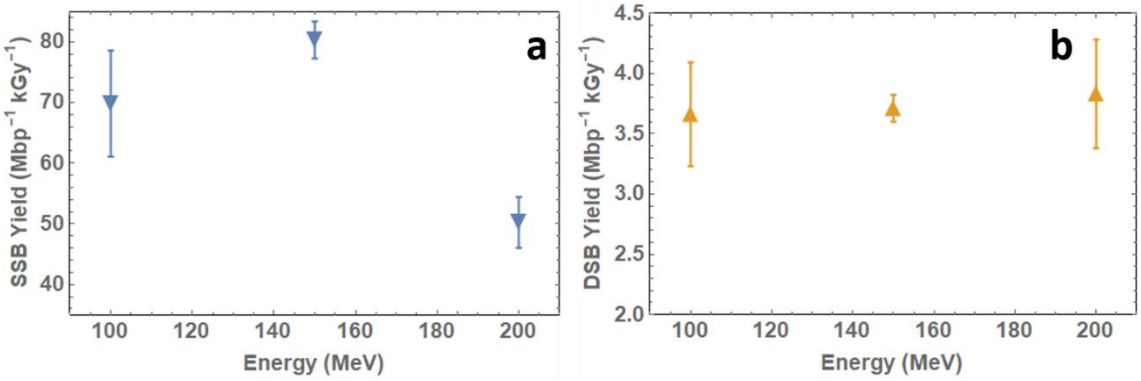

Figure 4.25 - a) Single-strand break yields and b) double-strand break yields for 100-200 MeV electron beam irradiation of dry pBR322 plasmid DNA based on McMahon data fitting. Significant variation observed in SSB yield with energy due to the effect of transportation on the plasmid samples, reducing the reliability of SSB yield results

4.6.2.3. VHEE Irradiation of Wet Plasmid DNA at Conventional and FLASH Dose Rates

Wet plasmid samples were irradiated at a low dose rate (~0.5 Gy/s) and at a high dose rate (>10^8 Gy/s) to determine if a FLASH effect could be observed at the nanoscale level. As mentioned in the Introduction, a FLASH effect (if present) would be expected to present as a decrease in damage yield, though due to the nature of the experiment, little, if any, significant variation in damage yield is expected.

Control and sham-irradiated samples were compared as with the dry samples, to determine the effects of transportation on the plasmid samples, with the plasmid proportions shown in Table 4.11. The wet plasmid samples were prepared at CERN and contained plasmid from a shipment sent directly to CERN from New England BioLabs. As the plasmid was sent in a solution containing 10 mM Tris-HCL and 1mM EDTA, temperature fluctuations did not cause the supercoiled plasmid structure to relax. This meant that SSBs measured were the result of VHEE irradiation, rather than relaxing due to temperature fluctuations, making the SSB yield results for wet plasmids more accurate than those for dry plasmids.

Sample Type	SC	OC	L
Control	0.877 ± 0.008	0.096 ± 0.006	0.027 ± 0.002
Sham, 200 MeV	0.851 ± 0.009	0.115 ± 0.006	0.034 ± 0.003
Sham, 150 MeV	0.868 ± 0.003	0.096 ± 0.002	0.036 ± 0.001
Sham, 100 MeV	0.849 ± 0.005	0.110 ± 0.005	0.042 ± 0.001

Table 4.11. Comparison of supercoiled, open-circular and linear plasmid proportions for control and sham-irradiated wet plasmid samples. Standard error calculated based on three repeats

For each sample set, film was placed directly behind the samples (~0.5 cm) to measure the dose delivered to a sample. Following irradiation, the film was analysed with respect to film from the same batch, calibrated at the Christie, to determine the dose received by the samples. Relative error between expected dose and observed dose arose in part from the variation in the beam spot diversion (sigma) between trains and from the variation in beam size between testing, following which TOPAS simulations were performed to determine the required charge, and irradiating. Charge jitter was measured at 0.61%, 1.47% and 1.59% for 100, 150 and 200 MeV beams respectively in the case of conventional dose rate. For ultra-high dose rate irradiation, charge jitter was measured as 7.48%, 5.90% and 2.96% for 100, 150 and 200 MeV beams respectively, resulting in a corresponding dose variation. Increased charge jitter is observed for the ultra-high dose rate irradiations as, to reach the required dose rate, radiation was delivered in ultra-short, high charge pulses rather than a continuous bunch train as for the conventional dose rate irradiation. While

charge jitter is not insignificant, accurate dose measurements were still possible through the analysis of irradiated EBT-XD film behind the wet samples. As a result, charge jitter did not affect the calculation of plasmid damage yield.

Based on these dose measurements, plasmid proportions were fitted using the McMahon fit to determine SSB and DSB yields following VHEE irradiation at both conventional (Conv) and FLASH dose rates. This data is presented in Table 4.12 and Fig. 4.26.

	Conv (~0.5 Gy/s)		FLASH (> 10^8 Gy/s)	
Energy (MeV)	**SSB**	**DSB**	**SSB**	**DSB**
100	15.42 ± 0.86	0.35 ± 0.02	20.31 ± 1.20	0.37 ± 0.03
150	17.63 ± 0.57	0.35 ± 0.03	18.74 ± 0.52	0.37 ± 0.04
200	20.19 ± 0.56	0.38 ± 0.02	21.22 ± 0.38	0.38 ± 0.02

Table 4.12. SSB (μ) and DSB (φ) yields calculated using the McMahon fit for wet plasmid irradiation with 100, 150 and 200 MeV electron beams at Conv and FLASH dose rates. Standard error of the mean calculated based on six sample repeats for 200 MeV and five sample repeats for 150 and 100 MeV

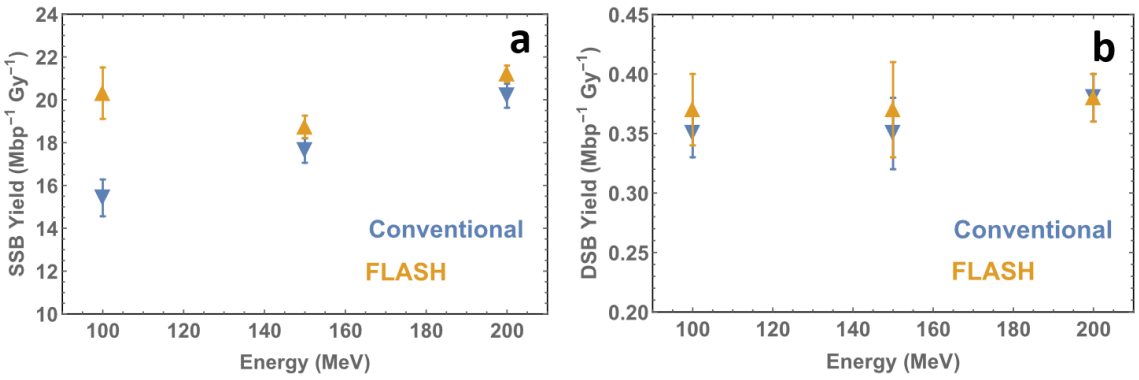

Figure 4.26 - a) Single-strand break yields and b) double-strand break yields for 100-200 MeV electron beam irradiation of wet pBR322 plasmid DNA based on data fitting to the McMahon fit. Plasmids irradiated at Conv (blue data) and FLASH (orange data) dose rates

4.6.2.4. Comparison of VHEE-irradiated Dry and Wet Plasmid DNA

In order to determine the contribution of direct and indirect radiation effects to total DNA damage following VHEE irradiation of plasmids, the damage yields from dry and wet plasmid irradiations are compared. The damage caused to wet plasmid DNA is the result of a combination of direct and indirect radiation

effects (however storage of plasmids in water can cause a small amount of relaxation from SC to OC), whereas dry plasmid DNA damage is purely due to direct radiation effects. This is because, in a dry environment, the highly reactive free radicals which are produced in water and which go on to interact with DNA are not produced. This contribution is calculated according to Eq. 4.12:

$$\text{Indirect damage (\%)} = \frac{\text{Wet Damage Yield} - \text{Dry Damage Yield}}{\text{Wet Damage Yield}} \times 100 \qquad (4.12)$$

where damage yield is either SSB or DSB yield. This calculation was performed for both SSB and DSB yields, and the data is presented in Table 4.13 below. It can be concluded that, as for protons, indirect radiation effects cause approximately 99% of DNA damage following irradiation.

Energy	% of SSB Yield from Indirect Damage	% of DSB Yield from Indirect Damage
200	99.5	99.0
150	99.5	99.0
100	99.7	99.0

Table 4.13. The contribution of indirect radiation effects to total DNA damage, calculated by comparing damage yields following dry and wet plasmid irradiation with 100-200 MeV electron beams

4.6.3. ^{60}Co X-ray Plasmid Irradiation at DCF

4.6.3.1. ^{60}Co X-ray Irradiation of Dry Plasmid DNA

X-rays emitted by the ^{60}Co sources had energies of 1.17 or 1.33 MeV and were used to irradiate dry samples over a dose range of 0-6000 Gy. Dry samples were prepared at the Manchester Cancer Research Centre and transported to the Dalton Cumbrian Facility in a cool box packed with ice to minimise temperature increase. On arrival, they were stored in a freezer at -20°C until required for irradiation. Once irradiation was complete, the samples were taken up from the slide with 5 µl distilled, deionised water, put into individual Eppendorf tubes and returned to the freezer.

The effect of transportation on the proportion of different dry plasmid forms was investigated by comparing the form proportions of control samples which had been taken to DCF to those which had remained in storage in the MCRC biology laboratory. The proportions are given in Table 4.14 below.

Sample Type	Supercoiled	Open-Circular	Linear
Control (DCF)	0.7105 ± 0.0112	0.2711 ± 0.0098	0.0184 ± 0.0014
Control (MCRC)	0.9228	0.0596	0.0176

Table 4.14. Comparison of supercoiled, open-circular and linear plasmid proportions for control dry plasmid samples. Standard error calculated based on three sample repeats

While not as significant as in the CLEAR experiment, the three hour journey did have an effect on the plasmid samples, with some relaxing of the supercoiled structure resulting in SSBs forming prior to irradiation. To reduce this effect, it would be desirable to prepare the samples onsite, having transported the plasmid in solution containing 10 mM Tris-HCL and 1mM EDTA. This would prevent relaxation of the plasmid structure.

The dry plasmid samples were successfully irradiated over the dose range 0-6000 Gy, with three repeats performed for each dose. The resulting SSB and DSB yields calculated using the McMahon fit are presented in Table 4.15. The DSB yield obtained from this dry plasmid irradiation experiment was used as the reference biological endpoint from which RBE calculations could be performed following dry plasmid irradiation experiments with electrons.

Sample	μ (Mbp^{-1} kGy^{-1})	φ (Mbp^{-1} kGy^{-1})
1	59.34	3.55
2	63.03	3.27
3	48.25	2.99
Average	56.87 ± 3.63	3.27 ± 0.13

Table 4.15. SSB (μ) and DSB (φ) yields calculated using the McMahon fit for dry plasmid irradiation with 1.03 and 1.17 MeV ^{60}Co X-rays. Standard errors calculated based on three sample repeats

4.6.3.2. ^{60}Co X-ray Irradiation of Wet Plasmid DNA

As detailed in section 4.4.2., wet samples were irradiated at a dose rate of ~2.5 Gy/min, to ensure dose uniformity with the use of the turntable and to improve the accuracy of dose delivery. Prior to sample irradiation, EBT-XD Gafchromic film was irradiated to measure the dose delivered and to compare measured values with the dose expected following measurements with the ionisation chamber. The EBT-XD films received 5, 10, 15, 20 and 25 Gy according to the measurements made using the ionisation chamber. The expected and measured dose data is presented in Table 4.16.

Ionisation Chamber Dose (Gy)	Gafchromic Film Dose (Gy)	% Difference
5	5.80	16.00
10	10.43	4.30
15	15.31	2.07
20	19.75	1.25
25	24.14	3.44

Table 4.16. Results of EBT-XD Gafchromic film irradiation with ^{60}Co X-rays at DCF. Irradiation based on ionisation chamber dosimetry, with Gafchromic Film Dose corresponding to dose measured following EBT-XD film analysis using 15 MeV electron calibration curve

Wet samples were then irradiated based on the experimental setup described in section 4.4.2, with dose delivery cumulatively as dose rate effects were not being investigated in this study. Four irradiations were carried out, with 15 µl plasmid samples used, providing three repeats at each dose for each irradiation. In total, AGE was performed for 12 wet plasmid samples. The resulting SSB and DSB yield data is presented in Table 4.17. The DSB yield obtained from this wet plasmid irradiation experiment was used as the reference biological endpoint from which RBE calculations could be performed following wet plasmid irradiation experiments with electrons.

The dry and wet plasmid yield data was compared, as with the electron data to determine the contribution of direct and indirect radiation effects on total DNA damage following ^{60}Co X-ray irradiation of plasmid DNA. This contribution is

calculated according to eq. 4.8. Indirect radiation effects were found to contribute ~99% of total DNA damage – this is consistent with literature results[157].

Gel Number	Repeat	μ (Mbp^{-1} Gy^{-1})	φ (Mbp^{-1} Gy^{-1})
1	1	16.09	0.27
	2	16.67	0.32
	3	15.21	0.40
2	1	21.32	0.28
	2	20.32	0.21
	3	23.47	0.30
3	1	16.13	0.25
	2	18.27	0.38
	3	16.78	0.35
4	1	23.66	0.28
	2	24.98	0.26
	3	25.58	0.41
Average		**19.87 ± 1.06**	**0.32 ± 0.02**

Table 4.17. SSB (μ) and DSB (φ) yields calculated using the McMahon fit for wet plasmid irradiation with 1.03 and 1.17 MeV ^{60}Co X-rays. Standard errors calculated based on twelve sample repeats

4.6.3.3. 6-15 MeV Electron Plasmid Irradiation at the Christie

As detailed in section 4.4.3, the plasmid samples were irradiated with a 20x20 cm^2 flat field from an Elekta Synergy treatment unit. The treatment machine was reported to be running at a daily output of 98.7% (the amount of dose actually delivered compared with the amount of dose expected) for 6 MeV electron delivery, 100% for 10 MeV and 99.6% for 15 MeV. Dose values were adjusted accordingly in the analysis.

Comparison between control samples taken to the Christie and samples which remained in the MCRC biology laboratory were deemed unnecessary as transportation time between the two facilities was around five minutes – less than the time taken for the samples to defrost. On completion of the plasmid irradiations, samples were returned to the MCRC biology laboratory.

The resulting SSB and DSB yields calculated following AGE analysis on the irradiated samples are presented in Table 4.18 and Fig. 4.27. Standard error was calculated for each energy based on three AGE repeats.

Energy (MeV)	LET (keV/µm)	µ (Mbp^{-1} Gy^{-1})	φ (Mbp^{-1} Gy^{-1})
6	0.1911	14.84 ± 0.58	0.32 ± 0.01
10	0.1968	18.51 ± 1.25	0.31 ± 0.01
15	0.2014	15.03 ± 0.21	0.30 ± 0.01

Table 4.18. SSB (µ) and DSB (φ) yields calculated using the McMahon fit for wet plasmid irradiation with 6-15 MeV electrons. Standard errors calculated based on three repeats

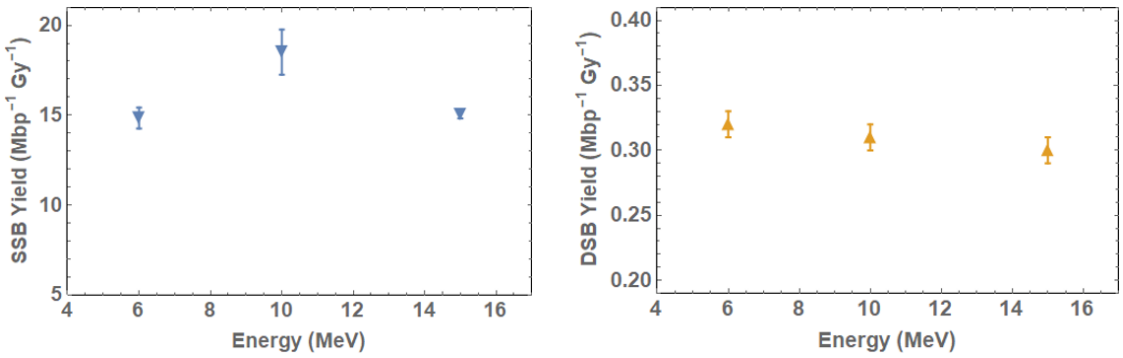

Figure 4.27 – (Left) Single-strand break yields and (right) double-strand break yields for 6-15 MeV electron beam irradiation of wet pBR322 plasmid DNA based on McMahon data fitting. Standard error calculated based on three sample repeats

4.6.3.4. Calculation of Low and High Energy Electron RBE

Following the analysis of X-ray and electron irradiation of plasmid DNA, the DSB yield was used as the biological endpoint for the calculation of electron RBE, with ^{60}Co X-ray DSB yield used as the reference point for both dry and wet plasmid irradiations.

RBE was calculated using the following equation[197]:

$$RBE_{e^-} = \frac{\phi_{e^-}}{\phi_{^{60}Co}} \tag{4.13}$$

where Y_{e^-} is the DSB yield for plasmids irradiated with electrons and $Y_{^{60}Co}$ is the DSB yield for plasmids irradiated with ^{60}Co X-rays. The results of RBE calculation for 6-15 MeV and 100-200 MeV electrons are presented in Table 4.19 and Fig. 4.28. The errors stated in the RBE values were calculated through

error propagation, with errors based on the specified number of sample repeats – 5-6 for the 100-200 MeV samples and 6 for the 6-15 MeV samples.

Low energy electron RBE, defined here as 6-15 MeV, was found to be equal to or close to one. RBE is observed to decrease slightly with increasing energy, though it is noted that all values are within error. VHEE RBE is also close to one in the case of dry plasmid DSB yield, while increasing slightly to 1.09-1.19 for the wet plasmid case.

Energy (MeV)	RBE (Dry Environment)	RBE (Wet Environment)
6	-	1.00 ± 0.07
10	-	0.97 ± 0.07
15	-	0.94 ± 0.06
100	1.02 ± 0.10	1.09 ± 0.09
150	1.01± 0.05	1.09 ± 0.12
200	1.04 ± 0.12	1.19 ± 0.10

Table 4.19. RBE values calculated based on DSB yield following plasmid irradiation experiments at 6-15 MeV (Christie) and 100-200 MeV (CLEAR), with ^{60}Co X-ray irradiation used as a reference. RBE error calculated through error propagation based on a specified number of sample repeats for each radiotherapy modality

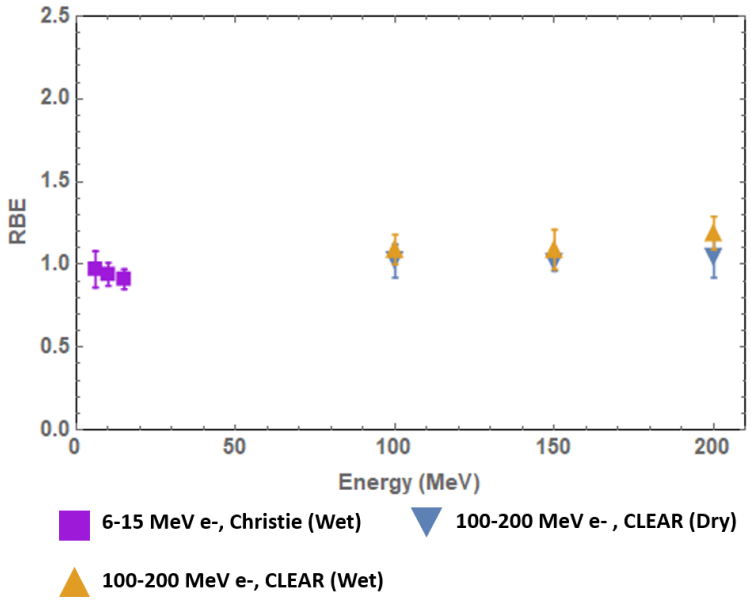

Figure 4.28 - RBE values calculated following 6-15 MeV plasmid irradiation experiments at the Christie NHS Foundation Trust and 100-200 MeV experiments at the CLEAR user facility

RBE values calculated for 6-15 MeV and 100-200 MeV electrons were then compared to RBE values for other radiotherapy modalities, specifically 20-50 MV X-rays, 10-30 MeV protons and 10-50 MeV electrons[157,198–200]. While DSB yield was the endpoint in the case of protons, V79 and CHO cell survival fraction was used as the endpoint in the electron and X-ray cases. The results of this comparison are shown in Table 4.20 and Fig. 4.29.

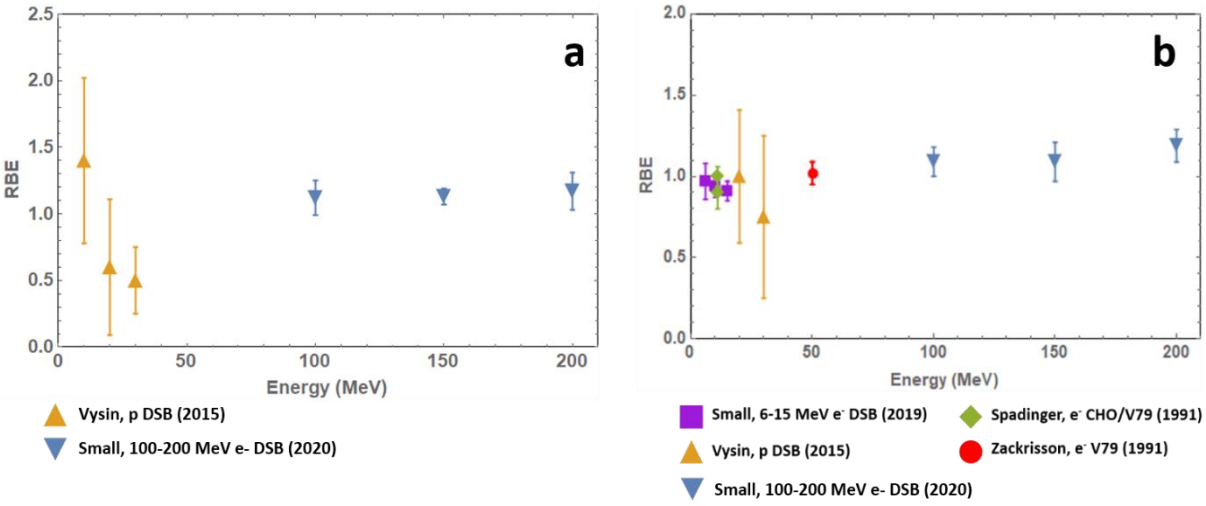

Figure 4.29 - RBE values for a) VHEE and protons with dry plasmid DSB yield as the biological endpoint and b) VHEE, low-energy electrons and protons with wet plasmid DSB yield (Small, Vysin, CLEAR) or cell survival fraction of 0.01 (Spadinger, Zackrisson). Experimental data taken from references 158 and 199201

Particle	Energy (MeV)	RBE	Biological Endpoint
e- (Small)	100	1.12 ± 0.13 1.09 ± 0.09	Dry plasmid DSB yield Wet plasmid DSB yield
	150	1.13± 0.06 1.09 ± 0.12	Dry plasmid DSB yield Wet plasmid DSB yield
	200	1.17 ± 0.14 1.19 ± 0.10	Dry plasmid DSB yield Wet plasmid DSB yield
e- (Small)	6	0.97 ± 0.11	Wet plasmid DSB yield
	10	0.94 ± 0.07	Wet plasmid DSB yield
	15	0.91 ± 0.06	Wet plasmid DSB yield
e- (Herskind)	10	0.94 ± 0.02 0.98 ± 0.01	V79 survival fraction = 0.0003 (rel. to 6 MV X-rays) MCF7 survival fraction = 0.0003 (rel. to 6 MV X-rays)
e- (Spadinger)	11	1.1 ± 0.08 1.0 ± 0.04 1.0 ± 0.06 0.9 ± 0.1	V79 survival fraction of 0.1 (0-10 Gy) CHO survival fraction of 0.1 (0-10 Gy) V79 survival fraction of 0.1 (0-3 Gy) CHO survival fraction of 0.1 (0-3 Gy)
e- (Zackrisson)	50	1.03 ± 0.08 1.02 ± 0.07	V79 survival fraction of 0.1 (rel. to 4 MV X-rays) V79 survival fraction of 0.01 (rel. to 4 MV X-rays)
p (Vysin)	10	1.4 ± 0.62	Dry plasmid DSB yield
	20	1.00 ± 0.41 0.6 ± 0.51	Wet plasmid DSB yield Dry plasmid DSB yield
	30	0.75 ± 0.5 0.5 ± 0.25	Wet plasmid DSB yield Dry plasmid DSB yield
X-rays (Zackrisson)	20	0.99 ± 0.07 1.00 ± 0.05	V79 survival fraction of 0.1 (rel. to 4 MV X-rays) V79 survival fraction of 0.01 (rel. to 4 MV X-rays)
	50	1.14 ± 0.07 1.12 ± 0.05	V79 survival fraction of 0.1 (rel. to 4 MV X-rays) V79 survival fraction of 0.01 (rel. to 4 MV X-rays)

Table 4.20. RBE for various particle modalities with particle, energy and biological endpoint specified. Standard error of the mean for Small data calculated based on gel repeats. RBE data taken or calculated from references 156 and 197-199. All RBE calculations relative to ^{60}Co X-ray data unless otherwise specified

4.7. Discussion and Conclusion

The aim of this chapter was to investigate the radiobiological effects of electrons on biological structures through the irradiation of pBR322 plasmid DNA and the measurement of resulting single- and double-strand breaks. The experimental setup was based on earlier studies by Vysin, Leloup and Souici[157,168,169], who investigated the DNA damage yield caused by proton irradiation. Plasmid DNA was irradiated in both wet and dry environments over a range of energies to determine the variation in damage yield with energy and LET. SSB and DSB yields in different environments were then compared to determine the contributions of direct and indirect radiation effects to total DNA damage.

The DSB yields from these experiments were then used as the biological endpoint for the calculation of Relative Biological Effectiveness (RBE), allowing the effectiveness of VHEE as a potential clinical treatment to be compared with that of traditional radiotherapy modalities including X-rays, protons and low-energy electrons.

Plasmid irradiation experiments were performed at the following facilities:

- Dalton Cumbrian Facility, Whitehaven – A ^{60}Co source was used to deliver 1.17 and 1.33 MeV X-rays. ^{60}Co X-rays were used as the reference radiation for RBE calculations.
- Christie NHS Foundation Trust, Manchester – an Elekta Synergy treatment machine was used to deliver electrons at current clinical energies (6-15 MeV)
- CLEAR user facility, CERN, Geneva – CLEAR, an S-band linear accelerator, was used to deliver electron beams at 100-200 MeV, energies within the anticipated clinical range for VHEE treatment

Plasmid irradiation experiments in dry and wet environments were carried out in Feb 2019 at the Dalton Cumbrian Facility using a ^{60}Co source to irradiate plasmids with 1.17 and 1.33 MeV X-rays. The DSB yields obtained following both wet and dry plasmid irradiation were used as the reference point for calculating electron RBE.

Wet plasmid irradiations only were carried out at the Christie NHS Foundation Trust as a hospital treatment machine was used for irradiation. Such machines are not designed to deliver the high doses required for significant dry DNA damage and we could not risk damaging a vital treatment machine. Irradiations were carried out over this energy range to provide a relevant clinical comparison to later VHEE irradiations at CLEAR, both for DNA damage yield and RBE. Little statistically significant variation was observed in DSB yield over 6-15 MeV, likely due to there being correspondingly little variation in electron LET over this energy range.

Plasmid irradiation experiments were performed at the CLEAR user facility in July 2019 to determine the DNA damage yield caused by irradiation with electrons within the clinical VHEE range of 100-250 MeV. Plasmid samples were irradiated with electron beams of energy 100-200 MeV at a conventional dose rate (~0.5 Gy/s), allowing the effect of increasing energy and, correspondingly, LET on damage yield to be determined. Plasmids were also irradiated in wet and dry environments, as for ^{60}Co X-ray irradiations, to determine the contribution of direct and indirect radiation effects to the total DNA damage.

In both dry and wet plasmid irradiation cases, the DSB yield was found to exhibit no statistically significant variation with energy. As with the low energy electron irradiation, this can be explained by the relatively low variation in LET over this energy range, with NIST data[201] giving LET values of 0.2202, 0.2238 and 0.2263 keV/μm) for 100, 150 and 200 MeV electrons respectively. For dry plasmids, SSB results exhibited significant variation with energy. These results are likely to be unreliable, however, due to the measured adverse effect of transportation on the proportion of open-circular plasmid – temperature fluctuation resulted in the significant relaxing of the supercoiled structure, causing SSBs to form on the DNA structure. As a result, a firm conclusion on the variation of SSB yield with energy for dry plasmids could not be made due to the contribution of SSBs from external factors. In the case of wet plasmid irradiation, unaffected by transportation, SSB yield was observed to increase linearly with energy.

The effect of dose rate on DNA damage following VHEE irradiation was also investigated due to the potential suitability of VHEE as a modality for FLASH

radiotherapy. The aim of this study was to determine if varying the dose rate of VHEE radiation had any effect on SSB and DSB yields and, consequentially, if a FLASH effect could be observed at the nanoscale.

Comparison of DSB yields indicated that there was no statistically significant difference in DSB yield over 100-200 MeV. Little difference is observed between conventional and ultra-high dose rate SSB yields for 150 and 200 MeV. These results indicate that a FLASH effect, in the form of increased DNA damage, is not observed for electrons in the VHEE range within the constraints of this experiment. This agrees with the original hypothesis – that, due to the experimental conditions for plasmid irradiation lacking the key features understood to result in a FLASH effect, a significant difference in damage yield following irradiation at Conv and ultra-high dose rates was not expected.

This conclusion is similar to those drawn by other ultra-high dose rate radiobiological studies, though this is understood to be the first study of its kind involving ultra-high dose rate irradiation of plasmid DNA with VHEE – other ultra-high dose rate irradiation studies have typically involved cellular irradiation[202–208].

It is important to note, however, that there is limited experimental data on the effects of dose rate variation on plasmid DNA damage. To better understand the FLASH mechanism, further experimentation would be required using an environment more closely matching cellular conditions. Cellular irradiation would also be a key extension to this work. There may, for example be a FLASH effect present during damage repair – this is not possible to measure in plasmid irradiation experiments – or due to the environmental differences mentioned between a plasmid irradiation experiment and the conditions within a cell. As VHEE is an increasingly popular potential modality for FLASH therapy, a fundamental understanding of nanoscale radiobiology and the FLASH mechanism is crucial[123].

The DSB yields obtained from the 6-15 MeV and 100-200 MeV electron plasmid irradiation experiments were then used as the biological endpoint to calculate values of electron RBE, with the DSB yield from ^{60}Co X-ray plasmid irradiation used as the reference. RBE values for 6-15 MeV electrons, calculated using wet plasmid DSB yield, were found to be close to 1 (0.94 – 1), as expected for low-

LET radiation, supporting the clinical use of 1 for low-energy electron RBE. RBE was calculated separately for both dry and wet plasmid DSB yields. Dry plasmid electron RBE was also determined to be close to 1, with values of 1.12 ± 0.13, 1.13 ± 0.06 and 1.17 ± 0.14 for 100, 150 and 200 MeV respectively. Wet plasmid electron RBE was calculated as slightly higher, with values of 1.09 ± 0.09, 1.09 ± 0.12 and 1.19 ± 0.10 for 100, 150 and 200 MeV respectively. In the dry case, little statistically significant variation in RBE is observed with energy variation. Wet plasmid RBE was found to be slightly higher than dry RBE, with values varying between 1.1-1.2. On comparison of RBE of low and high energy electrons, the results indicate that RBE may increase with electron energy.

To confirm this hypothesis, irradiation of plasmids with electrons of intermediate energies would be desirable. A series of plasmid irradiation experiments were planned at the Compact Linear Accelerator for Research and Applications (CLARA) user facility at Daresbury Laboratory for April 2020 over an energy range of 20-40 MeV which would have provided these intermediary results. However, the experiment was postponed due to the Covid-19 pandemic.

The values of low energy electron RBE and VHEE RBE were compared with RBE values for various radiotherapy modalities, which used DSB yield as the endpoint in some cases and cell survival fraction in others. The data presented in Table 4.18 and Fig, 4.26 shows the comparison of these values. In the case of low-energy electron RBE, the low energy Christie data was found to be in good agreement with the values calculated by Herskind[198] and Spadinger[199], in which the biological endpoint was CHO or V79 cell survival fraction. Comparison of the VHEE RBE with the Herskind[198], Spadinger[199] and Zackrisson[200] may also indicate a slight increase in RBE over the energy range 6-200 MeV. Vysin[157] proton RBE was calculated based on the DSB yields in the study, though are not considered particularly reliable due to the large errors associated with the DSB yield and consequently the RBE.

Overall, the first calculations for VHEE RBE were made using DSB yield as the biological endpoint. On comparison with electron RBE clinically relevant energies, VHEE RBE was found to be slightly higher, particularly for wet plasmid RBE.

The contribution of direct and indirect radiation effects to overall DNA damage was measured following plasmid irradiation by both VHEE and ^{60}Co X-rays by irradiating the plasmids under dry and wet conditions. Dry plasmid damage is the result of direct radiation effects only, while wet plasmid damage is the result of both direct and indirect effects. In both cases, indirect effects were determined to contribute ~99% of total plasmid damage. Such results appear to contradict the conclusions of Ward *et al.*[209] as well Roots and Okada[210], who suggested that 65% of total radiation effects are the result of indirect radiation effects. However, this work was performed in a cellular environment, rather than the environment outlined for this experiment. Such cellular environments have a significantly higher free radical scavenging capacity than the diluted buffer solution used in this experiment – equivalent to a concentration of 200 mM Tris compared with the diluted 1mM Tris solution used for the aqueous plasmid samples. In the dilute solution, fewer free radicals are destroyed following irradiation, meaning more are able interact with and damage the plasmid DNA. This results in the significantly higher contribution of indirect damage in these experiments compared with those of Ward.

Comparison was made between these results and those of Vysin[157] and Leloup[168] following ^{60}Co and proton irradiation of pBR322 plasmid under dry and wet conditions, and results were found to be consistent.

In terms of limitations within the experiments, the setup resulted in reliable results for wet plasmid irradiation, though some unreliability was observed in the SSB yields for dry plasmid irradiation. The effect of transportation and resulting temperature fluctuation on the plasmid samples was significant, resulting in high proportions of open-circular plasmid and so numbers of SSBs before irradiation. It is concluded that this issue can be mitigated by transporting the plasmid in the buffer solution in which it is shipped from New England BioLabs. This buffer solution prevents plasmid relaxation so, even if the plasmid is held at room temperature for a prolonged period of time (as was the case for the CLEAR dry samples), the supercoiled structure will remain stable. This will mean that dry plasmid samples must, in future, be prepared on the irradiation site rather than at the Manchester Cancer Research Centre.

On analysis of the low energy electron experiment at the Christie, the geometry of the Eppendorf tubes was identified as a potential source of dose uncertainty,

as the reference tables used for the dose correction factor assume dose delivery to a flat surface geometry. As a similar experimental setup was used for CLEAR experiments and measured dose was found to be correct to within 5%, a roughly similar error would be expected for the Christie dose values.

One solution to address this uncertainty in future experiments could be to include a control sample containing a dosimeter – this could be as simple as a small piece of Gafchromic film inside an Eppendorf tube filled with water. While the clinical dose values are considered to be highly accurate and consistent due to ongoing, thorough quality assurance, introduction of this simple dosimeter would reduce any dose uncertainty within the unconventional irradiation setup.

Following the successful calculation of VHEE RBE based on DSB yield, and the indication that VHEE is similar in biological effectiveness to ^{60}Co X-rays at least in terms of physical DNA damage, the next step towards clinical implementation of VHEE is to calculate VHEE based on different, more complex biological endpoints. Based on the comparative RBE study in this chapter, the next logical endpoint will be cell survival fraction to determine if the biological effect of VHEE will be similar to that of ^{60}Co X-rays and other traditional radiotherapy modalities. For such a study, cells would receive a range of doses from electron or ^{60}Co X-ray irradiation and the number of surviving cells determined through a clonogenic assay[211]. From this, a cell survival curve could be plotted over the dose range for the specified radiotherapy modality. The dose resulting in a specified survival fraction (typically 0.1 or 0.01) would then be recorded and RBE calculated based on the dose required for each modality to achieve the specified survival fraction.

Further plasmid irradiation studies are also possible. The contribution of indirect damage for VHEE was measured as 99% - significantly higher than that measured by Ward following cellular irradiation. To replicate the scavenging capacity within the cellular environment, plasmid samples can be irradiated in buffer solution with a high scavenging capacity. Similar experiments have been performed by Leloup[168] using protons as the radiation modality, in which the concentration of scavenging solutions such as glycerol is varied.

In conclusion, a series of successful and reliable plasmid irradiation experiments were carried out, achieving the primary aims of determining SSB and DSB yield following irradiation with electrons over a range of energies and subsequently calculating RBE values. Plasmids were irradiated at clinical energies at the Christie and energies in the VHEE range at the CLEAR user facility to investigate variation in DNA damage yield and RBE for the two modalities. Low-energy electron irradiations indicated little variation over the energy range 6-15 MeV and were found to have an RBE close to one. This is in keeping with the current clinical assumption that electrons have an RBE of one. RBE results were also shown to be in good agreement with other low energy electron RBE studies using cell survival, rather than DSB yield, as an endpoint. VHEE irradiations also showed little variation in DSB yield with energy and dose rate – in agreement with the original hypothesis due to the experimental conditions. VHEE RBE_{DSB} was shown to be slightly higher than 1, suggesting on comparison with values for other modalities that electron RBE may increase with energy.

Future VHEE radiobiology studies will look at more realistic dose delivery setups as well as calculating RBE based on more complex biological endpoints – in particular cell survival fraction. We have successfully shown that through DSB yield RBE calculations that the physical damage caused to DNA by VHEE is similar to that caused by ^{60}Co X-rays. This provides confidence that the complex biological effects such as cell death are also likely to be similar – a key step on the way to the clinical implementation of VHEE radiotherapy.

Chapter 5 – An Optimisation Study of Plasmid Irradiation Modelling in GEANT4-DNA

5.1. Introduction

So far, the importance of the RBE has been highlighted in Chapters 1 and 4 with regard to optimising radiotherapy treatments using different modalities, with plasmid irradiation experiments presented in Chapter 4 indicating that VHEE RBE_{DSB} is consistent with that of established modalities.

However, the results also highlight the sensitivity of experimental RBE calculation, with unavoidable experimental error resulting in uncertainties in the RBE values obtained. Similar issues have been observed for other radiotherapy modalities, particularly protons, with significant uncertainties measured as well as variation between studies[157,212]. To improve the understanding of experimental data and to be able to make predictions of radiation effects without the need for experiments, a number of models have been developed.

Radiobiological models, used to determine or predict a particular biological effect following exposure to ionising radiation, can vary in their complexity and in the mechanisms used, whether physical, chemical or biological[213]. The key outcome for such models is to be predictive, or to infer results between experimental data points and to understand the phenomena behind the biological effect. If the model differs significantly from the experimental results, this suggests that a particular mechanism has been modelled incorrectly or may have been left out of the model entirely. However, the level of complexity required for a model capable of accurately predicting experimental results through modelling of physical, chemical and biological mechanisms is very high, resulting in the need for simplification of the mechanisms.

This chapter presents the development and optimisation of a nanodosimetric model for the simulation of plasmid irradiation with VHEE beams, based on an existing model for protons created by Henthorn *et al*[212]. The model, developed in

GEANT4-DNA (a module of the Monte Carlo particle tracking code GEANT4[42]), simulates the interaction of particles with plasmid DNA and scored the damage. This allows the SSB and DSB yields to be determined and compared with yields obtained in the experiments detailed in Chapter 4. Optimisation of various model parameters was performed, with the motivation being reasonable agreement between the experimental and computational DNA damage yields.

This chapter is structured in the following manner. Section 5.2 will provide the background on radiobiological models, including a history of different models, the shift from phenomenological to nanodosimetric models and a literature review of recent nanodosimetric models for DNA damage.

The methodology and simulation setup of dry and wet plasmid irradiation will be covered in Section 5.3, with an overview of GEANT4-DNA, a description of the plasmid irradiation code and the adaptations required for use with high-energy electrons. Section 5.4 will present results of a parameter variation study and dry and wet plasmid irradiations, with comparisons between the experimentally- and computationally-obtained SSB and DSB yields. The chapter will conclude with a discussion of the results and of the issues which arose during the study. Finally, future extensions for a VHEE radiobiological model will be outlined.

5.2. Background

5.2.1. Phenomenological Models

Since clinicians began treating cancer with radiotherapy at the end of the 19th century, modelling has been a key tool in treatment planning – to optimise plans and to calculate doses delivered to patients[214]. Biological modelling is also widely used in radiotherapy to improve our understanding of how ionising radiation affects biological structures from the DNA level to the patient level. Translation across scales from DNA damage to *in vivo* cellular response to patient response has proven extremely difficult, with research into the development of multi-scale models increasing in recent years. This understanding can be used to further optimise radiotherapy treatment and to increase the therapeutic benefits to the patient.

Many of these radiobiological models are phenomenological in nature, defined as a scientific model that describes the empirical relationship between phenomena[215]. Such models are not derived directly from theoretical principles but may be consistent with the theory. Early radiobiological models are prime examples, with single-hit, single-target and single-hit, multi-target models resulting from observing the response curves following early irradiation studies of simple organisms[34,216].

Expansion of these early models resulted in the development of the LQ model by Chadwick and Leenhouts[10], which based cell survival following irradiation on DSB dependence:

$$S = \exp[-\alpha D - \beta D^2] \tag{5.1}$$

where D is the radiation dose and α and ß are fitted parameters based on the DSB induction mechanisms, with each tissue type having specific values. For a detailed overview of the LQ model, please refer to Chapter 1, section 5.

While the LQ model has proven to be a key clinical tool in radiobiology in the last 50 years, questions have been raised regarding its applicability to different radiotherapy techniques, and whether it can be considered a truly mechanistic model[40]. To successfully measure RBE, α and ß parameters must be determined for each cell type and each radiation type. Difficulties in the experimental measurement of these parameter values (or, more commonly, the α/ß ratio) have been faced, with significant inter-study variation between values, with models predicting tumour response to radiation highlighted as one reason for discrepancies[39,217,218].

Further discrepancies have been observed in between experimental data and model predictions of cell survival at low and high doses[41] – a particular issue for hypo-fractionated treatment, in which a patient receives a smaller number of larger dose fractions. This further highlights the potentially limited scope of the LQ model.

Overall, the LQ model has proven a successful cell survival model and extremely well-established for radiosensitivity studies in the clinic. It is, however, increasingly being viewed as a fit to cell survival data, rather than a mechanistic predictive model. Alternative phenomenological models have been put forward to describe more fully the cell response to radiation, including the

Repair-Misrepair (RMR) model[219] and the Lethal-Potentially Lethal (LPL) model[220].

The RMR model takes into account the cellular repair mechanisms activated following detection of radiation-induced lesions. The initial yield of these lesions is assumed to be proportional to dose:

$$U_0 = \delta D \tag{5.2}$$

The cell will then try to repair these lesions, with the number of lesions varying according to:

$$\frac{dU}{dt} = -\lambda U(t) - \kappa(t) \tag{5.3}$$

where λ is the linear self-repair coefficient (the successful repair pathway) and κ is the quadratic repair pathway coefficient (the misrepair pathway, where pairs of lesions interact). Eq. 5.3 can be integrated to give the yield for unrepaired lesions:

$$U(t) = \frac{U\, e^{-\lambda t}}{\left(1 + \frac{U_0(1 - e^{-\lambda t})}{\epsilon}\right)} \tag{5.4}$$

where $1 - e^{-\lambda t}$ is a time saturation term and ε is the repair ratio, λ/κ. Two repair states are then defined: $R_L(t)$ is the number of self-repaired lesions and $R_Q(t)$ is the number of quadratic misrepaired lesions, representing non-lethal and lethal repairs respectively:

$$R_L(t) = \int_0^t \lambda U \, dt \tag{5.5 a}$$

$$R_Q = \int_0^t \kappa U^2 \, dt \tag{5.5 b}$$

Assuming that no further lesions arise during the repair process:

$$U_0 = U(t) + R_L(t) + R_Q(t) \tag{5.6}$$

It is assumed that all lesions will eventually be repaired, so as $t \to \infty$:

$$R_Q(t \to \infty) = U_0 - R_Q(t) \tag{5.7}$$

By using Poisson statistics, an equation for the cell survival can be obtained:

$$S = e^{-R_Q(t\to\infty)} = e^{-U_0}\left[1 + \frac{U_0}{\epsilon}\right]^{\epsilon} \tag{5.8}$$

Curtis expanded on this work[220], proposing that lesions can be categorised into two groups – 'unrepairable and therefore lethal' and 'potentially lethal, for which the repair process is activated.' These potentially lethal lesions are either correctly repaired at a rate constant ε_{PL} or interact with each other, producing a lethal (irreparable) lesion at a rate constant ε_{2PL}. The cell survival equation for this lethal potentially-lethal (LPL) model, based on a Poisson assumption for the lethal lesion distribution per cell, is as follows:

$$S = e^{-N_{Tot}} \times \left[1 + \frac{N_{PL}}{\epsilon(1 - \exp[-\epsilon_{PL} t_r])}\right] \tag{5.9}$$

where N_{Tot} is the sum of lethal and potentially lethal lesions, ε_{PL} is the constant per unit of time repair rate, ε is the ratio of correctly repaired and incorrectly repaired lesions and t_r is the amount of time available for repair following radiation exposure.

While these models have had some success in incorporating a more mechanistic understanding of cell survival by including cell repair, there are still limitations. In the years following the development of these models, advances in experimental radiobiology have resulted in discrepancies in the assumptions made. A key example is in the work by Jeggo and Lobrich[221], indicating that misrepaired lesions are involved in genomic instability or cell transformation rather than cell death.

Phenomenological models, while they have been successfully used widely in clinical settings, are increasingly viewed as fitting methods rather than predictive models for cell survival. This is due to assumptions within models being invalidated by advances in experimental radiobiology, discrepancies in low- or high-dose treatments (particularly hypofractionation) and a lack of experimental repeatability in determining key parameters. Modelling of the biological effects of radiation is increasingly moving towards a more mechanistic approach in radiobiological modelling research (though not yet in clinical practice due to difficulties in experimental validation), an overview of which will be given in the following section.

5.2.2. Mechanistic Models

The limitations of the phenomenological models detailed in the previous section and advances in the understanding of mechanisms behind radiations response have contributed to the growing interest in mechanistic models[213]. Similarly to phenomenological models, mechanisms such as DNA damage and subsequent lesion repair can be used to determine cell survival and RBE following irradiation by a particular modality. Such models typically determine DNA damage through Monte Carlo computational simulations, rather than by experimental methods. Two examples of mechanistic models in radiobiology are the Local Effect Model (LEM)[222] and the Microdosimetric Kinetic Model (MKM)[223]. The aim of both models is to derive the biological effects of ionising radiation through cellular or tissue response.

The LEM model, used to model the effect of ions on DNA and cell survival, uses the concept of local dose, defined as 'the expectation value of the energy deposition at any position in the radiation field for a given pattern of particle trajectories.'[222] The assumption that the same local dose will result in the same local effects is made, regardless of the radiation modality. An amorphous track structure, in which radial dose is scored from individual particles to produce a 3D dose map, is used to derive the local dose as a function of radial distance to the particle's trajectory[224]. The sensitive target is considered to be the cell nucleus, with the key output being the mean number of lethal lesions per cell:

$$\overline{N_{l,ion}} = \int \frac{\ln S_x\big(d(x,y,z)\big)}{V_{nucleus}}\, dV_{nucleus} \tag{5.10}$$

where S_x is the effect after X-ray radiation as a function of dose D, d(x,y,z) is the local dose distribution within a cell nucleus of volume V. Assuming a Poisson distribution of lethal events, cell survival is calculated using:

$$S_{ion} = e^{-\overline{N_{l,ion}}} \tag{5.11}$$

The RBE of the ion being investigated can then be determined by calculating the ratio of X-ray to ion doses resulting in the same survival:

$$RBE_{ion} = \frac{D_\gamma}{D_{ion}} \tag{5.12}$$

The first version of this model (LEM-I[222]) derives local dose directly from an X-ray dose response curve, represented by α and ß values from specific experimental or clinical data. For doses > 10 Gy the LQ model breaks down. This is referred to as a threshold dose in the LEM and, above this threshold dose, a correction was applied to account for a more linear cell survival curve. This model is currently employed in carbon ion treatment planning within Europe[225].

The LEM model has been extended over the years to include more mechanistic effects, resulting in improved agreement with experimental data. The induction of DSBs resulting from two SSBs occurring on opposite strands within 25 base pairs was included in LEM-II[226] along with a more detailed description of radical diffusion. LEM-III[227] implemented an improved particle track-structure description.

The most recent extension, LEM-IV[228], introduces an intermediate step based on the assumption that it is the microscopic spatial distribution of DSBs which ultimately determines a cell's fate. A new measure was devised, based on chromatin structure (large loops of DNA with length ~ 2 Mbp) as the sensitive target. Two types of damage are defined – induction of a single, isolated DSB (iDSB) within a loop or a clustered DSB (cDSB) consisting of two or more DSBs within a loop[229]. Using this, a metric defined as the cluster index (C) can be determined:

$$C = \frac{N_{cDSB}}{N_{iDSB} + N_{cDSB}} \tag{5.13}$$

where N_{iDSB} and N_{cDSB} are the number of chromatin structures with isolated and clustered DSBs respectively. If multiple DSBs occur within the same loop, there is a possibility of two DSBs misrepairing, resulting in the loss of a few Mbps of DNA. RBE can then be calculated following determination of the X-ray dose required to achieve the same clustering index.

The MKM is used in clinical carbon ion therapy within Japan[225] and, similarly to the LEM, cell survival is determined through the summing of the local effect of a radiation dose within a cell nucleus. However, the MKM differs in that it considers the energy deposition in sub-volumes of the nucleus (known as domains) on the microscale, while the LEM considers nanoscale sub-volumes

(the chromatin structures). MKM cell survival is predicted using the specific energy, defined as the ratio of energy impacted and mass of a domain. The model accounts for the overkill effect in high specific energy regions. Cell survival fraction is predicted using the following[223]:

$$-\ln S = (\alpha_0 + \beta z_{1D}^{*})D + \beta D^2 \quad (5.14)$$

where α_0 is the initial slope of the cell survival curve, ß is the quadratic parameter of the LQ for the tissue in question, D is the dose and z_{1D}^{*} is the corrected dose-mean specific energy of the domain delivered in a single energy deposition event.

While both models have proven to agree reasonably well with experimental cell survival data, input parameters are frequently determined from experimental data, particularly for the MKM. Uncertainties in experiments lead to uncertainties in the input parameters and, in turn, in the model predictions[230]. This, coupled with increasing evidence that DNA (rather than the cell nucleus) is the critical target for ionising radiation, has resulted in the shifting in focus for radiobiological models predicting cell fate. It is also noted that, while these models have been successful in modelling effects of ion radiotherapy, there is currently no data available on their use with electrons.

5.2.3. Track Structure Codes

Track structure is defined as the way in which energy is deposited by charged particles as they travel through a medium[231]. The rate of energy depositions per unit length, or LET, of a particle depends on its velocity, mass and charge. Track structure varies between particles even if they have the same LET due to differences in patterns of energy distribution[232]. Studies of radiation track structures have allowed estimates to be made of various parameters in radiotherapy and radiation protection.

Monte Carlo track structure (MCTS) codes allow the simulation of particle tracks and their interaction with matter and are used across a range of radiation-related fields, including space radiation, high-energy particle physics and, most relevant to this project, radiation biology[233].

To achieve a realistic mechanistic model of radiation interaction with matter using MCTS codes, the physical and chemical description of track structure

must be simulated as realistically as possible. This requires the knowledge of accurate experimental measurements of particle-matter interaction cross-sections, or the probability of an interaction occurring. These are then used to describe the features of particle structures based on the likelihood of energy deposition and subsequently the induction of DNA damage[234].

The track structure of a particle is produced using this interaction cross-section data by using a random number generator to determine the probability of interaction of a particle. Each interaction represents an interaction between the particle and the medium through which it is travelling. As the particle is stepped through the medium, a pattern of interactions, or track structure, is generated. Many MCTS codes use water as the medium due to its abundance in cells and its key role in free radical production – allowing indirect damage (from interaction between free radicals and the sensitive target) to be included in the model[235].

MCTS codes have advanced significantly in recent decades due to the growing availability of high-powered computing and increasingly sophisticated DNA models. Widely used models include TOPAS-nBio[43], KURBUC[236], GEANT4-DNA[42] (which will be covered in greater detail in section 5.3) and, the most advanced model, PARTRAC[56].

PARTRAC consists of a suite of Monte Carlo simulation codes, capable of calculating track structures for a number of radiation modalities. Different modules within the code model different interactions with and responses to ionising radiation, and PARTRAC is capable of modelling the physical and chemical stages of radiation interaction within a medium along with early biological effects including DNA damage and damage repair[237].

The physical stage of the code involves radiation transport, energy depositions and generations of secondary particles, with PARTRAC capable of simulating photons, electrons, protons and ion tracks in liquid water[238]. The physico-chemical stage occurs within 1 ps and involves the excitation and ionisation of water molecules to produce free radicals, which can go on to cause DNA damage. SSBs are induced following energy deposition in a sugar-phosphate group, with the probability of SSB induction increasing linearly from 0-1 as the energy deposited increases from 5-37.5 eV[56]. DSBs are induced when two SSBs are

induced on opposite strands within a given distance – conventionally set at 10 bp though other values have been tested. In addition, 1% of SSBs are transferred to DSBs following results from studies on other DSB mechanisms[239] and from experiments on low-energy electrons[240] and photons[161]. A clustered DSB is considered to have been induced when two or more DSBs occur.

PARTRAC can then model the response to induced DNA damage with the repair model based on the Non-Homologous End Joining (NHEJ) pathway[241]. This pathway has been described and reviewed by a number of resources[242,243], with the overall result being the DNA damage being correctly repaired, incorrectly repaired or left unrepaired. While DNA damage repair modelling has been found to be consistent with biological experiments, cell survival predictions are still some way off.

Further DNA repair models are available in the codes mentioned earlier, in particular GEANT4-DNA. Similarly to PARTRAC, *in silico* modelling of the NHEJ pathway has been developed and presented by Henthorn and Warmenhoven[45,46]. This model, known as DaMaRiS (DNA Mechanistic Repair Simulator), was developed in GEANT4-DNA based on mechanisms proposed for the NHEJ pathway to predict the proportions of repaired, misrepaired and unrepaired DSBs up to 24 hours after irradiation. DaMaRiS has since been extended by Ingram *et al.*[244] to include the Homologous Recombination (HR) repair pathway. While the NHEJ pathway is more frequently used due to its availability in all phases of the cell cycle, it is more prone to error than the HR pathway. Including both repair pathways provides a more complete model for DNA damage repair. Furthermore, it has been suggested that the HR pathway may be more effective at repairing proton-induced DSBs. The mechanistic models of DNA damage and repair developed by the Manchester group have been used in the calculation of proton RBE, which has subsequently been applied to proton treatment planning with comparable results to phenomenological models in terms of RBE-weighted dose distributions[245].

5.3. Methods

Modelling DNA damage is the first step in the mechanistic modelling of biological effects of ionising radiation. Irradiation of pBR322 plasmid DNA was

carried out (covered in Chapter 4) to experimentally measure DNA damage caused by VHEEs. A detailed model simulating VHEE irradiation of pBR322 plasmid DNA has been built in GEANT4-DNA, with the experimental results from Chapter 4 used to validate this model for the measurement of resulting SSBs and DSBs. This section consists of an overview of GENAT4-DNA, the code built using GEANT4-DNA which simulates VHEE irradiation of pBR322 plasmid and of the experiments performed using this code.

5.3.1. GEANT4-DNA

As detailed in Chapter 3, GEANT4 is an open-source Monte Carlo particle tracking code initially designed to model interactions between particles and matter for high-energy particle physics applications[8]. Work on the GEANT4-DNA collaboration began in 2001, with the aim of extending the existing GEANT4 toolkit to estimate the effects of ionising radiation on biological structures at the molecular and cellular scales[42,235,246,247]. GEANT4 and GEANT4-DNA were used in this study due to the ability to model the track structures of higher energy electrons with energies up to the GeV region. While MCTS codes do exist which are capable of modelling electron track structure, the energies are typically lower than those required for this study – PARTRAC, for example, can model electron track structure from 10 eV – 10 MeV[56].

As DNA ionisation occurs following very low energy depositions (<5 eV), a key challenge for GEANT4-DNA was being able to track particle interactions at the eV scale. The GEANT4-DNA module is part of the Low Energy Electromagnetic Physics group[248], now merged into the Electromagnetic Physics working group[249], which aims to compile, analyse and develop models of cross-sections for very low energy interactions to improve low-energy particle track structure simulation.

GEANT4-DNA is currently able to model the physical interactions of electrons, protons and α particles, describing the cross-sections and final state of the interactions which have occurred. While heavier ions can also be used, only ionisation can be modelled. The processes which can be simulated for each particle are detailed below:

1. **Electrons –** The initial work to lower GEANT4's modelling ability was performed by Chauvie *et al.*[250], allowing simulation of electrons down to

7.4 eV by modelling the excitation and ionisation of electrons. Francis *et al.*[251] extended this by investigating the processes which electrons can undergo below the last excitation state of water (8.22 eV), including vibrational excitation, elastic scattering and electron attachment. Vibrational excitation cross-sections were determined experimentally from 1.7 – 100 eV and extrapolated down to 25 meV. GEANT4-DNA is therefore capable of modelling electron track structure between 25 meV and 1 MeV.

2. **Protons and α –** At energies > 500 keV, a First Born Approximation (FBA)[252] is used to model inelastic processes such as ionisation and excitation. As the FBA breaks down as proton energy approximates the target electrons (within the DNA) orbital speed, ionisation cross-sections are calculated using the Rudd approach[253] and excitation cross-sections calculated using the Miller and Green model[254]. Elastic scattering interactions are modelled using the standard GEANT4 multiple scattering model. Cross-sections for α interactions are calculated using the same models as for protons but including a correcting effective charge term. GEANT4-DNA is capable of modelling proton and α track structures from 100 eV – 100 MeV and 1 keV – 400 MeV respectively.

These physical processes are collected into a pre-built physics constructor within GEANT4-DNA, containing all of the particles, processes and models for GEANT4-DNA applications. The first of these was 'G4EmDNAPhysics,' which also contains processes for photons and positrons[255]. Various options based on this constructor have been developed for more specific applications[256], again thanks to the modular design of GEANT4.

An important extension to GEANT4-DNA was the addition of a model of water radiolysis and transport of the resulting free radicals[235,246]. This allows the simulation of indirect radiation effects – the dominant effect causing DNA damage This water radiolysis model consists of three stages (physical, physico-chemical and chemical) over a timescale of 1 μs.

During the physical stage, from 0-1 fs, all physical interactions between the particle and the medium occur. From 1 fs – 1 ps, the physico-chemical stage occurs, including 'fast' events, such as electronic recombination (resulting in the breaking of chemical bonds), the decay of excited water molecules and proton

transfer between ionised and neutral water molecules. These processes result in the production of the free radical species. During the chemical stage, lasting from 1 ps – 1 µs, these free radicals diffuse through the medium via Brownian diffusion[257] and can interact with each other, the target DNA molecule or the bulk water. A list of possible chemical reactions, along with their rate of reaction, following water radiolysis is given in Table 5.1 below[258].

Chemical Reaction	Reaction Rate (10^7 m^3 mol^{-1} s^{-1})
$H_3O^+ + OH^- \rightarrow 2H_2O$	14.3
$OH + e^-_{aq} \rightarrow OH^-$	2.95
$H + e^-_{aq} + H_2O \rightarrow OH^- + H_2$	2.65
$H_3O^+ + e^-_{aq} \rightarrow H + H_2O$	2.11
$H + OH \rightarrow H_2O$	1.44
$H_2O_2 + e^-_{aq} \rightarrow OH^- + OH$	1.41
$H + H \rightarrow H_2$	1.20
$e^-_{aq} + e^-_{aq} + 2H_2O \rightarrow 2OH^- + H_2$	0.50
$OH + OH \rightarrow H_2O_2$	0.44

Table 5.1 – List of chemical reactions modelled in GEANT4-DNA following water radiolysis with reaction rates[258] – values proposed by PARTRAC[238]

5.3.2. Plasmid Irradiation Code

The aim of the plasmid irradiation simulation is to investigate the modelling of VHEE track structure to score DNA damage, resulting from both direct and indirect radiation effects, in order to validate the MCTS VHEE DNA damage model and increase understanding of VHEE radiobiology with applications to VHEE treatment planning. DSB yields based on the simulations can then be compared to those from the plasmid irradiation experiments carried out in Chapter 4 to determine the optimal parameters within the code for scoring DNA damage. The code used to simulate particle irradiation of pBR322 plasmid DNA was built using GEANT4.10.2 (patch 01) and is part of a larger code developed by Nicholas Henthorn[212] to measure DNA damage and its complexity following proton and photon irradiation. This section details how the code works and the parameters which can be varied when investigating parameter optimisation.

5.3.2.1. DNA Model

The code is capable of building DNA using one of three geometric models, all of which have been used in published work investigating DNA damage through track structure simulation. The first DNA geometry is referred to as 'QuartCyl' and is based on a study by Bernal and Liendo[259] on DNA damage probability using the Monte Carlo code PENELOPE. This geometry consists of a backbone made up of sugar-phosphate groups structured as discrete quarter-cylinder volumes with radius 1.5 nm and the DNA bases structured as half-cylinders with radius 0.5 nm and thickness 0.34 nm.

The second geometry, referred to as 'HalfCyl' was proposed by Charlton, Nikjoo and Humm[260] in their study on SSB and DSB calculation for various radiotherapy modalities. Similarly to the QuartCyl, this geometry consists of sugar-phosphate and base groups, though both are structured as discrete half-cylinders. The base half-cylinder structures have a radius of 0.5 nm and thickness of 0.34 nm, while backbone structures have a radius of 1.5 nm and a thickness of 0.34 nm with a small groove to fit the bases. This model has also been used to validate TOPAS-nBio[261], an extension of the TOPAS code detailed in Chapter 3 developed to model biologically relevant properties up to 1 µs after irradiation.

The third geometry, referred to as 'Spherical,' constructs both DNA backbone and bases as spheres with radii 0.24 nm and 0.208 nm respectively and was used in Henthorn *et al.*'s work on radiation-induced chromatin damage[262]. All three DNA geometries are shown in Fig. 5.1.

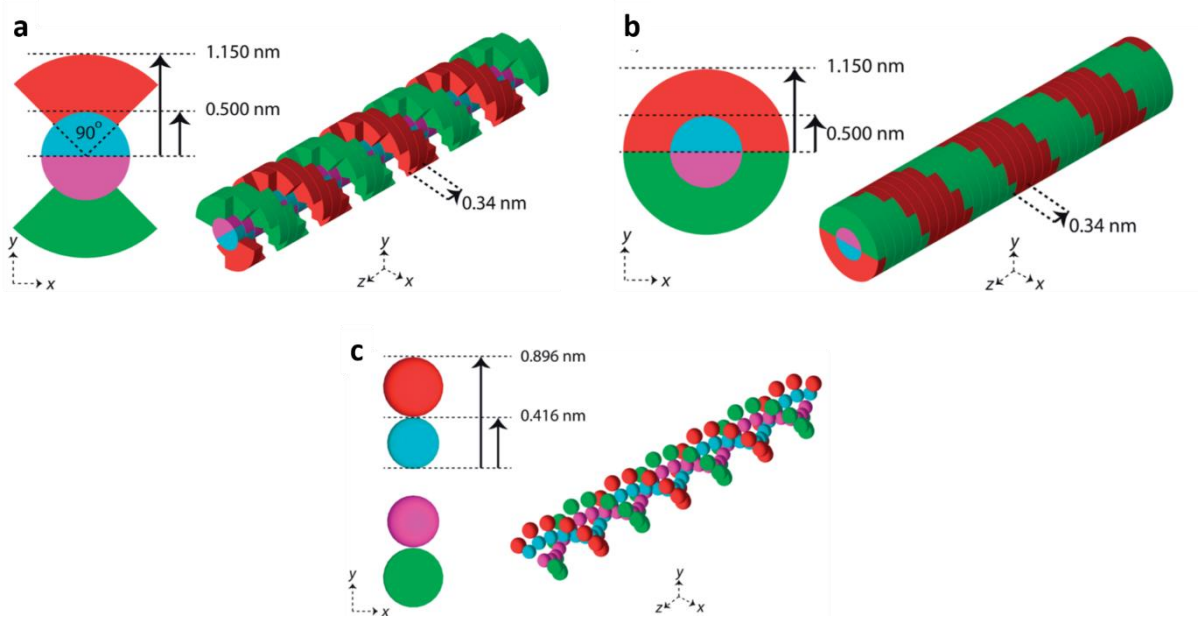

Figure 5.1 - Different geometries for building plasmid DNA in GEANT4-DNA plasmid simulation code, including dimensions - a) QuartCyl, b) HalfCyl, c) Spherical. Figure reproduced from [2]

5.3.2.2. DNA Irradiation

The DNA built using the geometries listed above is a model of the pBR322 plasmid DNA[170] used in the experiments detailed in Chapter 4. The plasmid consists of 4361 base pairs and is initially organised in a closed, perfectly circular loop with radius 236 nm. The plasmid is placed on a slab of glass with length and width 500 nm and thickness 50 nm – this setup is shown in Fig. 5.2 and represents the glass microscope slides on which the plasmid solution is dried in the experiment. The plasmid and microscope slide are placed in a 700 x 700 x 700 nm^3 volume, set as air for dry plasmid samples and water for aqueous samples.

The particle beam is directed perpendicular to the plasmid, travelling through the air volume, the plasmid and then the microscope slide. The dose delivered to the plasmid depends on the fluence of the particle beam, which can be varied by changing the number of particles or the radius of the beam according to the following equation:

$$D = 10^9 \frac{NLe}{\pi \rho r^2} \tag{5.15}$$

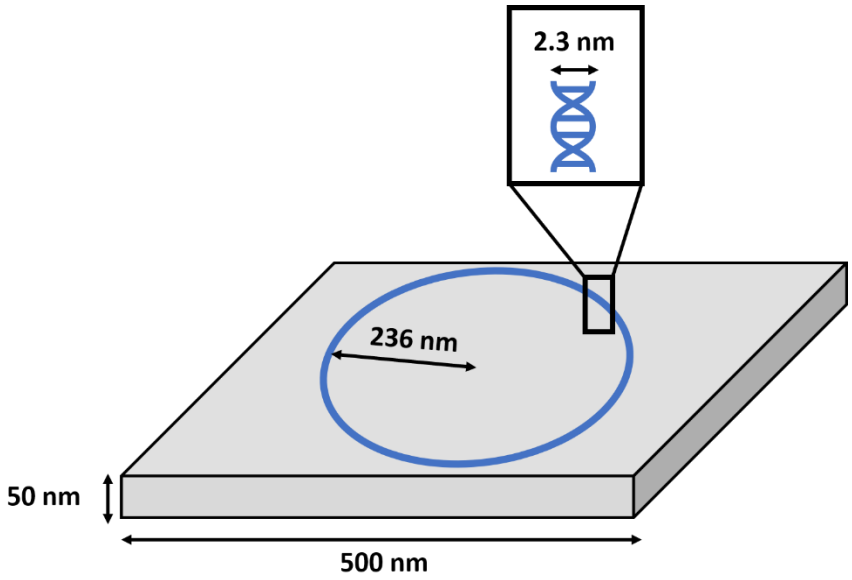

Figure 5.2 - Plasmid irradiation setup in GEANT4-DNA with plasmid placed on a glass microscope slide

where D is the dose in Gy, N is the number of particles, L is the track-averaged LET in keV/µm, r is the beam radius in nm and ρ is the plasmid density, set at 1407 kg/m^3. Simulations were run using the University of Manchester Condor cluster.

5.3.2.3. Scoring DNA Damage

Energy depositions modelled during irradiation are converted into DNA damage using one of three methods. The first was the energy range method, in which it is assumed that the probability of DNA damage occurring is linearly proportional to the energy deposited within a specified range. The probability increases linearly from 0 to 1 over the energy range 5-37.5 eV, based on experimental studies by Prise *et al.*[161] on the critical energies required for DNA damage following low energy electron and photon irradiation.

The second was the energy threshold method, in which a threshold energy value is defined and energy depositions to the DNA volume above this value are considered to have caused a damage. 17.5 eV is a commonly used threshold value following a DNA damage modelling study by Nikjoo *et al.*[263], though threshold values from 8.22-22.5 eV have been used in various studies[264] due to variation in the number of ionisations required to break DNA and because a true value for this threshold has not yet been experimentally validated.

The third method was the ionisation method, in which ionisation events in the DNA volume are scored. If an ionisation event has occurred within a DNA volume, the DNA is considered to have been damaged[49].

On completion of modelling the physical interactions between the ionising radiation and the DNA, the code offers the option of invoking the GEANT4 chemistry processes to model the indirect radiation effects. This allows the production of free radicals to be simulated, with the species and yield recorded, and tracked for up to 1 ns after irradiation begins. The diffusion of the free radicals and their interactions with other molecules is modelled using Brownian motion.

Hydroxyl (OH^-) radicals are assigned as the radicals which cause DNA damage due to their high reaction rate with DNA components. The OH^- radicals are assigned a probability of causing damage to a DNA component within the DNA volume following interaction. The probability of backbone damage in this model is fitted to match the 35:65 ratio of direct to indirect damage as measured by Roots and Okada[210] for ^{60}Co photons. The probabilities of an OH^- radical causing a base or backbone damage are set at 0.8 and 0.5 respectively, based on MCTS DNA damage modelling by Nikjoo *et al.*[234]. For both base and backbone, damage is recorded if the OH^- radical meets the probability requirements, assuming that if an OH^- radical meets the DNA volume, a reaction will occur. If the probability requirements are not met, damage will not be recorded and the radical will be removed from the simulation (reaction without damage).

All backbone damages resulting from the interaction of primary particles and OH^- radicals with the DNA volume are defined as SSBs. If a DNA volume is damaged, it is then analysed by a clustering algorithm which searches through the volume for SSBs which occur on opposite backbone strands within a specified distance. This separation is typically set at 10 bp, though separations of up to 25 bp are found in the literature[56,265,266]. If the SSBs occurs on opposite backbones within this distance, a DSB is scored.

The code has the ability to score DSBs according to their complexity, considering base damages within a DSB which go on to form complex DSBs. Such considerations are important when investigating DNA damage repair after irradiation. As we are only concerned with determining SSB and DSB yield for

comparison with experimental yields, the complexity of induced DSBs were not explored. A more detailed description of the types of DSB which can be induced and scored in this code is given in Henthorn *et al.*'s work[262].

5.3.3. Experiment Setup

This section details the different simulations performed, with the overall aim being to determine model parameters resulting in the closest approximation of DSB yield with the CLEAR experimental data from Chapter 4. Agreement between the model and experiment will give confidence in the model and open doors to extending the work, including investigations into chromatin damage, DSB complexity, DNA damage repair and damage yield within a cell model[212].

VHEE simulations of dry plasmids were performed using the optimal parameters for modelling DNA damage following proton irradiation, as concluded by Henthorn *et al.*[212]. These parameters were determined based on comparison with experimental damage yields using protons and α particles, with DNA geometry and energy deposition method varied. VHEE-induced damage yields were compared with dry plasmid experimental yields to see if these parameters resulted in good agreement for VHEE-induced plasmid damage.

As these parameters did not result in reasonable approximation to experimental data, a parameter variation study was performed for dry plasmid samples to investigate the variation in DSB yield with DNA geometry, energy deposition method and base pair separation, with values for the parameters taken from similar published works.

Different plasmid structures, based on a TOPAS-nBio geometry study[267], were also investigated to determine DSB yield sensitivity with plasmid configuration. As plasmids do not naturally have a perfectly circular configuration, the use of different configurations, incorporating twists and folds within the plasmid, may serve to make the simulations more realistic.

For dry plasmids, it is assumed that all damage is the result of direct radiation effects as free radicals such as OH^- cannot be produced. By invoking the indirect radiation effects within the code and building the experimental setup within a water volume (as opposed to an air volume for dry plasmids), the aim was to simulate the aqueous plasmid irradiation experiment using the optimised

parameters and to compare DSB yields with those from the aqueous plasmid irradiation experiment.

5.4. Results

5.4.1. High Energy Electron Physics Constructor

As mentioned in the previous section, the GEANT4-DNA physics constructor G4EmDNAPhysics is capable of modelling the track structure of electrons with energy up to 1 MeV – insufficient for simulating DNA damage caused by 100-200 MeV electrons. A physics constructor combining both the GEANT4-DNA physics processes and high-energy electron physics processes is required.

For simulation involving >1 MeV electrons, a physics constructor was built based on earlier work by M Sotiropoulis[268], involving the combining of physics lists and processes to simulate the effect of gold nanoparticles as a radiosensitiser. This work combined the Livermore and Penelope physics lists with the main G4EmDNAPhysics constructor[269]. These physics lists use condensed history algorithms to calculate the energy loss of radiation, taking into account the cumulative effect of multiple interactions, rather than calculating energy loss on an event-by-event basis.

The Livermore model was selected for inclusion within this plasmid irradiation code because of the high energy applicability limit of the physics processes within the list – both the G4LivermoreIonisationModel and G4LivermoreBremsstrahlungModel processes (covering low energy electron ionisation and Bremsstrahlung production respectively) are applicable for electrons from 10 eV – 100 GeV[269]. As such a large range is not required for this investigation, the low and high-energy limits are set at 1 MeV and 300 MeV respectively. These processes were combined with those in the default G4EmDNAPhysics constructor to produce a constructor to model the track structure of electrons > 1 MeV while still being able to model the low energy depositions following interaction with the DNA volume. Simulations involving electrons below this 1 MeV limit continued to be modelled using the standard G4EmDNAPhysics constructor – the constructor required could be selected within the 'Options' file in the code.

5.4.2. Initial Simulations

To accurately replicate the track structure of the CLEAR beam, the GEANT4-DNA was modelled using a Gaussian beam with the same fluence. The dose received by experimental samples was calculated using the following:

$$D = 10^9 \frac{NLe}{\pi\rho\sigma_x\sigma_y} \tag{5.16}$$

where the number of particles N is calculated from the charge measured by the Integrated Current Transformer (ICT) and σ_x and σ_y are the beam sigma in the x and y planes, measured in m. σ were calculated based on measurements from the YAG screen placed behind the experimental setup. Following sample irradiation, some scattering of the beam was observed as it travels through the sample and approximately 3 cm of air before reaching the YAG screen. A correction factor was therefore applied to the YAG σ values, calculated from the average discrepancy between YAG and film σ measurements following aqueous sample irradiation. The film σ values were obtained by fitting the optical density across the film to a 2D Gaussian equation as detailed in Chapter 4.

Measurements for σ could not be made from the irradiated film placed behind the dry samples due to saturation of the film following exposure to doses in excess of the film's working range (60 Gy). The discrepancies between the YAG screen and film measurements of σ_x and σ_y for 100 MeV electron beams are detailed in Table 5.7 below.

Dose (Gy)	Film σ_x (mm)	Film σ_y (mm)	YAG σ_x (mm)	YAG σ_y (mm)
5	4.19	4.08	5.42	5.40
10	4.08	4.20	5.38	5.36
20	4.12	3.95	4.88	5.01
30	4.10	3.97	4.87	5.11
40	4.11	3.97	5.15	5.33
50	3.94	4.07	5.11	5.31

Table 5.7 – Measurements for σ_x and σ_y of the CLEAR beam at 100 MeV from the Gafchromic film placed directly behind aqueous samples and the YAG screen placed 3 cm behind the samples

The percentage difference in film and YAG measurements were measured for 100, 150 and 200 MeV, resulting in correction factors to the YAG measurements of 0.814 and 0.847 for σ_x and σ_y respectively.

These values were then used in eq. 5.16 to determine the dose received by the dry plasmid samples. This dose value was then used in the GEANT4-DNA simulations. It is important to note that the number of particles used in the experiment ($> 10^{12}$) would have proven extremely time-consuming to simulate despite the considerable computational power available. Simulations were therefore scaled down – a single plasmid was irradiated by a beam of radius 300 nm. The beam is a flat circular beam, rather than a Gaussian beam as in the experiment. Over such a small radius, however, a flat beam approximation is acceptable.

To ensure that the simulation beam fluence is consistent with the experiment, the experimental dose was used to determine the number of particles required:

$$N = 10^{-9}\frac{\pi D \rho r^2}{eL} \tag{5.17}$$

where r is the beam radius, set at 300 nm and L is the track-averaged LET.

Preliminary simulations were carried out with 100, 150 and 200 MeV electron beams to model the CLEAR dry plasmid experimental setup using the parameters found to most closely approximate proton and α particle experimental data. The parameters varied in this study were the DNA geometry and the method of conversion of energy deposition to DNA damage. This optimal setup used the QuartCyl geometry and the energy range method between 5 and 37.5 eV. Simulations were repeated 5000 times and SSBs and DSBs for each repeat appended to an output file. The average SSB or DSB yield was then determined by dividing the mean of the yield by the product of the dose in kGy and number of Mbp of which the plasmid is made up. This gives the average yield in units of (Mbp^{-1} kGy^{-1}). The standard error is calculated based on the number of repeats. The results for the preliminary simulations are detailed in Fig. 5.3 and Table 5.8 below, including the experimental results reported in Chapter 4 for comparison.

	GEANT4-DNA		Experimental	
Energy (MeV)	SSB (Mbp^{-1} kGy^{-1})	DSB (Mbp^{-1} kGy^{-1})	SSB (Mbp^{-1} kGy^{-1})	DSB (Mbp^{-1} kGy^{-1})
100	57.63 ± 1.52	0.21 ± 0.05	69.81 ± 8.47	3.66 ± 0.43
150	56.23 ± 1.50	0.12 ± 0.03	80.30 ± 3.06	3.71 ± 0.11
200	58.20 ± 1.66	0.13 ± 0.03	50.27 ± 4.19	3.83 ± 0.45

Table 5.8 – DSB yields following plasmid irradiation at 100, 150 and 200 MeV using parameters based on conclusions by Henthorn – plasmid built with QuartCyl geometry and damage scored using energy threshold method at 17.5 eV

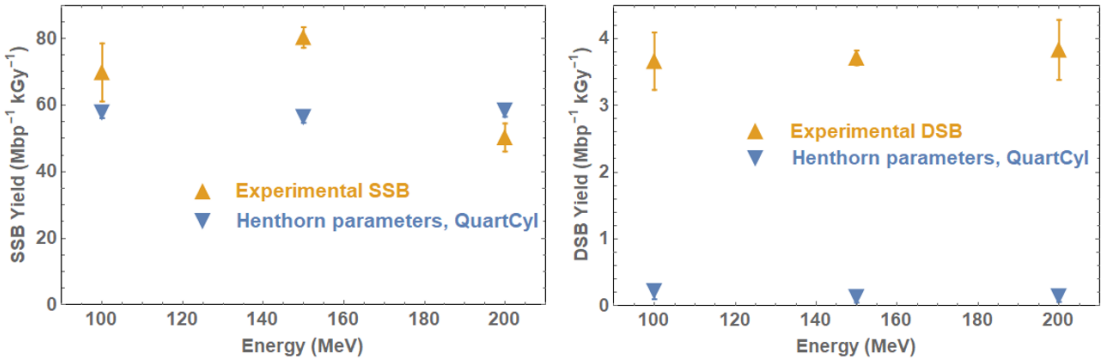

Figure 5.3 – GEANT4-DNA SSB and DSB yields (blue) following plasmid irradiation at 100, 150 and 200 MeV using parameters from Henthorn et al.*'s work with comparison between experimental DSB yields (yellow)*

While the simulated SSB yield data shows reasonable agreement with experimental data, simulated DSB damage is significantly under-estimated. Due to the unreliability of the experimental SSB data, it cannot be reliably concluded that these parameters correspond to good approximation of model SSB yield data to experimental data. From this point on, only DSB yield data will be considered. The following section details a parameter variation study to determine the parameters which are required to provide a more reasonable agreement between simulation and experimental DSB yield data.

5.4.3. Parameter Variation

To investigate the dependency of DSB yield on various parameters and to subsequently optimise those parameters to obtain reasonable approximation with experimental DSB yield, parameters within the model were varied. To

allow for consistent comparison, the parameters detailed by Henthorn *et al.*[262] were considered the 'default.' For each test, just one parameter was varied and the others left unchanged. The parameters varied, in order of testing, are the DNA geometry, DNA damage method, the base pair separation determining DSB induction and the energy threshold above which a damage occurs. All simulations consist of 10^5 primary electrons.

5.4.3.1. DNA Geometry Variation

Simulations were performed using the parameters detailed above using electron beams of 100, 150 and 200 MeV. The plasmid DNA was constructed using the QuartCyl, HalfCyl or Spherical geometries and 5000 repeats made. The DSB yield results are presented in Table 5.9 and Fig. 5.4.

Energy (MeV)	Geometry	DSB (Mbp^{-1} kGy^{-1})
100	QuartCyl	0.21 ± 0.05
	HalfCyl	1.00 ± 0.09
	Spherical	0.04 ± 0.01
150	QuartCyl	0.12 ± 0.03
	HalfCyl	0.95 ± 0.09
	Spherical	0.011 ± 0.0
200	QuartCyl	0.13 ± 0.03
	HalfCyl	0.84 ± 0.08
	Spherical	0.04 ± 0.01

Table 5.9 – DSB yields following plasmid irradiation at 100, 150 and 200 MeV, with plasmid constructed using QuartCyl, HalfCyl or Spherical geometry

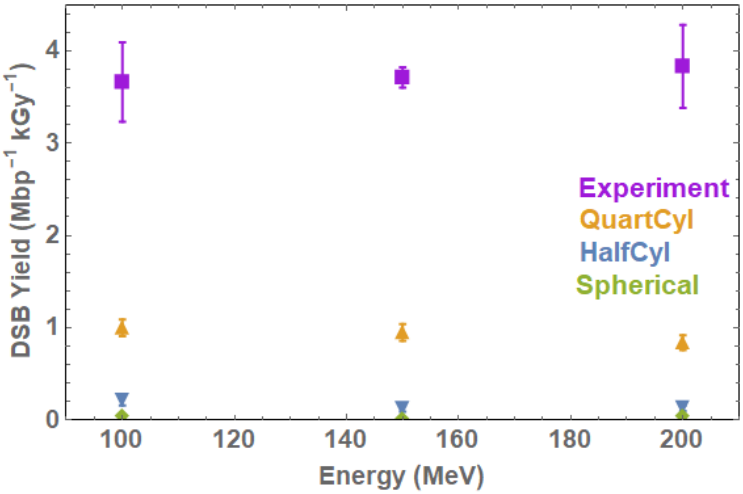

Figure 5.4 - DSB yields following plasmid irradiation at 100, 150 and 200 MeV showing yield variation with plasmid geometry. Experimental data included for comparison

Based on the results of the first test, it can be concluded that the spherical geometry significantly under-estimates the DNA damage caused by VHEE irradiation compared with the other geometries. This is likely to be the result of the spherical DNA geometry having the smallest volume of the three geometries. A smaller volume makes it less likely that a particle will interact with the DNA volume, therefore resulting in a lower damage yield. As a similar conclusion was made by Henthorn *et al.*[262], the spherical geometry was not included in further tests.

5.4.3.2. Energy Deposition Method Variation

The second test involves varying the energy deposition method (energy range, energy threshold, ionisation) used for scoring the DNA damage. As with test 1, all other parameters are set to their default values and simulations are performed using 10^5 primaries at 100, 150 or 200 MeV with DNA constructed using the QuartCyl or HalfCyl geometries. The energy range is set from 5-37.5 eV and the energy threshold is set to 17.5 eV. The results are presented below in Table 5.10 and Fig. 5.5.

Energy (MeV)	Deposition Method	QuartCyl DSB (Mbp^{-1} kGy^{-1})	HalfCyl DSB (Mbp^{-1} kGy^{-1})
100	Threshold	0.21 ± 0.05	1.00 ± 0.09
	Range	0.28 ± 0.05	0.44 ± 0.07
	Ionisation	0.05 ± 0.02	0.19 ± 0.05
150	Threshold	0.13 ± 0.03	0.95 ± 0.09
	Range	0.24 ± 0.04	0.46 ± 0.07
	Ionisation	0.09 ± 0.03	0.21 ± 0.05
200	Threshold	0.12 ± 0.03	0.84 ± 0.08
	Range	0.28 ± 0.05	0.52 ± 0.08
	Ionisation	0.11 ± 0.03	0.24 ± 0.05

Table 5.10 – DSB yields following plasmid irradiation at 100, 150 and 200 MeV, with plasmid constructed using QuartCyl or HalfCyl geometry and energy deposition method varied

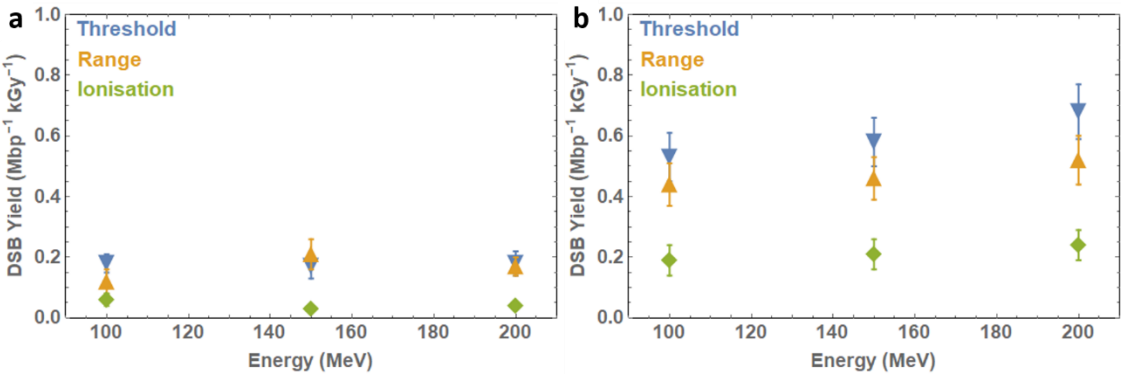

Figure 5.5 - DSB yields following plasmid irradiation at 100, 150 and 200 MeV with energy deposition method varied between range, threshold and ionisation methods. a) shows yields for plasmid built with QuartCyl geometry and b) shows results for plasmid built with HalfCyl geometry

Following this test, it was concluded that the ionisation energy deposition method was not suitable, resulting in significant under-estimates for DNA damage. As with the Spherical geometry, this energy deposition method was not used in further simulations.

5.4.3.3. Base Pair Separation Variation

As with the energy threshold value, the separation between SSBs on opposite strands to determine DSB induction has also been found to vary within the literature. While a separation of 10 base pairs is considered the standard, separations of up to 25 base pairs have been incorporated in DNA damage models (LEM[222]). In this test, the separation is therefore varied to look into DSB yield dependency on separation. 100 MeV electron beams will be simulated, with the plasmid built using the QuartCyl geometry and damage scored using the energy range method. The results are presented in Table 5.11 and Fig. 5.6.

Separation (base pairs)	SSB (Mbp^{-1} kGy^{-1})	DSB (Mbp^{-1} kGy^{-1})
5	55.11 ± 0.68	0.20 ± 0.04
10	55.98 ± 0.69	0.24 ± 0.04
15	55.38 ± 0.69	0.32 ± 0.06
20	56.93 ± 0.67	0.44 ± 0.06
25	56.83 ± 0.66	0.50 ± 0.07

Table 5.11 – SSB and DSB yields following plasmid irradiation at 100 MeV with the separation within which two SSBs on opposite backbones can form a DSB varied from 5-25 base pairs

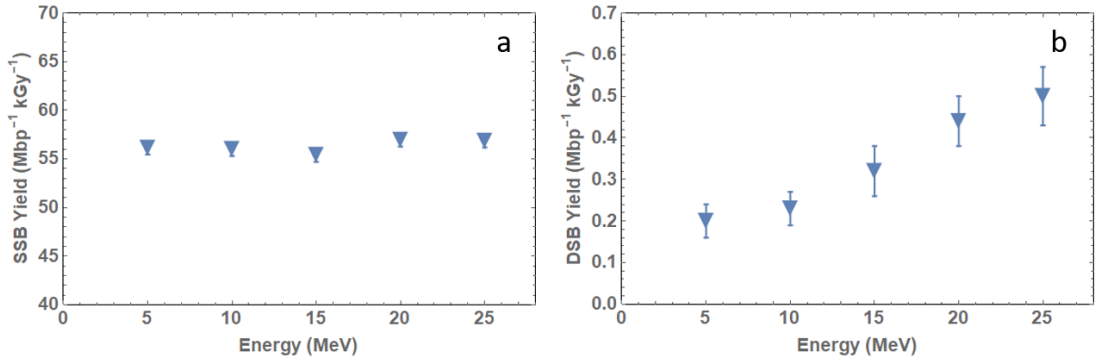

Figure 5.6 – a) SSB yield and b) DSB yield following plasmid irradiation at 100 MeV with SSB separation varied from 5-25 base pairs

As expected, the results indicate that the SSB yield remains unchanged and the DSB yield increases linearly as the separation between which two SSBs on opposite backbones can induce a DSB increases. This is unsurprising as increasing the separation increases the probability of a DSB being induced.

5.4.3.4. Energy Threshold Variation

While the energy threshold value (an energy deposition above which will cause a DNA damage) is set, as default, at 17.5 eV, a review of the literature has shown the use of alternative values. Energy threshold values were varied within the limits observed in the literature from 8.22 – 22.5 eV, with DNA built using the QuartCyl geometry, with simulations carried out using electrons at 100 MeV only. The results are given in Table 5.12 and Figure 5.7.

Threshold Energy (eV)	QC DSB (Mbp^{-1} kGy^{-1})	HC DSB (Mbp^{-1} kGy^{-1})
8.22	0.91 ± 0.19	3.56 ± 0.38
10.79	0.45 ± 0.14	1.74 ± 0.26
15	0.37 ± 0.12	1.03 ± 0.21
17.5	0.29 ± 0.11	1.00 ± 0.09
19	0.17 ± 0.08	0.55 ± 0.15
22.5	0.17 ± 0.08	0.42 ± 0.10

Table 5.12. DSB yields following plasmid irradiation at 100 MeV using the energy threshold deposition method, with threshold value varied between 8.22 and 22.5 eV

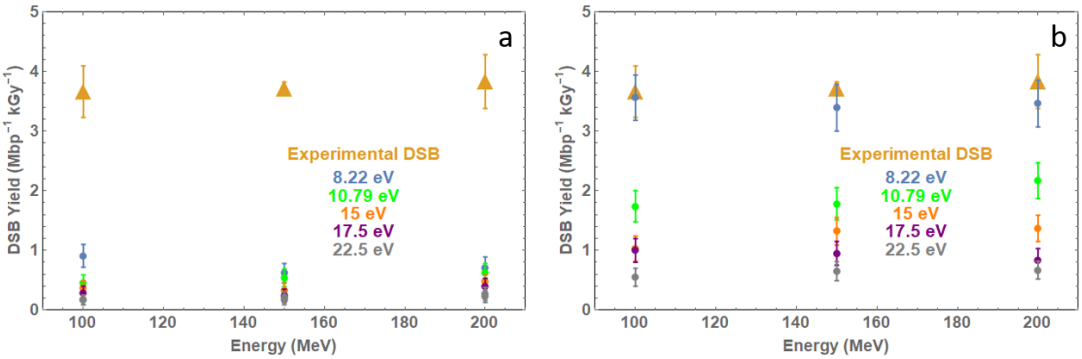

Figure 5.7 - DSB yield following plasmid irradiation at 100 MeV with energy threshold above which damage occurs varied over 8.22-22.5 eV

Unsurprisingly, the DSB yield decreases as the energy threshold value increases. This is due to fewer SSBs being induced as the probability of a sufficiently high energy deposition lowers as the threshold value increases. As a result, fewer SSBs results in a lower probability of DSBs being induced – hence the lower DSB yield.

5.4.4 – Optimisation of Plasmid Irradiation Parameters for VHEE

The results of the parameter variation study indicated that a simulation in which plasmid DNA was built with a HalfCyl geometry, the damage scored using the energy threshold mechanism at 8.22 eV and a DSB induced if two SSBs on opposite backbones occur within 10 base pairs result in a DSB yield which most closely approximates the experimental DSB yield data. This data is presented in Table 5.13 and Fig. 5.8.

	Threshold = 8.22 eV	**Experiment**
Energy (MeV)	**DSB (Mbp^{-1} kGy^{-1})**	**DSB (Mbp^{-1} kGy^{-1})**
100	3.56 ± 0.38	3.66 ± 0.43
150	3.39 ± 0.39	3.71 ± 0.11
200	3.46 ± 0.39	3.83 ± 0.45

Table 5.13 – DSB yields for 100, 150 and 200 MeV irradiated plasmid simulations with DNA built using HalfCyl geometry and damage scored using the energy threshold method at 8.22 eV with separation set at 10 bp. Experimental results included for comparison

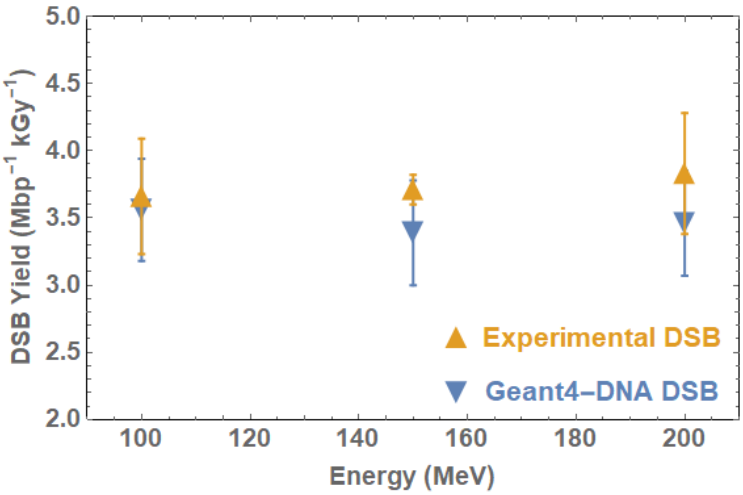

Figure 5.8 - DSB yields following plasmid irradiation at 100, 150 and 200 MeV with plasmid built using HalfCyl geometry and damage scored using the energy threshold method at 8.22 eV with base pair separation of 10 bp. Simulation data (blue) compared with experimental data (yellow)

5.4.5. Plasmid Configuration

While reasonable agreement has been observed between experimental and simulation DSB yields following VHEE irradiation, it must be noted that the plasmid model being used is not particularly realistic. In nature, it is highly unlikely that a plasmid will consist of a perfectly circular closed loop. Instead, plasmids are twisted and folded, as shown in an electron microscope image of a plasmid (Fig. 5.9)[152]. It can therefore be suggested that more accurate DSB yields can be obtained by simulating a more realistic plasmid structure. Simulations were therefore carried out, irradiating a number of plasmid structures developed for TOPAS-nBio validation[267] – shown in Fig. 5.10. Simulations were performed using the optimised parameters in section 5.4.3, with a 100 MeV electron beam simulated with the number of particles set to model the CLEAR beam fluence. The results for the six plasmid configurations are presented in Table 5.14 and Figure 5.11.

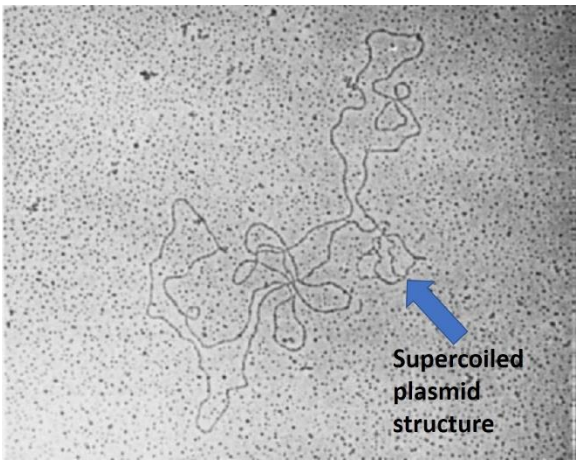

Figure 5.9 - Electron microscope image of a supercoiled plasmid structure. Image reproduced from [77]

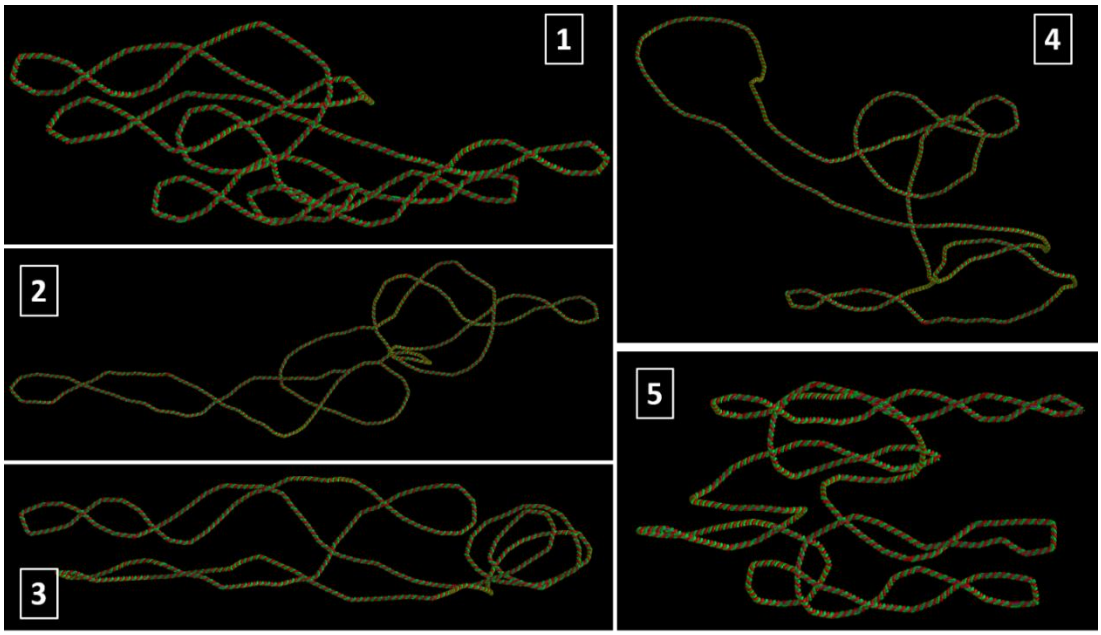

Figure 5.10 - Examples of plasmid configurations in GEANT4-DNA taken from TOPAS-nBio geometry study [74]

Plasmid Configuration	DSB (Mbp^{-1} kGy^{-1})
Circular	3.56 ± 0.38
1	2.99 ± 0.33
2	2.94 ± 0.35
3	2.97 ± 0.34
4	2.94 ± 0.35
5	2.86 ± 0.35
6	2.79 ± 0.34
Experiment	3.66 ± 0.43

Table 5.10 – DSB yields for 100 MeV plasmid simulations using various plasmid configurations, compared the experimental yield

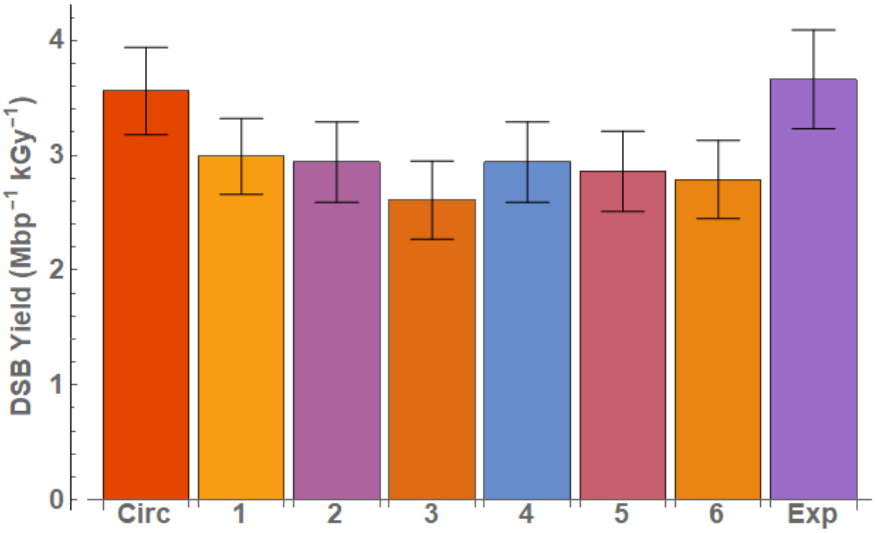

Figure 5.11 - DSB yields following irradiation at 100 MeV with plasmid configuration varied. Circ represents the circular plasmid, 1-5 are the different plasmid configurations shown in Fig. 5.10 and Exp represents the experimental DSB yield following plasmid irradiation at 100 MeV. Simulation standard errors based on 10^3 repeats

5.4.6. Aqueous Plasmid Irradiation Simulation

Following the irradiation of dry plasmids and the comparison of simulation DSB yields with experimental DSB yields, aqueous plasmid samples were irradiated to investigate the contribution of indirect radiation effects to total DSB yield. Indirect radiation effects are induced in the code by initiating the GEANT4-DNA chemistry processes, i.e. the production of free radicals following the interaction of the primary radiation with water molecules as detailed in section 5.3. The experimental setup is altered from that of the dry plasmid samples as the plasmid is constructed within a water volume. In the wet plasmid experimental setup, a plasmid solution is contained in an Eppendorf tube.

Simulations were performed using the same parameters as in section 5.4.3 for dry plasmid irradiation, with a circular plasmid built using the HalfCyl geometry and damage scored using the energy threshold deposition method at 8.22 eV, since this combination most closely reproduced the direct effect. Plasmids were irradiated with electron beams at 100, 150 and 200 MeV with 10^3 repeats performed for each energy. Again, the modified physics constructor was used to allow simulation of high-energy electron track structure. The results of these simulations are presented in Table 5.11 and Fig. 5.12, with experimental results included for comparison.

Energy (MeV)	Geant4-DNA DSB (Mbp^{-1} Gy^{-1})	Experiment DSB (Mbp^{-1} Gy^{-1})
100	$(5.17 \pm 1.46) \times 10^{-3}$	0.35 ± 0.02
150	$(7.33 \pm 2.07) \times 10^{-3}$	0.35 ± 0.03
200	$(4.82 \pm 1.46) \times 10^{-3}$	0.38 ± 0.02

Table 5.11 – DSB yields from GEANT4-DNA simulations and CLEAR experiments with aqueous plasmid samples. Standard error for GEANT4-DNA data based on 10^4 simulation repeats

The DSB yield following plasmid irradiation is significantly underestimated compared with the experimental DSB yield.

It was postulated that the discrepancy in simulation and experimental yields was due to an issue with the GEANT4-DNA chemistry processes. On induction, chemical processes are modelled using the G4EmDNAChemistry constructor. As with the G4EmDNAPhysics constructor, the chemical processes can only be modelled using electrons with energy up to 1 MeV. This therefore suggests that the relevant chemical species are not being produced when modelling plasmid irradiation with electrons >1 MeV.

This idea was tested by running simulations to determine the quantity and type of chemical species being produced following the interaction of electrons with water when using the different physics constructors.

For this model, the plasmid was not built, leaving an empty water box. This box was irradiated with 10^4 electrons and the chemical species produced were counted cumulatively over 1 ns. Two separate simulations were run – in the first, physical processes were built with the G4EmDNAPhysics constructor, 'DNA,' and the simulation run with electrons at 0.999999 MeV (due to the 1 MeV hard limit for the physics constructor). In the second, the modified physics constructor 'electron' was used to build physics processes and the simulation run with electrons at 1 MeV. Ten repeats were run for each and the average yield per primary (i.e. the number of radicals produced for each electron) calculated

for each chemical species. The results of these simulations are presented in Table 5.12 and Fig. 5.13 respectively.

Chemical Species	Default Physics yield/primary	Modified Physics yield/primary
H^+	15.54	0
H_2O	0.91	0.26
H_2O_2	6.51	0.03
H_3O	78.35	1.69
H_2	6.75	0.002
OH^-	94.41	1.64
e^-_{aq}	76.36	0.02

Table 5.12 – Chemical species produced following water radiolysis in GEANT4-DNA using standard physics constructor (G4EmDNAPhysics) and modified physics constructor

Table 5.12 and Fig. 5.13 show the significant difference in the chemical species being produced when using the different physics constructors – note the difference in scale between the Default and Modified physics constructors in Fig. 5.13. This can also be highlighted by visualising the simulation of electrons travelling through the water volume, as can be seen in Fig. 5.14. Fig. 5.14a shows plasmid irradiation using the G4EmDNAPhysics constructor while 5.14b uses the modified physics list. The coloured lines represent the tracks of particles and free radicals as they travel through the water volume and interact with the DNA volume. Evidence of a significant difference in radical production is clear.

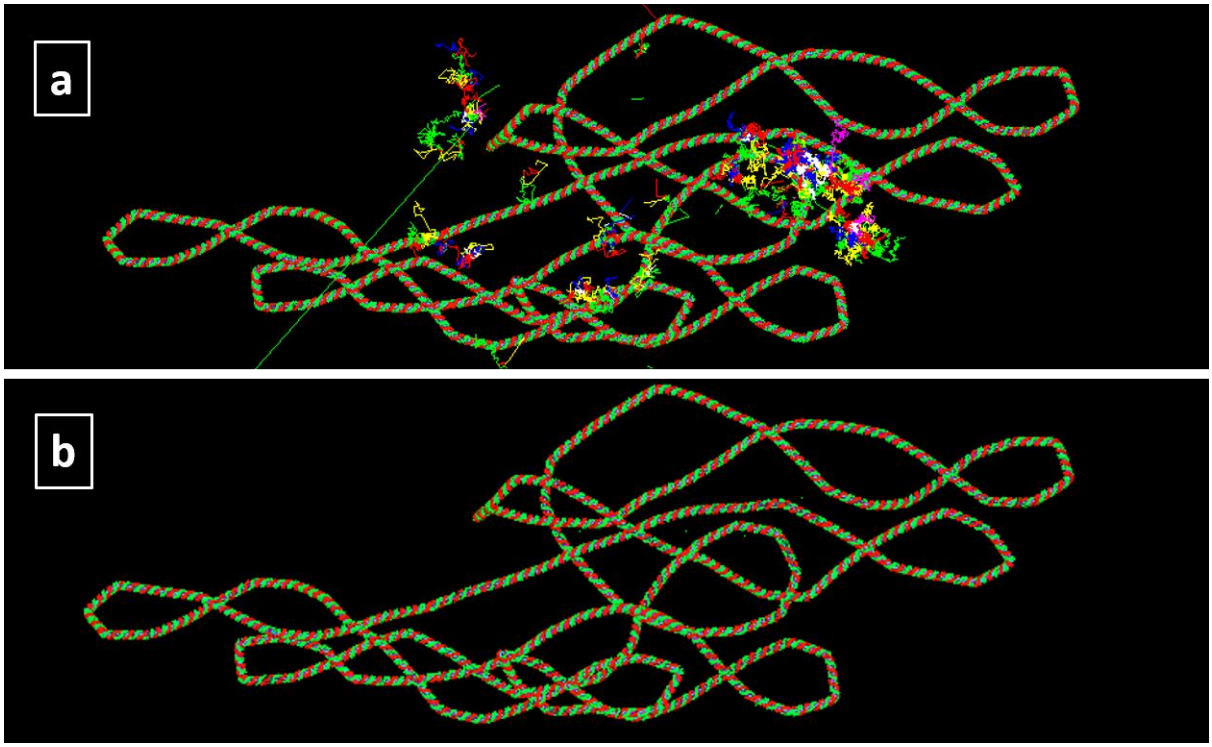

Figure 5.14 - Visualisation of chemical species production following plasmid irradiation with electrons using a) the G4EmDNAPhysics constructor at 0.999999 MeV and b) the modified physics constructor at 1 MeV

Based on these results, it can be concluded that the lack of free radical production in simulations involving > 1 MeV electrons is resulting in a lack of indirect damage effects. Within the simulation, the interaction of a OH^- radical with the DNA volume has an 80% probability of causing a damage to a base and a 50% probability of causing a damage to a backbone. When using the modified physics constructor, the radicals which go on to produce OH^- (H^+, H_2O_2 and e^-_{aq}) are produced in very low quantities, therefore producing very low quantities of OH^-. As a result, very few DNA damages are caused by the OH^- radicals, i.e. by indirect radiation effects.

5.5. Discussion and Conclusion

The aim of this chapter was to produce a model for plasmid DNA damage following irradiation with VHEE which would closely approximate the DNA damage data measured in the CLEAR experiments presented in Chapter 4. A model was developed in GEANT4-DNA based on an earlier model from Henthorn *et al.*[212] for proton-induced damage, with the GEANT4-DNA physics constructor adapted to allow the modelling of electron track structures above 1 MeV.

Initial simulations indicated that the parameters resulting in close approximation of damage yields to experimental data for proton irradiation of dry plasmids underestimated the DSB yields following VHEE irradiation. Good approximation was observed with SSB yields, but due to the unreliability of the experimental SSB data, it cannot be confirmed that these are the best parameters for modelling SSB damage. A parameter variation study was therefore performed, in which the damage scoring mechanism and DNA geometry were varied along with the distance between which two SSBs on opposite backbones can form a DSB. These parameters were varied according to data available in published literature and compared with the dry plasmid experimental DSB yields.

Analysis of the parameter variation data showed that simulations involving plasmid DNA built with a HalfCyl geometry, damage scored using the energy threshold mechanism at 8.22 eV and DSBs induced if two SSBs on opposite backbones occur with 10 base pairs result in DSB yields which most closely approximate the experimental data. The resulting parameters are similar, with small differences (likely due to differences between experimental and *in silico* configuration), compared with previous *in silico* studies based on published experimental data over a range of radiation modalities, though it is noted that large variation across datasets is frequently observed as highlighted by Henthorn *et al.*. In particular, the SSB separation of 10 base pairs is in agreement with the separation quoted across many published models, giving confidence in the scoring method used as well as the adapted physics constructor for VHEE simulation.

The plasmid configuration was varied to investigate the difference in DSB yields between a perfectly circular plasmid and a more realistic plasmid, including twists and folds within the structure. Simulations based on the experimental setup were performed at 100 MeV for the circular plasmid and five plasmid configurations based on Ramos-Mendez's work. The average DSB yield over these five plasmids was calculated and compared with the DSB yield of the circular plasmid and to experimental results. The average DSB yield was found to be 20% lower than that of the circular plasmid, though the yield was still found to be a good approximation to experimental data at 100 MeV indicating

that using the more realistic plasmid model could result in an accurate model of plasmid damage following irradiation.

While successful simulations were performed with dry plasmid samples, significant issues arose when initiating the chemical processes to investigate the contribution of indirect effects following irradiation of aqueous plasmid samples due to GEANT4 chemistry processes being restricted to 1 MeV for electrons. Unlike the physics processes, high energy chemistry processes were not available to be combined with the GENAT4-DNA chemistry constructor. As a result, the yield of free radicals following the interaction of electrons with water molecules was extremely low, resulting in extremely low incidences of DNA damage due to indirect radiation effects. Correspondence with S. Incerti, one of the main developers of GEANT4-DNA, indicated that the current code is not capable of simulating chemical processes with electrons of energy > 1 MeV, though work is ongoing within the GEANT4 collaboration to extend the capability of GEANT4-DNA to model electrons with energy up to 10 MeV. It is likely to be 1-2 years before this update is available to users.

The next step following successful modelling of the physical effects of VHEE irradiation on DNA is to extend the usability and scale of the model, including simulation of DNA damage complexity and repair processes. PARTRAC is currently capable of modelling DNA damage repair through the Non-Homologous End-Joining pathway, while the Manchester model is capable of modelling repair through both the NHEJ and HR repair pathways. The DSB damage complexity is related to repair, with base damage close to (within 1-3 base pairs) a DSB proving more difficult to repair. By determining the DSB complexity following irradiation by VHEE and different radiotherapy modalities, the likelihood of successful damage repair can be predicted. This can then be validated by modelling DNA repair processes to see how DSB complexity and damage repair processes following VHEE irradiation compare with those for established modalities. From a clinical perspective, understanding if electrons behave more like photons or protons in terms of their repair mechanisms (one of the 5 Rs of radiotherapy) will help to inform the clinician in their choice of treatment for a patient.

The modelling of different biological structures on increasingly large scales can also be investigated, including chromatin fibres and cell nuclei. By determining

the DSB yields to a cell nucleus following irradiation with VHEE and photons, a value for RBE based on DNA damage using a mechanistic radiobiological model can be calculated. A similar study has been carried out by Henthorn[267] on the RBE of protons based on DSB yield within a cell nucleus, in which the resulting RBE values over a given track-averaged LET range was found to be similar in value and trend to RBE values calculated using phenomenological models with cell survival as an endpoint. By performing similar calculations for VHEE RBE based on mechanistic DNA damage and making comparisons to similar calculations for established modalities and to experimental data, the reliance on phenomenological models is decreased. Instead the move is made towards an improved understanding of VHEE effects on biological structures based on radiobiological mechanisms. Such an understanding will help to answer key questions for the implementation of VHEE radiotherapy in the clinic, such as whether VHEEs will have a different response on the tumour microenvironment compared to protons or X-rays, if a different immune response is triggered by VHEE treatment or if different repair mechanisms are triggered for different types of radiation-induced damage.

Chapter 6 – Conclusions and Future Outlook

6.1. Key Results

This thesis presents an investigation of the radiobiological effects of VHEE, specifically physical damage caused to DNA, to provide the first experimental characterisation of VHEE RBE and to compare this value to those of clinically established radiotherapy modalities. This was achieved through a series of pBR322 plasmid irradiation experiments with 100-200 MeV VHEEs, 6-15 MeV electrons (in the clinical energy range) and ^{60}Co photons as described in Chapter 4. Following irradiation, the SSB and DSB yields for the stated modalities were determined, with DSB yield used as the biological endpoint for the calculation of RBE_{DSB} for clinical electrons and VHEEs.

Low energy electron RBE_{DSB} was found to be consistent with the assumption made in the clinic that electron RBE can be approximated to 1 and good agreement was observed between clinical electron RBE_{DSB} and RBE calculated for similar energies using cell survival as the biological endpoint. VHEE RBE_{DSB} was also found to be reasonably consistent with published results on electron RBE, with evidence suggesting that electron RBE may increase slightly with energy and LET – varying from 0.97 ± 0.11 at 6 MeV to 1.19 ± 0.10 at 200 MeV. This cannot be stated without any doubt, however, due to the variation observed – it is clear that more evidence is required to conclude that VHEE show a variable RBE. It can, however, be concluded that VHEEs cause similar physical effects on DNA to clinically established radiotherapy modalities, with early indications of a variable RBE suggesting that they may behave more like protons than photons in terms of DNA damage. This result gives confidence that biological effects such as cell death (widely acknowledged to be directly caused by DNA damage) could also be similar. From a clinician's point of view, understanding the behaviour of a novel radiotherapy treatment relative to an established treatment will help to inform the decision on the modality to use in patient treatment, in terms of Tumour Control Probability and Normal Tissue Complication Probability. This is a key step towards the clinical implementation of VHEEs as a cancer treatment.

Further investigations within the plasmid irradiation experiments provided further insight into the interactions between VHEEs and DNA. Variation between a dry and aqueous plasmid environment indicated that ~99% of DNA damage was the result of indirect radiation effects (from secondary particles) in the case of both VHEEs and ^{60}Co photons. This result was consistent with similar published measurements by Vysin[157], who irradiated aqueous plasmids in a solution with a similarly low free radical scavenging capacity compared to a cellular environment.

Dose rate variation with VHEEs was studied at the CLEAR user facility to determine if a difference in DSB yield was present. No statistically significant variation was observed between the ultra-high (FLASH) and conventional dose rate irradiations. This result suggests that a FLASH effect is not observed under these experimental conditions. This was in agreement with the hypothesis – it was anticipated that little variation would be observed between Conv and FLASH-irradiated plasmid samples due to the experimental conditions – plasmid simulation does not involve the use of highly oxygenated water to replicate cell conditions, understood to be key to the production of a FLASH effect. Further investigation under experimental conditions more similar to a cellular environment may provide more weight to this conclusion. While a FLASH effect was not observed at the nanoscale, this conclusion could help to inform future FLASH radiobiological studies, as it indicates that the FLASH effect occurs on the cellular or tissue level, rather than at the nanoscale.

The experimental data from Chapter 4 was used as a baseline for the development of a mechanistic model of the irradiation of pBR322 plasmid DNA with VHEEs, covered in Chapter 5. The model was based on one developed by Henthorn *et al.*[212] *hent* for proton irradiation of plasmids in dry and aqueous conditions. Vital adaptations were required for the physics constructor to enable track structure modelling of electrons with energies > 1 MeV by combining the GEANT4-DNA physics constructor with high-energy physics processes.

Initial modelling focussed on dry plasmid irradiation, in which DNA damage was caused by direct radiation effects only. A parameter variation study was performed for dry plasmids, in which the DNA geometry, damage mechanism and distance within which two SSBs would form a DSB were varied according to the available literature. Simulations based on the experimental conditions

outlined in Chapter 4 were performed to determine the DSB yield following VHEE irradiation.

Simulations in which the plasmid was built with HalfCyl geometry, damage scored using the energy threshold mechanism at 8.22 eV and DSBs scored if two SSBs on opposite strands occur within 10 base pairs resulted in DSB yields which most closely approximated experimental data. These parameters are broadly similar to published *in silico* studies of DNA damage modelling using a range of radiation modalities, with small differences likely due to differences in experimental and *in silico* setups. The agreement between the VHEE experimental and simulated direct damage yields, however, is a crucial result for VHEE radiobiological modelling, giving confidence in the GEANT4-DNA model and in the methods used to determine DSB yields.

Aqueous plasmid irradiations were modelled based on these parameters with chemistry processes activated to score damage resulting from indirect radiation effects. Limitations within the GEANT4 chemistry processes, specifically the electron energy range being limited to 1 MeV, resulting in significant underestimation of DSB yields compared to experimental data. This therefore indicated that, while GEANT4-DNA is capable of modelling the direct effects of VHEE irradiation on plasmid DNA, it is currently unable to model the indirect effects of electrons at clinically relevant energies.

Moving away from radiobiology, a further study involved determining a semi-empirical method of calculating the range of an electron beam as it travels through a material was presented in Chapter 3. This method was based on an expression developed for the range of proton beams by Bortfeld[125,126], with range dependent on beam energy and material density and effective atomic mass.

Therapeutic and practical ranges for electron beams at 10-250 MeV were calculated following the fitting of on-axis PDD curves using the Meigooni-Das equation[145]. These PDD curves were generated from the simulation of electron beams traversing various clinically relevant materials using TOPAS. An investigation of range dependency on the parameters mentioned above indicated that the Bortfeld expression was an appropriate fit for electron beams, though it is noted that the was no physical basis for this – the conclusion was based on the fit to simulation data.

The therapeutic and practical range data was then fitted to the Bortfeld expression to determine constants for each material. R^2 and X^2 calculation for each material indicated that the range from TOPAS simulations and the Bortfeld range for electron beams were in good agreement.

It was therefore concluded that the Bortfeld equation used to calculate proton beam range is suitable for use with electron beams at energies 10-250 MeV. This allows simple analytical calculations to be made for VHEE beam range, which may reduce the need for time-consuming Monte Carlo calculations to determine beam range in treatment planning. The time and computational resources required to produce an accurate treatment plan can be reduced and amendments or corrections to a plan can be easily and rapidly implemented as a patient progresses through their treatment. Such modifications are often required due to changes in a patient's physiology, such as tumour shrinkage or weight loss.

6.2. Study Limitations

While the studies outlined in chapters 3, 4 and 5 have provided useful insights into the radiobiology of VHEEs and the behaviour of VHEE beams, it is inevitable that there are some limitations faced in the research. This section looks into these limitations and the solutions to them.

Firstly, while the Bortfeld expression was shown to accurately determine electron beam range in Chapter 3, it must be noted that the equation has been used purely as a fit to the range data. The equation has been used as a phenomenological model for electron beam range calculation. The equation was developed based on physical processes for protons rather than electrons. As there is no physical justification for the equation's use with electrons (range dependencies to different parameters were determined through fits to simulation data), it cannot be considered a mechanistic model. While the equation fit has been shown to provide a good agreement to TOPAS range data for electron beams up to 250 MeV, the phenomenological nature of the model may not lend itself to extrapolation for higher energies. A more mechanistic approach would require the development of a model based on the physical processes of electron beams as they travel through matter. This may, however,

result in the loss of the ability to rapidly calculate beam range and the related benefits as mentioned earlier. A careful balance between the two is required.

With regard to the experiments described in Chapter 4, there were associated limitations, including the possible unreliability of SSB yields for the dry plasmid irradiations. Due to significant temperature fluctuation and time spent at room temperature in water during transportation, the supercoiled structure of the plasmid samples relaxed, resulting in SSBs on the plasmid. Tests were performed to confirm that this was due to transportation rather than the effects of drying the plasmid – control samples were found to have similar proportions of supercoiled and open-circular plasmid to undried control samples (taken from stock solution). This issue affected the accuracy of SSB yield, as damage came from both transportation and radiation effects. This in turn affected the calculation of direct and indirect radiation effect contribution.

This issue was not observed in aqueous plasmid samples, which were prepared onsite and transported to the facility in 10mM Tris-HCl and 1mM EDTA, preventing the plasmid structure relaxing at room temperature. In future experiments, the plasmid should remain in the buffer solution during transportation and dry samples prepared onsite, as with wet samples. This should be simple to accommodate as pBR322 plasmid is classified as a non-toxic substance (for transportation purposes it is classified as water-equivalent) and sample preparation requires minimal equipment. SSBs measured following analysis of dry samples prepared onsite will be the result of radiation only, providing a more accurate damage yield.

A further limitation in the dry plasmid irradiation experiment is the efficiency. The rapid irradiation time of wet samples and the ability to irradiate larger samples within Eppendorf tubes before splitting into sub-samples for analysis made the wet plasmid experiments reasonably efficient. Dry samples required much higher doses, increasing the irradiation time, and samples had to be irradiated individually. This was a particular issue at CLEAR, as access to the accelerator hall was only permitted with a member of the Radiation Protection team – typically 3-4 accesses per day were possible. As only 10 samples could be irradiated per access, the process was inefficient.

To improve the efficiency of dry sample irradiation, the idea of a robotic arm has been suggested. Based on a similar design to one currently installed as part of the Christie proton research beamline for hypoxia studies, the arm would grip the microscope slide and place it in front of the beam. Following irradiation, the slide would be removed from the beam path and the process would be repeated for remaining samples. This will allow a greater volume of samples to be irradiated during each access, thereby improving the efficiency of the process. The increased sample size should also result in a reduction in standard error of the DSB yield and subsequently RBE_{DSB} values. These more accurate values will give a clearer indication of any trends for electron RBE_{DSB} with energy and LET.

A limitation highlighted in Chapter 5 is the incorrect modelling of indirect radiation effects in the experimental energy range. GEANT4 is currently limited to modelling chemical processes for electrons with energy below 1 MeV. Over the energy range (100-200 MeV) required, the yield of chemical species produced during water radiolysis such as OH^- radicals are produced, resulting in low incidences of DNA damage caused by indirect radiation effects. The obvious solution to this issue is to increase the upper energy limit to allow the chemical processes following VHEE irradiation to be modelled. This, unfortunately, is far beyond the scope of this PhD project – correspondence with the GEANT4-DNA software developers revealed that, while work is ongoing to raise this energy limit, it is likely to be 1-2 years before this limit increases to 10 MeV for electrons.

6.3. Future Outlook and Final Remarks

The work in this thesis has provided some exciting results including the first characterisation of VHEE RBE, the development of a nanodosimetric model for VHEE-induced DNA damage and a phenomenological model for VHEE beam range in matter. These results can provide a springboard for validation and extension of key ideas in research on VHEE beam behaviour and radiobiology, both experimentally and through further simulation work.

Chapter 3 resulted in the development of an expression for electron beam range, providing an excellent fit to range data produced in TOPAS. The next logical step in this work is the experimental validation of this expression.

An experiment, based on Lagzda's earlier VHEE work[4,105], could be set up involving the irradiation of EBT-XD films at varying depths within a water phantom. Similar phantoms could be built using various tissue-equivalent materials, to measure range variation with material composition and density. Dose would be determined at regular intervals along the phantom to build up a PDD curve, which would be used to determine range at a particular energy. Experimental range can then be compared with the range predicted by the expression. By making repeat irradiations at different energies, a range-energy plot can be built up and compared to that produced by the range expression, to determine the level of agreement. This would provide validation for the expression based on experimental data comparison.

Further extension could involve developing a more mechanistic model for the range of VHEE beams in matter to provide a predictive model, rather than one based on fitting to data. The model would be based on electron physics processes, rather than the proton physics processes on which the Bortfeld expression is based. By producing a mechanistic model which approximates experimental data well, the model can be used to predict range under constraints outside of experiments. This would give clinicians greater freedom in planning VHEE treatments for patients, along with confidence in the model's accuracy.

The plasmid irradiation experiments in Chapter 4 led to the first calculations of VHEE RBE, based on DSB yield as the biological endpoint, showing consistency with clinically established radiotherapy modalities. As experiments have indicated that the physical effects of VHEEs are similar to current modalities, the next desirable step is to determine if the biological effects are also similar.

Cell survival fraction is an established biological endpoint for RBE calculation, with CHO or V79 cell lines commonly used[198–200]. Determining RBE through cell survival would involve the irradiation of cell cultures over a range of doses. A clonogenic assay would be performed to determine the fraction of survival cells after a length of time. The dose required to produce a particular survival

fraction, typically 0.1 or 0.01, for a particular modality can then be compared to that for a reference modality (typically ^{60}Co X-rays) to determine the RBE. Confidence in the experimental method could be provided by calculating RBE for clinical electrons (6-15 MeV) as there is a great deal of RBE data from cell survival fraction in this energy range (see Chapter 4). VHEE RBE can then be determined to see if the value varies with energy, as has been indicated for electron RBE_{DSB}.

A further important biological effect is DNA damage repair. As detailed briefly in Chapter 5, irradiated cells can activate mechanisms to repair DNA damage. Successful damage repair is desirable for healthy tissues, while mis-repair is desirable in cancerous tissue as it can lead to cell death. When a DSB occurs, phosphorylation (the addition of a phosphoryl group PO_3^- to an organic molecule) of H2AX occurs to produce γ-H2AX. γ-H2AX can be used as a biomarker to detect the presence of DSBs in a cell as γ-H2AX accumulates around DSB sites to form foci. These foci can be detected through immunostaining using flow cytometry, and the number of foci detected will give the number of DSBs present. Cells can be irradiated and analysed at various points in time post-irradiation to determine the DNA damage repair rate. The repair rate following VHEE can be compared to those for other modalities, to see if VHEEs illicit a similar repair response. A further advantage to this technique is the ability to irradiate different cell types. This allows the repair rate of different cell types (e.g. late- or early-responding) to be measured, potentially identifying specific cancers which may be more responsive to VHEE treatment.

Plasmid irradiation simulation studies using GEANT4-DNA in Chapter 5 proved reasonably successful for dry samples with good approximation of DSB yield to experimental data observed. Aqueous sample irradiation proved less successful due to limitations in the chemical processes resulting in significant under-estimation of DNA damage caused by indirect radiation effects.

However, dry plasmid work can be extended to model DNA damage complexity and the probability and success of repair mechanisms initiated by a cell following radiation-induced damage. DSB complexity has been modelled by Henthorn for protons, with different types of DSB identified according to the inclusion of base damage as well as backbone damage. DSBs with a higher degree of complexity are more difficult to repair, with a higher probability of

mis-repair and subsequently cell death. By comparing DSB complexity for VHEEs with established modalities, predictions can be made as to how successful DNA damage repair is likely to be following VHEE irradiation.

These predictions can be tested by modelling the repair kinetics following VHEE irradiation. Mechanistic models in GEANT4-DNA have been designed at the University of Manchester which are capable of simulating damage repair following DNA irradiation with protons[46,244,245]. Adaptation of the physics processes may allow this to be performed with VHEE. PARTRAC is also capable of modelling repair kinetics[56].

This model extension can be validated by comparing the repair rate to those of other radiotherapy modalities and to rates determined experimentally through γ-H2AX analysis as mentioned earlier in this section. By understanding the complexity of DSBs induced by VHEE irradiation and its effect on repair mechanisms, this can help to optimise fractionated treatment planning for patients, as repair is one of the key components in the 5 Rs of radiotherapy. Such modelling will also indicate if VHEEs are more similar in terms of their repair mechanisms to protons or photons – the proportion of damage repaired by the different pathways will provide a clearer indication of this.

The extensions outlined in this section provide a series of steps with the overall aim of treating cancer patients in a clinical setting with VHEEs. There is still a great deal of research required in several areas, however, before this is possible, with work currently underway at the University of Manchester on VHEE machine design, specialised VHEE treatment planning software, dosimetry and imaging through collaborations with CERN, the Christie and Elekta.

While there is still a significant amount of research to be carried out, this thesis has produced results that encourage the further study of VHEE as a radiotherapy modality. Research into VHEE beam behaviour has resulted in a semi-empirical model for beam range in different materials, allowing for rapid range calculation with applications to treatment planning. Modelling DNA damage, while currently limited, showed that GEANT4-DNA can be used to determine DSB yields induced by direct radiation effects with good approximation to experimental data, paving the way to investigating more complex, post-physical effects of VHEE including DSB complexity and damage

repair. Finally, the calculation of VHEE RBE_{DSB} as close to 1 indicates the similarity in physical effects of VHEE to established clinical modalities. This gives confidence in the similarity of biological effects and provides a series of possible extensions to determine this. Determining VHEE RBE is a key pre-clinical step on the path towards clinical implementation of VHEE, with the overarching aim of improving patient outcomes through radiotherapy.

References

1. DesRosiers, C., Moskvin, V., Bielajew, A. F. & Papiez, L. 150-250 MeV electron beams in radiation therapy. *Phys. Med. Biol.* **45**, 1781–1805 (2000).

2. DesRosiers, C. M. *An evaluation of very high energy electron beams (up to 250 MeV) in radiation therapy*. http://search.proquest.com/docview/305153807 (2004).

3. Lagzda, A. *et al.* Relative insensitivity to inhomogeneities on Very High Energy Electron dose distributions. in *IPAC 2017* 4791–4794 (2017).

4. Lagzda, A. *et al.* Very-High Energy Electron (VHEE) studies at CERN's CLEAR user facility. in *IPAC 2018* 445–448 (2018). doi:10.18429/JACoW-IPAC2018-MOPML023.

5. Bazalova-Carter, M. *et al.* Treatment planning for radiotherapy with very high-energy electron beams and comparison of VHEE and VMAT plans. *Med. Phys.* **42**, 2615–2625 (2015).

6. Schuler, E. *et al.* Very high-energy electron (VHEE) beams in radiation therapy; Treatment plan comparison between VHEE, VMAT, and PPBS. *Med. Phys.* **44**, 2544–2555 (2017).

7. Subiel, A. *et al.* Dosimetry of very high energy electrons (VHEE) for radiotherapy applications: Using radiochromic film measurements and Monte Carlo simulations. *Phys. Med. Biol.* **59**, 5811–5829 (2014).

8. Agostinelli, S., Allison, J., Amako, K., Apostolakis, J. & Araujo, H. GEANT4 — a simulation toolkit. *Nucl. Instruments Methods Phys. Res. Sect. A Accel. Spectrometers, Detect. Assoc. Equip.* **506**, 250–303 (2003).

9. Perl, J., Shin, J., Faddegon, B. & Paganetti, H. TOPAS : An innovative proton Monte Carlo platform for research. **39**, 6818–6837 (2012).

10. Chadwick, K. H. & Leenhouts, H. P. A molecular theory of cell survival. *Phys. Med. Biol.* **18**, 78–87 (1973).

11. King, R. J. B. & Robins, M. W. What is cancer? in *Cancer Biology* 1–8 (Pearson Education Limited, 2006).

12. Cancer. *NHS UK* (2019).

13. Hanahan, D. & Weinberg, R. A. The hallmarks of cancer. *Cell* **100**, 57–70 (2000).

14. Shay, J. W. & Wright, W. E. Role of telomeres and telomerase in cancer. *Semin. Cancer Biol.* **21**, 349–353 (2011).

15. Cancer Statistics for the UK. *Cancer Research UK* (2020).

16. Major causes of death and how they have changed. in *Health profile for England: 2017* (UK Government, 2017).

17. Cancer incidence statistics. *Cancer Research UK* https://www.cancerresearchuk.org/health-professional/cancer-statistics-for-the-uk/incidence (2020).

18. Cancer mortality statistics. *Cancer Research UK* https://www.cancerresearchuk.org/health-professional/cancer-statistics/mortality (2020).

19. Cancer mortality by age. *Cancer Research UK* https://www.cancerresearchuk.org/health-professional/cancer-statistics/mortality/age (2020).

20. Cancer survival statistics. *Cancer Research UK* https://www.cancerresearchuk.org/health-professional/cancer-statistics/survival (2020).

21. Cancer diagnosis and treatment statistics. *Cancer Research UK* https://www.cancerresearchuk.org/health-professional/cancer-statistics/diagnosis-and-treatment (2020).

22. Stephens, F. O. *et al.* Treating Cancer. in *Basics of Oncology* 87–120 (Springer, 2009).

23. Neal, A. J. & Hoskin, P. J. Principles of surgical oncology. in *Clinical Oncology* 36–41 (CRC Press, 2012).

24. Neal, A. J. & Hoskin, P. J. Principles of systemic treatment. in *Clinical Oncology* 52–66 (CRC Press, 2012).

25. Rontgen, W. C. On a new kind of ray. *Science (80-.).* **3**, 227–231 (1896).

26. Grubbe, E. H. X-rays in the treatment of cancer and other malignant diseases. *Med. Rec.* **62**, 692–695 (1902).

27. Neal, A. J. & Hoskin, P. J. Principles of radiotherapy. in *Clinical Oncology* 42–51 (CRC Press, 2012).

28. Chang, D. S., Lasley, F. D., Das, I. J., Mendonca, M. S. & Dynlacht, J. R. Molecular mechanisms of DNA damage and repair. in *Basic Radiotherapy Physics and Biology* 201–210 (Springer, 2014). doi:10.1007/978-3-319-06841-1.

29. Eriksson, D. & Stigbrand, T. Radiation-induced cell death mechanisms. *Tumour Biol.* **31**, 363–372 (2010).

30. Lazar, A. A., Schulte, R., Faddegon, B. & Blakely, E. A. Clinical Trials Involving Carbon-Ion Radiation Therapy and the Path Forward. *Cancer* **124**, 4467–4476 (2018).

31. What is brachytherapy? *Cancer Research UK* https://about-cancer.cancerresearchuk.org/about-cancer/cancer-in-general/treatment/radiotherapy/internal/radioactive-implant-treatment/what-is-brachytherapy (2020).

32. Suntharalingam, N., Podgorsak, E. B. & Hendry, J. H. Basic Radiobiology. in *Radiation Oncology Physics: A Handbook for Teachers and Students* (ed. Podgorsak, E. B.) 485–504 (International Atomic Energy Agency, 2005).

33. Crowther, J. A. Some considerations relative to the action of X-rays on tissue cells. *R. Soc.* **96**, 207–211 (1924).

34. Fowler, J. F. Differences in Survival Curve Shapes for Formal Multi-

target and Multi-hit Models. *Phys. Med. Biol.* **9**, 177–188 (1964).

35. Kellerer, A. M. & Rossi, H. H. RBE and the Primary Mechanism of Radiation Action. *Radiat. Res.* **47**, 15–34 (1971).

36. Brenner, D. J. Point: The linear-quadratic model is an appropriate methodology for determining iso-effective doses at large doses per fraction. *Semin. Radiat. Oncol.* **18**, 234–239 (2008).

37. Lea, D. E. & Catcheside, D. G. The mechanism of the induction by radiation of chromosome aberrations in tradescantia. *J. Genet.* **44**, 216–245 (1942).

38. Williams, M. V. & Fowler, J. F. A review of alpha/beta ratios for experimental tumours: Implications for clinical studies of altered fractionation. *Int. J. Radiat. Oncol. Biol. Phys.* **11**, 87–96 (1985).

39. Leeuwen, C. M. Van *et al.* The alfa and beta of tumours : a review of parameters of the linear-quadratic model , derived from clinical radiotherapy studies. *Radiat. Oncol.* **13**, 1–11 (2018).

40. McMahon, S. J. The linear quadratic model: Usage, interpretation and challenges. *Phys. Med. Biol.* **64**, (2019).

41. Santiago, A., Barczyk, S., Jelen, U., Engenhart-cabillic, R. & Wittig, A. Challenges in radiobiological modeling : can we decide between LQ and LQ-L models based on reviewed clinical NSCLC treatment outcome data ? *Radiat. Oncol.* 1–13 (2016) doi:10.1186/s13014-016-0643-5.

42. Incerti, S. *et al.* The Geant4-DNA project. *Int. J. Model. Simulation, Sci. Comput.* **1**, 157–178 (2010).

43. Schuemann, J. *et al.* TOPAS-nBio: An Extension to the TOPAS Simulation Toolkit for Cellular and Sub-cellular Radiobiology. *Radiat. Res.* **191**, 125–138 (2019).

44. Mcmahon, S. J., Schuemann, J., Paganetti, H. & Prise, K. M. Mechanistic Modelling of DNA Repair and Cellular Survival Following Radiation-Induced DNA Damage. *Sci. Rep.* **6**, 1–14 (2016).

45. Henthorn, N. T. *et al.* In Silico Non-Homologous End Joining Following Ion Induced DNA Double Strand Breaks Predicts That Repair Fidelity Depends on Break Density. *Sci. Rep.* **8**, 1–11 (2018).

46. Warmenhoven, J. W. *et al.* Insights into the non-homologous end joining pathway and double strand break end mobility provided by mechanistic in silico modelling. *DNA Repair (Amst).* **85**, (2020).

47. Nettelbeck, H. & Rabus, H. Nanodosimetry : The missing link between radiobiology and radiation physics ? *Radiat. Meas.* **46**, 893–897 (2011).

48. Brenner, D. J. & Ward, J. F. Constraints on energy deposition and target size of multiply damaged sites associated with DNA double-strand breaks. *Int. J. Radiat. Biol.* **61**, 737–748 (1992).

49. Rabus, H. & Nettelbeck, H. Nanodosimetry: Bridging the gap to radiation biophysics. *Radiat. Meas.* **46**, 1522–1528 (2011).

50. Grosswendt, B. Nanodosimetry, from radiation physics to radiation

biology. *Radiat. Prot. Dosimetry* **115**, 1–9 (2005).

51. Garty, G. *et al.* First attempts at prediction of DNA strand-break yields using nanodosimetric data. *Radiat. Prot. Dosimetry* **122**, 451–454 (2006).

52. Pszona, S. & Gajewski, R. An approach to experimental microdosimetry at the nanometre scale. *Radiat. Prot. Dosimetry* **52**, 427–430 (1994).

53. Nardo, L. De *et al.* A detector for track-nanodosimetry. *Nucl. Instruments Methods Phys. Res. Sect. A Accel. Spectrometers, Detect. Assoc. Equip.* **484**, 312–326 (2002).

54. Garty, G. *et al.* The performance of a novel ion-counting nanodosimeter. *Nucl. Instruments Methods Phys. Res. Sect. A Accel. Spectrometers, Detect. Assoc. Equip.* **492**, 212–235 (2002).

55. Team, X.-5 M. C. *MCNP - A General Monte Carlo N-Particle Transport Code Version 5*. vol. 1 (2003).

56. Friedland, W. *et al.* Simulation of DNA damage after proton and low let irradiation. *Radiat. Prot. Dosimetry* **99**, 99–102 (2002).

57. Hill, M. A. Radiation Track Structure: How the Spatial Distribution of Energy Deposition Drives Biological Response. *Clin. Oncol.* **32**, 75–83 (2020).

58. Beyzadeoglu, M., Ozyigit, G. & Ebruli, C. Radiobiology. in *Basic Radiation Oncology* 71–144 (Springer, 2010).

59. Dowdy, S., Weardon, S. & Chilko, D. Poisson Distributions. in *Statistics for Research* 81–94 (John Wiley & Sons, Inc., 2004).

60. Chang, D. S., Lasley, F. D., Das, I. J., Mendonca, M. S. & Dynlacht, J. R. Therapeutic Ratio. in *Basic Radiotherapy Physics and Biology* 277–282 (Springer, 2014).

61. Berthelsen, A. K. *et al.* What's new in target volume definition for radiologists in ICRU Report 71? How can the ICRU volume definitions be integrated in clinical practice? *Cancer Imaging* **7**, 104–116 (2007).

62. Beyzadeoglu, M., Ozyigit, G. & Ebruli, C. Clinical Radiation Oncology. in *Basic Radiation Oncology2* 145–174 (Springer, 2010).

63. 3DSlicer. slicer.org (2020).

64. Fedorov, A. *et al.* 3D Slicer as an image computing platform for the quantitative imaging network. *Magn Reson Imaging* **30**, 1323–1341 (2012).

65. Withers, H. R. The Four R's of Radiotherapy. 241–271 (1975) doi:10.1016/b978-0-12-035405-4.50012-8.

66. Steel, G. G., Mcmillan, T. J. & Peacock, J. H. The 5Rs of radiobiology. *Int. J. Radiat. Biol.* **56**, 1045–1048 (1989).

67. Cooper, G. M. The Cell Cycle. in *The Cell: A Molecular Approach* (Sinauer Associates, 2000).

68. Lederman, M. The early history of radiotherapy: 1895-1939. *Int. J.*

Radiat. Oncol. Biol. Phys. **7**, 639–648 (1981).

69. Podgorsak, E. B. Basic Radiation Physics. in *Radiation Oncology Physics: A Handbook for Teachers and Students2* (ed. Podgorsak, E. B.) 1–43 (International Atomic Energy Agency, 2005).

70. Tonkopi, E., McEwen, M. R., Walters, B. R. B. & Kawrakow, I. Influence of ion chamber response on in-air profile measurements in megavoltage photon beams. *Med. Phys.* **32**, 2918–2927 (2005).

71. Wilson, R. R. Radiological use of fast protons. *Radiology* **47**, 487–491 (1946).

72. Paganetti, H. Proton therapy : history and rationale. *Prot. Ther. Phys.* **1895**, 1–18 (2012).

73. Eye Proton Therapy. *Clatterbridge Cancer Centre* https://www.clatterbridgecc.nhs.uk/patients/treatment-and-support/proton-therapy (2020).

74. Particle facilities in clinical operation. *PTCOG* https://www.ptcog.ch/index.php/facilities-in-operation (2020).

75. Proton beam therapy. *NHS England* https://www.england.nhs.uk/commissioning/spec-services/highly-spec-services/pbt/ (2020).

76. Bragg, W. H. & Kleeman, R. LXXIV. On the ionization curves of radium. *Philos. Mag. Ser. 6* **8**, 726–738 (1904).

77. Newhauser, W. D. & Zhang, R. The physics of proton therapy. *Phys. Med. Biol.* **60**, R155–R209 (2015).

78. Jette, D. & Chen, W. Creating a spread-out Bragg peak in proton beams. *Phys. Med. Biol.* **56**, 131–138 (2011).

79. Brualla, L., Palanco-Zamora, R., Wittig, A., Sempau, J. & Sauerwein, W. Comparison between PENELOPE and electron Monte Carlo simulations of electron fields used in the treatment of conjunctival lymphoma. *Phys. Med. Biol.* **54**, (2009).

80. Favaudon, V. *et al.* Ultrahigh dose-rate FLASH irradiation increases the differential response between normal and tumor tissue in mice. *Sci. Transl. Med.* **6**, (2014).

81. Vozenin, M. C., Hendry, J. H. & Limoli, C. L. Biological Benefits of Ultra-high Dose Rate FLASH Radiotherapy: Sleeping Beauty Awoken. *Clin. Oncol.* **31**, 407–415 (2019).

82. Yeboah, C., Sandison, G. A. & Pawlicki, T. Optimization of intensity-modulated very high energy (50 – 250 MeV) electron therapy. *Phys. Med. Biol.* **47**, 1285–1301 (2002).

83. Yeboah, C. & Sandison, G. A. Optimized treatment planning for prostate cancer comparing IMPT, VHEET AND 15 MV IMXT. *Phys. Med. Biol.* **47**, 2247–2261 (2002).

84. Lundh, O. *et al.* Comparison of measured with calculated dose distribution from a 120-MeV electron beam from a laser-plasma

accelerator. *Med. Phys.* **39**, 3501–3508 (2012).

85. Anania, M. P. *et al.* The ALPHA-X beam line: Toward a compact FEL. in *IPAC 2010 - 1st International Particle Accelerator Conference* 2263–2265 (2010).

86. Alesini, D. *et al.* The SPARC project: A high-brightness electron beam source at LNF to drive a SASE-FEL experiment. *Nucl. Instruments Methods Phys. Res. Sect. A Accel. Spectrometers, Detect. Assoc. Equip.* **507**, 345–349 (2003).

87. Battistoni, G. *et al.* Overview of the FLUKA code. *Ann. Nucl. Energy* **82**, 10–18 (2015).

88. Bohlen, T. T. *et al.* The FLUKA Code: Developments and challenges for high energy and medical applications. *Nucl. Data Sheets* **120**, 211–214 (2014).

89. Thwaites, D. I. & Tuohy, J. B. Back to the future: The history and development of the clinical linear accelerator. *Phys. Med. Biol.* **51**, (2006).

90. Kim, Y., Setiniyaz, S., Titberidze, M. & Jang, K. H. Overall performance comparison of S-band C-band, and X-band based compact XFEL facilities. in *FEL 2012 - 34th International Free Electron Laser Conference* 149–152 (2012).

91. Wangler, T. P. *RF Linear Accelerators*. (Wiley-VCH, 2007).

92. Michizono, S. The International Linear Collider. *Nat. Rev. Phys.* **1**, 244–245 (2019).

93. CLIC, T. *et al. Updated baseline for a staged Compact Linear Collider*. http://arxiv.org/abs/1608.07537%0Ahttp://dx.doi.org/10.5170/CERN-2016-004 (2016) doi:10.5170/CERN-2016-004.

94. Jones, R. M., Adolphsen, C. E., Miller, R. H., Wang, J. W. & Higo, T. Influence of fabrication errors on wake function suppression in NC X-band accelerating structures for linear colliders. *New J. Phys.* **11**, (2009).

95. Gamba, D. *et al.* The CLEAR user facility at CERN. *Nucl. Instruments Methods Phys. Res. Sect. A Accel. Spectrometers, Detect. Assoc. Equip.* **909**, 480–483 (2018).

96. Esarey, E., Schroeder, C. B. & Leemans, W. P. Physics of laser-driven plasma-based electron accelerators. *Rev. Mod. Phys.* **81**, 1229–1285 (2009).

97. Hooker, S. M. Developments in laser-driven plasma accelerators. *Nat. Photonics* **7**, 775–782 (2013).

98. Leemans, W. P. *et al.* GeV electron beams from a centimetre-scale accelerator. *Nat. Phys.* **2**, 696–699 (2006).

99. Loo, B. W., Maxim, P. G. & Dolgashev, V. A. Pluridirectional Very High Electron Energy Radiation Therapy Systems and Processes. (2013).

100. Paganetti, H. The Physics of Proton Biology. 593–626 (2011) doi:10.1201/b11448-20.

101. Moskvin, V., Cheng, C. W., Fanelli, L., Zhao, L. & Das, I. J. A semi-empirical model for the therapeutic range shift estimation caused by inhomogeneities in proton beam therapy. *J. Appl. Clin. Med. Phys.* **13**, 3–12 (2012).

102. Uries, M., Goiteins, M., Holleyo, W. R. & Cheno, G. T. Y. Related content Degradation of the Bragg peak due to inhomogeneities Degradation of the Bragg peak due to inhomogeneitiest. *Phys. Med. Biol.* **31**, 1–15 (1986).

103. Baro, J., Sempau, J., Fernandez-Varea, J. M. & Salvat, F. PENELOPE: An algorithm for Monte Carlo simulation of the penetration and energy loss of electrons and positrons in matter. *Nucl. Instruments Methods Phys. Res. B1* **100**, 31–46 (1995).

104. Allison, J. *et al.* Recent developments in G EANT 4. *Nucl. Instruments Methods Phys. Res. A R* **835**, 186–225 (2016).

105. Lagzda, A. *et al.* Influence of heterogeneous media on Very High Energy Electron (VHEE) dose penetration and a Monte Carlo-based comparison with existing radiotherapy modalities. *Nucl. Instruments Methods Phys. Res. Sect. B Beam Interact. with Mater. Atoms* **482**, 70–81 (2020).

106. Glinec, Y., Faure, J. & Malka, V. Radiotherapy with laser-plasma accelerators : Monte Carlo simulation of dose deposited by an experimental quasimonoenergetic electron beam. *Med. Phys.* **33**, 155–162 (2006).

107. Humphries, S. 3. Electric and Magnetic Forces. in *Principles of Charged Particle Acceleration* 104–159 (Dover Publications, 2012).

108. Kokurewicz, K. *et al.* Focused very high-energy electron beams as a novel radiotherapy modality for producing high-dose volumetric elements. *Sci. Rep.* **9**, 1–10 (2019).

109. Wiedemann, H. Particle Dynamics in Electro-Magnetic Fields. in *Particle Accelerator Physics* (eds. Hassani, S. et al.) 99–124 (Springer International Publishing, 2015).

110. Bert, C. & Durante, M. Motion in radiotherapy : particle therapy. *Phys. Med. Biol.* **56**, 113–144 (2011).

111. Hornsey, S. & Bewley, D. K. Hypoxia in mouse intestine induced by electron irradiation at high dose- rates. *Int. J. Radiat. Biol. Relat. Stud. Physics, Chem. Med.* **19**, 479–483 (1971).

112. Field, S. B. & Bewley, D. K. Effects of dose-rate on the radiation response of rat skin. *Int. J. Radiat. Biol. Relat. Stud. Physics, Chem. Med.* **26**, 259–267 (1974).

113. Hendry, J. H., Moore, J. V., Hodgson, B. W. & Keene, J. P. The constant low oxygen concentration in all the target cells for mouse tail radionecrosis. *Radiat. Res.* **92**, 172–181 (1982).

114. Montay-Gruel, P. *et al.* Irradiation in a flash: Unique sparing of memory in mice after whole brain irradiation with dose rates above 100 Gy/s. *Radiother. Oncol.* **124**, 365–369 (2017).

115. Vozenin, M. *et al.* The advantage of FLASH radiotherapy confirmed in

mini-pig and cat-cancer patients. *Clin. Cancer Res.* **25**, 35–42 (2019).

116. Bourhis, J. *et al.* Treatment of a first patient with FLASH-radiotherapy. *Radiother. Oncol.* **139**, 18–22 (2019).

117. Maxim, P. G., Keall, P. & Cai, J. FLASH radiotherapy: Newsflash or flash in the pan? *Med. Phys.* **46**, 4287–4290 (2019).

118. Bourhis, J. *et al.* Clinical translation of FLASH radiotherapy: Why and how? *Radiother. Oncol.* **139**, 11–17 (2019).

119. Lempart, M. *et al.* Modifying a clinical linear accelerator for delivery of ultra-high dose rate irradiation. *Radiother. Oncol.* **139**, 40–45 (2019).

120. Gonçalves Jorge, P. *et al.* Dosimetric and preparation procedures for irradiating biological models with pulsed electron beam at ultra-high dose-rate. *Radiother. Oncol.* **139**, 34–39 (2019).

121. Montay-Gruel, P. *et al.* X-rays can trigger the FLASH effect: Ultra-high dose-rate synchrotron light source prevents normal brain injury after whole brain irradiation in mice. *Radiother. Oncol.* **129**, 582–588 (2018).

122. Buonanno, M., Grilj, V. & Brenner, D. J. Biological effects in normal cells exposed to FLASH dose rate protons. **139**, 51–55 (2019).

123. Maxim, P. G., Tantawi, S. G. & Loo, B. W. PHASER : A platform for clinical translation of FLASH cancer radiotherapy. *Radiother. Oncol.* **139**, 28–33 (2019).

124. Schüler, E. *et al.* Experimental Platform for Ultra-high Dose Rate FLASH Irradiation of Small Animals Using a Clinical Linear Accelerator. *Int. J. Radiat. Oncol. Biol. Phys.* **97**, 195–203 (2017).

125. Bortfeld, T. & Schlegel, W. Physics in Medicine & Biology Related content An analytical approximation of depth - dose distributions for therapeutic proton beams for therapeutic proton beams. (1996).

126. Bortfeld, T. An analytical approximation of the Bragg curve for therapeutic proton beams. *Med. Phys.* **24**, 2024–2033 (1997).

127. Paganetti, H. Range uncertainties in proton therapy and the role of Monte Carlo simulations. *Phys. Med. Biol.* **57**, (2012).

128. Andreo, P. Monte Carlo simulations in radiotherapy dosimetry. *Radiat. Oncol.* **13**, 1–15 (2018).

129. Chetty, I. J. *et al.* Report of the AAPM Task Group No. 105: Issues associated with clinical implementation of Monte Carlo-based photon and electron external beam treatment planning. *Med. Phys.* **34**, 4818–4853 (2007).

130. Frass, W. C4: Particle Physics Major Option Passage of Particles Through Matter. (2009).

131. Andreo, P. *et al.* External Photon Beams: Physical Aspects. in *Radiation Oncology Physics: A Handbook for Teachers and Students* (ed. Podgorsak, E. B.) 161–218 (International Atomic Energy Agency, 2005).

132. Gottschalk, B. Physics of Proton Interactions in Matter. in *Proton*

Therapy Physics (ed. Paganetti, H.) 19–60 (CRC Press, 2012).

133. Andreo, P. *et al.* Electron Beams: Physical and Clinical Aspects. in *Radiation Oncology Physics: A Handbook for Teachers and Students* (ed. Podgorsak, E. B.) 273–300 (International Atomic Energy Agency, 2005).

134. Khan, F. M. *et al.* Clinical electron-beam dosimetry: Report of AAPM Radiation Therapy Committee Task Group No. 25. *Med. Phys.* **18**, 73–109 (1991).

135. Barbu, A. & Song-Chun, Z. Introduction to Monte Carlo Methods. in *Monte Carlo Methods* 1–18 (Springer, 2020). doi:10.1145/1953611.1953626.

136. Spezi, E. & Lewis, G. An overview of Monte Carlo treatment planning for radiotherapy. *Radiat. Prot. Dosimetry* **131**, 123–129 (2008).

137. Faddegon, B. *et al.* The TOPAS tool for particle simulation, a Monte Carlo simulation tool for physics, biology and clinical research. *Phys. Medica* **72**, 114–121 (2020).

138. Allison, J. *et al.* Recent developments in GEANT4. *Nucl. Instruments Methods Phys. Res. Sect. A Accel. Spectrometers, Detect. Assoc. Equip.* **835**, 186–225 (2016).

139. Allison, J. *et al.* Geant4 developments and applications. *IEEE Trans. Nucl. Sci.* **53**, 270–278 (2006).

140. Geant4 Collaboration. Book For Application Developers, Release 10.6. 437 (2019).

141. Fippel, M. & Soukup, M. A Monte Carlo dose calculation algorithm for proton therapy. *Med. Phys.* **31**, 2263–2273 (2004).

142. Perl, J., Shin, J., Schuemann, J., Ramos-Méndez, J. & Hall, D. *TOPAS Documentation, Release 3.1*. (2020).

143. Berger, M. J. *et al. Stopping powers and ranges for protons and alpha particles (ICRU Report 49). International Commission on Radiation Units and Measurements* (1993).

144. PSTAR - Stopping-Power and Range Tables for Protons. *National Institute of Standards and Technology* https://physics.nist.gov/PhysRefData/Star/Text/PSTAR.html.

145. Meigooni, A. S. & Das, I. J. Parametrisation of depth dose for electron beams. *Phys. Med. Biol.* **32**, 761–768 (1987).

146. Testa, M. *et al.* Range verification of passively scattered proton beams based on prompt gamma time patterns. *Phys. Med. Biol.* **59**, 4181–4195 (2014).

147. Testa, M. *et al.* Experimental validation of the TOPAS Monte Carlo system for passive scattering proton therapy. *Med. Phys.* **40**, (2013).

148. Willers, H. *et al.* Toward a variable RBE for proton beam therapy. *Radiother. Oncol.* **128**, 68–75 (2018).

149. Radiotherapy. *The Christie NHS Foundation Trust*

https://www.christie.nhs.uk/patients-and-visitors/your-treatment-and-care/treatments/radiotherapy (2020).

150. Dalton Nuclear Institute. *University of Manchester* https://www.dalton.manchester.ac.uk/research/ (2020).

151. CERN. CLEAR. https://clear.cern/ (2020).

152. Summers, D. K. The Anatomy of Bacterial Plasmids. in *The Biology of Plasmids* 1–19 (Blackwell Science Ltd., 1996). doi:10.1002/9781444313741.

153. Rogers, K. Eukaryote. *Britannica* https://www.britannica.com/science/eukaryote (2020).

154. Hayes, F. The function and organisation of plasmids. in *E. coli Plasmid Vectors* (eds. Casali, N. & Preston, A.) (Humana Press, 2003).

155. Thomas, C. M. & Summers, D. Bacterial Plasmids. *Encycl. Life Sci.* 1–9 (2008) doi:10.1002/9780470015902.a0000468.pub2.

156. McMahon, S. J. & Currell, F. J. A robust curve-fitting procedure for the analysis of plasmid dna strand break data from gel electrophoresis. *Radiat. Res.* **175**, 797–805 (2011).

157. Vyšín, L. *et al.* Proton-induced direct and indirect damage of plasmid DNA. *Radiat. Environ. Biophys.* **54**, 343–352 (2015).

158. Davis, L. G., Dibner, M. D. & Battey, J. F. Agarose gel electrophoresis. in *Basic Methods in Molecular Biology* 58–61 (Elsevier Science Publishing, 1986). doi:10.1101/pdb.prot100404.

159. Folkard, M. *et al.* Measurement of DNA damage by electrons with energies between 25 and 4000 EV. *Int. J. Radiat. Biol.* **64**, 651–658 (1993).

160. Michael, B. D. *et al.* Action spectra for single- and double-strand break induction in plasmid DNA: Studies using synchrotron radiation. *Int. J. Radiat. Biol.* **66**, 569–572 (1994).

161. Prise, K. M. *et al.* Critical energies for SSB and DSB induction in plasmid DNA by low-energy photons: Action spectra for strand-break induction in plasmid DNA irradiated in vacuum. *Int. J. Radiat. Biol.* **76**, 881–890 (2000).

162. Urushibara, A. *et al.* LET dependence of the yield of single-, double-strand breaks and base lesions in fully hydrated plasmid DNA films by 4He(2+) ion irradiation. *Int. J. Radiat. Biol.* **84**, 23–33 (2008).

163. Scholz, V., Weidner, J., Kohnlein, W., Frekers, D. & Wortche, H. J. Induction of single- and double-strand breaks in plasmid DNA by monoenergetic alpha-particles with energies below the Bragg maximum. *Z Naturforsch C J Biosci* **52**, 364–372 (1997).

164. Garty, G. *et al.* A nanodosimetric model of radiation-induced clustered DNA damage yields. *Phys. Med. Biol.* **55**, 761–781 (2010).

165. Francis, Z., Villagrasa, C. & Clairand, I. Simulation of DNA damage clustering after proton irradiation using an adapted DBSCAN algorithm. *Comput. Methods Programs Biomed.* **101**, 265–270 (2011).

166. Nikjoo, H. & Lindborg, L. RBE of low energy electrons and photons. (2010) doi:10.1088/0031-9155/55/10/R01.

167. Davis, L. G., Dibner, M. D. & Battey, J. F. pBR322. in *Basic Methods in Molecular Biology* 24–25 (Elsevier Science Publishing, 1986). doi:10.1016/b978-0-444-01082-7.50010-2.

168. Leloup, C. *et al.* Evaluation of lesion clustering in irradiated plasmid DNA. *Int. J. Radiat. Biol.* **81**, 41–54 (2005).

169. Souici, M. *et al.* Single- and double-strand breaks of dry DNA exposed to protons at Bragg-peak energies. *J. Phys. Chem. B* **121**, 497–507 (2017).

170. pBR322 Vector. *New England BioLabs* https://www.neb.uk.com/products/neb-catalogue/nucleic-acids-%28cloning%29/pbr322-vector (2020).

171. Manchester Cancer Research Centre. http://www.mcrc.manchester.ac.uk/Home (2020).

172. Soares, C. G. Radiochromic film dosimetry. *Radiat. Meas.* **41**, 100–116 (2006).

173. Gafchromic. *Gafchromic dosimetry media, type EBT-XD*. (2020).

174. Gafchromic. GAFChromic™ EBT3 film specifications. (2014).

175. EPSON. EPSON Expression 10000XL Pro. https://www.epson.co.uk/products/scanners/business-scanners/epson-expression-10000xl-pro#specifications (2020).

176. Physics Dosimetry Quality Manual - Work instructions for using, scanning and calibrating Gafchromic films. 1–5 (2017).

177. Sjobak, K. N. *et al.* Status of the CLEAR electron beam user facility at CERN. *Int. Part. Accel. Conf.* 983–986 (2019) doi:10.18429/JACoW-IPAC2019-MOPTS054.

178. Lindstrøm, C. A. *et al.* Emittance preservation in an aberration-free active plasma lens. *Phys. Rev. Lett.* **121**, 1–6 (2018).

179. Curcio, A. *et al.* Beam-based sub-THz source at the CERN linac electron accelerator for research facility. *Phys. Rev. Accel. Beams* **22**, 1–10 (2019).

180. Kokurewicz, K. *et al.* Focused very high-energy electron beams as a novel radiotherapy modality for producing high-dose volumetric elements. *Sci. Rep.* **9**, 1–10 (2019).

181. CERN. VESPER. (2017).

182. Model 812 Irradiator. *Foss Therapy Services, Inc.* http://www.fosstherapyservices.net/id12.html (2020).

183. Elekta Synergy. *Elekta* (2020).

184. Chang, D. S., Lasley, F. D., Das, I. J., Mendonca, M. S. & Dynlacht, J. R. Production and properties of radiation. in *Basic Radiotherapy Physics and Biology* 23–34 (Springer, 2014). doi:10.1007/978-3-319-06841-1.

185. Mayles, P., Nahum, A. & Rosenwald, J.-C. From measurements to

calculations. in *Handbook of Radiotherapy Physics: Theory and Practice* 433–438 (CRC Press, 2007).

186. Serwer, P. Agarose gels: Properties and use for electrophoresis. *Electrophoresis* **4**, 375–382 (1983).

187. Gas, B. ELECTROPHORESIS | Principles. in *Encyclopedia of Analytical Sciences* (eds. Worsfold, P., Townshend, A. & Poole, C. B. T.-E. of A. S. (Second E.) 363–370 (Elsevier, 2005). doi:https://doi.org/10.1016/B0-12-369397-7/00121-7.

188. Thermo Fisher. *USER GUIDE SYBR ™ Safe DNA Gel Stain*. (2016).

189. Supercoiled DNA Ladder. *New England BioLabs* https://international.neb.com/products/n0472-supercoiled-dna-ladder#Product Information (2020).

190. 1 kb plus ladder. *New England BioLabs* https://international.neb.com/products/n3200-1-kb-plus-dna-ladder#Product Information (2020).

191. EcoRI. *New England BioLabs2* https://international.neb.com/products/r0101-ecori#Product Information (2020).

192. Schindelin, J. *et al.* Fiji - an open platform for biological image analysis. *Nat. Methods* **9**, (2009).

193. Schneider, C. A., Rasband, W. S. & Eliceiri, K. W. NIH Image to ImageJ: 25 years of image analysis. *Nat. Methods* **9**, 671–675 (2012).

194. Rueden, C. T. *et al.* ImageJ2: ImageJ for the next generation of scientific image data. *BMC Bioinformatics* **18**, 1–26 (2017).

195. Cowan, R., Collis, C. M. & Grigg, G. W. Breakage of double-stranded DNA due to single-stranded nicking. *J. Theor. Biol.* **127**, 229–245 (1987).

196. Inc., W. R. *Mathematica*. (Wolfram Research Inc., 2017).

197. Ou, H., Zhang, B. & Zhao, S. Monte Carlo simulation of the relative biological effectiveness and DNA damage from a 400 MeV/u carbon ion beam in water. *Appl. Radiat. Isot.* **136**, 1–9 (2018).

198. Herskind, C. *et al.* Biology of high single doses of IORT: RBE, 5 R's, and other biological aspects. *Radiat. Oncol.* **12**, 1–14 (2017).

199. Spadinger, I. & Palcic, B. The relative biological effectiveness of 60Co γ-rays, 55 kVp X-rays, 250 kVp X-rays, and 11 MeV electrons at low doses. *Int. J. Radiat. Biol.* **61**, 345–353 (1992).

200. Zackrisson, B., Johansson, B. & Ostbergh, P. Relative biological effectiveness of high-energy photons (up to 50 MV) and electrons (50 MeV). *Radiat. Res.* **128**, 192–196 (1991).

201. ESTAR - Stopping-power and range tables for electrons. *National Institute of Standards and Technology* https://physics.nist.gov/cgi-bin/Star/e_table.pl.

202. Town, C. D. Effect of high dose rates on survival of mammalian cells.

Nature **215**, 847–848 (1967).

203. Hanton, F. *et al.* DNA DSB Repair Dynamics following Irradiation with Laser-Driven Protons at Ultra-High Dose Rates. *Sci. Rep.* **9**, 1–10 (2019).

204. Beyreuther, E. *et al.* Radiobiological response to ultra-short pulsed megavoltage electron beams of ultra-high pulse dose rate. *Int. J. Radiat. Biol.* **91**, 643–652 (2015).

205. Yogo, A. *et al.* Application of laser-accelerated protons to the demonstration of DNA double-strand breaks in human cancer cells. *Appl. Phys. Lett.* **94**, 1–3 (2009).

206. Babayan, N. *et al.* Dose-rate effect of ultrashort electron beam radiation on DNA damage and repair in vitro. *J. Radiat. Res.* **58**, 894–897 (2017).

207. Ozols, A., Prise, K. M. & Michael, B. D. A comparison of the radiosensitivity of relaxed and supercoiled plasmid DNA. *Int. J. Radiat. Biol.* **75**, 83–90 (1999).

208. Rigaud, O. *et al.* Exploring ultrashort high-energy electron-induced damage in human carcinoma cells. *Cell Death Dis.* **1**, 1–3 (2010).

209. Ward, J. F. Biochemistry of DNA Lesions. *Radiat. Res.* **104**, 103–111 (1985).

210. Roots, R. & Okada, S. Estimation of Life Times and Diffusion Distances of Radicals Involved in X-Ray-Induced DNA Strand Breaks or Killing of Mammalian Cells. *Radiat. Res.* **64**, 306–320 (1975).

211. Chang, D. S., Lasley, F. D., Das, I. J., Mendonca, M. S. & Dynlacht, J. R. Cell death and survival assays. in *Basic Radiotherapy Physics and Biology* 211–220 (Springer, 2014).

212. Henthorn, N. T. *et al.* Clinically relevant nanodosimetric simulation of DNA damage complexity from photons and protons. *RSC Adv.* **9**, 6845–6858 (2019).

213. Rockne, R. C. & Frankel, P. Mathematical Modeling in Radiation Oncology. in *Advances in Radiation Oncology* (eds. Wong, J. Y. C., Schultheiss, T. E. & Radany, E. H.) 255–271 (Springer, 2017).

214. Bodgi, L. *et al.* Mathematical models of radiation action on living cells: From the target theory to the modern approaches. A historical and critical review. *J. Theor. Biol.* **394**, 93–101 (2016).

215. Guan, F. *et al.* A mechanistic relative biological effectiveness model-based biological dose optimization for charged particle radiobiology studies. *Phys. Med. Biol.* **64**, (2019).

216. Lea, D. E. *Actions of radiations on living cells*. (Cambridge University Press, 1955).

217. Brenner, D. J., Hlatky, L. R., Hahnfeldt, P. J., Huang, Y. & Sachs, R. K. The linear-quadratic model and most other common radiobiological models result in similar predictions of time-dose relationships. *Radiat. Res.* **150**, 83–91 (1998).

218. Zaider, M. There is no mechanistic basis for the use of the linear-

quadratic. *Med. Phys.* **25**, 791–792 (1998).

219. Tobias, C. A. The Repair-Misrepair Model in Radiobiology : Comparison to Other Models. *Radiat. Res.* **104**, 77–95 (1985).

220. Curtis, S. B. Lethal and Potentially Lethal Lesions Induced by Radiation -- A Unified Repair Model. *Radiat. Res.* **106**, 252–270 (1986).

221. Jeggo, P. A. & Löbrich, M. DNA double-strand breaks: Their cellular and clinical impact? *Oncogene* **26**, 7717–7719 (2007).

222. Scholz, M., Kellerer, A. M., Kraft-Weyrather, W. & Kraft, G. Computation of cell survival in heavy ion beams for therapy: The model and its approximation. *Radiat. Environ. Biophys.* **36**, 59–66 (1997).

223. Hawkins, R. B. A statistical theory of cell killing by radiation of varying linear energy transfer. *Radiat. Res.* **140**, 366–374 (1994).

224. Kase, Y. *et al.* Biophysical calculation of cell survival probabilities using amorphous track structure models for heavy-ion irradiation. *Phys. Med. Biol.* **53**, 37–59 (2008).

225. Dahle, T. J. *et al.* Sensitivity study of the microdosimetric kinetic model parameters for carbon ion radiotherapy. *Phys. Med. Biol.* **63**, (2018).

226. Elsisser, T. & Scholz, M. Cluster Effects within the Local Effect Model. *Radiat. Res.* **167**, 319–329 (2007).

227. Elsässer, T., Krämer, M. & Scholz, M. Accuracy of the Local Effect Model for the Prediction of Biologic Effects of Carbon Ion Beams In Vitro and In Vivo. *Int. J. Radiat. Oncol. Biol. Phys.* **71**, 866–872 (2008).

228. Elsässer, T. *et al.* Quantification of the relative biological effectiveness for ion beam radiotherapy: Direct experimental comparison of proton and carbon ion beams and a novel approach for treatment planning. *Int. J. Radiat. Oncol. Biol. Phys.* **78**, 1177–1183 (2010).

229. Friedrich, T., Durante, M. & Scholz, M. The Local Effect Model – Principles and Applications. 5–7 (2013).

230. Stewart, R. D. *et al.* A comparison of mechanism-inspired models for particle relative biological effectiveness (RBE). *Med. Phys.* **45**, 925–952 (2018).

231. Curtis, S. B. Introduction to Track Structure and z*2 /ß2. (2016).

232. Hill, M. A. Radiation damage to DNA: The important of track structure. *Radiat. Meas.* **31**, 15–23 (1999).

233. Nikjoo, H., Uehara, S., Emfietzoglou, D. & Cucinotta, F. A. Track-structure codes in radiation research. *Radiat. Meas.* **41**, 1052–1074 (2006).

234. Nikjoo, H., O'Neill, P., Terrissol, M. & Goodhead, D. T. Quantitative modelling of DNA damage using Monte Carlo track structure method. *Radiat. Environ. Biophys.* **38**, 31–38 (1999).

235. Bernal, M. A. *et al.* Track structure modeling in liquid water: A review of the Geant4-DNA very low energy extension of the Geant4 Monte Carlo

simulation toolkit. *Phys. Medica* **31**, 861–874 (2015).

236. Uehara, S., Nikjoo, H. & Goodhead, D. T. Cross-sections for water vapour for the Monte Carlo electron track structure code from 10 eV to the MeV region. *Phys. Med. Biol.* **38**, 1841–1858 (1993).

237. Friedland, W., Jacob, P. & Kundrát, P. Stochastic simulation of DNA double-strand break repair by non-homologous end joining based on track structure calculations. *Radiat. Res.* **173**, 677–688 (2010).

238. Friedland, W., Dingfelder, M., Kundrát, P. & Jacob, P. Track structures, DNA targets and radiation effects in the biophysical Monte Carlo simulation code PARTRAC. *Mutat. Res. - Fundam. Mol. Mech. Mutagen.* **711**, 28–40 (2011).

239. Siddiqi, M. A. & Bothe, E. Single- and Double-Strand Break Formation in DNA Irradiated in Aqueous Solution : Dependence on Dose and OH Radical Scavenger Concentration. *Radiat. Res.* **112**, 449–463 (1987).

240. Boudaïffa, B., Cloutier, P., Hunting, D., Huels, M. A. & Sanche, L. Resonant formation of DNA strand breaks by low-energy (3 to 20 eV) electrons. *Science (80-.).* **287**, 1658–1660 (2000).

241. Friedland, W., Jacob, P. & Kundrát, P. Stochastic simulation of DNA double-strand break repair by non-homologous end joining based on track structure calculations. *Radiat. Res.* **173**, 677–688 (2010).

242. Lieber, M. R., Ma, Y., Pannicke, U. & Schwarz, K. Mechanism and regulation of human non-homologous DNA end-joining. *Nat. Rev. Mol. Cell Biol.* **4**, 712–720 (2003).

243. D'Andrea, A. D. DNA Repair Pathways and Human Cancer. in *The Molecular Basis of Cancer: Fourth Edition* 47–66 (Elsevier Saunders, 2014). doi:10.1016/B978-1-4557-4066-6.00004-4.

244. Ingram, S. P. *et al.* Mechanistic modelling supports entwined rather than exclusively competitive DNA double-strand break repair pathway. *Sci. Rep.* **9**, 1–13 (2019).

245. Smith, E. A. K. *et al.* In Silico Models of DNA Damage and Repair in Proton Treatment Planning: A Proof of Concept. *Sci. Rep.* **9**, 1–10 (2019).

246. Incerti, S. *et al.* Geant4-DNA example applications for track structure simulations in liquid water: A report from the Geant4-DNA Project. *Med. Phys.* **45**, 722–739 (2018).

247. Incerti, S. *et al.* Comparison of GEANT4 very low energy cross section models with experimental data in water. *Med. Phys.* **37**, 4692–4708 (2010).

248. Low Energy Electromagnetic Physics Working Group. *GEANT4* https://geant4.web.cern.ch/collaboration/working_groups/low_energy_electromagnetic (2019).

249. Electromagnetic Physics. *GEANT4* https://geant4.web.cern.ch/collaboration/working_groups/electromagnetic (2020).

250. Chauvie, S. *et al.* GEANT4 physics processes for microdosimetry simulation: Design foundation and implementation of the first set of models. *IEEE Trans. Nucl. Sci.* **54**, 2619–2628 (2007).

251. Francis, Z. *et al.* Calculation of lineal energies for water and DNA bases using the Rudd model cross sections integrated within the Geant4-DNA processes. *J. Appl. Phys.* **122**, 1–10 (2017).

252. Dingfelder, M. Track structure simulations for charge particles. *Health Phys.* **103**, 1–7 (2012).

253. Rudd, M. E., Kim, Y. K., Madison, D. H. & Gay, T. J. Electron production in proton collisions with atoms and molecules: Energy distributions. *Rev. Mod. Phys.* **64**, 441–490 (1992).

254. Miller, J. H. & Green, A. E. S. Proton Energy Degradation in Water Vapor. *Radiat. Res.* **54**, 343–363 (1973).

255. Processes. *GEANT4-DNA Collaboration* http://geant4-dna.in2p3.fr/styled-3/styled-8/index.html (2020).

256. Wang, Y. *et al.* The influence of Geant4-DNA toolkit parameters on electron microdosimetric track structure. *J. Radiat. Res.* **61**, 58–67 (2019).

257. Karamitros, M. *et al.* Diffusion-controlled reactions modeling in Geant4-DNA. *J. Comput. Phys.* **274**, 841–882 (2014).

258. Karamitros, M. *et al.* Modeling Radiation Chemistry in the Geant4 Toolkit. *Prog. Nucl. Sci. Technol.* **2**, 503–508 (2011).

259. Bernal, M. A. & Liendo, J. A. An investigation on the capabilities of the PENELOPE MC code in nanodosimetry. *Med. Phys.* **36**, 620–625 (2009).

260. Charlton, D. E., Nikjoo, H. & Humm, J. L. Calculation of initial yields of single- and double-strand breaks in cell nuclei from electrons, protons and alpha particles. *Int. J. Radiat. Biol.* **56**, 1–19 (1989).

261. McNamara, A. *et al.* Validation of the radiobiology toolkit TOPAS-nBio in simple DNA geometries. *Phys. Medica* **33**, 207–215 (2017).

262. Henthorn, N. T. *et al.* Nanodosimetric Simulation of Direct Ion-Induced DNA Damage Using Different Chromatin Geometry Models. *Radiat. Res.* **188**, 770–783 (2017).

263. Nikjoo, H. *et al.* Modelling of Auger-induced DNA damage by incorporated 125I. *Acta Oncol. (Madr).* **35**, 849–856 (1996).

264. Chatzipapas, K. P. *et al.* Quantification of DNA double-strand breaks using Geant4-DNA. *Med. Phys.* **46**, 405–413 (2019).

265. Georgakilas, A. G., O'Neill, P. & Stewart, R. D. Induction and repair of clustered DNA lesions: What do we know so far? *Radiat. Res.* **180**, 100–109 (2013).

266. Xu, X. *et al.* Direct observation of damage clustering in irradiated DNA with atomic force microscopy. *Nucleic Acids Res.* **48**, 18–27 (2020).

267. McNamara, A. L. *et al.* Geometrical structures for radiation biology research as implemented in the TOPAS-nBio toolkit. *Phys. Med. Biol.* **63**,

(2018).

268. Sotiropoulos, M. *et al.* Modelling direct DNA damage for gold nanoparticle enhanced proton therapy. *Nanoscale* **9**, 18413–18422 (2017).

269. Low Energy Electromagnetic Physics - Livermore. *GEANT42* https://geant4.web.cern.ch/node/1619 (2020).

Appendix

Attached is a pre-print version of a paper 'Evaluating Very High Energy Electron RBE from nanodosimetric pBR322 plasmid DNA damage.' This paper comprises work done in Chapters 4 and 5 and was published on 8th February 2021.

https://doi.org/10.1038/s41598-021-82772-6

Evaluating Very High Energy Electron RBE from nanodosimetric pBR322 plasmid DNA damage

K. L. Small*[1,2], N. T. Henthorn[3,4], D. Angal-Kalinin[1,2,7], A. L. Chadwick[3,4], E. Santina[3,4], A. Aitkenhead[3,5], K. J. Kirkby[3,4], R. J. Smith[2,7], M. Surman[2,7], J. Jones[2,7], W. Farabolini[6,8], R. Corsini[6], D. Gamba[6], A. Gilardi[6,9], M. J. Merchant[3,4], R. M. Jones[1,2]

[1] The University of Manchester, Manchester, United Kingdom

[2] The Cockcroft Institute, Daresbury, United Kingdom

[3] Division of Cancer Sciences, School of Medical Sciences, Faculty of Biology, Medicine and Health, The University of Manchester, United Kingdom

[4] The Christie NHS Foundation Trust, Manchester Academic Health Science Centre, Manchester, United Kingdom

[5] Christie Medical Physics and Engineering, The Christie NHS Foundation Trust, Manchester, United Kingdom

[6] CERN, Geneva, Switzerland

[7] ASTeC, STFC Daresbury Laboratory, Daresbury, Warrington, United Kingdom

[8] CEA Saclay, IRFU-DACM, France

[9] Federico II, DIETI, University of Napoli, Napoli, Italy

E-mail: kristina.small@manchester.ac.uk

Abstract

This paper presents the first plasmid DNA irradiations carried out with Very High Energy Electrons (VHEE) over 100-200 MeV at the CLEAR user facility at CERN to determine the Relative Biological Effectiveness (RBE) of VHEE. DNA damage yields were measured in dry and aqueous environments to determine that ~99% of total DNA breaks were caused by indirect effects, consistent with other published measurements for protons and photons. Double-Strand Break (DSB) yield was used as the biological endpoint for RBE calculation, with values found to be consistent with established radiotherapy modalities. Similarities in physical damage between VHEE and conventional modalities gives confidence that biological effects of VHEE will also be similar – key for clinical implementation. Damage yields were used as a baseline for track structure simulations of VHEE plasmid irradiation using GEANT4-DNA. Current models for DSB yield have shown reasonable agreement with experimental values. The growing interest in FLASH radiotherapy motivated a study into DSB yield variation with dose rate following VHEE irradiation. No significant variations were observed between conventional and FLASH dose rate irradiations, indicating that no FLASH effect is seen under these conditions.

Keywords: Very high energy electrons, FLASH, radiobiology, plasmid irradiation, RBE

Introduction

In the UK, 27% of cancer patients receive radiotherapy as part of their treatment[1], primarily with 12 MV X-rays though proton therapy treatments are increasing[2]. In the past two decades, developments in high-gradient linear accelerator technology[3,4] has motivated research into the use of Very High Energy Electrons (VHEE), typcially defined as electrons in the energy range 100-250 MeV, as a radiotherapy modality[5]. By adapting existing high-gradient accelerator technology from linear colliders for high energy particle physics, medical accelerators with accelerating gradients of ~100 MV/m could be capable of producing 250 MeV electrons with an accelerator length of 3-4 m.

VHEE radiotherapy has been shown to exhibit potential advantages such as sufficient penetrative range to treat deep-seated tumours, reduced lateral penumbra, relative insensitivity to tissue inhomogeneities[6] and rapid treatment delivery[7]. This makes VHEE an exciting potential radiotherapy modality and particularly applicable for tumours in highly heterogeneous regions such as the lung. The ability to deliver treatment rapidly makes VHEE a compatible modality for ultra-high dose rate radiotherapy (>40 Gy/s), referred to as FLASH radiotherapy[8]. At such high dose rates, side effects in normal, healthy tissue have been shown in several *in vivo* models to be drastically reduced while tumour control rates are maintained[9-11]. Although Bourhis *et al.*[12] have presented the first patient treatment by FLASH with favourable outcomes, further understanding of the mechanisms and long-term effects are required before widespread clinical implementation. Combining FLASH therapy with VHEE could provide a potential method to treat tumours in heterogeneous regions while exploiting the benefits of the FLASH effect[13].

The primary mechanism behind radiotherapy is considered to be DNA damage. Ionising radiation can cause direct or indirect damage to DNA: direct damage is caused by energy deposition from the radiation directly to the DNA structure while indirect damage is caused by free radical attack following the dissociation of water molecules by the radiation, in particular OH^- due to their high reaction rate with DNA components[14]. Indirect damage is the main contributor to the total damage following exposure to low Linear Energy Transfer (LET) radiation[15]. The cell is equipped with a complex machinery to attempt to resolve this damage, with Single-Strand Breaks (SSBs) and Double-Strand Breaks (DSBs)[16] being most difficult to repair. If these breaks are not repaired or are misrepaired, the cell may be unable to function or replicate correctly, potentially leading to cell death or senescence[17]. If physical damage resulting from VHEE irradiation is comparable to damage caused by traditional radiotherapy modalities, this will give confidence that the chemical and biological effects of VHEE are also comparable.

For successful clinical implementation of VHEE, a thorough radiobiological understanding is required along with comparison to well-established radiotherapy modalities through Relative Biological Effectiveness (RBE) to determine if dose prescription for VHEE requires biological augmentation. RBE is defined as the ratio of biological effectiveness of one type of ionizing radiation relative to another, conventionally ^{60}Co X-rays, given the same amount of absorbed energy (dose)[18]. This is measured using several endpoints, including DNA damage and, most commonly, cell survival[19].

This study presents the first pBR322 plasmid irradiations with VHEE beams, over a clinically relevant energy range. Plasmids are ring-like structures of DNA found in bacteria[20] and were employed to investigate the potential of VHEE to induce DNA damage due to their lack of repair mechanism and ability to study in aqueous and dry environments, allowing the decoupling of direct and indirect damage. Irradiations were carried out at the CERN Linear Electron Accelerator for Research (CLEAR) facility[21,22]. SSB and DSB yields were measured to determine how DNA damage varied with energy and environment. The DSB yields following both dry and aqueous irradiation were used as the biological endpoint for the calculation of VHEE RBE, which was compared to RBE of other radiotherapy modalities. A parameter variation study was then performed for a GEANT4-DNA plasmid irradiation model to determine the parameters which would result in DSB yields which best approximated the experimental data.

The capability of CLEAR to deliver radiation at ultra-high dose rates through ps pulses also allowed the investigation of damage caused to aqueous plasmid samples following irradiation at ultra-high and conventional dose rates. While there is a great deal of research available on ultra-high dose rate irradiation dating back to the 1960s[23], it typically involves cellular irradiation[24-29]. This study focuses on plasmid irradiation at conventional and ultra-high dose rates to determine the presence of a FLASH effect at the nanoscale. Such an effect would be expected to be a decrease in DNA damage yields however, as plasmid irradiation

experiments lack many of the key features that lead to the FLASH mechanism, it was not expected that such a decrease would be observed.

Results

Plasmid Stability during Transportation

For dry plasmid samples, the diluted plasmid solution was transported to CERN and dry samples prepared onsite. For wet samples, a shipment of pBR322 plasmid, held in a solution of 10 mM Tris-HCl and 1mM EDTA[30,31], was sent from New England BioLabs to CERN. This was then diluted and wet samples prepared onsite. For both wet and dry samples, control samples were prepared and stored at the Oglesby Cancer Research Centre.

Sham samples were prepared at CERN, mounted on to the sample holder but not directly exposed to the beam. Supercoiled (SC), open-circular (OC) and linear (L) plasmid proportions for control and sham samples were compared to determine the effect of transportation, preparation and indirect radiation exposure. The results are presented in Table 1.

Table 1 – Comparison of the proportions of supercoiled (SC), open-circular (OC) and linear (L) plasmid in control and sham (unirradiated samples transported to and from CLEAR) plasmid samples. Standard error based on three gel electrophoresis repeats and four control samples for each gel

Sample Type	SC	OC	L
Control (Dry)	0.867 ± 0.004	0.100 ± 0.003	0.033 ± 0.001
Sham (Dry)	0.270 ± 0.013	0.690 ± 0.011	0.038 ± 0.002
Control (Wet)	0.877 ± 0.008	0.096 ± 0.006	0.027 ± 0.002
Sham (Wet)	0.882 ± 0.008	0.091 ± 0.007	0.027 ± 0.001

The plasmid proportion data indicates that transportation in dilute solution did have a significant effect on the dry plasmid samples, with high proportions of open-circular plasmid observed compared to the control samples – indicating a relaxing of the plasmid structure, resulting in SSBs that are not caused by irradiation. Transportation had little effect on the linear plasmid proportion. The effects of transportation were not as severe on the aqueous samples due to transportation in undiluted buffer, which prevented the relaxation of the plasmid structure. Comparison of the dry and wet control samples indicate that the plasmid drying process does not result in significant damage to the plasmid structure.

Dry Sample Irradiations

The damage yields, calculated using the McMahon DNA damage fit[32], over 100-200 MeV are shown in Fig. 1a and 1b and in Table 2 below, with standard errors calculated based on three Agarose Gel Electrophoresis (AGE) repeats.

Table 2 – SSB and DSB yields following dry plasmid irradiation with 100-200 MeV electrons calculated using the McMahon DNA damage fit[32]. Standard error based on three AGE repeats

Energy (MeV)	LET (keV/µm)	SSB (Mbp^{-1} kGy^{-1})	DSB (Mbp^{-1} kGy^{-1})
100	0.2202	69.81 ± 8.72	3.66 ± 0.43
150	0.2238	80.30 ± 3.06	3.71 ± 0.11
200	0.2263	50.27 ± 4.19	3.83 ± 0.45

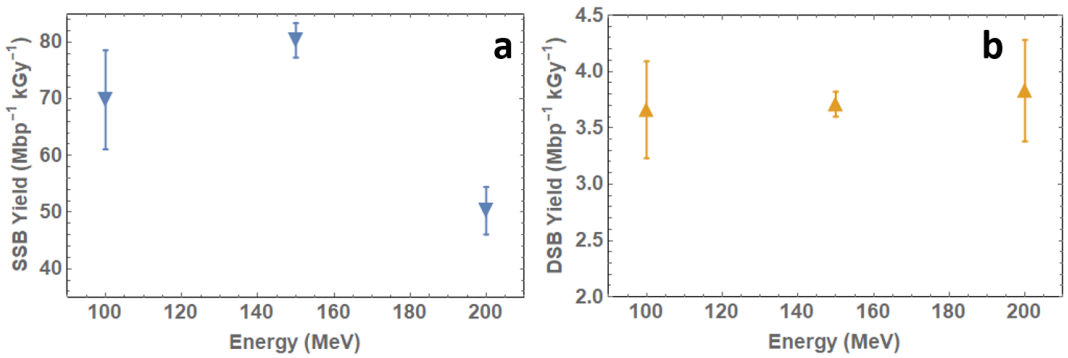

Figure 1 - a) Single-strand break yields and b) double-strand break yields for 100-200 MeV electron beam irradiation of dry pBR322 plasmid DNA based on McMahon data fitting[32]

Wet Sample Irradiations

Break yields were compared between plasmid DNA irradiated at a low dose rate (~0.5 Gy/s) and at FLASH dose rate (> 10^8 Gy/s). As discussed in the Introduction, significant differences in DSB yield were not anticipated due to the experimental conditions lacking key features understood to result in a FLASH effect. The plasmid was diluted as appropriate and samples placed in Eppendorf tubes. The SSB and DSB yields based on the McMahon fit are shown in Table 3 and Fig. 2.

Table 3 – Single- and double-strand break yields following aqueous plasmid irradiation with 100-200 MeV electrons at Conventional and FLASH dose rates, calculated using the

	VHEE Dose rate			
	Conventional (~0.5 Gy s^{-1})		FLASH (>10^8 Gy s^{-1})	
Energy (MeV)	**SSB (Mbp^{-1}Gy^{-1})**	**DSB(Mbp^{-1}Gy^{-1})**	**SSB (Mbp^{-1}Gy^{-1})**	**DSB (Mbp^{-1}Gy^{-1})**
100	15.42 ± 0.86	0.35 ± 0.02	20.31 ± 1.20	0.37 ± 0.03
150	17.63 ± 0.57	0.35 ± 0.03	18.74 ± 0.52	0.37 ± 0.04
200	20.19 ± 0.56	0.38 ± 0.02	21.22 ± 0.38	0.38 ± 0.02

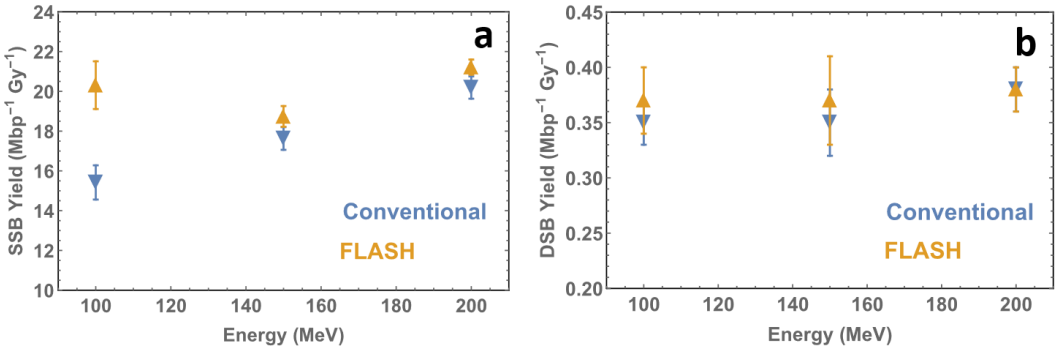

Figure 2 - a) Single-strand break yields and b) double-strand break yields for 100-200 MeV electron beam irradiation of wet pBR322 plasmid DNA based on data fitting to the McMahon fit[32]. Plasmids irradiated at Conventional (~0.5 Gy/s) and FLASH (>10^8 Gy/s) dose rates

McMahon[32] fit. Standard error based on six agarose gel electrophoresis repeats for 200 MeV and five for 150 and 100 MeV

To determine the contribution of direct and indirect effects to overall DNA damage, damage yields for dry and aqueous plasmid samples irradiated at Conventional dose rate were compared, with dry yields assumed to be caused by direct effects only and aqueous yields by both direct and indirect effects. The data is shown in Table 4, indicating that, as for protons and photons[31], indirect effects from VHEE cause > 99% of damage in aqueous solutions with low scavenging capacity.

Table 4 – Percentage of total DNA damage caused by indirect radiation effects for SSBs and DSBs

Energy (MeV)	% of SSBs from Indirect Damage	% of DSBs from Indirect Damage
100	99.54 ± 0.03	99.0 ± 0.05
150	99.54 ± 0.01	98.9 ± 0.07
200	99.75 ± 0.01	99.0 ± 0.05

RBE Calculation

DSB yields from dry and aqueous plasmid irradiations were used as the endpoint for calculating VHEE RBE[33], referred to from this point as RBE_{DSB}:

$$RBE_{DSB} = \phi_{e^-} / \phi_{\gamma} \quad (1)$$

where Y_{e^-} is the DSB yield following plasmid irradiation by electrons and Y_{γ} is the DSB yield following irradiation by ^{60}Co X-rays – measured as 3.27 ± 0.13 Mbp^{-1} kGy^{-1} for dry and 0.32 ± 0.02 Mbp^{-1} Gy^{-1} for wet plasmids based on experiments performed at the Dalton Nuclear Facility (UK)[34]. RBE_{DSB} values over the energy range 100-200 MeV are given in Table 5 below, along with values for other radiotherapy modalities[35-38] in Fig. 3 and Table 5.

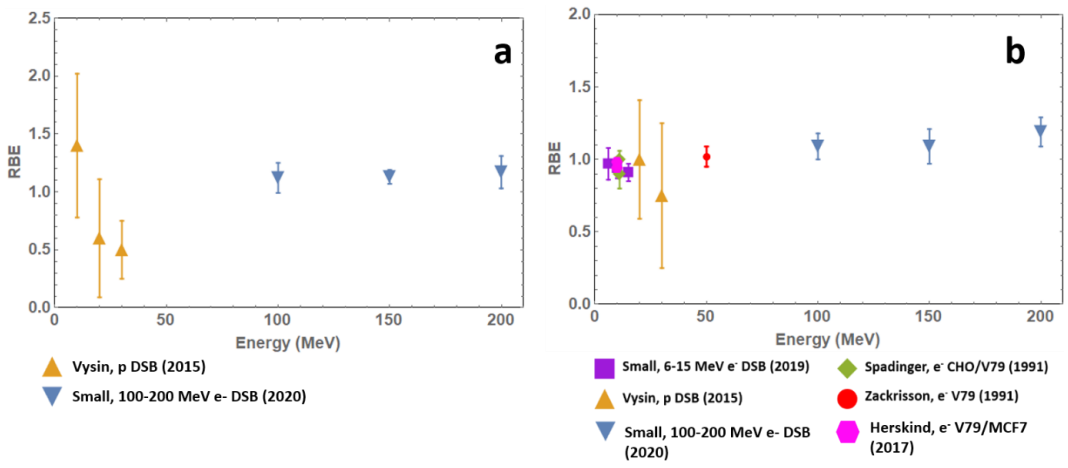

Figure 3 - RBE values for a) VHEE and protons with dry plasmid DSB yield as the biological endpoint and b) VHEE, low-energy electrons and protons with wet plasmid DSB yield (Small, Vysin, CLEAR) or cell survival fraction (Herskind, Spadinger, Zackrisson) as the biological endpoint. Experimental data taken from references 35-38

Table 5 – RBE for various particle modalities with particle, energy and biological endpoint specified. Standard error of the mean for Small data calculated based on gel repeats. RBE data taken or calculated from references 27-31. All RBE calculations relative to ^{60}Co X-ray data unless specified

Particle	Energy (MeV)	RBE	Biological Endpoint
e^- (This work, CLEAR)	100	1.12 ± 0.13 1.09 ± 0.09	Dry plasmid DSB yield Wet plasmid DSB yield
	150	1.13± 0.06 1.09 ± 0.12	Dry plasmid DSB yield Wet plasmid DSB yield
	200	1.17 ± 0.14 1.19 ± 0.10	Dry plasmid DSB yield Wet plasmid DSB yield
e^- (Small)	6	0.97 ± 0.11	Wet plasmid DSB yield
	10	0.94 ± 0.07	Wet plasmid DSB yield
	15	0.91 ± 0.06	Wet plasmid DSB yield
e^- (Herskind)	10	0.94 ± 0.02 0.98 ± 0.01	V79 survival fraction = 0.0003 (rel. to 6 MV X-rays) MCF7 survival fraction = 0.0003 (rel. to 6 MV X-rays)
e^- (Spadinger)	11	1.1 ± 0.08 1.0 ± 0.04 1.0 ± 0.06 0.9 ± 0.1	V79 survival fraction of 0.1 (0-10 Gy) CHO survival fraction of 0.1 (0-10 Gy) V79 survival fraction of 0.1 (0-3 Gy) CHO survival fraction of 0.1 (0-3 Gy)
e^- (Zackinsson)	50	1.03 ± 0.08 1.02 ± 0.07	V79 survival fraction of 0.1 (rel. to 4 MV X-rays) V79 survival fraction of 0.01 (rel. to 4 MV X-rays)
p (Vysin)	10	1.4 ± 0.62	Dry plasmid DSB yield
	20	1.00 ± 0.41 0.6 ± 0.51	Wet plasmid DSB yield Dry plasmid DSB yield
	30	0.75 ± 0.5 0.5 ± 0.25	Wet plasmid DSB yield Dry plasmid DSB yield
X-rays (Zackinsson)	20	0.99 ± 0.07 1.00 ± 0.05	V79 survival fraction of 0.1 (rel. to 4 MV X-rays) V79 survival fraction of 0.01 (rel. to 4 MV X-rays)
	50	1.14 ± 0.07 1.12 ± 0.05	V79 survival fraction of 0.1 (rel. to 4 MV X-rays) V79 survival fraction of 0.01 (rel. to 4 MV X-rays)

Comparison of GEANT4-DNA and Experimental DSB Yields

Experimental DSB data was then compared to GEANT4-DNA simulation data, modelling dry plasmid irradiation with VHEE beams at the same energies as those used at CLEAR. DSB data was chosen as experimental SSB data is likely to be less reliable due to transportation effects. As the parameters based on Henthorn's earlier work on protons resulted in a significant underestimate in DSB yield compared with experimental data for electrons, a parameter variation study was performed. The geometry, damage scoring method and base pair separation were varied according to similar studies on DNA damage modelling[39-41] to determine the optimal conditions for simulating plasmid damage with GEANT4-DNA following electron irradiation. This study indicated that use of the energy threshold damage mechanism at 8.22 eV with a separation of 10 bp for DSB induction results in DSB yields which most closely approximated experimental data (Fig. 4), with a more complete set of results available in the Supplementary Material (SF1-3).

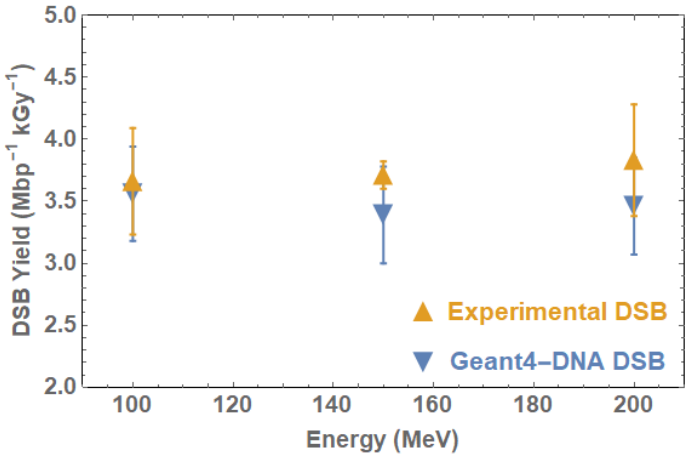

Figure 4 – Double-strand break yields for experimental and computational plasmid DNA irradiation with 100-200 MeV electrons. Geant4-DNA simulation performed with half-cylinder DNA geometry with a 10 bp separation defined for DSB induction and damage determined by an energy threshold of 8.22 eV. Standard errors calculated based on 10^3 repeats

Discussion

This work presents the results of the first plasmid irradiation experiments using VHEE at the CLEAR user facility with the aims of investigating the physical and chemical damage caused to DNA following VHEE irradiation. pBR322 plasmids were irradiated in both dry and aqueous environments to investigate the contributions from direct and indirect radiation effects arising from the production of hydroxyl and other radicals. The effect of dose-rate variation was also studied at the DNA damage level, following the rapid resurgence of FLASH radiotherapy and the potential suitability of VHEE as a FLASH radiotherapy modality. DSB yields were then used as the biological endpoint to calculate VHEE RBE.

pBR322 plasmids irradiated in dry and aqueous environments showed little variation in DSB induction over 100-200 MeV, likely due to there being correspondingly little variation in LET (0.220-0.226 keV/μm). Significant variation was observed in the dry SSB yield with electron energy. Relaxing of the supercoiled form of the plasmid to the open circular form was found to have occurred during transportation, resulting in a higher proportion of the plasmid being in an open-circular state before irradiation. For future experiments, it would be recommended that the pBR322 plasmid be shipped directly from New England BioLabs to the facility in the buffer to prevent relaxation and ensure the reliability of SSB measurement.

Comparison of the break yields in aqueous and dry environments allowed the contribution of indirect radiation effects to induced DNA damage to be measured. As anticipated, SSB and DSB yields indicate that indirect effects are the primary cause of DNA damage, causing in excess of 99% of damages. While this seems to contradict the conclusions of Ward *et al*[42]. that indirect effects contribute to ~65% of total radiation effects, it is important to note that Ward's conclusion is based on irradiation of cells, which typically have a scavenging capacity of approximately 200 times that of the diluted aqueous plasmid solution in this study (1mM Tris). As more radicals are able to cause DNA damage in this plasmid solution, a significantly higher proportion of indirect damage is therefore measured. These results are consistent with Vysin's measurements of the direct and indirect effect contributions to proton damage of plasmids, but are not directly translatable to cells or tissues due to the significantly lower scavenging capacity.

The effect of dose rate on the irradiation of aqueous plasmids was also investigated, with the aim to determine whether a 'FLASH' effect could be observed at the nanoscopic level, in the form of variation in DSB yields following irradiation at conventional or ultra-high dose rates. Fig. 2b indicates that there is no statistically significant variation in DSB yield with dose rate. This result is in agreement with our hypothesis that significant DSB variation would not be observed between plasmids irradiated by VHEE at conventional and ultra-high dose rates due to the lack of key experimental features which are the cause of the FLASH effect, notably the use of oxygenated purified water, and room temperature (25^{o}C) environment. This conclusion is similar to those drawn by other ultra-high dose rate radiobiological studies, though this is understood to be the first study of its kind involving ultra-high dose rate irradiation of plasmid DNA with VHEE. As VHEE is an increasingly popular potential modality for FLASH therapy, a fundamental understanding of the physical effects of FLASH irradiation is crucial.

DSB yields from the dry plasmid irradiation and conventional wet plasmid irradiation experiments were used as the biological endpoint for RBE calculation and compared with RBE of other radiotherapy modalities. VHEE RBE_{DSB} was found to be close to 1 for dry plasmids and 1.1-1.2 for wet plasmids. Comparison with values for clinical electrons suggests that electron RBE may increase with energy.

GEANT4-DNA simulations were carried out in parallel, modelling dry plasmid irradiation with 100-200 MeV electrons to determine the model parameters which could best approximate the experimental conditions. The results of plasmid irradiation simulations indicate that a DNA model built using half-cylinder geometry with damage scored using an energy threshold of 8.22 eV and in which DSBs are induced when two SSBs occur within a separation of 10 base pairs, most closely approximates the CLEAR data. The parameters used here are similar, with small differences, compared to previous *in silico* studies based on literature-reported experimental data using other radiation modalities including protons, albeit with large variation across datasets. Small differences are likely due to differences between experimental and *in silico* configuration.

In conclusion, a set of plasmid irradiation experiments was successfully performed at the CLEAR user facility using 100-200 MeV electrons. Little DSB yield variation was observed over the energy (and therefore LET) range. Indirect effects were calculated to contribute >99% of observed plasmid breaks, consistent with observations for other modalities. No significant variation in damage yield was observed with dose-rate variation, indicating that a FLASH effect is not present, at least for VHEE, at the nanoscale within the plasmid irradiations. Finally, it has been shown, through RBE_{DSB} calculations, that the physical damage caused to DNA by VHEE is similar to that caused by ^{60}Co X-rays and low-energy electrons. This provides an indication that more complex biological effects such as cell death could also be similar. This is a key initial pre-clinical step on the way to clinical implementation of VHEE radiotherapy.

Methods

Plasmid Sample Setup

pBR322 plasmid DNA (New England Biolabs) isolated from *E.Coli* (4361 base pairs)[30] was used in this study. This cloning vector has been extensively used as a plasmid model system in irradiation studies irradiation studies[38,44], allowing direct comparison to be made between this and earlier studies. The plasmid, in solution containing 10mM Tris-HCl and 1mM EDTA buffers to prevent degradation during freeze-thaw cycles, was diluted with purified water from 1000 ng/µl to 100 ng/µl. New England BioLabs quotes that ~90% of the plasmid is in a supercoiled (undamaged) form. Agarose gel electrophoresis confirmed that between 85 and 90% of the unirradiated plasmid was in this form.

Dry samples were prepared by pipetting 5 µl droplets of 100 ng/µl plasmid DNA directly on to the centre of Permafrost glass microscope slides (25 x 75 x 1 mm^3, Thermo Fisher Scientific). The droplets were left to dry at room temperature, leaving a thin layer of DNA on the slide. Aqueous samples were held in sealed 1.5 ml Eppendorf tubes, with each tube containing 30 µl of plasmid solution at 100 ng/µl. All samples were stored at -20ºC before and after irradiation.

Irradiation Setup

Plasmid irradiations were carried out at the CLEAR user facility (CERN, Geneva), an S-band linear accelerator designed primarily for research and development applications[21,22]. CLEAR is housed in the previous CLEX experimental area and consists of the 25 m CALIFES (*Concept d'Accélérateur Linéare pour Faisceau d'Electron Sonde*) injector, adapted from previous use to test and prove the feasibility of novel two-beam accelerator technology, and a 16 m user beamline. The beamline has two experimental areas, with the in-air beam end area selected for this experiment (see Fig. 5).

The CLEAR user facility was chosen for VHEE plasmid irradiation experiments as it can produce stable high-energy electron beams over an energy range of 60-220 MeV, with readily adaptable beam size, bunch charge and energy – see Table 6 for a full description of beam parameters. CLEAR also has a strong history of VHEE experiments over recent years, including inhomogeneity sensitivity and dosimetry studies from the University of Manchester[6,45,46].

The experiment was built in the in-air test area, a 1 m space beyond the exit window through which the beam travels before reaching a concrete beam dump. Beam energy and bunch charge were measured using a dipole spectrometer and a Bergoz Integrated Current Transformer respectively. A YAG screen, placed approximately 2 cm behind the plasmid samples measured the beam size, shape and position. Lead bricks provided shielding from secondary X-rays, with a small opening allowing the beam to reach the samples.

Table 6 – CLEAR beam parameters primarily taken from Gamba *et al.*[21] and Sjobak *et al.*[22] Beam charge and repetition rate updated based on current availability

Parameter	Value
Beam Energy	60-220 MeV
Bunch Charge	0.001-10 nC
No. Bunches	Variable: 0- >200
Beam Repetition Rate	0.833-10 Hz
Bunch Repetition Rate	1.5 GHz (high bunch charge) 3 GHz (low bunch charge)
RMS Energy Spread	< 0.2%
Typical Dose per Shot	34.29 Gy/shot (200 MeV, dry) 0.69 Gy/shot (200 MeV, wet, Conv)

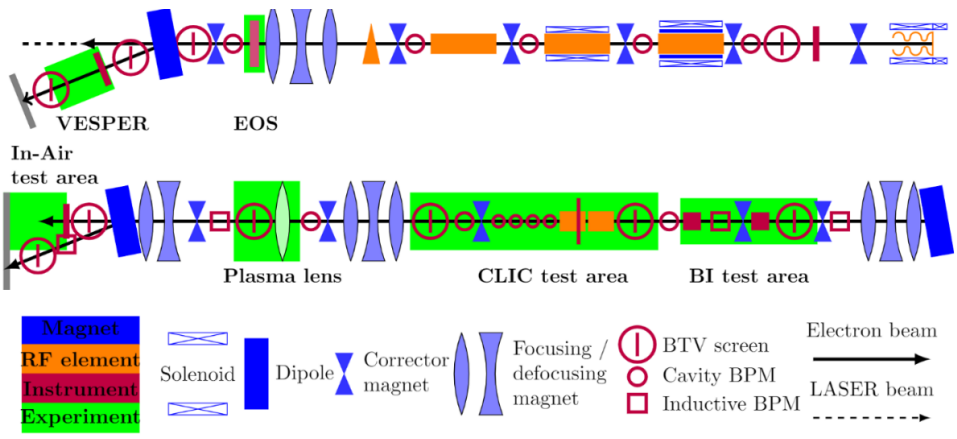

Figure 5 - Schematic of the CLEAR beamline and two experimental areas, Figure produced by Kyrre Sjobak [22] and reproduced here with kind permission from Kyrre Sjobak

Dry samples were slotted into a 3D-printed polylactic acid (PLA) slide holder, custom-designed and built at the Cockcroft Institute. This was mounted on to a transversely moving stage placed in front of the beam, presenting each sample to the beam in turn. Dry samples were irradiated at 100, 150 and 200 MeV over a dose range of 1000 – 6000 Gy with 3 repeats made for each energy and each dose rate. A schematic and image of the dry experiment setup is shown in Fig. 6.

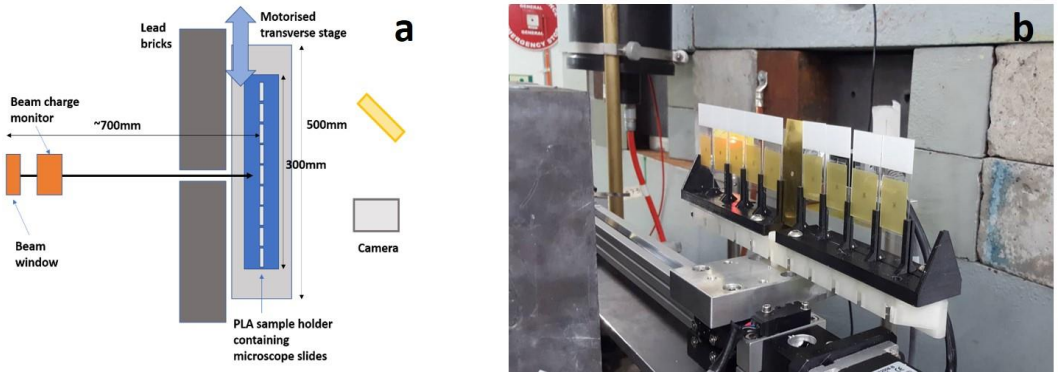

Figure 6 – a) Schematic (produced by author K.L.S.) and b) photograph (taken by author K.L.S.) of experimental set-up for irradiation of dry plasmid samples on glass microscope slides. EBT-XD film placed behind samples to show sample coverage by beam

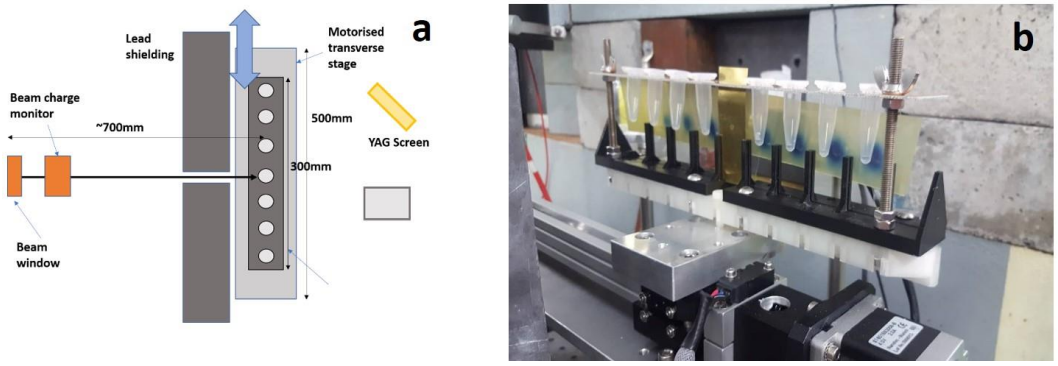

Figure 7 - a) Schematic (produced by author K.L.S. and b) photograph (taken by author K.L.S.) of experimental set-up for irradiation of wet plasmid samples in Eppendorf tubes. EBT-XD film placed behind samples to determine dose delivered to samples

Aqueous samples were held in 1.5 ml sealed Eppendorf tubes and mounted in an aluminium tube holder (see Fig. 7), with irradiation carried out in a similar manner to the dry samples. The samples were again irradiated at 100, 150 and 200 MeV, over a dose range of 0 – 50 Gy. The difference in dose between dry and aqueous samples arises due to the contribution of direct and indirect effects. To generate observable levels of damage, dry samples must receive a significantly higher dose.

To determine the charge required to deliver the required dose, simulations of the dry and aqueous experimental setups were performed in TOPAS. The dose delivered by 10^7 electrons was recorded, scaled up to the required dose and the corresponding charge determined. This method has been verified to within a maximum error of 5.26% by Lagzda *et al.*[6,45,46]. For both dry and wet irradiations, EBT-XD film, a radiochromic film commonly used in radiotherapy dosimetry with a dynamic range of 0.1-60 Gy[47], was placed behind the samples. For the aqueous samples, the film was used to determine the dose delivered to the film, based on 15 MeV electron beam calibration performed at the Christie NHS Foundation Trust using a Varian treatment linac. For the dry samples the film was used to confirm sample coverage only as the dynamic dose range of the film (0-60 Gy) is too low, with dose instead determined from the beam fluence, with beam σ measured using a YAG screen and charge from the beam measured using an ICT. TOPAS simulations revealed a 13-14% difference in dose across the glass slide, which was accounted for in final dose calculations. Further detail is given in the Supplementary material (SF4).

The effect of conventional and FLASH-level dose rates was investigated for aqueous samples to determine if a FLASH effect could be observed at the DNA damage level. The FLASH dose rates were reached by increasing the bunch charge and delivering the radiation in ultra-short (~ps) single pulses, resulting in dose rates calculated using individual bunch duration in excess of 10^8 Gy/s.

Agarose Gel Electrophoresis (AGE)

Unirradiated plasmid DNA exists in an undamaged, or supercoiled (SC), state. Ionising radiation causes SSBs and DSBs within the DNA, detectable as a change in the plasmid form. Open-circular (OC) plasmid results from a SSB, due to relaxation of the SC DNA. DSBs are detectable as linear (L) forms of plasmid[14]. Determination of plasmid forms was assessed through AGE.

Dry samples were recovered from the glass slides using 5 µl of purified water and the 30 µl aqueous samples were split into six 5 µl sub-samples. Each sample was mixed with 1 µl gel loading dye and loaded into 5 mm wells in a 1% w/v agarose gel in 1x TAE buffer stained with 20 µl SYBR Green. The gel was submerged in 0.5x TAE buffer and a 100 V voltage applied. The gel was run for 120 minutes or until the samples had migrated 70–80% through the gel. The gels were imaged using a ChemiDoc MP UV imager (BioRad). The plasmid forms appear as distinct bands along the gel (Fig. 8a). Fiji[48], an open-source image processing package based on ImageJ was used to determine the relative intensities of these bands for each sample, normalised with respect to the most intense band. The proportion of each plasmid form was calculated by integrating the signal over each band.

Modelling Plasmid Damage

While several potential fitting methods[49] are available to determine the yield of SSB and DSBs on DNA, the McMahon[32] fit was selected for this study based on it being specifically developed for fitting plasmid form proportion data obtained from AGE after irradiation and following a study by Vysin[31] on the robustness of different fits. The plasmid data are fitted to the following equations:

$$SC(D) = S_0 e^{-(\mu D + \phi D)} \quad (2)$$

$$OC(D) = e^{-\phi D}\left[e^{-\frac{1}{2}\mu^2 \rho D^2}(S_0 + C_0) - S_0 e^{-\mu D}\right] \quad (3)$$

$$L(D) = 1 - (S_0 + C_0)e^{-\left(\phi D + \frac{1}{2}\mu^2 \rho D^2\right)} \quad (4)$$

where $SC(D)$, $OC(D)$ and $L(D)$ are the proportion of supercoiled, open-circular and linear plasmid respectively after irradiation of dose D in Gy, μ and ϕ are the average SSB and DSB yields (Mbp^{-1} Gy^{-1}), S_0 and C_0 are the supercoiled and open-circular proportions at zero dose and ρ is the probability of a DSB arising due to two SSBs on opposite DNA strands within 10 base pairs. pBR322 plasmid consists of 4361 base pairs, giving ρ = 10/4361.

Fig. 8b shows the proportions of SC, OC and L plasmid forms as a function of dose. A least-square error non-linear fit was made to the SC and OC equations to obtain the SSB and DSB yields (μ and φ resepectively). The agreement between the L equation and the linear plasmid data, as observed in Fig. 8b, indicates the efficacy of the McMahon fit.

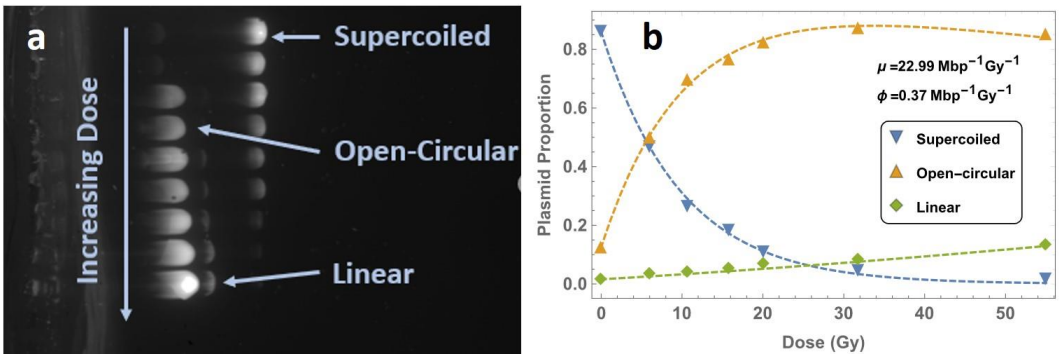

Figure 8 - a) Cropped UV image of agarose gel following electrophoresis containing wet plasmids irradiated by 100 MeV electrons. Labelled bands indicate presence of SC, OC and L plasmid forms. Uncropped image shown in SF5. b) SC, OC and L plasmid proportions as a function of dose following integration of band intensities, fitted to equations 2, 3 and 4. Error bars calculated based on five gel repeats

Plasmid Irradiation Simulations with GEANT4-DNA

Plasmid irradiation simulations were carried out to compare DNA damage yields with those obtained from experimental studies. The simulations were carried out using GEANT4-DNA, a module based on the Monte-Carlo particle tracking code GEANT4 (version 10.02-patch01)[50] designed to model biological damage induced by ionising radiation at the DNA scale[51-54].

The simulation is based on a plasmid irradiation model designed originally for interaction of proton beams with DNA by Henthorn *et al.*[55]. pBR322 plasmid DNA, consisting of 4361 base pairs and with radius 236 nm, was built and interaction with monoenergetic electron beams simulated. The GEANT4-DNA default physics list is capable of simulating electrons up to 1 MeV so, to allow use with high energy electrons, the Livermore physics list (G4EmLivermorePhysics) for electrons with energy > 1 MeV was added[56], with the energy range over which the model functions set to 1-300 MeV.

The irradiation model consists of a circular plasmid placed on a glass slab of density 2.23 g/cm^3, representing the microscope slide, held within air. The plasmid DNA is built based on a half-cylindrical geometry, as proposed by Charlton *et al.*[57]. As a simplification, the plasmid geometry is modelled as a closed circle, similar to the approach of McNamara *et al.*[58] with the simplified DNA geometry (half-cylinder) as published by Bernal[59]. Each discrete half cylinder is numbered to determine the base pair position on the plasmid. The

electron beam is directed perpendicular to the plasmid. Dose to the dry samples was calculated based on the beam fluence, determined using CLEAR beam diagnostics. As the simulation consisted of a single plasmid, the beam radius was scaled down to 300 nm. To ensure the same beam fluence as in the experiment, the number of particles N required to deliver the correct dose was calculated using the following:

$$N = \frac{\pi D \rho r^2}{10^9 eL} \quad (5)$$

where L is the electron LET in units of keV/μm, D is the radiation dose in Gray, r is the beam radius in m and ρ is the DNA density, set at 1407 kg m^{-3}.

DNA damage is scored using the same approach as Henthorn[47] of using two different energy deposition mechanisms to determine the sensitivity of DNA damage yield with energy deposition. The first is based on energy deposition corresponding to a damage probability which increases linearly from 0 to 1 over the energy range 5-37.5 eV, informed by photon and low energy electron DNA damage studies[60]. The second is based on an energy threshold – an energy deposition over this threshold is considered to have caused damage to the DNA. A commonly used value is 17.5 eV[40], though a review of several studies has shown a range of 8.22-22.5 eV in use[41].

The damages scored on the DNA volumes are defined as SSBs. DSBs are determined through a clustering algorithm searching for SSBs which have occurred on opposite DNA strands within a specified distance. Output files show the damage data as the number of damages occurring in a single run. The average DSB yields over 10^3 runs are reported per Mbp per kGy.

References

[1] National Cancer Registration & Analysis Service and Cancer Research UK. Chemotherapy, Radiotherapy and Tumour Resections in England: 2013-2014 Workbook. http://www.ncin.org.uk/cancer_type_and_topic_specific_work/topic_specific_work/main_cancer_treatments (2017)

[2] NHS. (2020). *Proton beam therapy.* Available: https://www.england.nhs.uk/commissioning/spec-services/highly-spec-services/pbt/. Last accessed 28th Jul 2020.

[3] Jones, R. M. Wakefield suppression in high gradient linacs for lepton linear colliders. *Phys. Rev. ST Accel. Beams* **12,** 104801 (2009)

[4] Jones, R. M. *et al.* Influence of fabrication errors on wake function suppression in NC X-band accelerating structures for linear colliders. *New J. Phys.* **11** (2009)

[5] DesRosiers, C., Moskvin, V., Bielajew, A. F. & Papiez, L. 150-250 MeV electron beams in radiation therapy. *Phys Med Biol.* **45,** 1781-1805 (2000)

[6] Lagzda, A. *et al.* Very-high energy electron (VHEE) studies at CERN'S CLEAR user facility. *Proc. 9th Int. Particle Accelerator Conf.* (2018)

[7] Bazalova-Carter, M. *et al.* Treatment planning for radiotherapy with very high-energy electron beams and comparison of VHEE and VMAT plans. *Med. Phys.* **42**, 2615-2625 (2015)

[8] Vozenin, M. C., Hendry, J. H., Limoli, C. L. Biological benefits of ultra-high dose rate FLASH radiotherapy: Sleeping Beauty awoken. *Clinical Oncology*. **31** 407-415 (2019)

[9] Favaudon, V. *et al.* Ultrahigh dose-rate FLASH irradiation increases the differential response between normal and tumour tissue in mice. *Sci. Transl. Med.* **6,** 1-9 (2014)

[10] Monte-Gruel, P. Irradiation in a FLASH: Unique sparing of memory in mice after whole-brain irradiation with dose rates above 100 Gy/s. *Radiotherapy and Oncology* **124,** 365-369 (2017)

[11] Vozenin, M. C. *et al.* The advantage of FLASH radiotherapy confirmed in mini-pig and cat-cancer patients. *Clinical Cancer Research* **25,** 35-42 (2018)

[12] Bourhis, J. *et al.* Treatment of a first patient with FLASH-radiotherapy. *Radiotherapy and Oncology* **139,** 18-22 (2019)

[13] Maxim, P. G., Tantawi, S. G., Loo, B. W. PHASER: A platform for clinical translation of FLASH cancer radiotherapy. *Radiotherapy and Oncology* **139,** 28-33 (2019)

[14] Scholes, G., Ward, J. F., Weiss, J. Mechanism of the radiation-induced degradation of nucleic acids. *J. Mol. Biol.* **2** 379-391 (1960)

[15] Suntharalingam, N., Podgorsak, E. B., Hendry, J. H. (2005). 14. Basic Radiobiology. In: *Radiation Oncology Physics: A Handbook for Teachers and Students*. (Vienna: International Atomic Energy Agency) 485-504

[16] Chang, D. S., Lasley, F. D., Das, I. J., Mendonca, M. S., Dynlacht, J. R. Molecular mechanisms of DNA damage and repair in: *Basic radiotherapy physics and biology* 201-208 (Springer, 2014)

[17] Eriksson, D., Stigbrand, T. Radiation-induced cell death mechanisms. *Tumor Biol.* **31** 363-372 (2010)

[18] Nikjoo, H., Lindborg, L. RBE of low energy electrons and photons. *Phys. Med. Biol.* **55** 65-109 (2010)

[19] Paganetti, H., Relative biological effectiveness (RBE) values for proton therapy. Variations as a function of biological endpoint, dose and linear energy transfer. *Phys. Med. Biol.* **59,** R419-R472 (2014)

[20] Thomas, C. M., Summers, D. Bacterial Plasmids in: *Encyclopedia of Life Sciences (ELS).* (John Wiley and Sons, Ltd, 2018)

[21] Gamba, D. *et al.* The CLEAR user facility at CERN. *Nuclear Inst. and Methods in Physics Research A.* **909,** 480-483 (2018)

[22] Sjobak, K. N. *et al.* Status of the CLEAR electron beam user facility at CERN. *Proc. 10th Int. Particle Accelerator Conf.* (2019)

[23] Town, C. D. Effect of high dose rates on survival of mammalian cells. *Nature.* **215,** 847-848 (1967)

[24] Beyreuther, E. *et al.* Radiobiological response to ultra-short pulsed megavoltage electron beams of ultra-high pulse dose rate. *Int. J. Radiat. Biol.* **91(8),** 643-652 (2015)

[25] Babayan, N. *et al.* Dose-rate effect of ultrashort electron beam radiation on DNA damage and repair *in vitro*. *Radiation Research.* **58(6),** 894-897 (2017)

[26] Rigaud, O. *et al.* Exploring ultrashort high-energy electron-induced damage in human carcinoma cells. *Cell Death and Disease.* **1** (2010)

[27] Yogo, A. *et al.* Application of laser-accelerated protons to the demonstration of DNA double-strand breaks in human cancer cells. *Appl. Phys. Lett.* **95,** 181502 (2009)

[28] Hanton, F. *et al.* DNA DSB repair dynamics following irradiation with laser-driven protons at ultra-high dose rates. *Sci. Rep.* **9,** 4471 (2019)

[29] Ozols, A., Prise, K., Michael, B. D. A comparison of the radiosensitivity of relaxed and supercoiled plasmid DNA. *Int. J. Radiat. Biol.* **75(1),** 83-90 (1999)

[30] pBR322 Vector. *New England BioLabs.* https://www.neb.uk.com/products/neb-catalogue/nucleic-acids-%28cloning%29/pbr322-vector (2020)

[31] Bolivar, F. *et al.* Construction and characterization of new cloning vehicles. II. A multipurpose cloning system. *Gene*. **2,** 95–113 (1977)

[32] McMahon, S. J., Currell, F. J. A robust curve-fitting procedure for the analysis of plasmid DNA strand break data from gel electrophoresis. *Radiat. Res.* **175,** 797-805 (2011)

[33] Ou, H. *et al.* Monte Carlo simulation of the relative biological effectiveness and DNA damage from a 400 MeV/u carbon ion beam in water. *Applied Radiation and Isotopes.* **136** 1–92 (2018)

[34] Small. K., *et al.* A comparative study of biological effects of electrons and Co-60 gamma rays on pBR322 plasmid DNA. *Proc. 10th Int. Particle Accelerator Conf.* (2019)

[35] Herskind, C. *et al.* Biology of high single doses of IORT: RBE, 5 R's and other biological aspects. *Radiation Oncology.* **12(24)** 1-14 (2017)

[36] Spadinger, I., Palcic, B. The relative biological effectiveness of ^{60}Co γ-rays, 55 kVp X-rays, 250 kVp X-rays and 11 MeV electrons at low doses. *Int. J. Radiat. Biol.* **61(3)** (1992)

[37] Zackrisson, B. *et al.* Relative biological effectiveness of high-energy photons (up to 50 MV) and electrons (50 MeV). *Radiation Research.* **128(2)** 192-196 (1991)

[38] Vysin, L. *et al.* Proton-induced direct and indirect damage of plasmid DNA. *Radiat. Environ. Biophys.* **54,** 343-352 (2015)

[39] Henthorn, N. T. *et al.* Clinically relevant nanodosimetric simulation of DNA damage complexity from photons and protons. *RSC Adv.* **9,** 6845-6858 (2019)

[40] Nikjoo, H, *et al.* Modelling of Auger-induced DNA damage by incorporated 125I. *Acta Oncol.* **35,** 849–856 (1996)

[41] Konstantinos, P. *et al.* Quantification of DNA double-strand breaks using Geant4-DNA. *Med. Phys.* **46(1),** 405-413 (2018)

[42] Ward, J. F. Biochemistry of DNA Lesions. *Radiat. Res.,* **Suppl. 8**(104) 103-111 (1985)

[43] Hayes, F. The function and organisation of plasmids. In: *E. coli plasmid vectors*. (Humana Press Inc., 2003) 1-18.

[44] Leloup, C. *et al.* Evaluation of lesion clustering in irradiated plasmid DNA. *Int. J. Radiat. Biol.* **81,** 41-54 (2005)

[45] Lagzda, A., Angal-Kalinin, D., Jones, J. K., Jones, R. M. & K. Kirkby. Relative insensitivity to inhomogeneities on very high energy electron dose distributions. *Proc. 8th Int. Particle Accelerator Conf.* (2017)

[46] Lagzda, A. *et al.* Influence of heterogeneous media on Very High Energy Electron (VHEE) dose penetration and a Monte Carlo-based comparison with existing radiotherapy modalities. *Nuclear Inst. and Methods in Physics Research, B.* **482**, 70-81 (2020)

[47] GAFChromic EBT-XD film specifications, Available at www.gafchromic.com

[48] Schindelin, J. et al. Fiji - an open platform for biological image analysis. Nat. Methods 9, (2009).

[49] Cowan, R., Collis, C. M., Grigg, G. W. Breakage of double-stranded DNA due to single-stranded nicking. *J. Theor. Biol.* **127,** 227-245 (1987)

[50] Agostinelli, S. *et al.* GEANT4 – A simulation toolkit. *Nuclear Inst. and Methods in Physics Research A.* **506,** 250-303 (2003)

[51] Incerti, S. *et al.* Geant4-DNA example applications for track structure simulations in liquid water: a report from the Geant4-DNA Project. *Med. Phys.* **45,** 722-739

[52] Bernal, M. A. *et al.* Track structure modeling in liquid water: A review of the Geant4-DNA very low energy extension of the Geant4 Monte Carlo simulation toolkit. *Phys. Med.* **31,** 861-874 (2015)

[53] Incerti, S. *et al*. Comparison of Geant4 very low energy cross section models with experimental data in water. *Med. Phys.* **37,** 4692-4708 (2010)

[54] Incerti, S. *et al.* The Geant4-DNA project. *Int. J. Model. Simul. Sci. Comput.* **1,** 157-178 (2010)

[55] Henthorn, N. T. *et al.* Clinically relevant nanodosimetric simulation of DNA damage complexity from photons and protons. *RSC Adv.* **9,** 6845-6858 (2019)

[56] Sotiropoulos, M. *et al.* Modelling direct DNA damage for gold nanoparticle enhanced proton therapy. *Nanoscale*. **9**, 18413–18422 (2017).

[57] Charlton, D. E., Nikjoo, H., Humm, J. L. Calculation of Initial Yields of Single- and Double-strand Breaks in Cell Nuclei from Electrons, Protons and Alpha Particles. *Int. J. Radiat. Biol*. **56,** 1–19 (1989)

[58] McNamara, A. L. *et al.* Validation of the radiobiology toolkit TOPAS-nBio in simple DNA geometries. *Phys. Med.* **33,** 207–215 (2016)

[59] Bernal, M. A., Liendo, J. A. An investigation on the capabilities of the PENELOPE MC code in nanodosimetry. *Med. Phys*. **36,** 620–625 (2009)

[60] Prise, K. *et al.* Critical energies for SSB and DSB induction in plasmid DNA by low-energy photons: action spectra for strand-break induction in plasmid DNA irradiated in vacuum. *Int. J. Radiat. Biol.* **76,** 881–890 (2000)

Author Contributions

Plasmid irradiation experiment was designed by K.L.S. with contributions to the conceptual development of the work by D.A-K., K.J.K., W.F., M.S., J.J., M.J.M. and R.M.J. Apparatus designed by K.L.S. and produced by R.J.S. Experiment carried out by K.L.S., N.T.H. and the CLEAR group (W.F., R.C., D.G., A.G.). Plasmid analysis carried out by K.L.S. and N.T.H., trained and supported by A.C. and E.S. EBT-XD film analysis carried out with A.A. Simulations performed by K.L.S. using code developed by N.T.H., K.L.S. and R.M.J. Supervision provided throughout by R.M.J. and M.J.M. K.L.S. wrote the main manuscript, with reviews by all authors.

Acknowledgements

This research was co-funded by the Cockcroft Institute of Science and Technology/ASTeC STFC core grant and the EPSRC Grand Challenge Network+ in Proton Therapy (grant no. EP/N027167/1). In addition, R.M.J. is pleased to acknowledge support via an STFC IAA (Impact Acceleration Account) 2015 grant. N.T.H. would like to acknowledge financial support from the European Union's Horizon 2020 research and innovation programme under grant agreement no. 730983. M.J.M. would like to acknowledge some financial support from the NIHR Manchester Biomedical Research Centre (grant no. BRC-1215-20007). The authors acknowledge the GMEE for supporting the research of A.G.